Clinically Feasible Model-Based Methods to Guide Cardiovascular Fluid Therapy in the ICU

Liam Murphy

A thesis submitted for the degree of

Doctor of Philosophy

in

Mechanical Engineering at the

University of Canterbury,

Christchurch, New Zealand

31 May 2022

Acknowledgements

I would like to thank a number of people who supported me along the journey of completing this thesis.

To Geoff Chase, and the rest of my supervisory team. Thank you for giving me the idea to pursue a PhD in the first place. For letting me pursue the areas of research I found most interesting, and for your guidance in the face of the extensive and varying area of research of biomedical research. To Shaun Davidson, thank you for all your help in the early stages of my PhD journey. It is easy to feel overwhelmed in the early days when everything is new and your guidance was much appreciated.

To Geoff Shaw for allowing me to come into the ICU and access the data that was critical to the completion of this work. And for the introduction to the intensive care unit, giving me context on how my work can actually make a difference.

To my family, completing this thesis was only possible with your help. From the trips you have made to see me, to the packages that turned up on my doorstep, your unconditional

support allowed me to keep moving forward during the stressful times, and be able to truly appreciate it when things were working well.

Finally, to all my friends. Completing this thesis wouldn't have the same feel to it unless I had you all to share it with. I couldn't ask for better group of people to have around me throughout this journey.

Contents

List of Figures

List of Tables

Acronyms and abbreviations

AI_x	Augmentation index
BSA	Body surface area
CO	Cardiac output
CVS	Cardiovascular system
ECG	electrocardiogram
EDPVR	End-diastolic pressure-volume relation
ESPVR	End-systolic pressure-volume relation
E_{ao}	Arterial elastance
E_{es}	End-systolic elastance
E_{lv}	Left ventricle elastance
E_{vc}	Venous elastance
FO	Fluid overload
HR	Heart rate
ICU	Intensive care unit
MCFP	Mean circulatory filling pressure
MSFP	Mean systemic filling pressure
PEEP	Positive end-expiratory pressure
PP	Pulse pressure

PPV	Pulse pressure variation
PTT	Pulse transit time
PWA	Pulse wave analysis
P-V	Pressure-volume
$P_{ao,est}$	Estimated aortic pressure using an arterial transfer function
$P_{lv,es}$	Left ventricle end-systolic pressure
$P_{lv,est}$	Estimated left ventricle pressure
$P_{ao,int}$	Initial aortic pressure approximation
$P_{ao,mea}$	Measured aortic pressure
P_f	Forward travelling pressure wave
$P_{fe,mea}$	Measured femoral pressure
$P_{lv,mea}$	Measured left ventricle pressure
P_r	Reflected pressure wave
$P_{vc,mea}$	Measured venous pressure
$pSBP_2$	late systolic shoulder
$Q_{ao,est}$	Estimated component of central flow from transfer function
$Q_{ao,int}$	Initial quadrangular aortic flow approximation
$Q_{ao,mea}$	Measured aortic flow
Q_c	Circulatory flow
Q_f	Forward travelling flow wave
Q_i	Cardiac input flow
Q_o	Cardiac output flow
Q_r	Reflected flow wave
Q_{tri}	Triangular aortic flow approximation
RAP	Right atrial pressure
RM	Recruitment manoeuvre

RMSE	Root mean squared error
ROC	Receiver operating characteristic curve
R_c	Circulatory resistance
R_i	Cardiac input resistance
R_o	Cardiac output resistance
R_{vr}	Resistance to venous return
SBV	Stressed blood volume
SBV_{index}	Model-based stressed blood volume per kg bodyweight
SBV_m	Model-based stressed blood volume
SP	Systolic pressure
SPV	Systolic pressure variation
SV	Stroke volume
SV_{est}	Estimated stroke volume
SV_{mea}	Measured stroke volume
SVV	Stroke volume variation
TCM	Three-chambered model
TCM_{CM}	Three-chambered model, clinically feasible reference set
TCM_{FM}	Three-chambered model, full measurement reference set
TCM_{RM}	Three-chambered model, reduced measurement reference set
TF	Transfer function
TF_{SM}	Single-measurement transfer function method
TVE	Time-varying elastance
t_{es}	time of end-systole
VAC	Ventriculoarterial coupling
VR	Venous return
V_{es}	End-systolic volume

$V_{lv,est}$	Estimated left ventricle volume
$V_{lv,mea}$	Measured left ventricle volume
$V_{s,ao}$	Arterial chamber stressed volume
$V_{s,lv}$	Left ventricle chamber stressed volume
$V_{s,vc}$	Venous chamber stressed volume
V_u	Left Ventricle unstressed volume
WSA	Wave seperation analysis
Z_c	Characteristic impedance

Abstract

Fluid therapy is one of the most commonly used clinical procedures employed in the ICU to treat circulatory shock. Approximately 30% of ICU patients receive a fluid therapy at some stage during their stay, with 20% of patients reviving it on the day of admission. By increasing the total volume in the circulation, clinicians aim to stimulate an increase in cardiac output, helping restore or maintain adequate organ and tissue perfusion.

However, only ≈50% of patients receiving a fluid therapy will have also have the desired increase in cardiac output. Furthermore, excessive fluids have been strongly associated with worsened patient outcome and can negate the effects of earlier successful treatment. Therefore, knowledge of a patient's fluid responsiveness, prior to administering of treatment is essential for safe treatment.

Current, clinically used, indices of fluid responsiveness have a number of inherent limitations restricting their applicability or invalidating their use altogether. A recently developed model of the cardiovascular system showed a new index, model based stressed blood volume, to be a potential improvement over currently available indices, but required

measurements from inside the cardiac chambers and central arteries for identification, which are not available in standard ICU care.

This thesis develops a series of novel methods for estimating the required cardiovascular waveforms required for model identification from currently available clinical measurements. Thus, developing a clinically feasible model-based method to guide fluid therapy in the ICU.

The first part of this work introduces the relevant physiology of the cardiovascular system is introduced along with the principles of the circulation driving flow to and from the heart. Next, a brief overview of current indices of fluid responsiveness is given, highlighting their advantages and limitations. Stressed blood volume, in the context of fluid responsiveness, is also introduced. The three-chamber lumped parameter model of the cardiovascular system is then introduced. Each component of the model and all model equations, including the equations governing model dynamics and equations for initial parameter estimation, are detailed.

An initial study showing the implementation of the three chambered model is performed to highlight the clinical utility of identified parameters in assessing changes in patient condition. This study was performed on several porcine endotoxin experiments and provided the reference model parameters used to compare the final, clinically feasible method. A subsequent study is performed using the first method introduced to achieve clinical feasibility by removing the requirement of direct cardiac measurements by estimating left ventricle pressure and volume from aortic pressure.

Because aortic pressure is also not available in standard ICU environments, the next section of work aimed to develop a method of estimating central pressure. A tube-load model of the arterial system was used to develop and test a novel method of estimating central pressure from commonly available peripheral pressure measurements, via an arterial transfer function, and nothing else. The transfer corresponding flow waveforms were then used, with an initial calibration measurement, to estimate stroke volume in the porcine endotoxin experiments.

The final part of his thesis begins by consolidating all developed methods to identify the three-chambered model parameters from an anticipated clinically available subset of measurements from the porcine experiments. Finally, the model, and associated methods for estimating the required inputs, are used to assess fluid responsiveness in patient data obtained from the Christchurch hospital ICU in New Zealand.

Overall, this thesis provides a method of identifying the parameters of model of the cardiovascular system model from a minimal, currently available, set of clinical measurements. Model-based stressed blood volume, identified using the three-chambered model, has the physiological basis, animal study validation, and now clinical feasibility, to be considered a potential diagnostic tool in the ICU. The intrinsic relation between stressed blood volume, perfusion pressure and fluid responsiveness means the methods proposed in this thesis may significantly improve a clinicians ability to safely and effective guide fluid therapy.

Chapter 1

Physiology of the Cardiovascular System

1.1 Introduction

This Chapter presents a macro view of the cardiovascular system (CVS) and the components relevant to this work. First, an introduction to the relevant physiological components of the circulatory system are presented, including the vessels and chambers comprising it, and how blood travels through the heart. Second, the fundamental principles relating to circulatory function are discussed, emphasising those clinically employed to assess cardiovascular function. Finally, a brief description of circulatory shock is presented, with specific attention paid to septic shock as it relates to the experimental data sets used throughout this work.

Broadly speaking, the CVS is responsible for transporting blood throughout the body to deliver nutrients and remove waste products. Blood is transported through a series of variable sized *blood vessels* including the *arteries*, *veins* and *capillaries*, each with different mechanical properties according to their physiological location allowing the circulation to function properly. The entire CVS can be categorized by three general components: 1) the *systemic circulation*, which transports blood throughout the head and body; 2) *pulmonary circulation*, which delivers de-oxygenated blood from the body to the lungs for gas exchange; and 3) the *heart*, which provides the restorative force to maintain arterial blood pressure.

1.2 The Heart

The left and right sides of the heart are separated by a thick muscular wall of cardiac tissue called the *septum*, an extension of the heart walls. The left heart is responsible for receiving blood from the lungs and delivering it to the systemic circulation. The opposite is true for the right side, receiving blood from the body and delivering it to the pulmonary circulation for re-oxygenation. Both sides of the heart are separated into two chambers, two smaller chambers called the *atria*, which receives blood from their respective feeding veins, and two larger chambers called the *ventricles*, responsible for pumping blood into the circulations.

To ensure blood flows only in the desired direction, the heart has four valves. Separating the atria from the ventricles are the two *atrioventricular valves* called the *tricuspid* and *mitral* valves for the right and left sides, respectively. Two additional valves downstream

of the ventricles prevent blood from returning to the heart: 1) the aortic (systemic); 2) and pulmonary valves. These valves are referred to as the *semilunar valves*.

Both ventricles are primarily comprised of a thick, muscular contractile tissue called the *myocardium*. The myocardium of the left ventricle is thicker than the right ventricle as a greater force is required to be generated to force blood into the systemic circulation, compared to the pulmonary circulation. The whole heart in encapsulated in a fibrous membrane called the *pericardium*, which acts as a reaction wall for heart contraction.

1.3 Cardiac Cycle

The *cardiac cycle* describes a complete heartbeat including contraction and relaxation of the cardiac muscles, resulting in the ejection of blood from, and filling of, the heart. Two key terms are used to describe the respective phases of the cycle, *systole*, describing contraction of the ventricle and ejection of blood, and *diastole*, the relaxation of the heart and re-filling phase. Tracking phases of the cardiac cycle in a clinical setting is typically achieved using an *electrocardiogram (ECG)* to monitor the electrical signals of the heart [1]. This section will describe the four major phases of the cardiac cycle, illustrated in Figure 1.1, starting at ventricular filling.

1.3.1 Filling

Ventricular filling occurs as blood flows from the atria to the ventricles. The atrioventricular valves are necessarily open and the arterial valves closed. An initial passive filling

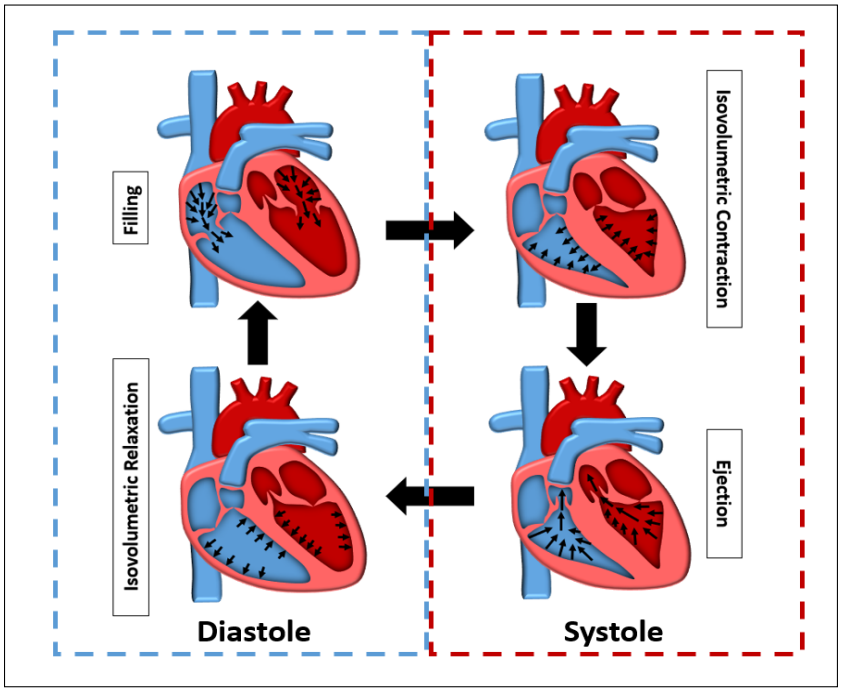

Figure 1.1: Diagram of the four general phases of the cardiac cycle.

stage occurs with blood flowing directly from the veins, through the atria, and into the ventricles. The increasing ventricular volume reduces the pressure differential between atria and ventricle, reducing flow rate. When flow nears zero the atria contract slightly forcing additional blood volume into the ventricle. Atrial contraction accounts for approximately 10% of ventricular filling in healthy subjects at rest and this contribution commonly increases with age.

1.3.2 Isovolumetric contraction

The initial contraction of the myocardium rapidly increases pressure in the ventricle to levels exceeding the atrium resulting in the atrioventricular valves closing. With all cardiac valves closed, including the ventricular valves located at the start of the systemic

and pulmonary circulations, pressure continues to rapidly rise reaching the maximal rate of pressure development. Because this initial contractile phase occurs all valves closed, the ventricular volume remains constant and is termed the *isovolumetric contraction* phase.

1.3.3 Ejection

Pressure in the ventricle continues to increase until ventricular pressure exceeds the downstream arterial pressure, causing the arterial valves to open and *ejection* to occur. During ejection not all blood is ejected from the ventricles with the remaining blood being called the *unstressed volume*, which is covered in more depth in Section 1.5.

1.3.4 Isovolumetric relaxation

While blood is being ejected from the heart, ventricular pressure steadily reduces and eventually falls below arterial pressure, with the kinetic energy of the blood driving the final stages of ejection. At the end of ejection the ventricles begin to relax causing the arterial valves to abruptly close. Once again all valves are closed and the muscle fibres continue to relax resulting in a rapid decline in ventricular pressure, a phase known as *isovolumetric relaxation*. Ventricular pressure continues to decline until pressure falls below atrial pressure, allowing the artioventricular valves to reopen. Blood begins to flow passively from the veins through the atria and into the ventricles and the cycle continues.

1.4 Blood Vessels

After blood is expelled from the heart it is transported throughout the body via a series of variable sized blood vessels, illustrated in Figure 1.2. The changing size and mechanical properties of these vessels allows large volumes of blood ($\approx 70 - 100ml$) to be received from the heart and redistributed to the organ and cellular levels [1].

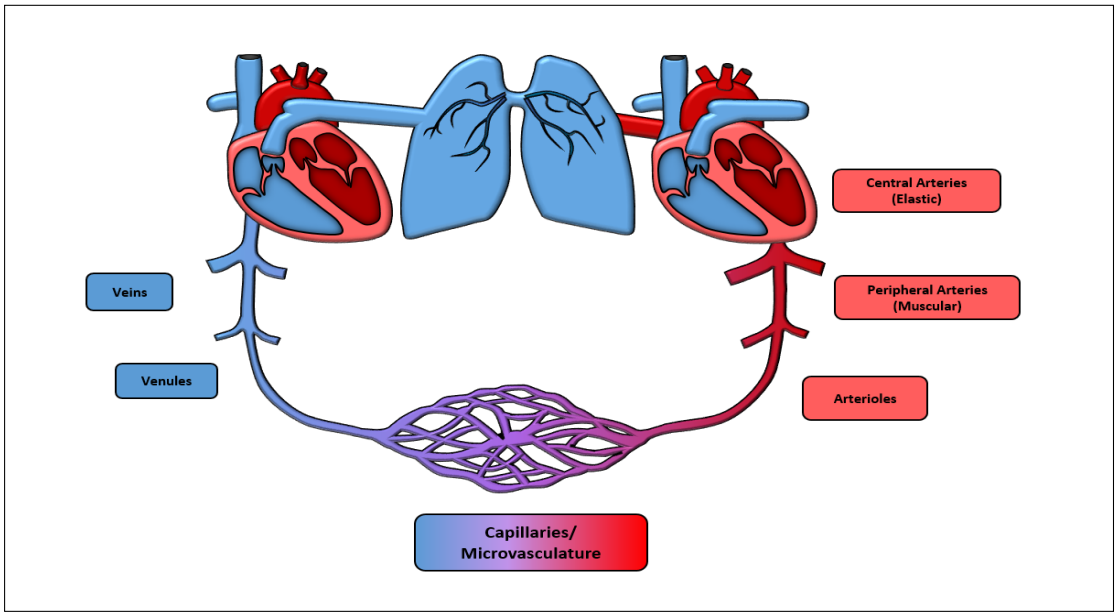

Figure 1.2: Schematic of the blood vessels comprising the systemic circulation. Blood is ejected from the left side of the heart, through the arteries to the microcirculation, returning to the right side of the heart via the veins.

1.4.1 Arteries

Arteries are the largest of the blood vessels in the body and are responsible for transporting of blood away from the heart. The arteries nearest the heart are the largest in

order to facilitate the larger volumes ejected from the ventricle and progressively reduce in size towards the periphery. The larger arteries have higher portions of elastic fibres to accommodate the high pressure blood flow delivered by the heart, and are commonly referred to as *elastic arteries* [2].

Distal arteries are smaller *muscular arteries* comprised of a thicker muscular layer allowing for the distribution of blood to specific organs and tissues of the body. Like the elastic arteries, muscular arteries are often referred to by name, such as the femoral and brachial arteries.

The smallest diameter arteries are called, *arterioles* and are high resistance blood vessels. Arterioles regulate blood flow through the body by variable contraction of smooth muscle in the vessel walls. This contraction increases vessel resistance and controls the blood flow entering a specific region of the circulation.

1.4.2 Capillaries

Capillaries receive blood from the arterioles and transport nutrients from the blood to the necessary tissues. Capillaries are thin walled vessels allowing diffusion of nutrients and oxygen from the blood to cells. Capillaries make up the micro-circulation and are the primary exchange vessels of the CVS. Although small in diameter, it is estimated ≈1 billion capillaries exist in the human body. By this stage blood pressure has dropped significantly and become relatively constant, in contrast to the high pressure, pulsatile blood flow seen in the central arteries.

1.4.3 VEINS

Veins deliver de-oxygenated blood back to the heart to be transported to the lungs for gas exchange. The smallest veins, called *venules*, collect blood from the micro-circulation and deliver it to the larger veins. Veins progressively increase in diameter nearer the heart to accommodate the cumulative blood flow being delivered from all regions of the body. Like their arterial counterparts, the larger veins near the heart are often referred to by name, most notably the superior and inferior vena cava, which directly feed the right atrium.

Crucial to the function of the CVS are the highly elastic vein walls, allowing them to serve as large reservoirs of blood while maintaining an almost constant pressure. This blood reserve provides the body with the ability to quickly alter flow by recruiting blood volume via vasoconstriction when required. This capacitive property of the veins means approximately 70% of total blood volume in the body resides in the systemic veins [3, 4]. Additionally, veins have a series of semilunar valves ensuring flow occurs only in one direction.

1.5 Principles of Circulation

For the CVS to function properly the heart must provide sufficient volume to the arterial system to maintain adequate pressure for tissue perfusion. When the body is stressed, the heart will often increase output to meet demand. Intensive care clinicians also

perform interventions designed to increase cardiac output by increasing total circulating volume, such as intravenous fluid administration. In any discussion relating to volume based treatment it is important to first understand the determinants of cardiac output and its relation to venous return.

1.5.1 Venous Return

Venous return (VR) refers to the volume of blood returning from the systemic circulation to the heart, and directly influences cardiac output (CO) in steady state flow as the heart is only able to pump out the volume of blood it receives [2, 5–7]. While this definition is seemingly redundant, it implies CO and circulatory flow are primarily governed by the venous system, not by the heart itself. The heart acts permissively by adjusting pressure and volume in the right atrium to mediate flow driven from the body by the elastic recoil of the veins. The heart provides the restorative force to the circulation, with the elastic recoil of the vasculature driving flow through the circulation [4].

This view is known as the Guytonian model of the CVS and describes VR through an ohmic relation between *right atrial pressure (RAP)*, the *mean systemic filling pressure (MSFP)* and the *resistance to venous return* (R_{vr}) [8, 9]

$$VR = \frac{MCFP - RAP}{R_{vr}} \tag{1.1}$$

The MSFP describes the pressure in the systemic circulation if the heart were stopped

and pressure allowed to reach an equilibrium. The MSFP is the driving force for VR, overcoming downstream RAP and R_{vr}.

Total blood volume in the circulation comprises of two theoretical components. The initial volume required to fill vessels to a point where the vessel walls begin to exert an elastic recoil force on the blood is called the *unstressed volume*, and does not contribute to the MSFP, illustrated in the left image of Figure 1.3. If blood volume were lowered to the unstressed volume, the MSFP falls to zero, and the vessel begins to collapse.

Volume in excess of the unstressed volume increases the elastic recoil of the vessel walls and generates the pressure inside the blood vessel. This volume is called the *stressed volume*, shown in the right image of Figure 1.3. As stressed volume is the pressure generating volume in the circulation it is a primary determinant of the MSFP and thus, per Equation 1.1, is also major determinant of VR. It is estimated the ratio of stressed to unstressed volume in the circulation is 1:4 [10, 11].

1.5.2 CARDIAC OUTPUT

Cardiac output (CO) defines the volume of blood ejected by the ventricle each minute, with *stroke volume (SV)* being the volume ejected each cycle. CO is proportional to SV multiplied by the *heart rate (HR)*:

$$CO[volume/min] = SV[volume] \cdot HR[beats/min] \tag{1.2}$$

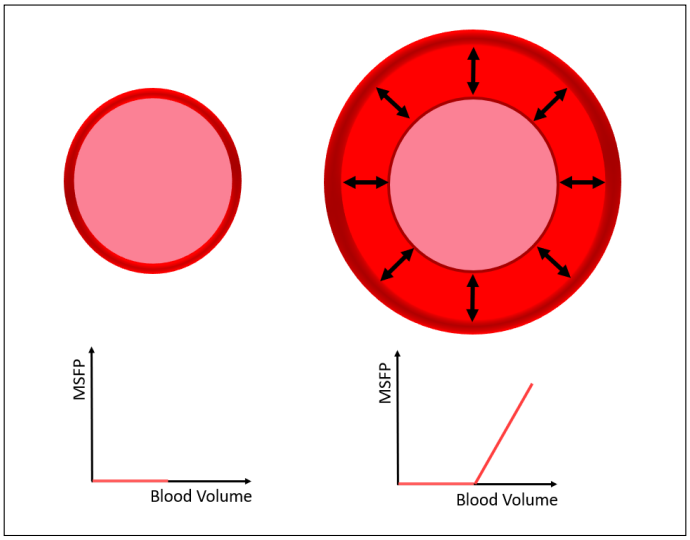

Figure 1.3: Diagram of unstressed (left) vs stressed (right) volume and their effect on the MSFP. Stressed blood volume represents the total pressure generating volume in the circulation, produced by the vessel walls exerting an elastic recoil force on the blood.

There are four determinants of CO: preload, afterload, contractility, and heart rate. These determinants are typically described in the context of the *Frank-Starling curve*, which represents the specific contractile state of the heart as defined through the relationship between cardiac preload and CO [12].

1.5.2.1 Preload

Preload indicates the degree to which myocardial fibres have been stretched as a result of the increasing volume in the heart during filling, essentially representing the hearts ability to fill. Increasing VR, increases the end-diastolic volume of the heart, producing a greater stretch of the muscle fibres, translating to an increased ability to generate a contractile force [13]. Figure 1.4 illustrates a Frank-Starling curve describing this preload-CO relation. These curves consist of an initial steep portion, where CO is

preload dependent, and a plateaued region, where further stretching of the myocardial fibres does not result in a significant increase of contractile force [13–15]. Preload is the foundation for volume based hemodynamic treatments, where patients who are deemed to be fluid responsive are also referred to as being preload responsive.

1.5.2.2 AFTERLOAD

Afterload describes the downstream load the ventricles must overcome in order to eject blood from the heart into the vasculature. This load is closely related to aortic pressure which in turn is affected by the vascular tone. *Systemic vascular resistance (SVR)* is commonly used as a clinical assessment of afterload.

Pharmacological interventions involving vasoactive drugs can alter afterload, resulting in a shift of the Frank-Starling curve. Reducing arterial blood vessel diameter, through the use of vasopressors, will increase vascular resistance and thus, increase afterload. This will result in a downward shift of the Frank-Starling, as shown in Figure 1.4. The opposite effect can be achieved using vasodilators to increase blood vessel diameter, reducing vascular resistance and afterload.

1.5.3 CONTRACTILITY

Contractility refers to the heart's ability to generate contractile forces for a given preload and afterload. Whereas preload is a measure of the force response due to the volume prior to ejection, contractility depends on the inherent properties of the muscle fibres,

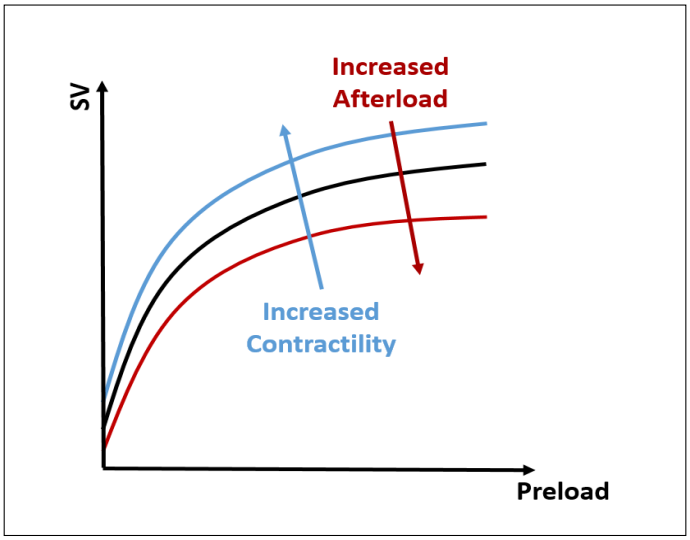

Figure 1.4: Illustration of the Frank-Starling curve and the effect of changing cardiac contractility and afterload on cardiac performance.

irrespective of the pre- and after load conditions [16, 17]. Increasing contractility shifts the Frank-Starling curve upwards, as depicted in Figure 1.4. Contractility can be clinically assessed using the ventricular end-systolic elastance (E_{es}), or alternatively as the maximum gradient of the aortic pressure pulse ($\frac{dP_{ao}}{dt}_{max}$) [18].

1.6 Cardiovascular Pressure-Volume Relations

Cardiovascular function is often assessed through analysis of ventricular *pressure-volume (P-V)* relations. Figure 1.5 shows an idealized example of this relation, commonly called a P-V loop, and is the P-V description of the phases of the cardiac cycle depicted in Figure 1.1.

The maximum P-V ratio during each cycle is located in the upper left corner of the loop, and corresponds to the maximum ventricular elastance. Early experimental work

exploring the effect of changing the cardiac loading conditions would have on the P-V loops found while the shape and location of the loop would be altered, the maximum P-V ratio of each curve lay on an approximately linear curve, as illustrated by the left image in Figure 1.6. As these points occur approximately at end-systole, this line was termed the *end-systolic pressure-volume relation (ESPVR)* [16]. These changes were found to be true for both preload and afterload changes, resulting in the ESPVR being considered a load independent measure of cardiac contractility. The intercept of the ESPVR and pressure axis is the ventricular unstressed volume (V_u). The gradient of the ESPVR, determined by the maximum P-V ratio and V_u, is the *end-systolic elastance* *(E_{es})*.

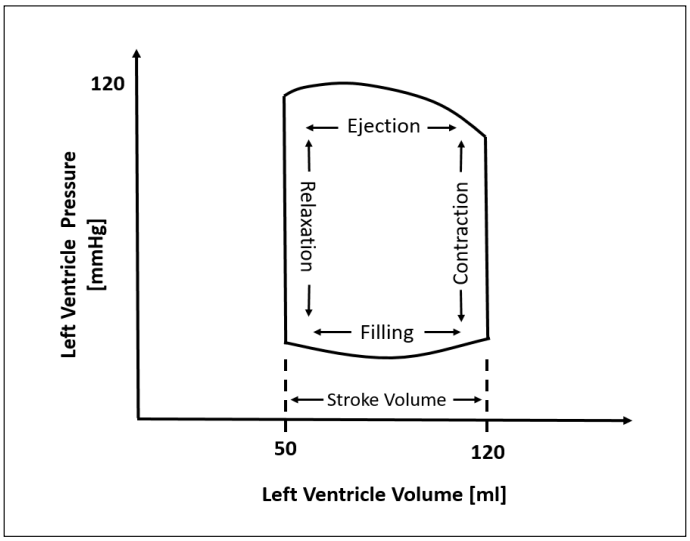

Figure 1.5: Idealized left ventricle pressure-volume loop illustrating each phase of the cardiac cycle.

Further experimentation found changes in contractile state, through epinephrine infusion, increased the slope of the ESPVR, but had little effect on V_u [17], illustrated in Figure 1.6. After epinephrine infusion, preload and afterload were adjusted and the

linear correlation was again evident. These results lead to E_{es} being considered a load independent index of cardiac contractility.

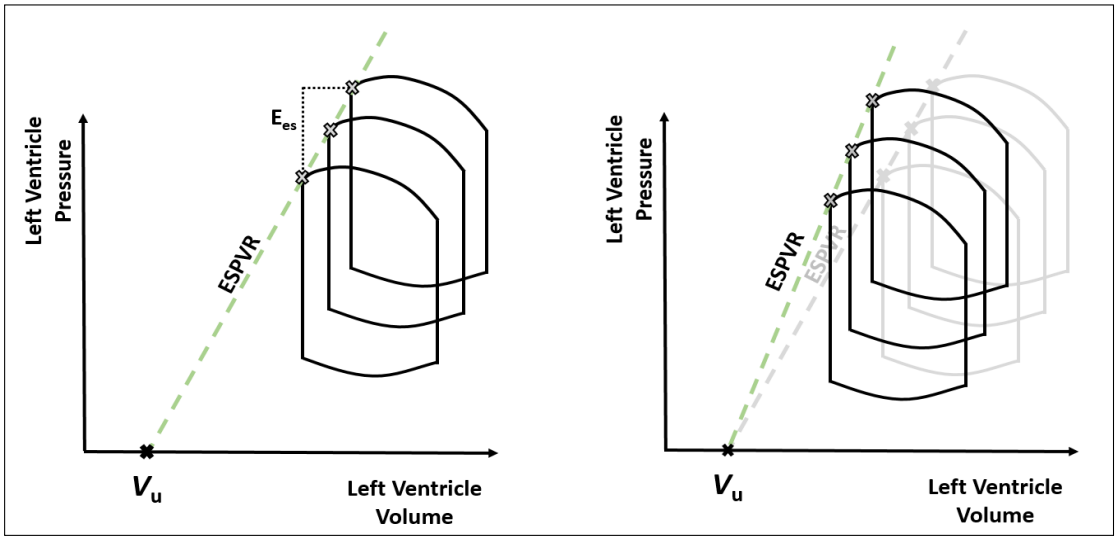

Figure 1.6: (left) Illustration of the experimental observations made by Suga *et. al.*, leading to E_{es} being considered as a load independent measure of cardiac contractility. Varying cardiac load produces P-V loops with end-systolic points producing a linear fit. (right) Changes in contractility have little effect on V_u.

Recordings from multiple ventricular P-V loops are typically limited to animal studies, due to the invasive sensors and procedures required for measurement. Thus, V_u is often assumed to be zero, allowing E_{es} to be calculated using P-V data from a single beat [19, 20]. P-V loops are also used to assess arterial elastance E_{ao}, by examining the relation between the end-systolic points and stroke volume [21], as shown in Figure 1.7.

Whereas E_{es} represents the contractile state of the ventricle, E_{ao} represents the elastic forces opposing ejection, afterload. The ratio of E_{ao}/E_{es} can be used to describe the energy transfer from the ventricle to the vasculature and thus, provides a useful metric of cardiac efficiency [22, 23]. The ratio between the two elastances is called *ventriculo-arterial coupling (VAC)*.

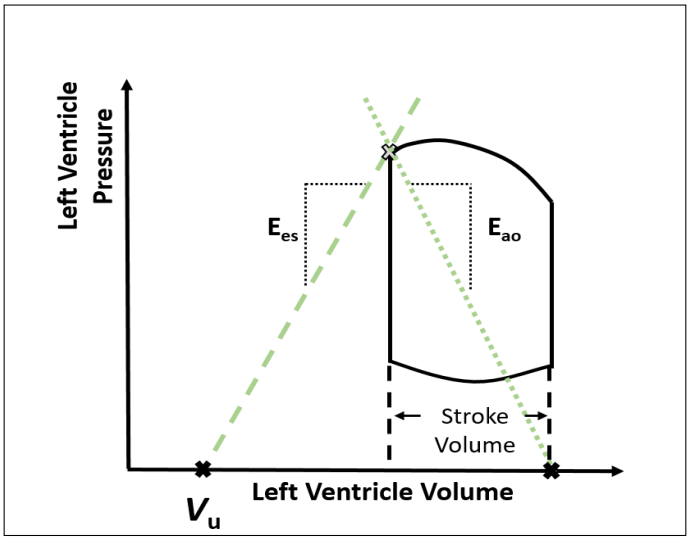

Figure 1.7: Illustration of a single-beat left ventricle P-V loop used to assess both end-systolic (E_{es}) and arterial (E_{ao}). The slope of the E_{ao} line is found using the end-systolic point and the intercept with the volume axis equal to SV

In non-stressed subjects, VAC is lower (≈0.5), indicating the CVS is operating in a manner which optimizes for ventricular oxygen consumption, and maximises cardiac efficiency. In states of increased cardiovascular demand, the heart sacrifices ventricular efficiency in favour of optimizing mechanical energy transfer from heart to arterial system, increasing VAC. Technically, decoupling occurs at a VAC value ≥1, but practically, healthy VAC values range from 0.6-1.2 [24, 25].

Clinically, E_{ao} can be calculated calculated as the ratio of ventricular end-systolic pressure ($P_{lv,es}$) to end-systolic volume:

$$E_{ao} = \frac{P_{lv,es}}{\mathrm{V_{es}}} \tag{1.3}$$

However, as $P_{lv,es}$ requires catheterization, peripheral pressure measurements are used as surrogates, with $P_{lv,es}$ equal to 90% peripheral systolic pressure [24].

1.6.1 Elastance

Blood vessel *elastance* is an essential property for pulsatile pressure transmission throughout the body. It is defined as the change in pressure per unit change in volume ($\frac{\Delta P}{\Delta V}$) and is the inverse of compliance. Elastance is commonly reported with units of $mmHg/ml$.

Blood vessel elastance allows high pressure waves generated by cardiac contraction to be safely transmitted to the arterial system. The elastic recoil generated from the uptake of volume then provides the force for transmitting blood to the next vascular segment [4]. Changes in elastic properties throughout the vasculature progressively dampen out the pulsatile central pressure waveforms, providing an almost constant pressure in the micro circulation for tissue perfusion.

1.7 Circulatory Shock

Circulatory shock is a common mode of cardiovascular dysfunction resulting from a number of clinical issues [26]. Regardless of the initial insult, shock results in systemic hypoperfusion caused by a reduction in cardiac output, reduced effective circulating volume, or both. Prolonged hypoperfusion can lead to cellular and tissue hypoxia, organ failure and death. Three general categories of shock exist: Septic, Hypovolemic and Cardiogenic.

Septic shock results from an inappropriate inflammatory response to a microbial infection, where the body's response to the infection is no longer localized to the infection site,

but disperses throughout the body. Septic shock results in a complex cascade of circulatory failures typically characterized by reduced peripheral vascular resistance through increased vasodilation, increased capillary permeability leading to capillary leakage, and a reduction in cardiac contractility [27–30].

Septic shock is a common mode of circulatory failure in critical care, resulting in an estimated 6 million deaths per year [31]. A recent meta-analysis, investigating the frequency of septic shock occurrence in Europe and North America, estimated 10.4% of patients presented with septic shock on admission to the ICU [32]. Another recent meta analysis estimated the average 30 and 90-day mortality rates in patients with septic shock to be 34.7% and 38.5%, respectively [31].

The experimental data available for the majority of this work was obtained from a series of endotoxin induced septic shock animal experiments. Therefore, specific attention is paid to this form of circulatory shock.

Cardiogenic shock is the result of any type of heart failure including myocardial damage, ventricular arrhythmias and outflow obstruction. Without proper cardiac function, blood pressure is not adequately maintained and the patient will slip into a state of shock.

Hypovolemic shock is caused by a loss of total blood volume, commonly cause by haemorrhage which removes blood from the circulation resulting in a drop in arterial and eventually shock. Fluid loss from blood vessels into the interstitial space can also result in shock.

Treatment of shock is governed by the insult causing it but often includes administering intravenous fluids to rapidly stabilize arterial pressure. Restoring arterial pressure ensures tissue and organ perfusion is maintained.

1.8 Experimental Animal Data

All experimental procedures and protocols were reviewed and approved by the Institutional Animal Care and Use Ethics Committee of the University of Liège, Belgium (Reference Number 14-1726). Their guidelines conform completely with the Guide for the Care and Use of Laboratory Animals published by the US National Institutes of Health (NIH Publication No. 85-23, revised 1996), as well as EU DIRECTIVE 2010/63/EU on the protection of animals used for scientific purposes.

Eight (8) male, pure Piétrain pigs weighing between 18.5 and 29 kg were sedated, anaesthetised and mechanically ventilated. Admittance pressure-volume catheter (Transonic, NY, USA) were inserted into the heart via an apical stab performed in the left ventricle. These devices recorded at a sampling rate of 250 Hz. Proximal aortic, femoral and central venous pressures were continually sampled using pressure catheters (Transonic, NY, USA), also recording at a sampling rate of 250 Hz.

Each experiment comprised of the following protocol:

- A baseline fluid bolus of 500ml given over approximately 30min.

- An endotoxin infusion (lipopolysaccharide from E. Coli, 0.5 mg/kg) over 30min
- Further fluid infusions of 500ml given over 30min to simulate volume based treatment
- Several positive end-expiratory pressure (PEEP) driven recruitment manoeuvres (RM).

Note, data from all pigs are used throughout this work. However, not all pigs were suitable for each stage due to issues with various measurements. Results are presented with consistent labelling of pigs throughout.

The length of each experiment depended on the amount of usable data prior to death, and ranged from $\approx 90 - 230$ minutes across the 8 pigs. Pigs 1, 4, 5 and 8 had a severe reactions to the endotoxin causing the experiments to conclude shortly after the endotoxin infusion. Pigs 2, 3, 6 and 7 survived post endotoxin infusion, allowing for an investigation during progressive circulatory failure and subsequent volume based treatment.

Each of the bullet pointed clinical procedures will be referred to heavily throughout the entirety of this work so a brief explanation of each is presented here.

1.8.1 Fluid Bolus

A fluid bolus is a known volume of fluid administered to a patient in order to improve some clinical metric, often blood pressure. The motivations for administering such a treatment are further detailed in the following chapter.

1.8.2 PEEP Driven RM

A PEEP driven RM refers to a process were pressure in the lungs is increased via mechanical ventilations in order to reopen, or recruit, collapsed alveoli. These manoeuvres are used to improve oxygenation in a patients. The changes in pressure in the thoracic chamber also affect performance of the heart and are useful for testing CVS models.

1.8.3 Endotoxin

An endotoxin infusion is administered to each pig to induce sepsis and septic shock. Sepsis is one of the most prevalent diseases in the ICU and causes a cascade of circulator failures affecting pulse wave propagation throughout the vasculature, volume of fluid volume in the body and vascular tone.

1.9 Summary

This chapter provides an overview of the physiology of the cardiovascular system. First the stages of the cardiac cycle are presented, detailing how blood is pumped through the heart, followed by a brief description of the blood vessels responsible for transporting blood away from the heart through their respective circulations. Several physiological principles are also introduced describing the determinants of venous return and cardiac output, as well as the contractile and loading conditions of the heart. Finally, an overview of experimental data used in this work is presented.

Chapter 2

Fluid Therapy

2.1 Introduction

A *fluid therapy* involves administering intravenous fluids to increase the MSFP, increasing the pressure differential driving VR and thus, increase CO. Fluid therapies are often a clinicians first line of defence in the event of circulatory shock and aim to maintain adequate perfusion pressure to avoid tissue and organ injury. Fluid therapy is also known as *fluid loading*[33], *volume expansion* [34–37] and *infusion therapy*[38]. The term *fluid resuscitation* [39, 40] is also commonly used, and refers to the initial, life saving volume of fluid given to treat the immediate life threatening effects of cardiovascular shock. Fluid therapies are administered to increase the total volume in the circulation, thereby increasing MSFP and VR. With a greater VR, ventricular preload is increased and finally, CO.

Two types of fluids are predominantly used for fluid therapies. *Crystalliods*, most commonly 0.9% saline solution, are recommended by the surviving sepsis campaign (SSC) guidelines [41]. They are inexpensive to manufacture and have been associated with a reduction in mortality compared to colloids [42]. *Colloid* solutions contain larger molecules less likely to cross the vascular endothelium into the interstitial space increasing fluid retention. This translates to a more efficient treatment, as smaller volumes are required to reach desired hemodynamic targets [43].

Although fluid therapies are commonly administered, multiple studies have shown the desired increase in CO, commonly defined as an increase of $\geq$ 12% after a 500ml fluid bolus, occurs in only approximately 50% of patients [14, 44, 45]. Patients who exceed this $\geq$ 12% threshold are termed *fluid responsive*, while those who do not are *fluid unresponsive*. Distinguishing between these two groups is of high clinical importance as excessive or unnecessary fluid infusions have been strongly correlated to worsened patient outcomes, resulting in a condition of fluid overload.

2.2 Fluid Overload

Fluid overload (FO) refers to patients presenting with a fluid accumulation $\geq$10%, relative to their admission bodyweight [46, 47]. Fluid overload has been linked to increased mortality, increased length of hospital stay and increased requirement of mechanical ventilation [48] and can be induced through continual, unguided administration of fluids or from an excessive initial large fluid bolus. The respiratory, cardiovascular, hepatic, central nervous, gastrointestinal and renal systems are all negatively affected by FO with

one study into the dose response association between FO and patient outcome found for every 10 ml/kg increase in maximum FO, the risk of in-hospital mortality increased by 4% [49]. A brief overview of the potential impacts of fluid overload on the major organs includes [50]:

Cardiovascular System: Fluid overload may result in delayed cardiovascular collapse due to vascular injury sustained from excessive fluids. *Symptoms*: Myocardial oedema; myocardial depression; increased filling pressures; reduction in cardiac output and increased vascular permeability.

Respiratory System: Increased pulmonary capillary permeability results in fluid accumulation in the lungs triggering the reduction in pulmonary compliance and increasing respiratory work. *Symptoms*: Pulmonary oedema, increased elastance of chest wall, pleural effusion, hypoxia, prolonged reliance on mechanical ventilation, increased extravascular lung water and decreased lung volumes.

Renal System: The kidneys are encapsulated organs meaning FO begins to physically distort the systems architecture through increased interstitial fluid accumulation. *Symptoms*: increased renal vascular resistance; increased renal and interstitial pressure; decreased blood flow; venous congestion; salt and water retention and uraemia.

Gastrointestinal system: Increased vascular permeability combined with large volume resuscitation allows fluid into the bowel compressing mesenteric vessels and the lymphatic system and increasing intraabdominal pressure. *Symptoms*: Bowel oedema, in-

creased intestinal permeability, increased bacterial translocation, increased intra-abdominal pressure and abdominal hypertension.

Hepatic System: The liver, also encapsulated in a membrane, experiences similar complications resultant of FO. *Symptoms*: Reduced liver perfusion, hepatic congestion, compartment syndrome.

Central nervous system: The brain can be particularly susceptible to FO due to being encapsulated in the rigid skull. *Symptoms*: impaired cognition, increased intracranial, intra-orbital and intra-ocular pressure, diminished cerebral perfusion pressure, and cerebral oedema.

2.3 Fluid Responsiveness

To distinguish between responsive and unresponsive patients, tests have been designed to assess which portion of the Frank-Starling curve a patient is operating on, and thus the level of preload reserves available, were developed [51]. Responsive patients operate on the steep portion of the curve and for a given change in preload, a large change in CO will occur. Unresponsive patients operate on the plateaued portion of the curve where, for the same change in preload, a negligible change in CO occurs [14, 51]. These differences are depicted in Figure 2.1.

It is important to note, a patient being deemed fluid responsive simply means the heart is preload dependent and additional volume will increase CO. This fact alone does not

necessitate administering fluids, and doing so in patients with healthy CVS may be redundant or even harmful [14].

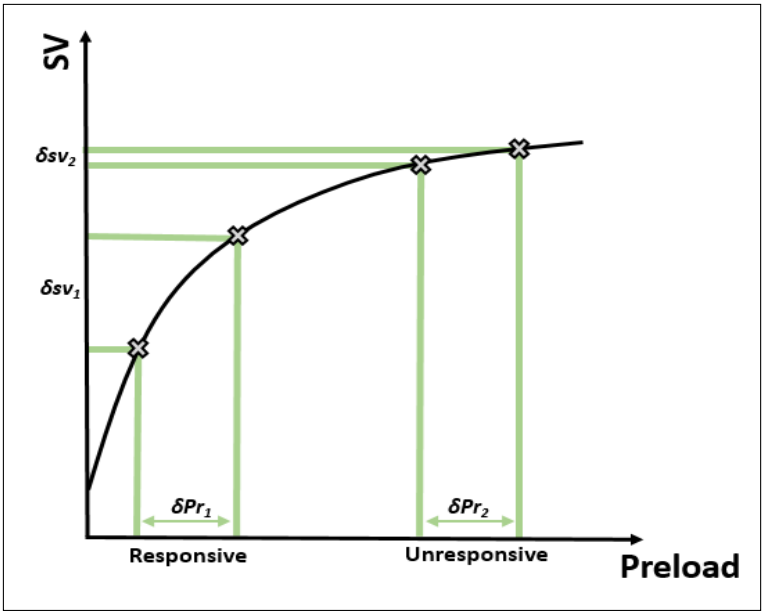

Figure 2.1: Comparison between fluid responsive and unresponsive patients with respect to the Frank-Starling curve. Responsive patients will, for a given preload increase, experience a significant increase in SV as they are acting on the steep portion of the Frank-Starling curve, whereas a minimal SV change occurs for the same preload increase in patients operating on the plateaued region of the curve.

When no preload reserves are available, the myocardial fibres are already in a stretched state and administering additional fluids causes right atrial pressure to increase in proportion to the MSFP. This synchronized pressure increase prevents the pressure differential driving VR from increasing, and CO remains unchanged. Continued fluid therapy in unresponsive patients can also damaged cardiac muscle fibres, reducing the preload dependent improvements in contractile force [52]. Because fluid responsiveness is inherently linked to preload, it is also referred to as *preload responsiveness*.

The gold standard method for assessing fluid responsiveness is to infuse fluids and directly measure the change in CO. However, the administration of intravenous fluid infusions is an irreversible process, and if the results of this infusion determines the patient to be unresponsive, unnecessary damage may have occurred. Furthermore, tests for fluid responsiveness need to be repeatable to account for changes in patient condition. Several repeatable *indices of fluid responsiveness* have been developed to predict the likelihood of a patient having a positive response (typically defined as a $\geq$12% increase in CO, but ranges of 10-15% are also commonly used). Indices of fluid responsiveness can be described in two categories: *static* and *dynamic* indices.

2.3.1 Static Indices

Static indices are singular measurements of a pressure or volume used to represent the cardiac preload of a patient. The discussion on static indices here is limited as several studies have shown an inability of static indices to predict fluid responsiveness. Despite a lack of evidence for their efficacy, static indices are widely used to guide fluid therapy [37], most commonly central venous pressure (CVP). Other common indices include: pulmonary artery occlusion pressure (PAOP); global end-diastolic volume (GEDV); inferior vena cava diameter; and left ventricle diastolic area [52].

While static indices can provide good assessments of the actual cardiac preload, they fail to distinguish which part of the Frank-Starling curve a patient is operating on and thus, how the patient is likely to respond to fluids. Because preload responsiveness is dependent on the contractile state of the heart, which is described by multiple curves,

static indices can reflect both responsive or unresponsive states [14, 45, 51]. Figure 2.2 illustrates how the same measurement of central venous pressure indicates both responsive and non-responsive states, during normal ventricular function and a reduced contractile state, respectively.

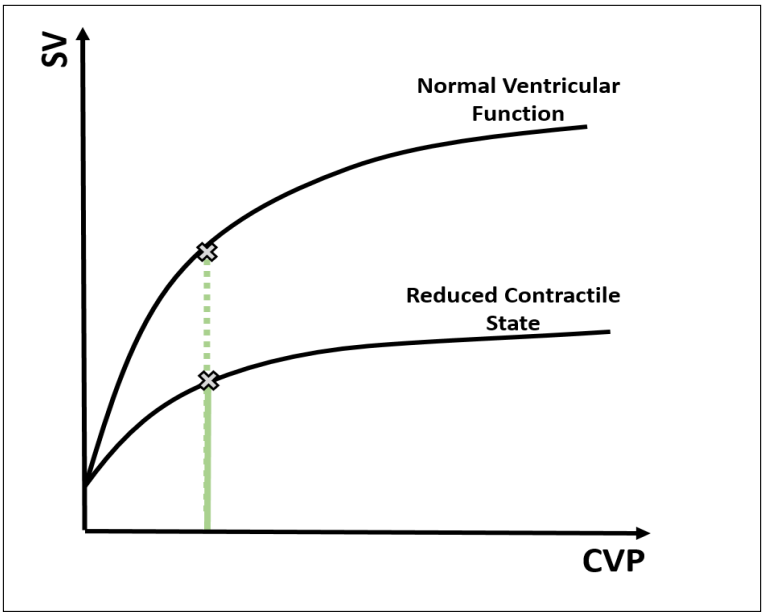

Figure 2.2: Illustration of how the contractile state of a patient determines whether a certain measurement of central venous pressure (CVP) indicates a fluid responsive or unresponsive patient.

2.3.2 Dynamic Indices

Dynamic indices monitor variations in some cardiovascular output in response to a preload challenge. Assessing the change in a cardiovascular output allows the portion of the Frank-Starling curve which the patient is operating on to be determined. Primarily,

these dynamic indices utilize carido-pulmonary interactions to investigate changes in CO in response to some preload challenge produced during mechanical ventilation.

2.3.2.1 CARDIO-PULMONARY RELATIONS

As the heart is enclosed in the thoracic chamber, pressure variations during breathing cyclically vary the external forces on the heart, affecting its ability to fill. Thus, they cyclically affect ventricular preload. These cardio-pulmonary interactions are used by clinicians to conduct a preload challenge in mechanically ventilated patients.

Stroke volume variation (SVV) and its surrogates *pulse pressure (PPV)* and *systolic pressure variation (SPV)* are frequently used dynamic indices [34, 37, 51–55]. Mechanically ventilated patients have their breathing controlled externally by a ventilator, allowing direct control over the pressure in the thoracic chamber. Increasing pressure in the thorax through mechanical inspiration, increases pressure on the right ventricle, reducing preload. Right ventricle afterload is also increased from the increased pulmonary vascular resistance. After a few heart beats, the effects of the altered loading conditions on the right ventricle are transmitted to the left ventricle, reducing SV. As clinicians are able to control ventilator settings, the change in left ventricle preload is known and monitoring the resulting changes in SV reveals the patients operating portion of the Frank-Starling curve. Due to the clinical complexity of directly measuring SV, PPV and SPV are often used as surrogates.

Figure 2.3 shows how SV, PP and SP vary with mechanical ventilation. Clinically,

these metrics are assessed by monitoring waveforms over a set period (≈30sec [56]) and calculating the difference between maximum and minimum values relative to the mean. Variations in these metrics above a threshold value, $\geq 8-15\%$ [34, 37, 53, 54], indicate fluid responsiveness.

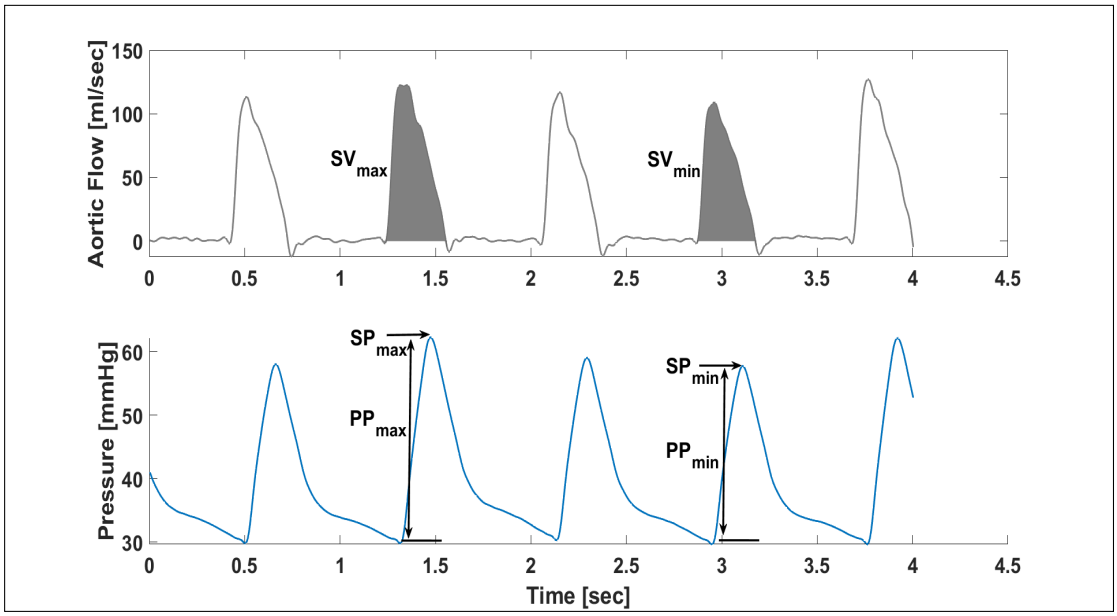

Figure 2.3: example of how aortic flow (top) and femoral pressure (bottom) vary over approximately one mechanical ventilator controlled breath.

Several other dynamic indices based on cardio-pulmonary relations have been developed using similar principles. *Inferior vena cava variation* monitors changes in vena cava diameter, which are correlated with VR and CO, during mechanical ventilation. *End expiratory occlusion (EEO)* interrupts mechanical ventilation at end-expiration for 12-15s and monitors the response of CO. Interrupting the ventilation cycle prevents the increase in thoracic pressure associated with inspiration, increasing cardiac preload, simulating a fluid challenge. An increase in arterial pressure ≥5% during an EEO test has been associated with fluid responsiveness [37].

2.3.2.2 LIMITATIONS

Indices utilizing heart-lung interactions have been shown to reliably predict fluid responsiveness in mechanically ventilated patients. However, the pre-requisite for patients to be mechanically ventilated presents a considerable limitation. In spontaneously breathing patients the mechanisms controlling breathing are significantly more complex making it difficult to assess changes in preload, limiting the applicability of such methods. Low tidal volume can also limit the accuracy of SVV/PPV, as it reduces the induced changes in intrathoracic pressure producing the desired variations [45]. Right heart failure and cardiac arrhythmias also present limitations. Equally, the repeatability of these metrics, and thus their translation to clinical use, has been poor.

2.3.3 PASSIVE LEG RAISE

The *passive leg raise manoeuvre(PLR)* utilizes the body's own reservoir of blood to perform an internal fluid challenge [35]. Elevating the legs while simultaneously lowering the torso through a combined angle of 45° forces blood to be directed from the capacitance veins in the lower body back to the heart. The PLR can recruit approximately 300ml blood from the lower body to the heart, large enough to assess fluid responsiveness by monitoring changes in CO [57].

The considerable advantage of the PLR is it uses a patients own blood to perform the preload challenge. Therefore, no external fluid is required and the process is entirely reversible, eliminating any risk of fluid overload. In a meta-analysis conducted by Monnet

et. al. [45] the PLR manoeuvre was found to have an excellent ability to predict fluid responsiveness. The pooled correlation coefficient between CO changes induced by PLR was 0.76.

2.3.3.1 Limitations

While the PLR is a safe and accurate method for assessing fluid responsiveness, there are several limitations to its applicability. Primarily, the PLR requires accurate assessment of CO over short time frames. Changes in CO produced by the PLR, begin almost immediately and dissipate rapidly, with the full effect of the volume recruitment concluding approximately 1-2 minutes after the initial positional movement. This short time frame means precise, real time measurements of CO are required for accurate assessment of fluid responsiveness using the PLR. This issue makes some current CO monitoring methods unreliable, especially non-invasive methods.

Attempts to uses arterial pressures as a surrogate for CO have shown a reduction in reliability of results [45, 51]. Changes in pulse pressure amplification mechanics induced by the PLR can impede the accuracy of peripheral pressure measurements in reflecting CO, which is not strong in any event [58–61].

Finally, the state of the patient must be considered when performing a PLR. The manoeuvre requires the bed be lifted up under the patient potentially causing discomfort, pain, awakening or other issues. This discomfort can elevate heart rate resulting in misleading changes in CO. Additionally, it is desirable for the bed to perform the positional

shift not the patient themselves. Movement of the patient of their own volition can cause a complex change in the vasculature, distorting the effects of the volume transfer.

2.3.4 Mini Fluid Challenge

The *mini fluid challenge* involves a rapid infusion of a smaller amount of fluid, approximately 100ml over 1min [52], and monitoring the changes in CO. Unsurprisingly, the mini fluid challenge has excellent accuracy when assessing fluid responsiveness as it is a direct test. However, the main limitation is the introduction of potentially unnecessary and harmful fluid, meaning tests can not be repeatedly performed. Furthermore, because a reduced volume is used, the devices monitoring changes in CO must be precise enough to accurately detect changes.

2.4 Stressed Blood Volume

Stressed blood volume (SBV) is defined as the total pressure generating volume in the circulation and is a major determinant of the MSFP. The Guytonian model of the CVS presents MSFP as force overcoming R_{vr} and RAP and under normal conditions is the major driving force for VR [4, 25]. Therefore, monitoring SBV gives direct insight into a primary determinant of VR and thus CO, making it a parameter of interest in terms of assessing fluid responsiveness [62–64].

A low SBV implies the vasculature can accommodate additional fluid during fluid therapy, elevating MSFP and VR. Indeed, under normal operating conditions both ventricles

are preload dependent thus, increasing SBV will produce an increase in SV [14]. Conversely, high SBV implies the patient is already 'full' and additional volume will likely be met with a proportional increase in right atrial pressure, maintaining VR at a constant level.

Continual SBV monitoring may also provide insight into the effectiveness of treatments involving inotropic and vasoactive drugs, as changes in arterial tone will shift blood volume from stressed to unstressed states, or visa versa. Assessing the effects of these treatments, combined with volume based treatment, in real time through monitoring of SBV levels could offer clinicians a powerful tool for providing patient specific treatment.

Direct measurement of SBV involves a series of cardiac arrests and fluid infusions, rendering it unsuitable for clinical care. First, the heart is stopped and pressure in the circulation allowed to reach the MSFP. Pressure is recorded, a known volume of fluid is introduced to the circulation, and the heart restarted. After several cardiac cycles the heart is again stopped and the new equilibrium pressure is reached. This process is repeated to form a trend, illustrated in Figure 2.4, showing the change in MSFP as a function of infused volume. Extrapolation of these data reveal the volume needed to be removed to give a MSFP of zero. This volume is equal to the negative of stressed blood volume or the amount of volume needed to be removed from the circulation to achieve a zero MSFP [62, 63]. Madger *et. al.* were able to perform a similar measurement on humans using an anaesthetic technique called *hypothermic circulatory arrest* [11].

Maas *et. al.* performed a version of this method using rapid 50ml infusions with a radial cuff to stop flow in the arm, not the whole body [63]. While obviously significantly less

damaging than performing multiple cardiac arrest, the method proposed by Maas *et. al.* still required the use of additional fluid infusions and stopping flow to areas of the body.

Pironet *et. al.* developed a model based surrogate for stressed blood volume (SBV_m) using a three chambered lumped parameter model of the CVS [62, 65, 66]. Their work showed SBV_m to be a potential index of fluid responsiveness with a threshold of 145ml predicting a positive response in a series of porcine endotoxin experiments. A sensitivity and specificity of 0.75 and 0.7, respectively, and an area under the ROC of 0.7 was achieved. The conventional indices of PPV, SVV and SPV, taken from the same experimental data sets, performed noticeably worse, producing areas under the ROC of 0.36, 0.58 and 0.54 for SVV, PPV and SPV, respectively.

These results, combined with the underlying physiology make SBV_m a desirable metric to have clinically available. However, the waveforms required to identify the three chambered model parameters, of which SBV_m is one, include continuous, invasive left ventricle pressure and volume and aortic pressure, all of which are not available from routine ICU measurements as they require time consuming, invasive procedures with an inherently higher risk of infection. These limitations must be considered for SBV_m to be adopted in clinical practice.

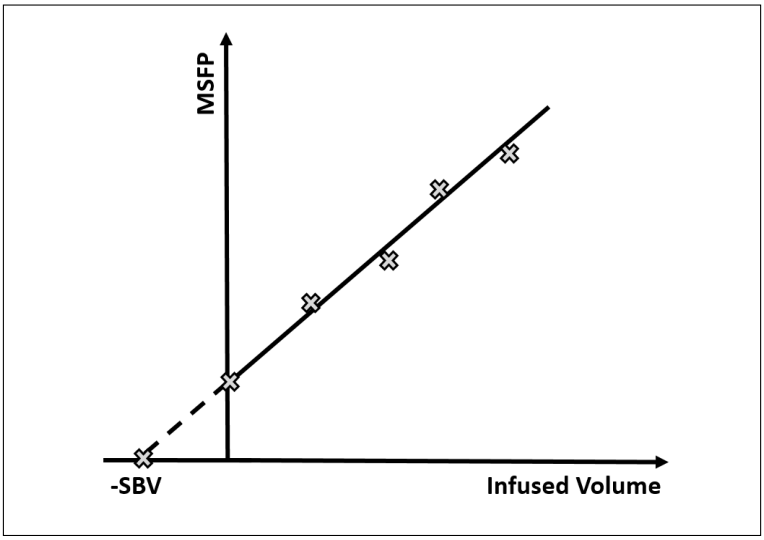

Figure 2.4: Illustration of the method used for direct assessment of stressed blood volume using progressive fluid infusions, cardiac arrests and measurements of the MSFP.

2.5 Summary

This chapter introduces the concept of a fluid therapy, a very common clinical procedure, and fluid responsiveness, the method by which a clinician determines whether or not to perform a fluid therapy. Several of the main, currently implemented indices of fluid responsiveness are presented with their underlying physiological assumptions and limitations. Finally, model based stressed blood volume, derived using a three-chambered lumped parameter model of the CVS, is introduced which will form the basis for the rest of the work presented here.

Chapter 3

Three-Chambered Model: Derivation and Identification

3.1 Introduction

Lumped parameter models compartmentalize a system into discrete nodes, each representing the distributed behaviour of a section of the system. Lumped parameter models are popular options for assessing CVS dynamics as they require only a modest set of parameters to accurately capture the complexities of the system. The availability of clinical measurements for model inputs is limited in ICU environments, so an inherent trade-off between model accuracy and practicality exists [67].

The *three-chambered model (TCM)* of the CVS is a lumped parameter model, develop to model dynamic behaviour of the systemic circulation from a clinically feasible set of

measurement inputs [62]. Pironet *et. al* used the TCM to identify model based stressed blood volume (SBV_m), one of the model parameters, to assess its potential as an index of fluid responsiveness in a series of porcine experiments. Their work concluded SBV_m to be a potential index of fluid responsiveness, showing a stronger correlation with relative changes in cardiac output than current clinical indices (PPV and SPV) during fluid therapies aimed to simulate clinical volume based treatment [62, 68].

This chapter first presents the components of the TCM and the physiological assumptions used to derive it. Second, the parameter identification procedure is presented, detailing the formulation of the error vector. Finally, the equations used to calculate initial estimates for each model parameter estimate are presented.

3.2 Model Overview

The TCM consists of three elastic chambers connected via three flow resistances, as shown in Figure 3.1. Model chambers represent the left ventricle, lv, arterial, ao, and venous, vc, systems, with resistances indicative of an input, R_i and output, R_o cardiac resistance and the systemic circulation resistance, R_c.

The venous and arterial systems are described as passive chambers, with the pressure in each chamber being the product of chamber volume and a constant elastance. The chamber elastance describes the ability of the chamber to deform under varying loads. Simplifying the arterial and venous system to behave passively allows the pressure dynamics to be described using a linear pressure-volume (P-V) relation. Assuming con-

servation of mass in the circulation, flow throughout the model is conserved. Therefore, blood entering the upstream end of a chamber causes blood to either be expelled from the downstream end, or accumulates in the chamber, causing pressure to increase as a result of the elastic recoil of the vessel walls. Flow into and out of the cardiac chamber is dictated by two pressure dependent valves. A schematic of the TCM model is shown in Figure 3.1.

The ventricles of the heart spontaneously contract ejecting blood into the circulation. These cyclic contractions result in pressures in the ventricles depending not only on the volume in the ventricle and the elastic properties of the ventricular muscles, but also on the specific time in the cardiac cycle. Therefore, the ventricle is described as an active chamber, with an additional parameter describing the time dependent elastance of the cardiac muscles.

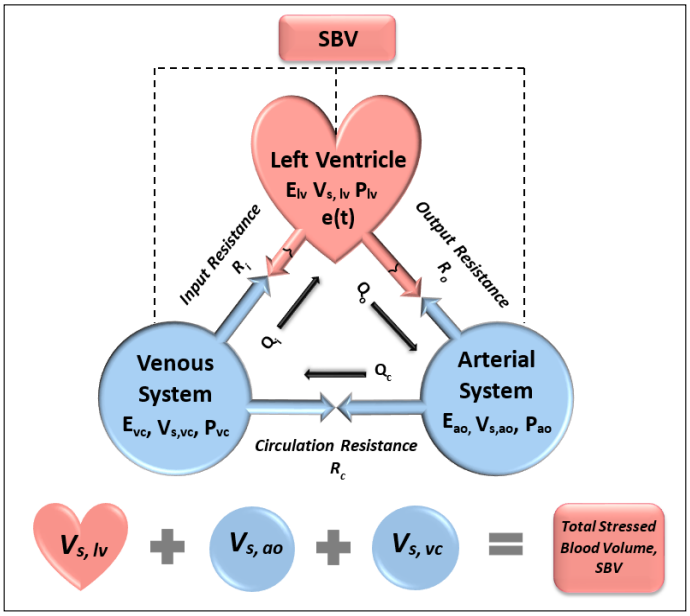

Figure 3.1: Schematic of the three-chamber lumped parameter cardiovascular system model.

3.3 Passive Chambers

As previously mentioned, the venous and arterial chambers are described using a linear P-V relation, relating chamber pressure and volume by a constant chamber elastance, $E_{chamber}$. Blood entering the vessel stretches the muscle fibres to accommodate the increase in volume, resulting in an elastic recoil force being applied to blood, generating pressure inside the chamber. This relationship is comparable to the mechanical ideas of stress (pressure) and strain (volume change). The change in pressure per one unit change in volume is the elastance [62, 69].

3.3.1 Passive chamber pressure-volume relation

Biological materials have the additional complexity of being comprised of materials with non-linear elastic properties. Muscle fibre elastance increases exponentially as volume is increased [70]. Figure 3.2 illustrates the generalized behaviour of the P-V relation describing passive chambers [2].

The non-linearity of the curve implies there is no single elastance for the material. Therefore, a working point at a volume ($V = \bar{V}$) is selected as a reference. At this working point the first order Taylor approximation of pressure is defined:

$$P(V) = P(\bar{V}) + \left(\frac{dP}{dV}\right)_{V=\bar{V}} (V - \bar{V}) \tag{3.1}$$

Chamber elastance is defined as the change in pressure resulting from the change in

volume:

$$E = \left(\frac{dP}{dV}\right)_{V=\bar{V}} \tag{3.2}$$

Substituting Equation 3.2 into Equation 3.1:

$$P(V) \approx P(\bar{V}) + E(V - \bar{V}) \tag{3.3}$$

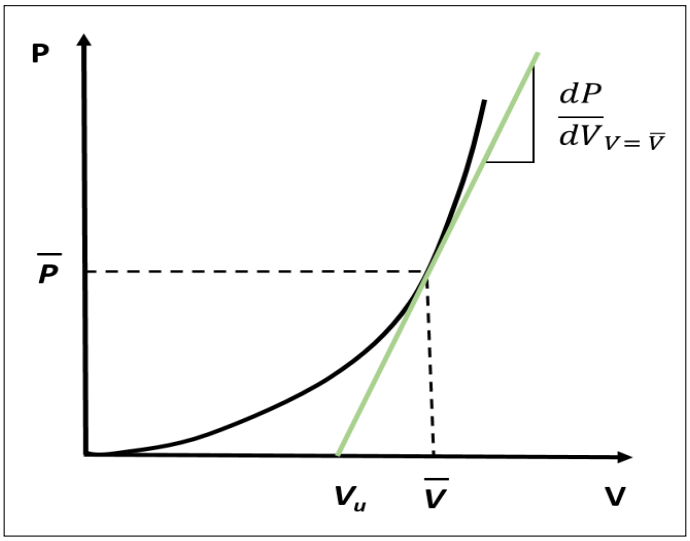

Figure 3.2: Generalized pressure-volume relationship in a passive chamber where pressure is dependent on the elastic properties of the vessel and the volume contained. The working point $\bar{V}$ is chosen in order to assess elastance.

Calculating chamber pressure from Equation 3.3 for a given volume requires knowledge of E, $\bar{V}$ and $P(\bar{V})$. To reduce the number of unknowns, the equation is simplified to be defined in terms of the stressed volume contained in the chamber. Substituting a limit point, at which zero pressure is generated in the chamber, into Equation 3.3 yields an expression for $P(\bar{V})$:

$$0 \approx P(\bar{V}) + E(V_u - \bar{V})$$
$$P(\bar{V}) = E(\bar{V} + V_u) \tag{3.4}$$

Substituting Equation 3.4 into Equation 3.3 gives an expression for the pressure in the chamber in terms of the chamber elastance and the stressed blood volume:

$$P(V) = E(V - V_u)$$
$$P(V_s) \approx E \cdot V_s \tag{3.5}$$

where $V_s = V - V_u$ is the stressed volume.

The linearised unstressed volume, shown in Figure 3.3, can be seen to differ significantly from true V_u. While this implies calculating pressure using Equation 3.5 will result in high errors at volume close to the unstressed volume, it provides a reasonable approximation in the expected operating volumes for a patient. It is also important to note, volumes in Equation 3.5 are the stressed volumes and not the actual volume contained in the blood vessels.

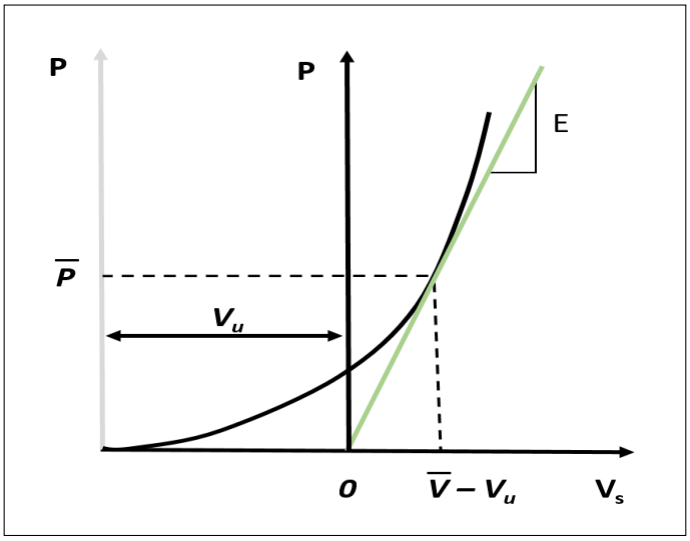

Figure 3.3: First order Taylor approximation of the passive chamber pressure-volume relation in terms of the *stressed volume* in the chamber

3.4 Resistances

The three resistances of the TCM describe the resistance to blood flow between each chamber. Output resistance (R_o) represents resistance from the aortic valve, R_c is the summation of all resistances to flow throughout the systemic circulation, and R_i is the resistance of the entire right side of the circulation, from vena cava to the left atrium. Because the TCM only accounts for the systemic circulation, R_i includes contributions from the right side circulation and care must be taken when assigning values for R_i to any specific aspect of the circulation.

Circulatory flow is analogous to an electrical circuit described by Ohm's law, where flow is driven by the pressure differential between successive chambers, divided by the

resistance. This work assumes the linear relationship defined.

$$Q(t) = \frac{P_{up}(t) - P_{down}(t)}{R} \tag{3.6}$$

Where *up* and *down* refer to the upstream and downstream chambers, respectively. R_i and R_o include the resistance from the cardiac valves restricting flow into and out of the heart, respectively.

Valve resistance is modelled using a pressure dependent piecewise function, stating flow through the valve can only occur if pressure in the preceding chamber exceeds pressure in the downstream chamber. If pressure downstream is greater, the valve is modelled as being perfectly closed and flow drops to zero. Thus valve behaviour is defined:

$$Q(t) = \begin{cases} \frac{P_{up}(t) - P_{down}(t)}{R} & if \quad P_{up} > P_{down} \\ \\ 0 & otherwise \end{cases} \tag{3.7}$$

Blood inertia is assumed to be negligible and blood flow stops when the pressure gradient reaches zero. Other works have proposed methods for accounting for flow inertia [71, 72]. However, this additional term requires the implementation of an additional differential equation, increasing the number of parameters required to be identified, increasing both the computational cost of the model and the required number of measurement inputs. Although inertial effects are known to significantly contribute to the ejection of blood from the ventricle to the aorta near the end of ejection, where the pressure differential between artery and ventricle is in the opposite direction of flow. Blood inertia effects

were observed to have little effect on model outputs in terms of global hemodynamic trends in lumped parameter models [71] and thus, the added model complexity is not justified.

3.4.1 CONTINUITY EQUATION

The continuity equation describes the conservation of mass in a system. The CVS is concerned with the conservation of blood as it flows through the circulation. Flow into a chamber either accumulates in the chamber, increasing the volume and subsequently pressure, or flows into the next chamber. Flow through each chamber is thus defined:

$$\frac{dV}{dt}(t) = Q_{in}(t) - Q_{out}(t) \tag{3.8}$$

The linear P-V assumptions used to describe the passive chambers can also be applied to Equation 3.8, establishing a relationship in terms of stressed volumes:

$$\frac{dV_s}{dt}(t) = Q_{in}(t) - Q_{out}(t) \tag{3.9}$$

Flow through the circulation is conserved. Thus, summing Equation 3.9 over all chambers gives a net zero change in total blood volume throughout the system.

$$\Sigma_i \frac{dV_s}{dt}(t) = \Sigma_i Q_{in}(t) - \Sigma_i Q_{out}(t) \tag{3.10}$$

$$\Sigma_i \frac{dV_s}{dt}(t) = 0 \tag{3.11}$$

Integrating Equation 3.11 gives the total stressed blood volume (SBV) of the system and is constant. In reality, given a long enough period of time SBV will be seen to change. Changes in patient condition either through the progression of disease or injury, the ensuing treatment, or changes in metabolic demand can alter SBV. However, over a single cardiac cycle, or a few cycles, SBV can be assumed to remain constant. Therefore, continuous measurements can be used to identify model parameters for each beat to track changes over time.

3.5 Active Chamber

Unlike the venous and arterial systems, the left ventricle is an *active chamber* and continuously contracts and relaxes to pump blood into the circulation. The contractions produce time dependent changes in ventricular elastance, meaning pressure in the chambers can no longer be closely approximated using the linear P-V relation described in Section 3.3. An additional variable, called the *time-varying elastance (TVE)*, is introduced into the ventricular pressure-volume equation to account for the changes in elastance driving cardiac contraction. TVE curves are used to illustrate changes in the ventricular P-V loop over one cycle [16, 17, 73–75].

3.5.1 Time-varying elastance (TVE)

TVE curves are derived from the ventricle P-V relations, presented in Chapter 1. They show the time series relation between simultaneously recorded ventricular pressure and

volume measurements [16, 17]. Because these loops are the ratio of pressure to volume they can be used to describe the changing elastic properties of the ventricle [73]. Figure 3.4 illustrates how plotting P-V ratios throughout a cardiac cycle can be used to derive the TVE curve.

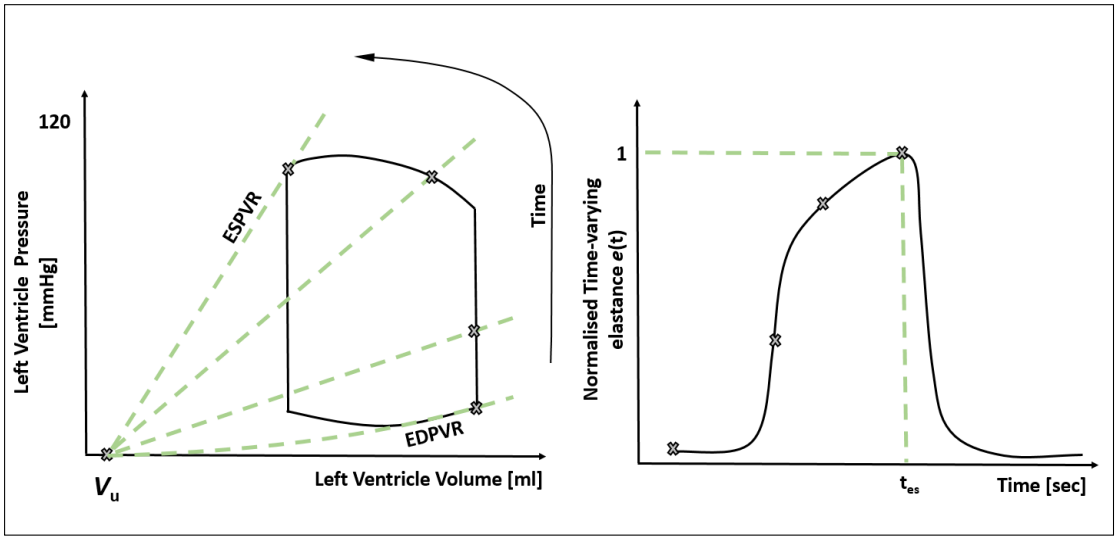

Figure 3.4: Relation of TVE curves to the ventricular pressure-volume relations over one cardiac cycle. (left) Left ventricle P-V loop over one cardiac cycle. (right) time varying elastance (TVE) curve derived from the P-V loop and normalized by the end-systolic elastance.

TVE curves are usually normalized by the E_{es} resulting in a time series curve like the one depicted in Figure 3.4. Mathematically, TVE curves can be expressed:

$$e(t) = \frac{P_{lv}(t)}{E_{es} \cdot (V_{lv}(t) - V_{lv,u})} \tag{3.12}$$

where $P_{lv}(t)$ and $V_{lv}(t)$ are the pressure and volume in the left ventricle, respectively, V_u is the unstressed volume, and $e(t)$ is the normalized time varying slope of the P-V regression line, ranging from the EDPVR to ESPVR.

More specifically, $e(t)$ can be then be used to describe the pressure and volume in the ventricle:

$$P_{lv}(t) = e(t) \cdot E_{es} \cdot (V_{lv}(t) - V_{lv,u}) \tag{3.13}$$

3.5.2 Non-linearity of ESPVR

Some scepticism exists as to whether or not the ESPVR is truly linear [76–78], citing the original experiments were not performed over a sufficiently wide enough range of operating conditions to expose any non-linear behaviour. The issue of linearity is also highlighted when fitting linear regression lines to experimentally derived data for the ESPVR, which often yields physiologically inconsistent negative values for V_u [76, 78].

Severe levels of cardiac depression have been reported to produce a non-linear ESPVR as a result of the complex interaction of cardiovascular mechanisms present. Some authors have speculated other cardiac auto-regulatory mechanisms characterize the ESPVR during extreme loading conditions, in addition to the Frank-Starling mechanism, producing the observed non-linear behaviour. Alternate bi-linear and curvilinear approaches have been suggested to better capture the ESPVR when a wider loading range is examined [76, 78, 79].

However, a significant limitation of proposed non-linear methods is the requirement for large amounts of ventricular pressure and volume data required to properly fit the models. Such data is highly unlikely to be available in a clinical environment. Therefore, the linear approximation was deemed more suitable for this work.

3.6 Model Equations

This section summarizes the equations used to fully describe the TCM. Using the passive P-V relationship detailed in Section 3.3, pressure in the venous and arterial chambers is defined:

$$P_{ao}(t) = E_{ao}V_{s,ao}(t) \tag{3.14}$$

$$P_{vc}(t) = E_{vc}V_{s,vc}(t) \tag{3.15}$$

where E is the chamber elastance and $\mathrm{V_s}$ is the stressed volume of the chamber. The time-varying elastance model is implemented to describe ventricular dynamics allowing pressure in the chamber to be defined:

$$P_{lv}(t) = e(t)E_{es}V_{s,lv}(t) \tag{3.16}$$

where $\mathrm{E_{es}}$ is the end systolic elastance, $\mathrm{V_{s,lv}(t)}$ is the stressed volume of the left ventricle, and $e(\mathrm{t})$ is the normalised time-varying function. Flow through the circulation is defined by the pressure differential between arterial and venous chambers, divided by the resistance to flow given as:

$$Q_c(t) = \frac{P_{ao}(t) - P_{vc}(t)}{R_c} \tag{3.17}$$

where R_c is the value of the resistance of the circulation, capturing the capillary and surrounding arterial-venous resistance. Flow into and out of the left ventricle is described by Equation 3.7, applied to the appropriate upstream and downstream chambers:

$$Q_i(t) = \begin{cases} \frac{P_{vc}(t) - P_{lv}(t)}{R_i} & if \quad P_{vc} > P_{lv} \\ 0 & otherwise \end{cases} \tag{3.18}$$

$$Q_o(t) = \begin{cases} \frac{P_{lv}(t) - P_{ao}(t)}{R_o} & if \quad P_{vl} > P_{ao} \\ 0 & otherwise \end{cases} \tag{3.19}$$

Calculating flows using direct pressure measurements and back calculation allows for properties such as viscosity to be incorporated without the need for direct measurement. Finally, the continuity equation is used to give the rate of change of stressed volume in each of the chambers.

$$\dot{V}_{s,lv}(t) = Q_i(t) - Q_o(t) \tag{3.20}$$

$$\dot{V}_{s,ao}(t) = Q_o(t) - Q_c(t) \tag{3.21}$$

$$\dot{V}_{s,vc}(t) = Q_c(t) - Q_i(t) \tag{3.22}$$

Where Q_i, Q_o and Q_c represent flow in and out of the heart, and through the systemic circulation, respectively, and $\dot{V}_{s,c}$ is the rate of change of stressed blood volume in chamber $c = ao, vc, lv$. Summing the rate of change of volume for all three chambers

and taking the integral gives the total stressed volume for the system:

$$V_{s,lv}(t) + V_{s,vc}(t) + V_{s,ao}(t) = SBV_m(t) \tag{3.23}$$

The complete system is defined by 7 model parameters (3 chamber elastances: E_{lv}; E_{ao}; and E_{vc}; 3 flow resistances: R_i; R_o; and R_c; and total stressed blood volume, SBV_m) and a cardiac driver function $e(t)$. The parameter vector, $\boldsymbol{p}$, for the TCM is thus defined:

$$p = \{E_{lv}, E_{ao}, E_{vc}, R_i, R_o, R_c, SBV_m\} \tag{3.24}$$

Measurements of aortic pressure, left ventricle pressure, left ventricle volume and central venous pressure can be used to derive the necessary initial estimates for all model parameters, allowing parameters to be optimized. Measured data is also used to construct error metrics corresponding to their representative parameters for parameter identification and validation.

3.7 Simulation

For a given set of model parameters p, simulation of the TCM waveforms begins at a time dictated by the cardiac driver function, $e(t)$. Using the example presented in Figure 3.4 as a reference, the simulation begins during diastole and thus, the output valve is closed and the ventricle is filling. The driver function then initiates cardiac contraction causing a rapid rise in pressure to a value in excess of the arterial chamber and blood is

ejected. As ejection continues, arterial chamber pressure increases, eventually exceeding the ventricular chamber pressure causing the output valve to close again. Ventricular chamber pressure continually decreases until falling below the venous chamber pressure, allowing the ventricle to again fill.

3.8 Parameter Identification

Model parameters are identified by minimizing an error function comprised of a set of error metrics relating model outputs to their corresponding reference values [62, 80, 81]. The specific composition of the error function will depend on the measurements available. However, to ensure structural identifiability one volumetric reference value must be used in addition to the readily available pressure measurement reference values [65].

For a given parameter set, the TCM outputs can be used to define a set of output values, $\mathbf{y(p)}$, where $\mathbf{p}$ denotes the parameter set, which can be compared to the corresponding values obtained from the reference measurements, y_{mea}, to calculate the error. The absolute error between measured and model values is given:

$$e_i^{abs} = |y_{i,mea} - y(\mathbf{p})_i| \tag{3.25}$$

Given the expected availability of data in a clinical environment and the data required form structural identifiability of the model, the following outputs are assumed available for inclusion in the output vector [65, 66, 69]

- Mean central venous pressure, $\bar{P}_{vc}$
- Range of central venous pressure, ΔP_{vc}
- Mean arterial pressure, $\bar{P}_{ao}$
- Range of arterial pressure, ΔP_{ao}
- Mean ventricle volume, $\bar{V}_{lv}$
- Range of ventricle volume, ΔV_{lv}
- Maximum arterial pressure gradient, $\frac{P_{oa}(t)}{dt}_{max}$

The output vector **y** is thus defined:

$$y = \left(\bar{P}_{vc}, \Delta P_{vc}, \bar{P}_{ao}, \Delta P_{ao}, \bar{V}_{lv}, \Delta V_{lv}, \frac{P_{oa}(t)}{dt}_{max}\right) \tag{3.26}$$

As the various error metrics will have different magnitude, using percentage or absolute errors can lead to favouring of some metrics over the others. Calculating errors as a percentage will favour optimising venous pressures, which have values of $\approx 2-10 mmHg$ and thus, small deviations from the reference value can result in significant relative errors, causing them to be prioritized in the optimization to make the most significant improvements to the objective function. Conversely, using absolute errors will tend to neglect venous pressure influence.

To ensure each component of the error vector, **e(p)**, has similar contribution to the error vector, they are initially independently optimized to give an upper and lower bounds of each error metric [82, 83]. These bounds can be applied to their respective components

of the error function by:

$$e_i^N = \frac{e_i^{abs} - e_i^L}{e_i^U - e_i^L} \tag{3.27}$$

where e_i^N is the normalized component of the error vector e_i, with respect to the upper, e_i^U, and lower, e_i^L bound. The final objective function, γ, is then the mean of the normalized errors:

$$\gamma = \frac{1}{N_y} \sum_{i=1}^{N_y} e_i^N \tag{3.28}$$

3.8.0.1 Practical non-identifiability of R_i

Early attempts to identify the TCM parameters encountered a potential contradiction between the model and available clinical data [66]. The structure of the TCM dictates flow into the ventricle can only occur if venous pressure exceeds ventricular pressure, under the assumption central venous pressure is a direct surrogate for left ventricle filling pressure. However, although central venous and left atrium pressure are similar, left atrium pressure typically exceed venous pressure by ≈2-5mmHg. Therefore, there is no guarantee measurements of central venous pressure and left ventricle pressure intercept in a manner allowing normal ventricular filling to occur.

Figure 3.5 shows two examples of left ventricle and central venous pressure measurements taken invasively from two separate porcine experiments. The left image shows $P_{vc,mea}$ greater than $P_{lv,mea}$ during diastole, allowing blood to flow into the ventricle. The right image shows no intercept between the two waveforms, but normal CVS function

continues, indicating a disparity between $P_{vc,mea}$ and left atrial pressure, largely due to the effects of atrial contraction of the ventricles ability to fill.

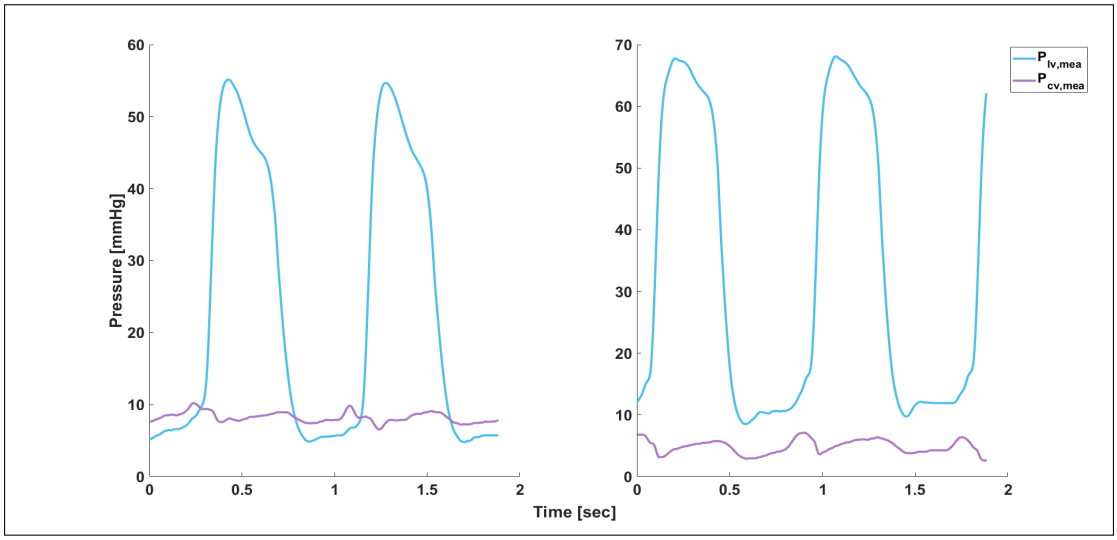

Figure 3.5: Comparison of two sets of waveforms taken from the intact and healthily operating CVS of the porcine experiments. (left) $P_{vc,mea}$ falls below $P_{lv,mea}$ during diastole. (right) an instance of $P_{vc,mea}$ not intersecting with $P_{lv,mea}$ at any point during the cycle, potentially causing identifiability issues for the TCM.

As $P_{lv,mea}$ is included into the cardiac driver function and $P_{vc,mea}$ is directly used for model reference values, the resulting TCM waveforms will conform closely to their respective reference measurements. However, in situations where $P_{vc,mea}$ does not exceed $P_{lv,mea}$ at any stage during the cycle it will causes a contradiction between reference values and model dynamics. As a consequence, the optimization process will continually reduce R_i to achieve normal ventricular filling, tending toward zero and breaking the model.

To ensure practical identifiability, the cardiac driver function can be normalized between 0 and 1, as shown in Figure 3.6 ensuring model ventricular pressure falls below venous

pressure during diastole [66]. Essentially, this is the inverse of shifting the central venous pressure as it forces left ventricle pressure down to zero at some point during the cycle. Simulated left ventricle pressure is not included in the output vector. Hence, this approach was favourable over arbitrarily adjusting $P_{vc,mea}$ to represent left atrial pressure.

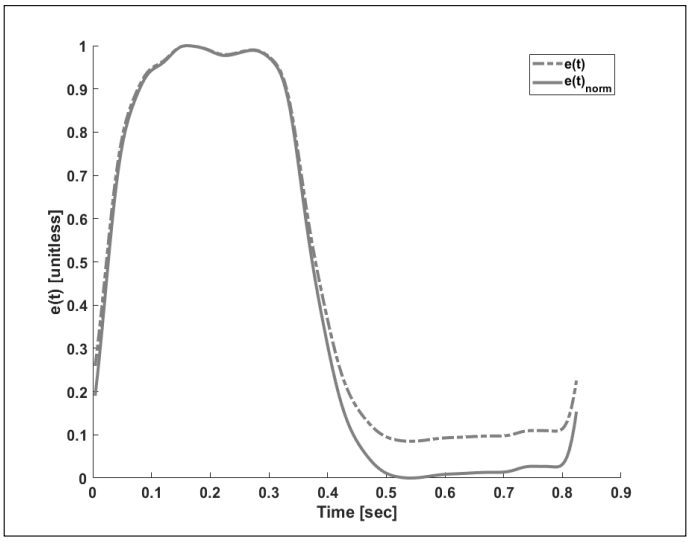

Figure 3.6: Normalization of e(t), to give $e(t)_{norm}$, used as the cardiac driver function for the TCM, ensuring practical identifiability of R_i by forcing model-based left ventricle pressure to zero during diastole.

3.8.1 Initial parameter estimates

To initiate the parameter ID process the model requires initial estimates for each parameter. This section provides the equations used to calculate each initial parameter estimate.

Systemic circulatory resistance (R_c) is estimated from Equation 3.17 integrated over

one cardiac cycle.

$$\int_0^T Q_c(t)dt = \frac{\int_0^T (P_{ao}(t) - P_{vc}(t))dt}{R_c} \tag{3.29}$$

Taking the integral of Equation 3.21 over one cardiac cycle yields:

$$\int_0^T \dot{V}_{s,ao}(t)dt = \int_0^T Q_o(t)dt - \int_0^T Q_c(t)dt \tag{3.30}$$

$$\Rightarrow V_{s,ao}(T) - V_{s,ao}(0) = \int_0^T Q_o(t)dt - \int_0^T Q_c(t)dt \tag{3.31}$$

Because pressure in the CVS are cyclic, the left side of Equation 3.31 becomes zero and the integral of flow through the arterial chamber equals flow though the circulation. Substituting this equivalence into Equation 3.31, and rearranging for R_c yields:

$$R_c = \frac{\int_0^T (P_{ao}(t) - P_{vc}(t))dt}{\int_0^T Q_o(t)dt} \tag{3.32}$$

$$\Rightarrow R_c = \frac{\bar{P}_{ao}(t) - \bar{P}_{vc}(t)}{\int_0^T Q_o(t)dt} \cdot T \tag{3.33}$$

Where $\bar{\mathrm{P}}_{\mathrm{ao}}$ and $\bar{\mathrm{P}}_{\mathrm{vc}}$ are the mean arterial and venous pressures over one cycle. The integral of $\mathrm{Q_o}$ is the blood volume exiting the heart and is equal to the change in ventricular stressed volume. This equivalence allows for aortic flow probe and ventricular admittance catheter measurements to be used interchangeably for $\Delta \mathrm{V_{s,lv}}$, $\mathrm{SV} = \Delta \mathrm{V_{s,lv}}$. Thus, an initial estimate of R_c is defined:

$$R_c \approx \frac{\bar{P}_{ao} - \bar{P}_{vc}}{SV} \cdot T \tag{3.34}$$

Input resistance (R_i) can be evaluated from the $\mathrm{P_{vc,mea}}$ and $\mathrm{P_{lv,mea}}$ pressure differential

during filling. The area between the two pressure waveforms is equal to the product of input resistance and change in ventricular volume, shown in Figure 3.7. Combining Equations 3.18 and 3.20 and integrating over the duration of filling, form before filling (BF) to end of filling (EF), as shown in Figure 3.7, gives:

$$\dot{V}_{s,lv}(t) = \frac{P_{vc}(t) - P_{lv}(t)}{R_i}$$

$$\Rightarrow V_{s,lv}(t_{EF}) - V_{s,lv}(t_{BF}) = \frac{\int_{t_{BF}}^{t_{EF}} (P_{vc}(t) - P_{lv}(t))}{R_i} \tag{3.35}$$

The left side of Equation 3.35 describes the change in ventricle volume during filling, which takes the ventricle from a minimum to maximum volume. Therefore, the left side is equal to the change in ventricular volume and thus, $\Delta V_{s,lv}$. Substituting $\Delta V_{s,lv}$ into Equation 3.35 and rearranging for R_i gives:

$$R_i = \frac{\int_{t_{BF}}^{t_{EF}} (P_{vc}(t) - P_{lv}(t))dt}{\Delta V_{s,lv}} \tag{3.36}$$

Output valve resistance (R_o) is described similarly to R_i. Combining Equations 3.34 and 3.20 and integrating of the duration of ejection gives:

$$\dot{V}_{s,lv}(t) = \frac{-P_{lv}(t) - P_{ao}(t)}{R_o}$$

$$\Rightarrow V_{s,lv}(t_{EE}) - V_{s,lv}(t_{BE}) = \frac{-\int_{t_{BE}}^{t_{EE}} (P_{lv}(t) - P_{ao}(t))}{R_o} \tag{3.37}$$

where BE and EE indicate before and end of ejection, respectively, as shown in Figure 3.7. Because $V_{s,lv}$ goes from a maximum at t_{BE} to a minimum at t_{EE}, the left side of

Equation 3.37 equals $-\Delta V_{s,lv}$. Substituting $-\Delta V_{s,lv}$ into Equation 3.37, and rearranging for R_o gives:

$$R_o \approx \frac{\int_{t_{BE}}^{t_{EE}} \left(P_{lv}(t) - P_{ao}(t)\right) dt}{\Delta V_{s,lv}} \tag{3.38}$$

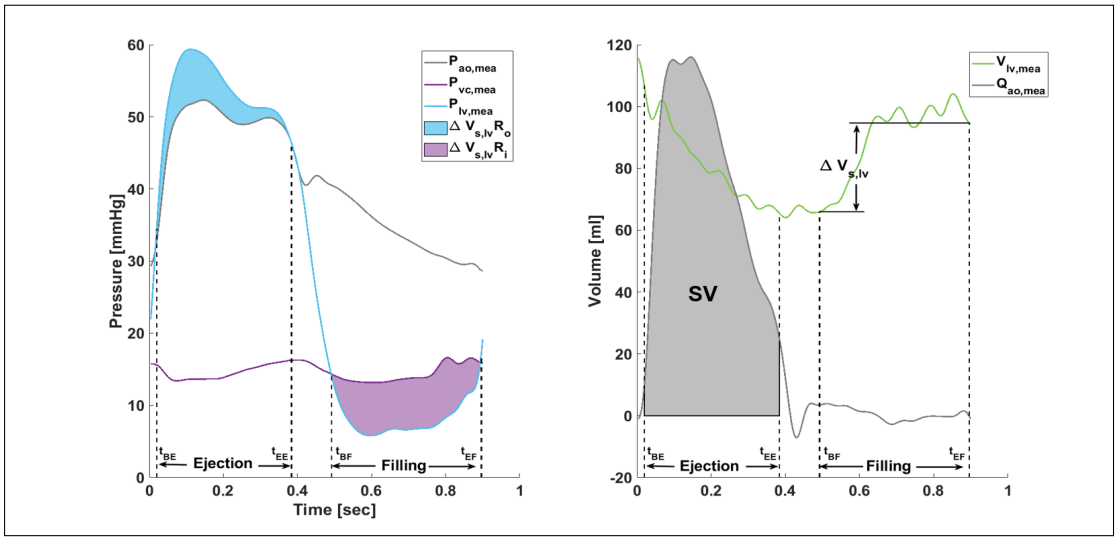

Figure 3.7: Graphical representation of pressure interactions used to provide initial estimates for R_i and R_o.

Arterial elastance (E_{ao}) if found by fitting to the aortic pressure pulse during diastole.

Change in arterial volume is given through the combination of Equations 3.17 and 3.21:

$$\dot{V}_{s,ao}(t) = \frac{-P_{ao}(t) - P_{vc}(t)}{R_c}$$

Neglecting P_{vc}, as it is much smaller relative to P_{ao}, and using the P-V relation describing

pressure in a changer as the product of volume and elastance gives:

$$\dot{V}_{s,ao}(t) = \frac{-E_{ao} \cdot V_{s,ao}}{R_c} \tag{3.39}$$

Solving Equation 3.39 for $V_{s,ao}$ yields:

$$V_{s,ao} \approx \exp\left(\frac{-E_{ao}(t - t_{BD})}{R_c}\right) \cdot V_{s,ao}(t_{BD}) \tag{3.40}$$

where t_{BD} denotes the beginning of diastole. Multiplying both sides of Equation 3.40 by E_{ao} gives:

$$P_{ao} \approx \exp\left(\frac{-E_{ao}(t - t_{BD})}{R_c}\right) \cdot P_{ao}(t_{BD}) \tag{3.41}$$

Using the value of R_c obtained from Equation 3.32, E_{ao} is determined by fitting Equation 3.41 to the aortic pressure waveform, shown in Figure 3.8.

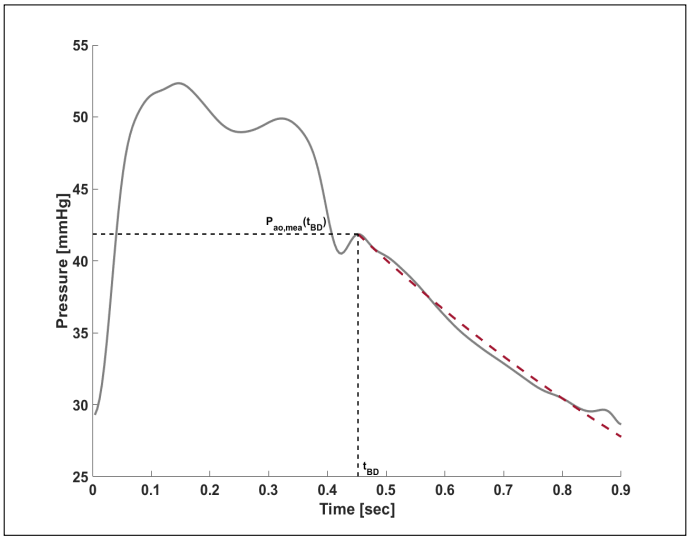

Figure 3.8: Illustration of the diastolic component of aortic pressure used to fit Equation 3.41 to for initial estimates of E_{ao}.

Venous elastance (E_{vc}) during systole is given by:

$$\dot{V}_{s,vc}(t) = Q_c(t) \tag{3.42}$$

Assuming flow through the circulation is constant and equal to its mean value gives:

$$\dot{V}_{s,vc}(t) \approx \frac{\Delta V_{s,lv}}{T} \tag{3.43}$$

Integrating over systole and multiplying both sides of the equation by E_{vc} gives:

$$V_{s,vc}(t_{ES}) - V_{s,vc}(t_{SS}) \approx \frac{\Delta V_{s,lv}}{T}(t_{ES} - t_{SS})$$

$$\Rightarrow P_{vc}(t_{ES}) - P_{vc}(t_{SS}) \approx E_{vc}\frac{\Delta V_{s,lv}}{T}(t_{ES} - t_{SS})$$

Assuming venous pressure change over systole is equal to ΔP_{vc} and systole is approximately half the cardiac period ($t_{ES} - t_{SS} = T/2$), Equation 3.44 can be simplified to yield:

$$E_{vc} \approx \frac{2\Delta P_{vc}}{\Delta V_{s,lv}} \tag{3.44}$$

Cardiac end-systolic elastance (E_{lv}) is calculated directly from left ventricle pressure and volume. Assuming unstressed ventricular volume, V_u, to be zero, cardiac elastance is taken as the maximum P-V ratio during a cardiac cycle.

$$E_{lv} = \left(\frac{P_{lv}(t)}{V_{lv}(t)}\right)_{max} \tag{3.45}$$

*Stressed blood volume (*SBV*)* is taken as the summation of the stressed volume approx-

imations of each chamber, using their respective stressed P-V relations, yielding:

$$SBV_m \approx \bar{V}_{lv} + \frac{\bar{P}_{ao}}{E_{ao}} + \frac{\bar{P}_{vc}}{E_{vc}} \tag{3.46}$$

3.8.2 Limitations

One primary limitation of the TCM is the omission of the pulmonary circulation. The model assumes the systemic and pulmonary circulations can be treated separately, which is not physiologically accurate. Only considering the left circulation negates the effects of ventricular interactions, which can influence pressure and volume in the ventricle through intrusion of the septum into the ventricular space [72].

The heart is enclosed a fibrous membrane called the pericardium, which causes a compressive force applied to the left ventricle when the right ventricle undergoes filling. With only one circulation being considered, this interaction cannot be accounted for. However, this effect is typically small, except in the case of pulmonary embolism [84, 85].

Physiologically, the left ventricle, and parts of the arterial and venous systems, are located inside the relatively rigid thoracic chamber. Therefore, changes in thoracic pressure during the respiratory cycle will be partially transmitted onto blood vessels contained inside the thoracic chamber. These changes in pressure are known to influence cardiac preload, and are the foundation of PPV and SVV as indices of fluid responsiveness. Again, with only one circulation accounted for, it is difficult to accurately account

for thoracic pressure. However, this influence likely only applies a smaller consistent bias, where trends over treatment are potentially more clinically important [86].

A noticeable difference in the model to true anatomy is the absence of an atrium, which provides part of the pressure required to properly fill the ventricle. It has not yet been shown that the time varying elastance theory can be applied to the atria, as is done for the ventricles. Other authors have developed alternate methods to represent the atria such as the multi-scale model [87]. However, the large number of additional parameters required for such methods to work cannot be identified using the limited data clinically available, making them unsuitable for this work.

Although the atria is excluded from the model, model parameters can be adjusted to account for this absence. Filling of the left ventricle is represented as a passive process. Thus, R_i the parameter describing the flow resistance into the ventricle, will likely be lower than reality to compensate for no atria, providing a totally passive equivalent filling.

Finally, there is no inertial effects included in this model. These were omitted from the model as they have been shown to have little effect on the model dynamics [71]. Due to this small effect on global dynamics, there is a large computational cost benefit to neglecting inertance due to the reduction in number of model parameters which need to be derived.

3.9 Summary

This chapter presented the Three-Chambered Model of the CVS. The model chambers represent the systemic arterial and venous systems, and the left ventricle. Pressure and volume in the arterial and venous systems are described using a passive P-V relation, whereas the ventricular chamber includes an additional time-varying elastance term to account for the hearts ability to contract and relax. The full model is able to be described by a very modest set of 7 parameters, allowing for identification from the limited data available clinically. Finally, the full set of model equations and equations for the initial estimates of each parameter used in the identification process are presented.

Chapter 4

Three-Chambered Model: Full Measurement Set

4.1 Introduction

Models of the CVS provide clinical utility by taking raw data from patient measurements to identify patient specific parameters capable of monitoring the CVS state through the progression of disease and ensuing treatment [86]. Model parameters, and their evolution over time and the course of treatment, can provide a more detailed explanation of how the body is responding to changes in CVS state, than simple pressure or intermittent volume measurements alone.

Chapter 3 presented the TCM of the CVS. Pironet *et al.* showed the TCM could be used to identify model based stressed blood volume (SBV_m) [65, 66] which, due to its

relation with MSFP, is likely a potential index of fluid responsiveness [62, 69]. The authors work found a consistent negative correlation between SBV_m and changes in SV during a series of porcine experiments. A lower SBV_m was found to suggest a higher likelihood of positive fluid response. Additionally, SBV_m displayed a stronger linear regression correlation with changes in SV than the clinically accepted SVV and PPV methods. These preliminary results, combined with the theoretical background for SBV, provide justification for pursuing SBV_m as an index of fluid responsiveness. However, the low number of subjects used in their study means further validation is required [62].

This chapter uses invasive measurements for all components of the output vector to identify the TCM parameters during in series of porcine endotoxin experiments. This work provides a further validation of SBV_m as an index of fluid responsiveness by investigating the correlation between changes in SV during several fluid therapies, before and after endotoxin induced septic shock. The remaining model parameters were also considered to investigate their potential clinical utility in explaining why a patient is responsive/un-responsive to fluid therapy.

4.2 Method

4.2.1 Experimental Data

Due to issues with their left ventricle catheters, both Pigs 3 and 5 were excluded from the work in this chapter, leaving data from 6 subjects to be used used. Sections of data 8 sec in duration were taken and averaged to limit measurement irregularities. Continuous

measurements for the following data were available for use as reference values for all subjects, with the exception of central venous pressure in Pig 1:

- left ventricle pressure ($P_{lv,mea}$)
- left ventricle volume ($V_{lv,mea}$)
- aortic pressure ($P_{ao,mea}$)
- central venous pressure ($P_{vc,mea}$)

An issue with the central venous line of Pig 1 resulted in only mean values of vena cava pressure being available. The range of venous pressure is necessary for practical identification of SBV. Therefore, an averaged venous pulse pressure taken across the remaining subjects was used as a reference value. Ventricular unstressed volume was assumed to be zero ($V_u = 0$).

4.2.2 Parameter Identification

Using the described reference measurements, model parameters are identified by minimizing an error function, $\boldsymbol{e}$, detailing the difference between model and reference output values. Data in the output vector included:

$$\mathbf{y} = \{\Delta P_{vc}, \Delta P_{ao} \Delta V_{lv} \bar{P}_{vc}, \bar{P}_{ao}, \bar{V}_{lv}, \left(\frac{dP_{ao}}{dt}\right)_{max}\} \tag{4.1}$$

The error function is constructed by first individually optimizing the errors corresponding to each output in $\mathbf{y}$, giving a range of error values for each parameter. This range

is used to normalize the absolute differences between model and reference outputs, per Equation 3.27, giving an error e_i^N, for the i^{th} parameter, ensuring outputs have similar weighting on the error function. The overall error function is taken as the mean normalized error vector:

$$\gamma = \frac{1}{N_y} \sum_{i=1}^{N_y} e_i^N \tag{4.2}$$

The equivalences between model and reference outputs are given in Table 11.3.

Table 4.1: Equivalences made between reference measurements and TCM outputs during the parameter identification process

Measurement	Model Output
$\Delta P_{vc,mea}$	$\Delta P_{vc,TCM}$
$\Delta P_{ao,mea}$	$\Delta P_{ao,TCM}$
$\Delta V_{lv,mea}$	$\Delta V_{s,lv,TCM}$
$\bar{P}_{vc,mea}$	$\bar{P}_{vc,TCM}$
$\bar{P}_{ao,mea}$	$\bar{P}_{ao,TCM}$
$\bar{V}_{lv,mea}$	$\bar{V}_{s,lv,TCM}$
$\left(\frac{dP_{ao,mea}}{dt}\right)_{max}$	$\left(\frac{dP_{ao,TCM}}{dt}\right)_{max}$

4.2.3 Initial Parameter Estimates

Initial parameter estimates were derived from the equations in Section 3.8.1:

1. Circulatory resistance (R_c) is estimated using Equation 3.31
2. Input resistance (R_i) is estimated using Equation 3.36
3. Output resistance (R_o) is estimated using Equation 3.38
4. Venous elastance (E_{vc}) is estimated using Equation 3.44
5. Arterial elastance (E_{ao}) is estimated using Equation 3.40

6. Ventricle elastance (E_{lv}) is estimated using Equation 3.45
7. Total stressed blood volume (SBV_m) is estimated using Equation 3.46

The parameter vector $\mathbf{p}$ to be optimized is defined:

$$\mathbf{p} = \{SBV_m, E_{lv}, E_{ao}, E_{vc}, R_i, R_o, R_c\} \tag{4.3}$$

The cardiac driver function ($e(t)$) uses direct measurements for $P_{lv,mea}$ and $V_{lv,mea}$ in Equation 3.12 and is normalized between 0 and 1 to ensure practical identifiability of R_i. Unstressed volume (V_u) is assumed to be zero. Identifying model parameters for each beat uses $e(t)$ repeated 50 times with output values taken from the final beat to ensure transient effects have dissipated.

Finally, the optimization is performed using a non-linear least squares method (Levenberg-Marquardt, as implemented by MATLAB's lsqnonlin function, R2020a, The Mathworks, Natwick, MA, USA).

4.2.4 SVV and PPV

Additional to the TCM parameters, SVV and PPV were calculated from the same sec sections of data, as they are clinically used to assess fluid responsiveness and CVS status [14, 34, 52]. Both SVV and PPV were calculated for the same sections of data as the TCM. However, these sections were extended to 15sec section to ensure variations were captured.

4.3 Results and Discussion

To ensure identifiability of R_i, the cardiac driver function was normalized between 0 and 1, compared to typical normalization by E_{es}, as shown in Figure 3.6. As mentioned in Section 3.8, vena cava measurements can produce pressures consistently lower than left ventricle pressure for the entire cardiac cycle. With left ventricle pressure being directly included in $e(t)$, the TCM simulated left ventricle pressure ($P_{lv,TCM}$) will closely approximate $P_{lv,mea}$. Additionally, $\Delta P_{vc,mea}$ and $\bar{P}_{vc,mea}$ are included in the output vector and thus, $P_{vc,TCM}$ will closely approximate $P_{vc,mea}$. Therefore, if $P_{lv,mea}$ and $P_{vc,mea}$ are not consistent with the models description of ventricular filling, R_i will be progressively reduced during optimization resulting in division errors as R_i tends towards zero.

Normalization of $e(t)$ between 0 and 1 ensures normal ventricular filling can occur. Normalization of $e(t)$, combined with the availability of invasive reference measurements, essentially eliminated model error relative to reference values. An example set of the models ability to fit data is shown in Figure 4.1.

4.3.1 Index of fluid responsiveness

Pironet *et. al.* previously proposed model based stressed blood volume (SBV_m) to be a potential index of fluid responsiveness, showing a negative correlation between SBV_m and relative change in SV, in porcine experiments given a series of 225ml fluid

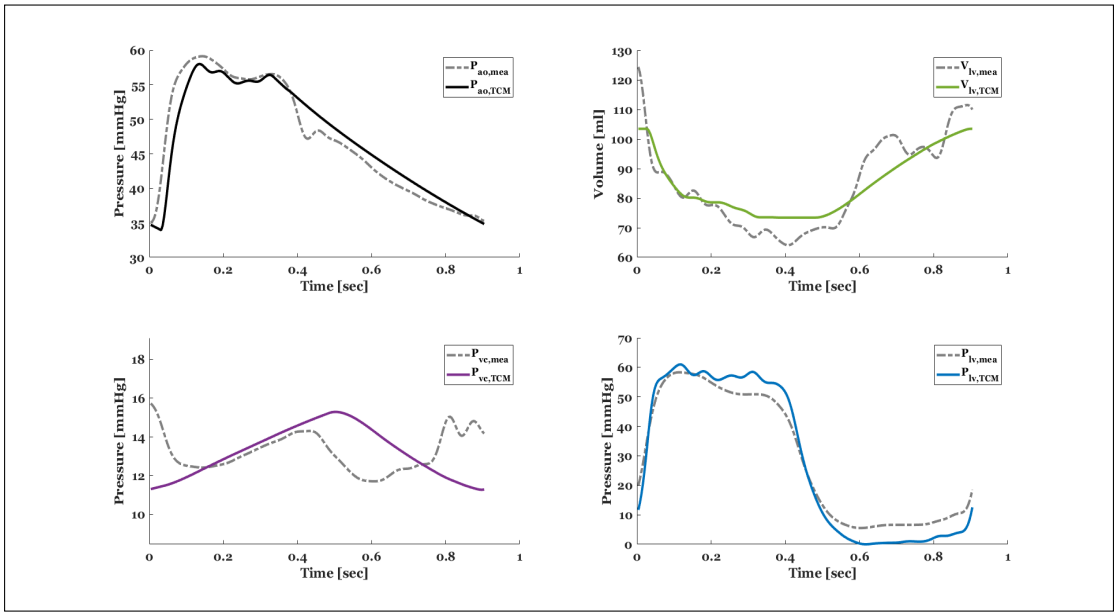

Figure 4.1: Example set of pressure and volume outputs from the TCM after parameter identification (TCM) compared to invasive reference waveforms (mea). From the top left image moving clockwise these figures represent; the aortic pressure, left ventricle volume, left ventricle pressure (although not directly included in the output vector), and the central venous pressure.

bolus [62]. A negative correlation between SBV_m and SV was also observed the work conducted in this section. Figure 4.2, shows SBV_m identified prior to, and the relative change in SV after, each 500ml bolus. While only a limited number of data points are available the results are consistent with those in [62], further validating the concept of SBV_m as a potential index of fluid responsiveness. The highlighted sections in the left image of Figure 4.2 are divided horizontally at the 12% change in SV threshold and vertically at 143 ml. The 143 ml threshold was determined using a receiver operator characteristic (ROC) curve analysis, not presented here. Green sections represent true positive (upper) and true negative values (lower) and the red false positive (lower) and false negative (upper).

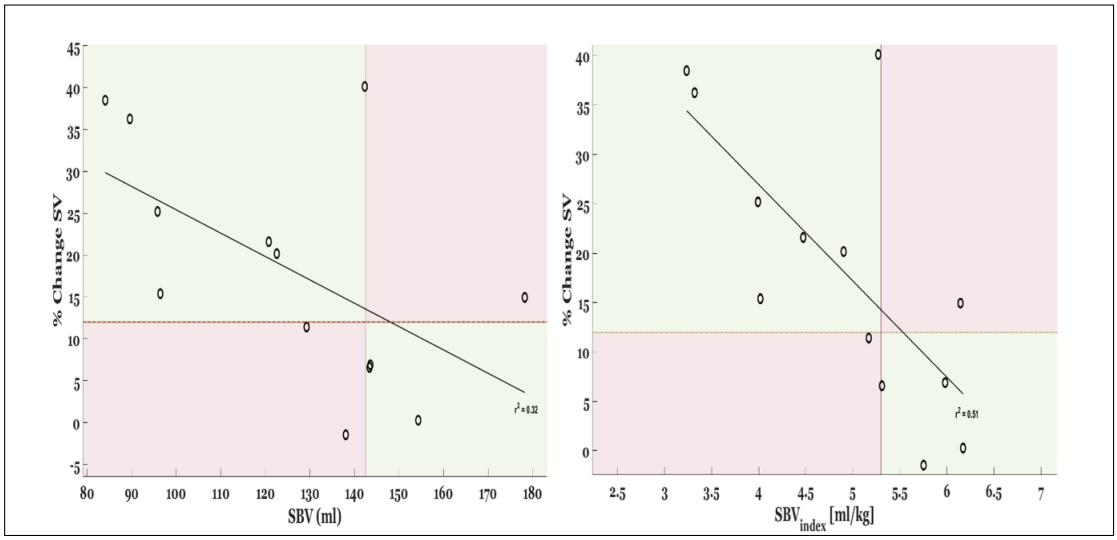

Figure 4.2: Values of (left) model-based stressed blood volume (right) stressed blood volume index, prior to receiving a 500ml fluid bolus administered over approximately 30min and the corresponding change in SV. Positive responses are defined as those exceeding a 12% increase in SV in response to the fluid bolus. The vertical threshold's are 143ml and 5.3 ml/kg for the left and right figures, respectively.

A stronger correlation between SBV_m and relative change in SV ($r^2 = 0.51$) is achieved when considering subject weight, shown in Figure 4.2. Individualization of clinical measurements on the basis of body weight or surface area is a common way of allowing clinicians to compare individual measurements to population averages and derive ideal values for goal directed treatment. Stressed blood volume per kilogram of bodyweight (SBV_{index}) presents a potentially useful metric of assessing a patients fluid responsiveness, applicable to the general population. The vertical threshold was reassessed, again using a ROC curve analysis, and found to be 5.3 ml/kg.

Figure 4.3 shows the corresponding SVV and PPV values prior to fluid therapy and the resulting change in SV. Both indices showed an inability to predict fluid responsiveness, producing a weak correlation with relative change in SV. These outcomes are possibly due to the chest of each animal having been opened to insert the measurement instru-

mentation and then clamped shut. Possible, imperfect closure may at least partially invalidate the cardio-pulmonary relations used to derive SVV and PPV as indices of fluid responsiveness.

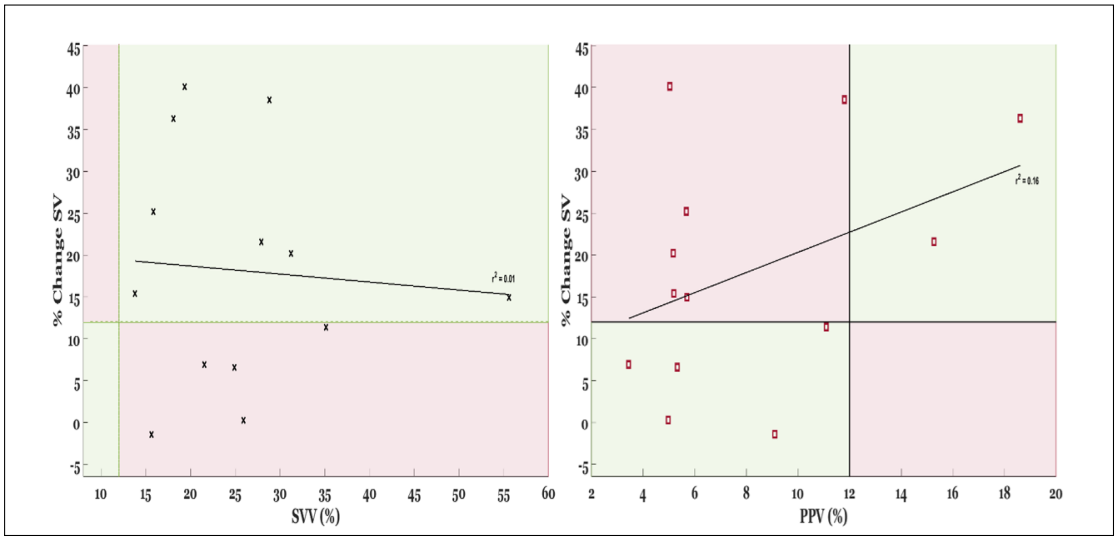

Figure 4.3: Values of (left) SVV and (right) PPV, prior to receiving a 500ml fluid bolus administered over approximately 30min and the corresponding change in SV. Positive responses are defined as those exceeding a 12% increase in SV in response to the fluid bolus. The vertical threshold for both metrics were set at 12%.

4.3.2 Time series response

A patients response to a fluid therapy is dependent on a series of not fully understood, complex, physiological mechanisms [14]. The simplicity of the TCM allows all model parameters to be identified in real time, providing a multi-dimensional assessment of a patients response to fluids [80, 81]. Figures 4.4-4.9 show the progression of SBV_{index} and SV over the duration of each experiment. The blue and green highlighted sections indicate when each 500ml saline solution bolus and e.coli endotoxin injections were

administered, respectively. The drop in SV and SBV_{index} prior to each fluid bolus is produced by the PEEP driven RM immediately preceding each fluid bolus. Similar peaks/troughs as a result of the RM's can be seen in Figures B.1-B.6 for the remaining TCM parameters. All subjects received an initial bolus prior to endotoxin infusion. However, due to the severity of reactions to the endotoxin infusion, only Pigs 2, 6 and 7 survived to receive additional fluids.

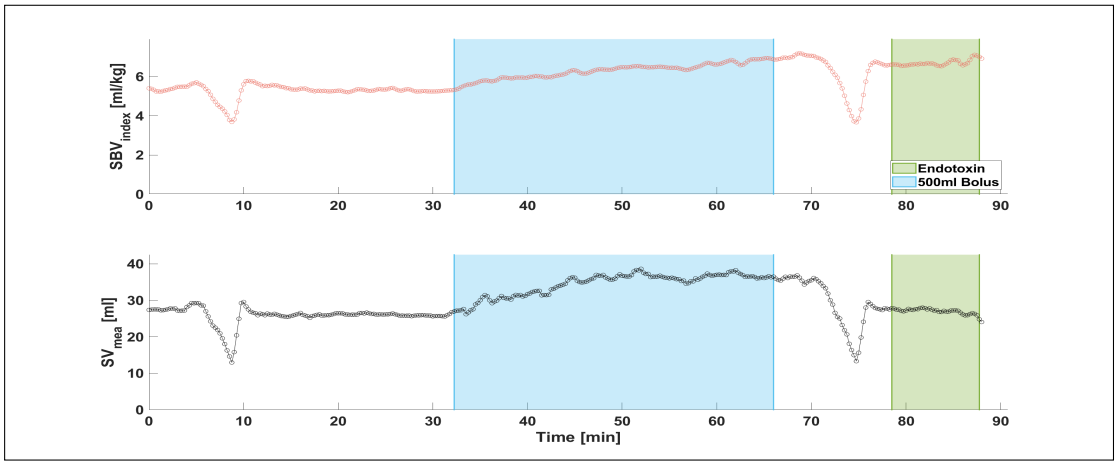

Figure 4.4: Time series analysis of SBV_{index} (top), and the associated SV (bottom), for Pig 1.

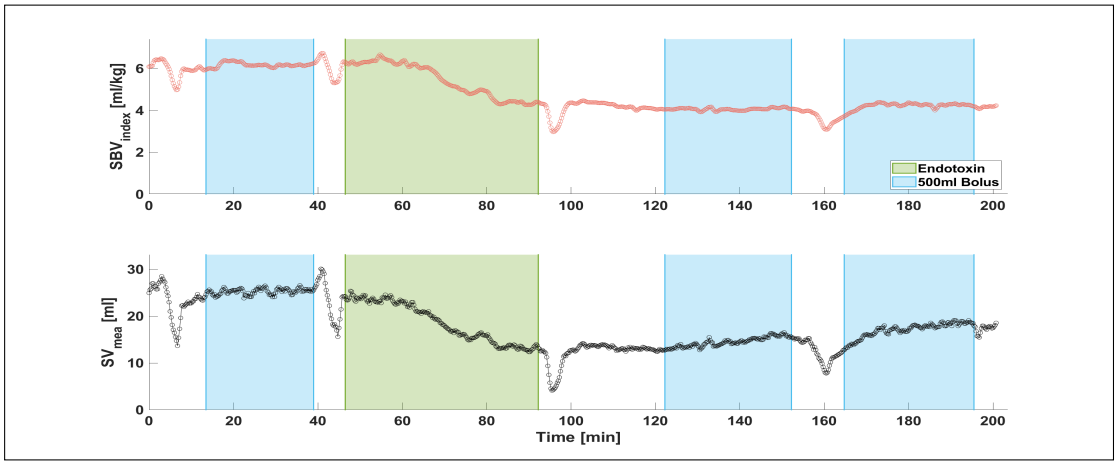

Figure 4.5: Time series analysis of SBV_{index} (top), and the associated SV (bottom), for Pig 2.

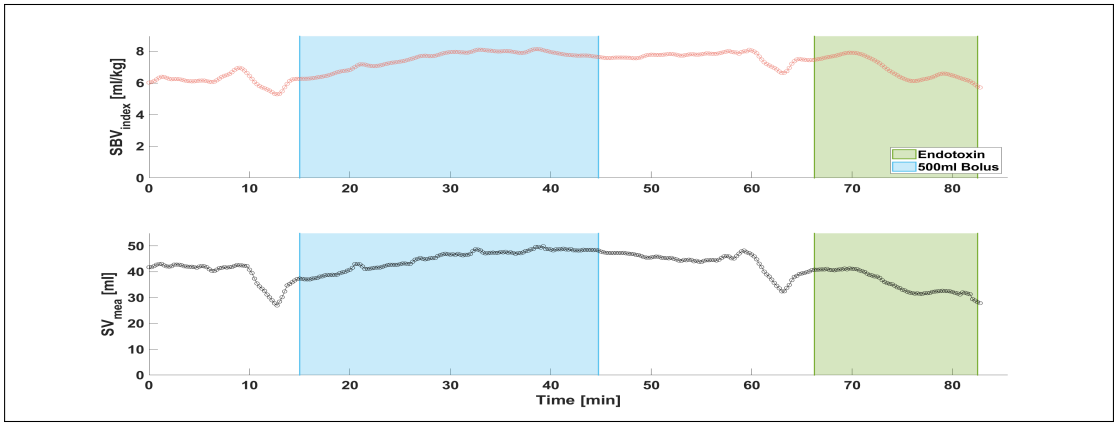

Figure 4.6: Time series analysis of $\mathrm{SBV}_{\mathrm{index}}$ (top), and the associated SV (bottom), for Pig 4.

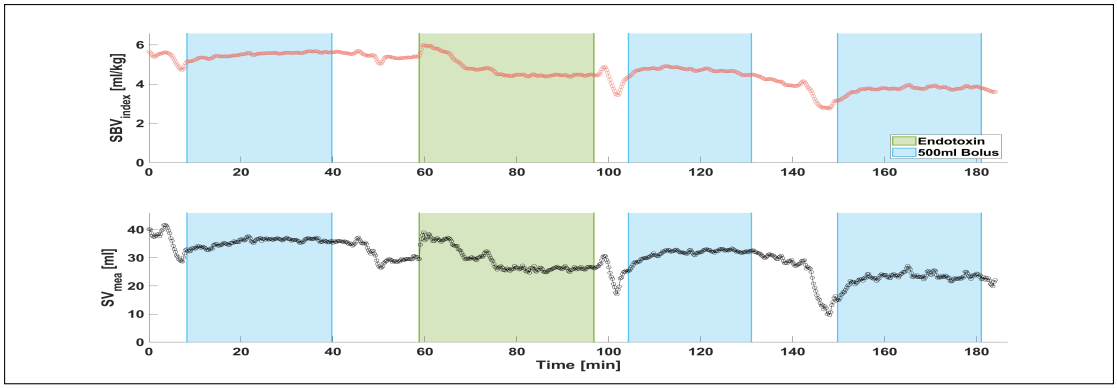

Figure 4.7: Time series analysis of $\mathrm{SBV}_{\mathrm{index}}$ (top), and the associated SV (bottom), for Pig 6.

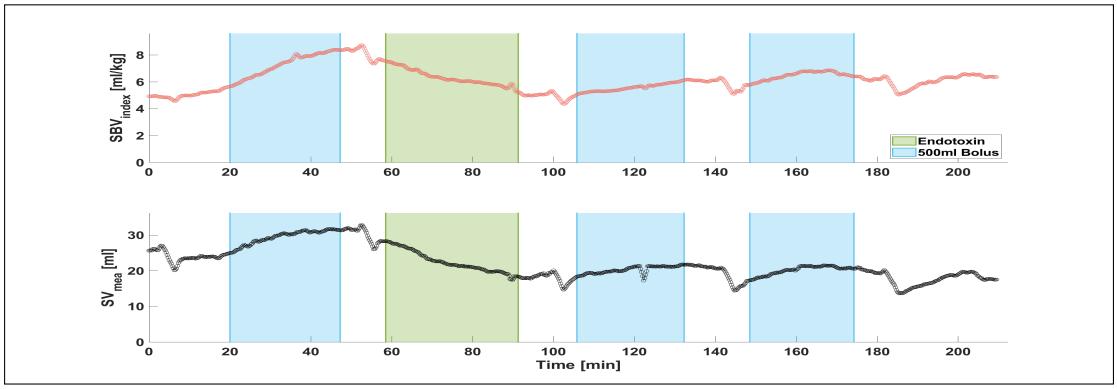

Figure 4.8: Time series analysis of $\mathrm{SBV}_{\mathrm{index}}$ (top), and the associated SV (bottom), for Pig 7.

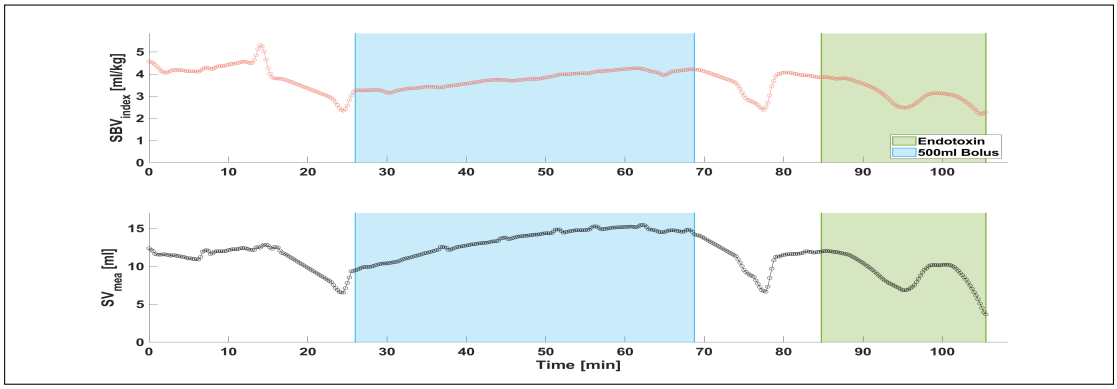

Figure 4.9: Time series analysis of SBV_{index} (top), and the associated SV (bottom), for Pig 8.

4.3.2.1 Pre-endotoxin

Despite some pigs not exceeding the $\geq$ 12% threshold defining fluid responsiveness, the initial fluid bolus produced an increase in SV for all pigs. This result is expected because the CVS can be considered healthy at this time and thus, the ventricles are likely operating on the ascending portion of the Frank-Starling curve and have adequate preload reserves to accommodate the additional volume [4, 13, 14]. Therefore, the fluid therapies will increase the pressure differential between the MSFP and right atrial pressure, increasing venous return and SV [33]. However, Pigs 1, 4, 7 and 8 displayed a perceptibly greater response to fluids compared to Pigs 2 and 6, whose SV remained relatively constant. These results are despite the same fluid amount and type being used in similar size animals, highlighting the complexity of fluid treatment.

The unresponsiveness of Pigs 2 and 6 may be explained by considering model based venous elastance E_{vc}, shown for each pig in Appendix B. Similar to how arterial elastance is indicative of the extra-cardiac forces opposing ventricular ejection (afterload) [22, 23,

25, 88, 89] E_{vc} can be considered as representing the forces opposing venous return. Additionally, increasing E_{vc} increases the rate at which pressure is transmitted to the right atrium, increasing the force opposing VR [4]. Pigs 2 and 6 experienced an increase in E_{vc} by 24.7 and 25.8%, respectively.

Interestingly, the unresponsive subjects presented relatively constant levels of SBV_{index} during fluid administration, despite total circulating volume increasing. One explanation is some level of volume vasodilation, induced by the autonomic nervous system [90, 91] to accommodate the additional fluid, is occurring. Experimental animal studies have shown aggressive fluid therapy resulted in the reduction of systemic vascular resistance through volume induced vasodilation [92]. Several potential mechanisms could cause this effect, including: the release of flow modulated nitric oxide in response to increase endothelial wall shear stress resulting in vascular relaxation; additional volume re-opening blood vessels previously closed to maintain pressure as a result of blood loss due to the procedures required to insert the measuring device; and the release of atrial natriuretic peptides in response to increased volume stretching the myocardium [50, 93]. These effects could explain why circulatory resistance R_c in Pig 2 falls with the volume infusion.

The clinical procedures required to open the chest of each pig and insert the measurement devices likely resulted in significant blood loss. This blood loss may result in portions of the peripheral vascualture to close in an attempt to preserve perfusion pressure, a process which can be undone when fluid therapy occurs. Pig 6 sees an increase in SBV_{index}, E_{vc}, R_c and R_i, indicating the ventricle has no prelaod reserves. A further

explanation is fluid is simply forced from the blood vessels into the lungs or interstitial space, initiating fluid overload.

The remaining Pigs, 1, 4, 7 and 8, displayed the opposite trends and were responsive to the fluid bolus. The most significant positive response is observed in Pig 7, where E_{vc} reduces by ≈20%, relative to the pre fluid infusion levels. This decrease in E_{vc} is accompanied by a decrease in R_c and increase in R_i, which is to expected as right ventricle preload is increased. These results indicate a successful fluid therapy, confirmed by the increase in SV. Pigs 1, 4 and 8 have similar trends in their parameters, also indicating positive responses confirmed with increases in SV $\geq$ 12%.

4.3.2.2 Post-endotoxin

The surviving Pigs 2, 6 and 7, each responded differently to fluid therapies after endotoxin. A plethora of changes occurs during sepsis and septic shock, which are not fully understood and often manifest differently depending on an individuals response to the initial insult and the state of the CVS prior to endotoxin . Generally speaking, septic shock will reduce stressed blood volume in the circulation by increasing vascular permeability and reducing vasomotor tone [26, 27, 30, 94–96].

One commonality between the 3 surviving pigs was a decline in SBV_{index} and SV immediately after endotoxin, possibly due to increased vascular permeability as a result of the aggressive endotoxin infusion. Additionally, all three pigs see an increase in E_{vc},

R_c and R_i indicating a likely early hyper-inflammatory response to the initial infection resulting in temporary vasoconstriction [92].

In response to both post-endotoxin fluid therapies, SBV_{index} remained steady, while SV increased. Low SBV_{index} levels indicate a higher likelihood of the subject being fluid responsive, implying the circulation is able to accommodate the additional volume, and allowing fluids to be transferred to the ventricle without any compensatory mechanisms being required to accommodate the volume. The readiness of the CVS for pig 2 to accept the fluid bolus is unsurprising as SV has fallen by $\geq$50% of the baseline values.

Pig 7 experienced increases in SBV_{index} with each post-endotoxin filling. However, changes in SV were low relative to pre-endotoxin fluid infusions. While increasing SBV_{index} is expected to increase VR and SV, each fluid bolus appears to have been met with a proportional increase in R_i, indicating the ventricle is no longer preload responsive.

Subject 6 displays a progressive loss of SBV_{index} after endotoxin infusion, with the effects of each subsequent fluid bolus having only a temporary effect. These results indicate sepsis induced structural damage to the CVS has begun.

4.3.3 Ventriculo-arterial coupling

The remaining two TCM parameters, arterial (E_{ao}) and cardiac (E_{lv}) elastance, can be used to describe cardiac efficiency using the notion of ventriculo-arterial coupling (VAC), discussed in Section 1.6. The ratio of the extra-ventricular forces opposing

ejection of blood during cardiac contraction to cardiac contractility, expressed by $\frac{E_{ao}}{E_{lv}}$, can be used to describe the interconnection between arterial and cardiac systems. During resting states, the CVS typically optimizes for cardiac efficiency and minimizes oxygen requirements, producing a VAC value of $\approx 0.5-1$. During periods of increased metabolic demand, mechanical energy transfer is optimized for and VAC increases $\approx 1-1.2$. Technically speaking, when VAC exceeds 1 decoupling occurs. Practically however, healthy values for VAC range from 0.5-1.2 and decoupling is often cited as VAC ≥ 1.36 during septic shock [21, 24, 25]. Monitoring VAC during fluid therapy can provide clinicians with a tool to assess the ventricles ability to accommodate changes in arterial load produced by clinical treatment or disease states [40, 88].

Figures 4.10 and 4.11 show the progression of E_{lv}, E_{ao} and VAC for each experiment. During the initial fluid therapies, relatively constant values for VAC are seen for all subjects. Pig 4 is seen to have a sharp increase in VAC, caused by a simultaneous increase in E_{ao} and decrease in E_{lv} produced by the RM, but remains relatively constant during fluid administration.

The 3 pigs surviving post endotoxin infusion see substantial increases in VAC, primarily caused by the increasing E_{ao} in Pigs 2 and 7, and simultaneous decrease of E_{lv} and increase of E_{ao} in Pig 6. Pig 2 appears to be severely impacted by the endotoxin, as E_{ao} quickly rises, possibly due an aggressive inflammatory response to the infection reducing arterial tone [92], increasing afterload. Pigs 6 and 7 maintain constant, but markedly elevated, VAC levels until the first post-endotoxin fluid bolus is given. Both Pigs then experience a steady increase in E_{ao} as the additional volume increases afterload. Septic

shock is known to impair left ventricle performance, which is evident in Pig 6, displaying a steady reduction in E_{lv}, which significantly contributes to the increase in VAC. These results highlight the increased demand on the heart during sepsis.

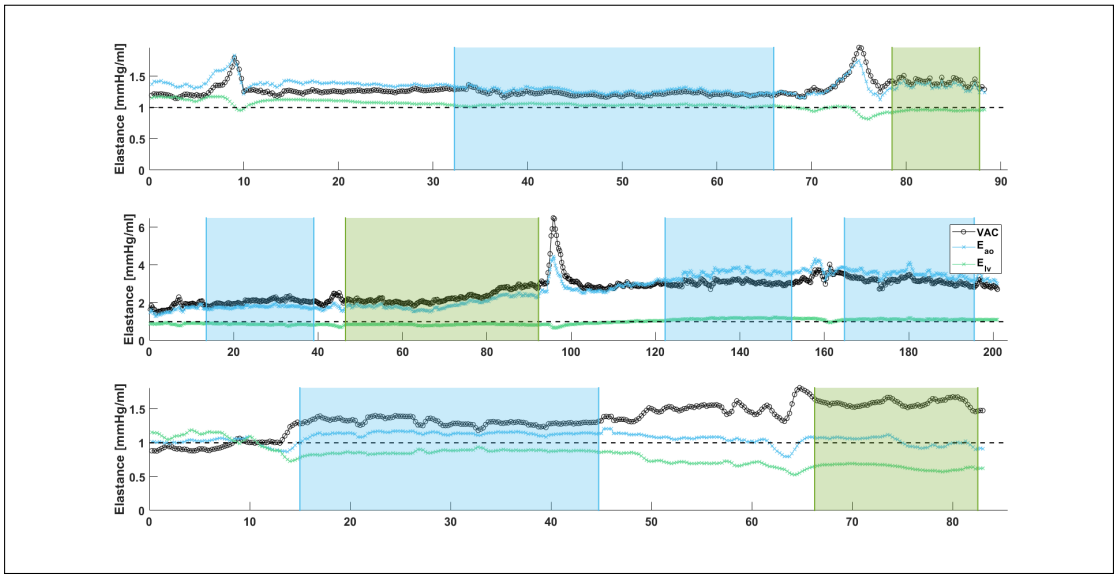

Figure 4.10: TCM identified cardiac and arterial elastance and the resutling VAC metric for Pigs 1, 2, and 3.

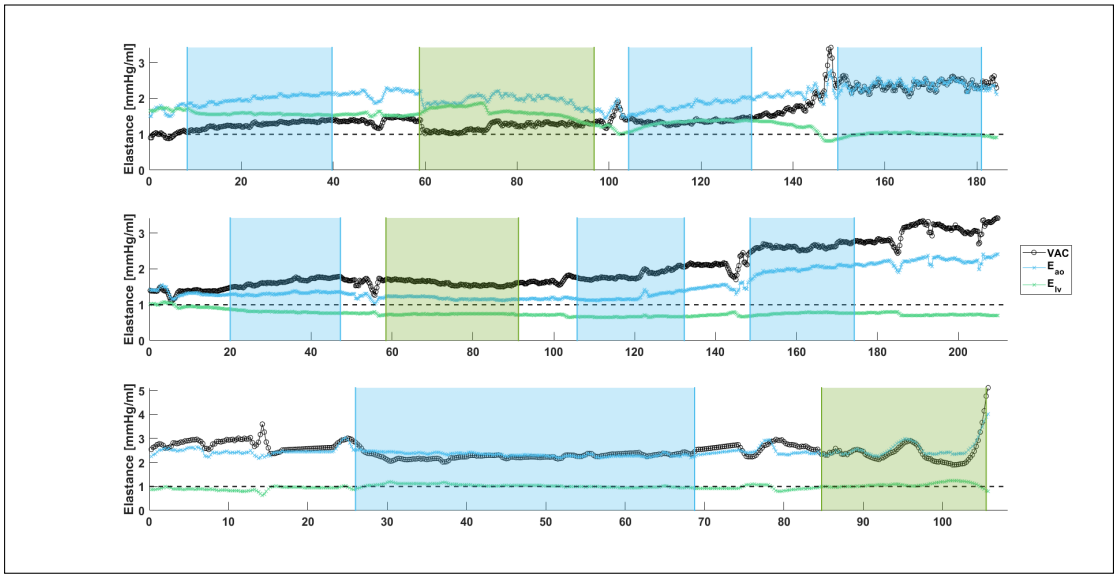

Figure 4.11: TCM identified cardiac and arterial elastance and the resulting VAC metric for Pigs 6, 7, and 8.

4.4 Limitations

This analysis has several limitations. First, although the TCM parameters show clinical utility, the measurements required for model reference values are highly unlikely to be available. Specifically, left ventricle pressure and volume measurements are never measured directly in humans due to the invasive, high risk procedures required. Hence, while results validate model dynamics, they are not clinically feasible and represent a best case.

Second, the PEEP driven recruitment manoeuvres were performed immediately prior to each fluid infusion, which reduced cardiac preload and SV. Because these manoeuvres were performed immediately prior to fluids being given, it is difficult to differentiate between the effects of the fluid therapy and the CVS naturally recovering from elevated PEEP. The depression in SV resulting from the RM means identifying the value of SV used to assess the change and thus, determine if the pig was responsive or not, became more difficult compared to if the RM had not occurred. This timing issue was especially difficult in the longer surviving pigs where the CVS took substantially longer to recover from the RM during septic shock. This effect is best illustrated in Figure 4.8. Where possible, the averaged SV values from before the RM and at the start of fluid infusion were used.

Additional to the limitations discussed in Chapter 3, the TCM is a lumped parameter model, so care must be taken when assigning physiological significance to identified parameters. Specifically, R_i is identified to account for the entire right side of the

circulation. Therefore, it is difficult to relate this parameter to an individual aspect of input resistance. However, it likely still provides useful information about long term trends to input resistance in response to evolving disease states or due to treatment.

Finally, the limited sample size available limits the ability to draw conclusions about the general population from these results. However, this data set provides accurate and direct measurements for all the required model inputs making it a valuable validation step, justifying further exploration.

4.5 Summary

This chapter presented the TCM of the CVS and used direct measurements for all required reference values to identify the model parameters. The identified SBV_{index} prior to fluid therapy showed a strong negative correlation with changes in SV, further validating its use as a potential index of fluid responsiveness.

The remaining model parameters were shown to provide useful insights into CVS dynamics during the various clinical procedures preformed in each experiment. Changes in E_{vc} and R_i may inform clinicians as to why fluid therapies were/were not successful. VAC can also be continuously modelled using the TCM, providing real time information on cardiac efficiency.

Chapter 5

Three-Chambered Model: Reduced Measurement Set

5.1 Introduction

Chapter 4 presented a first implementation of the TCM, highlighting the clinical usefulness of monitoring changes in model parameters during endotoxin induced septic shock and the ensuing treatment. The presented model utilized continuous measurements of left ventricle pressure ($P_{lv,mea}$) and volume ($V_{lv,mea}$) allowing for the accurate formulation of the time-varying elastance curves, used as the cardiac driver functions of the model, and direct assessment of the mean and range of $V_{s,lv}$ used in the identification process. However, these measurements would not be available in an ICU setting. Therefore, for the TCM to feasibly be implemented in a clinical environment, model

dependency on $P_{lv,mea}$ and $V_{lv,mea}$ needs to be eliminated, and accurate estimates for these waveforms derived from clinically available measurements used instead.

This chapter implements a method for estimating $P_{lv,mea}$ and $V_{lv,mea}$ from continuous aortic pressure measurements ($P_{ao,mea}$) and investigates the effect these estimates have on the identified model parameters. The $P_{lv,mea}$ and $V_{lv,mea}$waveforms were estimated using key features identified on continuous aortic pressure waveforms and simple physiological assumptions about ventricular pressure and flow characteristics [97]. The resulting waveforms are used as direct substitutes for their measured counterparts in formulating the cardiac driver function, used to simulate the TCM waveforms. The work presented in this chapter is a comparative study between the TCM parameters identified using the full set of invasive measurements as reference values (TCM_{FM}), and a reduced measurement set (TCM_{RM}), which excludes continuous ventricular measurements. It is a first step towards using far more distal measurements and estimates.

5.2 Method

Continuous $P_{ao,mea}$ waveforms are used to derive ventricular pressure ($P_{lv,est}$) and volume ($V_{lv,est}$) estimates using a modified method of the one originally proposed by Davidson *et al.* [73]. These authors showed the resulting $P_{lv,est}$ and $V_{lv,est}$ waveforms could be used to construct TVE curves, resulting in only an 11.4% median error relative to TVE curves constructed from $P_{lv,mea}$ and $V_{lv,mea}$ waveforms.

5.2.1 LEFT VENTRICLE PRESSURE

The physical connection between the left ventricle and the aorta means the two pressure waveforms are closely correlated when the aortic valve is open. Assuming negligible valve resistance, $P_{lv,est}$ can be equated to $P_{ao,mea}$ during systole, shifted by some constant phase lag, δ. During diastole, little information is contained in the $P_{ao,mea}$ waveform relating to $P_{lv,mea}$, as the aortic valve is now closed. However, ventricular diastolic behaviour is known to be largely passive, allowing $P_{lv,est}$ waveforms to be modelled using generalized exponentials. Increasing and decreasing exponentials are used for the contracting and relaxing portions of the pulse, respectively.

Assuming pressures in the aorta and ventricle are equal during ejection, $P_{lv,est}$ during systole can be directly estimated using $P_{ao,mea}$, taken from the maximum positive gradient of $P_{ao,mea}$, to the maximum negative gradient. The diastolic exponentials have decay and growth terms derived from a generalised best fit to the data, calibrated using the first heart beat of each pig.

The full set of model equations describing $P_{lv,est}$ in terms of $P_{ao,mea}$ is thus:

$$t_1 = t\left(\frac{dP_{ao}}{dt}_{max}\right)_n \tag{5.1}$$

$$t_2 = t\left(\frac{dP_{ao}}{dt}_{min}\right)_n \tag{5.2}$$

$$t_3 = 0.62t_2 + 0.38t_4 \tag{5.3}$$

$$t_4 = t\left(P_{ao,min}\right)_{n+1} \tag{5.4}$$

$$P_{lv} = \begin{cases} P_{ao}(t_1 + \delta < t < t_2 + \delta) & t_1 < t < t_2 \\ \alpha + (P_{ao(t_2)} - 6)e^{-16.2(t-t_2)} & t_2 < t < t_3 \\ P_{lv}(t_3) + (P_{ao}(t_4) - P_{lv}(t_3))e^{38.1(t-t_4)} & t_3 < t < t_4 \end{cases} \tag{5.5}$$

where $\delta = 0.016$s and α is the asymptotic pressure of $P_{lv,est}$ during diastole, set to a constant 6mmHg.

The exponential terms in Equation 5.5 govern the rate of increase and decrease during the systolic and diastolic components of the pulse, respectively. The values used the original work by Davidson *et. al.* were taken as initial references and adjusted to best fit the data, using an initial $P_{lv,mea}$ beat taken from the start of each experiment.

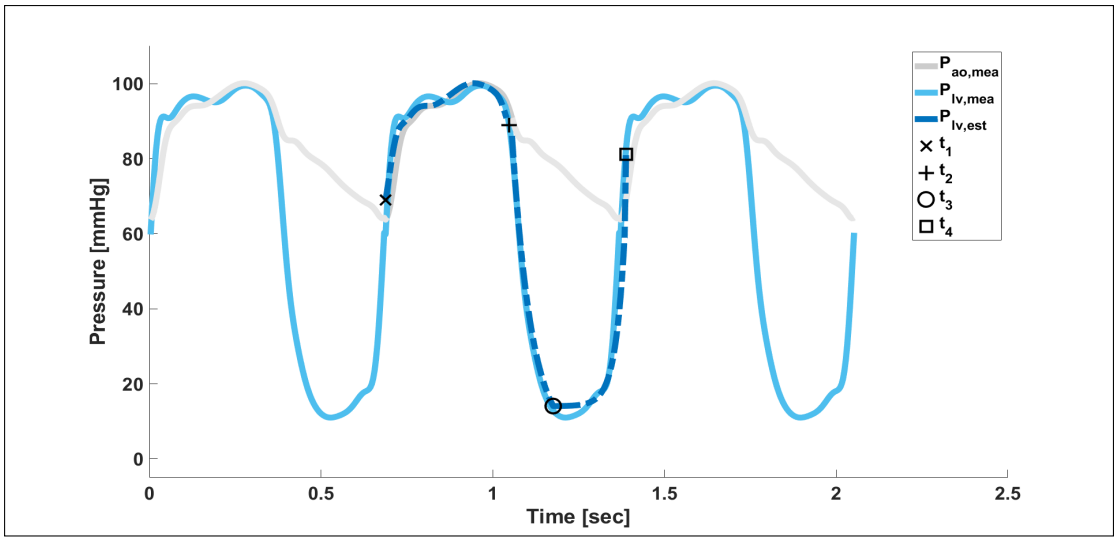

Figure 5.1: Example of $P_{lv,est}$ derived from $P_{ao,mea}$. Additionally, the corresponding $P_{lv,mea}$ waveforms are presented.

5.2.2 LEFT VENTRICLE VOLUME

The $V_{lv,est}$ waveform is estimated from $P_{ao,mea}$ and an initial calibration measurement for the end-systolic volume (V_{es}). End-systole and the diastolic feet of $P_{ao,mea}$ are used to locate timings (t_1, t_2, t_3) for the minimum and maximum points of $V_{lv,mea}$. The waveform shape is approximated using a piecewise sine function, as shown in Figure 5.2.

Specific values for $V_{lv,est}$ are obtained from the initial V_{es} calibration measurement. Intermittent measurements of ventricular volumes are becoming increasingly more available in clinical environments through use of echogardiography [98]. Calibration V_{es} is used to calculate the ventricular unstressed volume, V_u [97], according to:

$$V_u = 0.48 \cdot V_{es} \tag{5.6}$$

Once calculated, V_u is held constant for the duration of each experiment.

Forward simulation of the $V_{lv,est}$ is achieved by sequentially estimating values for V_{es}, through manipulation of the ESPVR, and using SV measurements to obtain the corresponding V_{ed} value. The ESPVR described in Section 3.5.1 is given:

$$P_{lv,es} = E_{es} \cdot (V_{lv,es} - V_{lv,u}) \tag{5.7}$$

Assuming pressure in the ventricle and aorta are approximately equal at end-systole,

$P_{lv,es}$ can be substituted for aortic pressure at the dicrotic notch (P_{DN}):

$$P_{lv,es} = P_{DN} = E_{es} \cdot (V_{lv,es} - V_0) \tag{5.8}$$

Davidson *et. al.* showed E_{es} can be effectively represented in terms of heart rate and a one off calculation for an elastic constant E_c. Heart rate variability is a primary response by the autonomic nervous system to adapt to changes in CVS condition and is a readily available measurement in all clinical settings. Therefore, it is a useful metric for tracking changes in pressure. E_{es} can be accounted for in the following manner:

$$P_{DN} = (E_c \cdot HR^3) \cdot (V_{lv,es} - V_u) \tag{5.9}$$

The cubic term was found to be an effective compromise between simplicity and ability to track data [97]. Equation 5.9 can be rearranged to give an equation for V_{es} in terms of readily available measurements:

$$V_{lv,es} = \frac{P_{DN}}{E_c \cdot HR^3} + V_u \tag{5.10}$$

The V_{lv} waveform ca now be expressed using the following piecewise function:

$$V_{lv}(t) = \begin{cases} (V_{ed})_n + ((V_{es})_n - (V_{ed})_n) \sin\left(\frac{\pi(t-t_1)}{2(t_2-t_1)}\right) & t_1 < t < t_2 \\ \\ (V_{es})_n + ((V_{ed})_{n+1} - (V_{ed})_n)\left(\frac{1}{2}\cos\left(\frac{\pi(t-t_2)}{(t_3-t_2)}\right) - \frac{1}{2}\right) & t_2 < t < t_3 \end{cases} \tag{5.11}$$

Where:

$$t_1 = t(P_{ao_{min}})_n \tag{5.12}$$

$$t_2 = t(P_{DN})_n \tag{5.13}$$

$$t_3 = t(P_{ao_{min}})_{n+1} \tag{5.14}$$

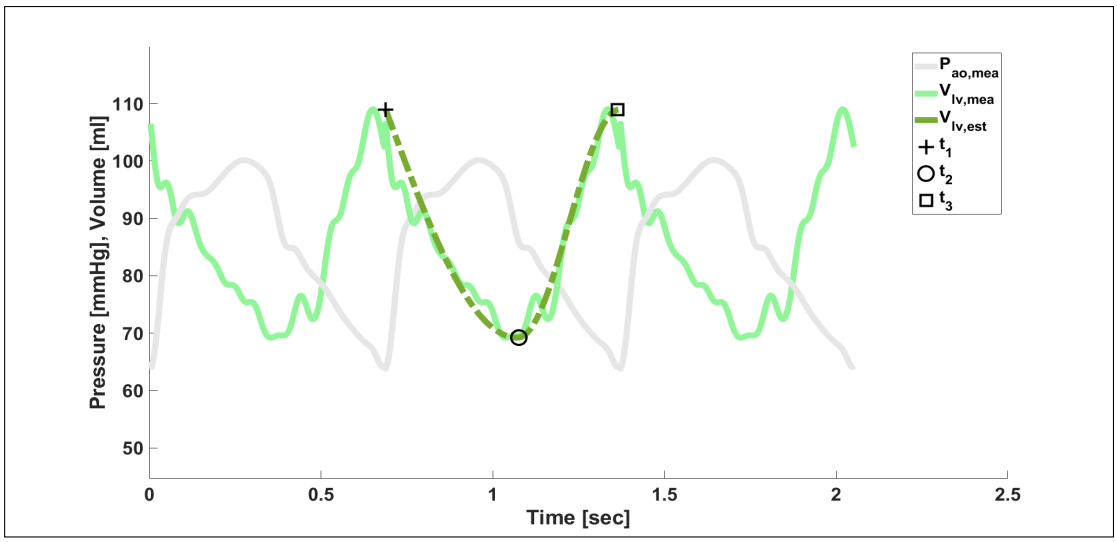

Figure 5.2: Example of $V_{lv,est}$ derived from $P_{ao,mea}$, and a calibration measurement for V_{es}, and the corresponding $V_{lv,mea}$ waveform.

5.2.3 PARAMETER IDENTIFICATION

The parameter ID process in this chapter was identical to the one performed in the previous chapter, detailed in Section 4.2, with the substitution of the mean and range of $V_{lv,est}$ used for $V_{lv,mea}$. The output vector is thus defined:

$$\mathbf{y} = \{\Delta P_{vc,mea}, \Delta P_{ao,mea}, \Delta V_{lv,est}, \bar{P}_{vc,mea}, \bar{P}_{ao,mea}, \bar{V}_{lv,est}, \left(\frac{dP_{ao,mea}}{dt}\right)_{max}\} \tag{5.15}$$

Table 5.1: Description of measurements used in the TCM

Measurement	Model Implementation
Continuous $P_{ao,mea}$	Provides reference ΔP_{ao}, $\bar{P}_{ao}$ and $\frac{dP_{ao}}{dt}$. Allows for estimation of $V_{lv,est}$ and $P_{lv,est}$
Continuous $P_{vc,mea}$	Provides reference ΔP_{vc} and $\bar{P}_{vc}$.
Continuous SV_{mea}	Used to obtain end diastolic volume once V_{es} is calculated from Equation 5.10, and is inherently equal to $\Delta V_{lv,est}$
Single beat $P_{lv,mea}$	Allows for and initial fit of the exponential terms in Equation 5.5
Single beat $V_{lv,mea}$	Provides and initial calibration measurement for V_{es}

Note, the construction of $V_{lv,est}$ uses aortic flow probe measurements of stroke volume thus, $\Delta V_{lv,est} = SV_{mea}$.

5.2.4 Experimental data

Data from Pigs 1, 2, 4-8 were used to provide a direct comparison with the model parameters identified in Chapter 4. The measurements used, and their implementation in the TCM, are summarized by Table 5.1.

5.3 Analysis and Validation

The proposed reduced measurement method (TCM_{RM}) is validated through direct comparison with the model parameters identified using the full measurement set (TCM_{FM}) of reference values. Standardized Bland-Altman plots are used to assess the beat to beat error of each parameter, providing the overall agreement between the methods. Time-series results are presented to show the direct comparison of model parameters

and highlight differences in parameter trends. which, clinically, are the most important feature to capture for clinical decision making.

5.4 Results

Figure 5.3 shows example output waveforms of the TCM_{RM} method and the corresponding reference waveforms, compared to the TCM_{FM} method for the same beat. Specifically, Figure 5.3 highlights the differences between $P_{lv,mea}$ and $V_{lv,mea}$ with $P_{lv,est}$ and $V_{lv,est}$ and the effect these estimates have on TCM simulated waveforms.

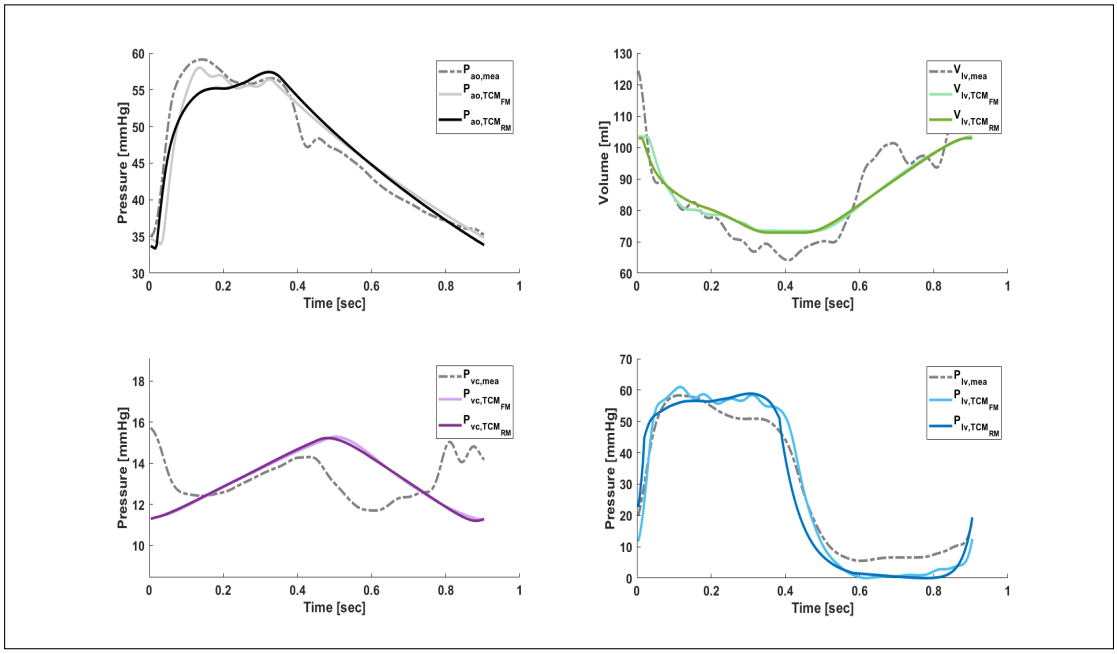

Figure 5.3: Example outputs of the TCM_{RM} output and reference waveforms after parameter identification compared to the TCM_{FM} method for the same beat

Table 5.2 summarizes the relative errors of each parameter identified from the TCM_{RM}

method, compared with values obtained using the TCM_{FM} method, given as a percentage, for all subjects.

Figures 5.4-5.9 show the identified TCM parameters compared to those obtained using direct measurements for all necessary model inputs. Note, these figures are intended to highlight how the proposed estimates for $P_{lv,est}$ and $V_{lv,est}$ can be used to obtain accurate parameter estimates relative to the full measurement set. Figure axes have different scaling between subjects and care should be taken when comparing parameters across subjects.

Figures 5.10 and 5.11 show the mean bias and limits of agreement between TCM_{RM} and TCM_{FM} identified parameters. Generally, TCM_{RM} identified parameters show good agreement with the TCM_{FM} sets. The primary parameter of interest is SBV_m, due to its relation with fluid responsiveness, which produced a mean bias and LoA of 0.2 (-14.5. 14.9)%, relative to the TCM_{FM}

Table 5.2: Relative errors of each parameter identified with the proposed method relative to parameters identified using the full set of measurement inputs, give as mean(std) [%]

Pig	SBV_m	E_{ao}	E_{vc}	R_c	R_i	R_o	E_{lv}
1	4.7(2.3)	1.7(2.4)	7.8(3.4)	0.3(0.3)	16.6(12.6)	126.1(80.7)	9.4(6.2)
2	5.6(3.0)	7.8(5.6)	5.9(4.2)	1.0(2.2)	24.9(19.3)	83.9(79.5)	10.1(5.7)
4	7.1(4.2)	4.2(2.0)	2.9(2.2)	0.2(0.7)	6.7(5.9)	31.7(26.5)	25.6(13.8)
6	4.3(3.5)	8.8(8.8)	5.9(8.6)	0.4(0.3)	32.1(20.2)	50.9(16.9)	7.0(5.0)
7	5.2(4.8)	6.5(5.2)	4.6(4.1)	0.4(2.1)	9.4(5.5)	34.9(41.1)	8.4(5.7)
8	11.3(5.8)	4.3(4.3)	9.2(3.9)	1.0(1.1)	8.1(13.6)	278.0(167.2)	16.6(7.3)
Mean	6.4(3.9)	5.3(4.7)	6.1(4.4)	0.6(1.1)	16.3(12.8)	100.9(68.7)	12.8(7.3)

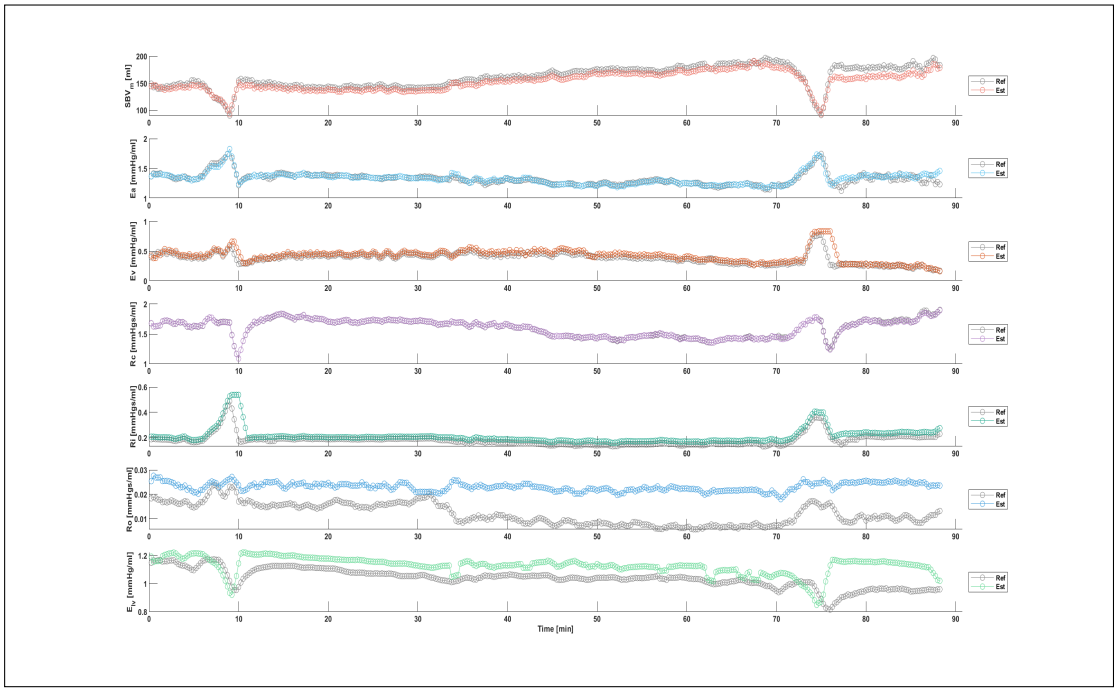

Figure 5.4: Time series direct comparison between TCM_{RM} identified parameters and TCM_{FM} identified parameters for Pig 1.

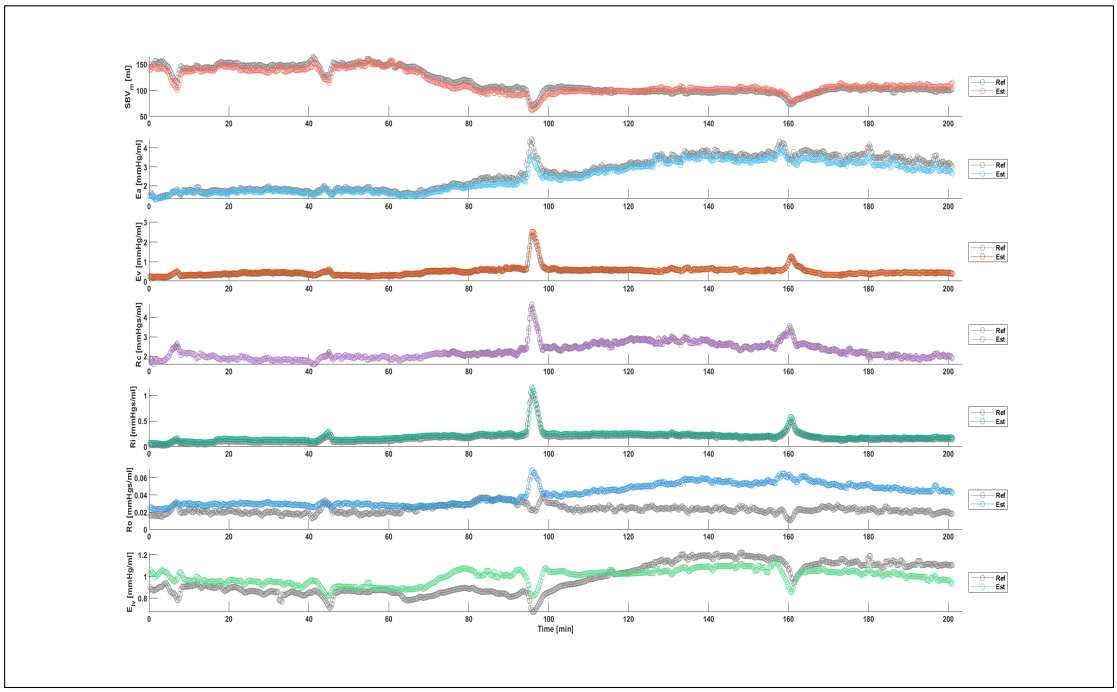

Figure 5.5: Time series direct comparison between TCM_{RM} identified parameters and TCM_{FM} identified parameters for Pig 2.

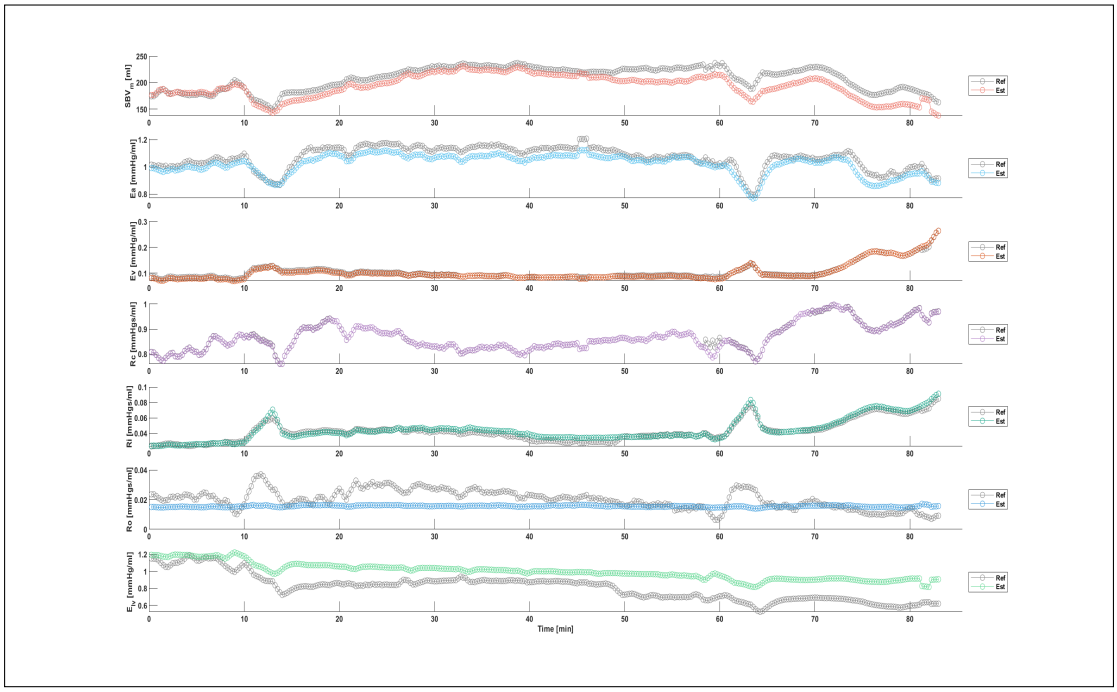

Figure 5.6: Time series direct comparison between TCM_{RM} identified parameters and TCM_{FM} identified parameters for Pig 4

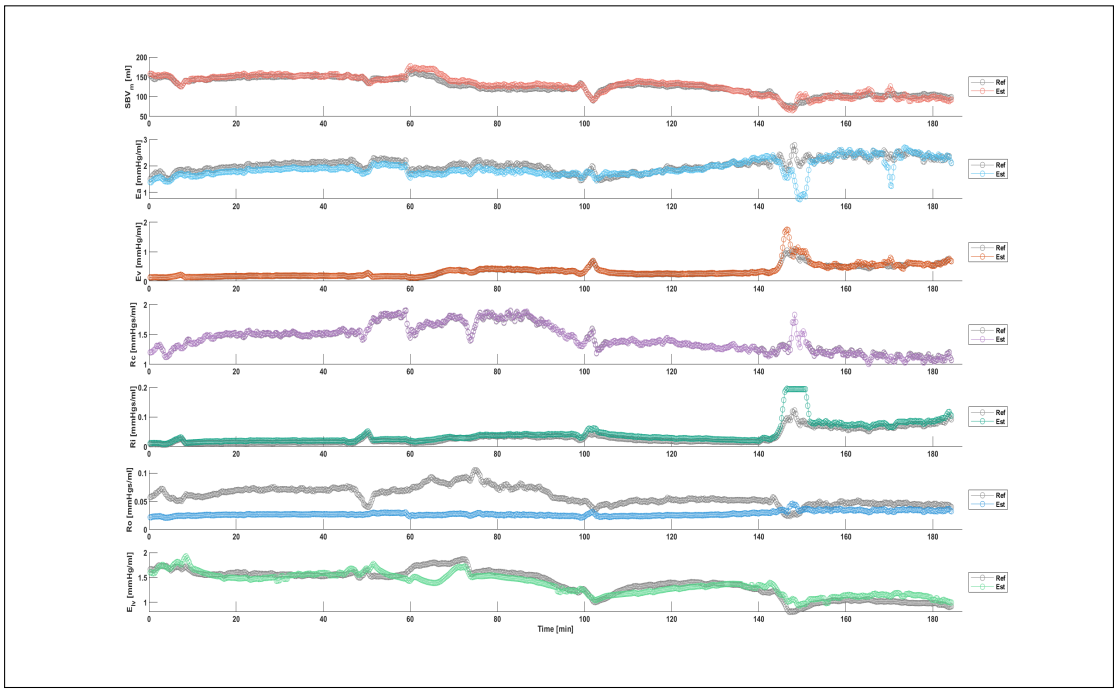

Figure 5.7: Time series direct comparison between TCM_{RM} identified parameters and TCM_{FM} identified parameters for Pig 6.

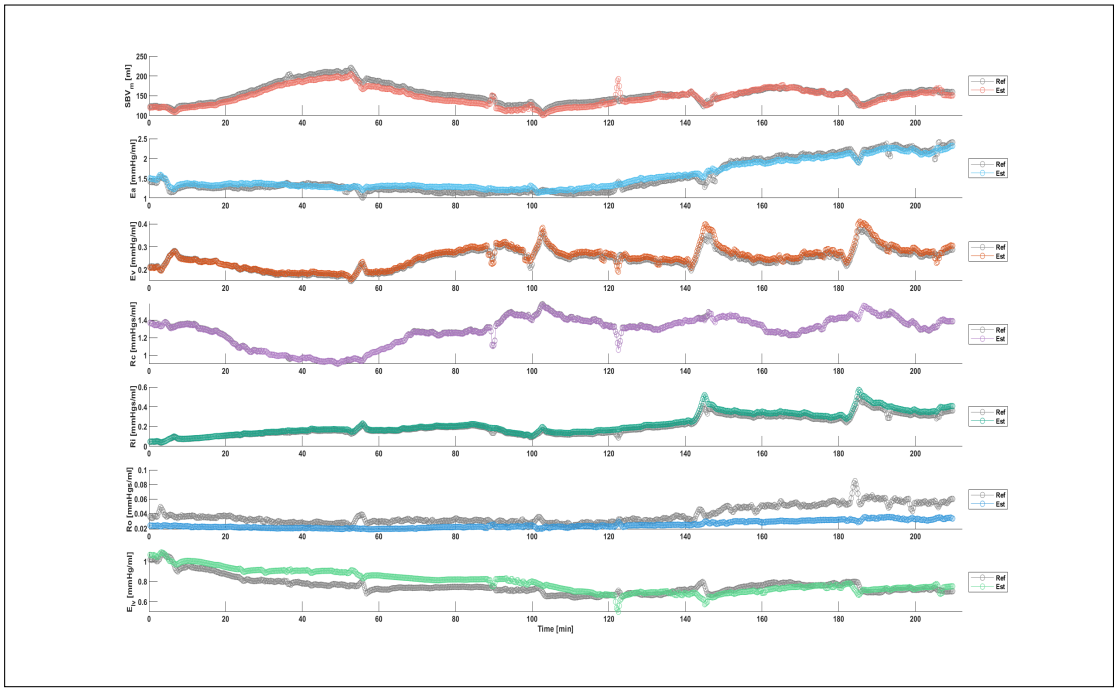

Figure 5.8: Time series direct comparison between TCM_{RM} identified parameters and TCM_{FM} identified parameters for Pig 7.

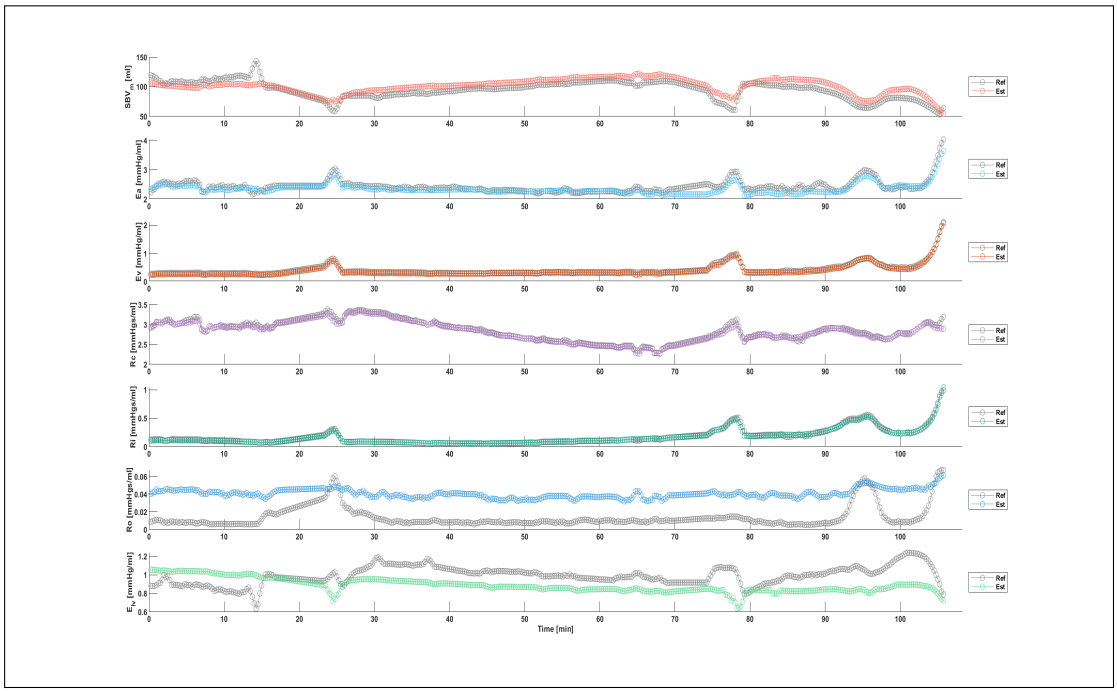

Figure 5.9: Time series direct comparison between TCM_{RM} identified parameters and TCM_{FM} identified parameters for Pig 8.

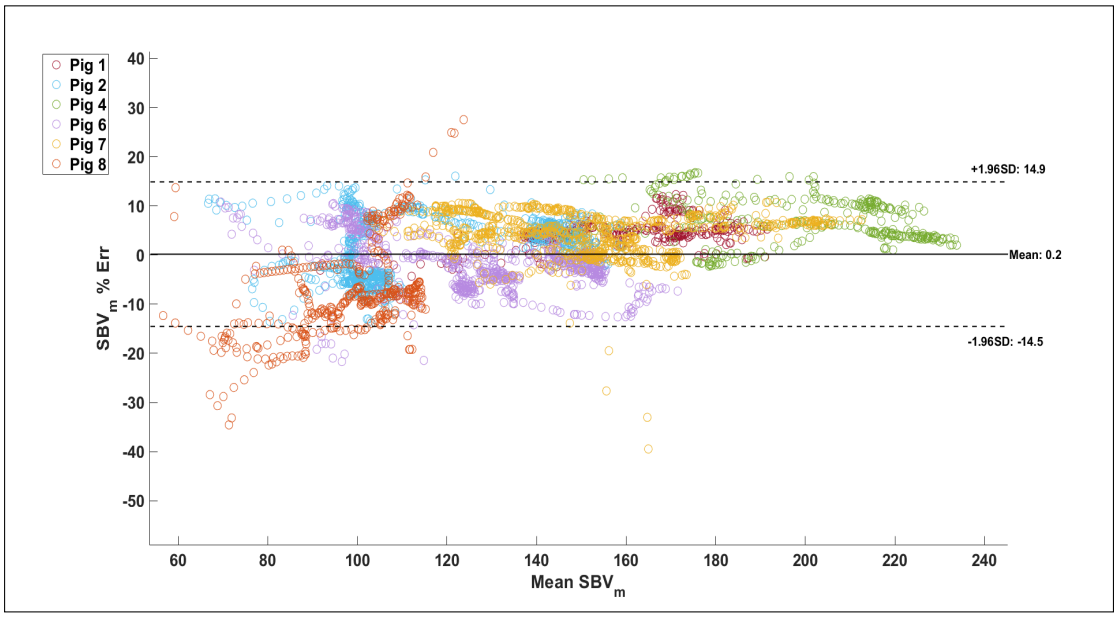

Figure 5.10: Bland-Altman analysis of SBV_m, given as a % error relative to TCM_{FM} identified SBV_m. Mean bias and limits of agreement ($\pm$ 1.96 standard deviations) are given to show expected variation.

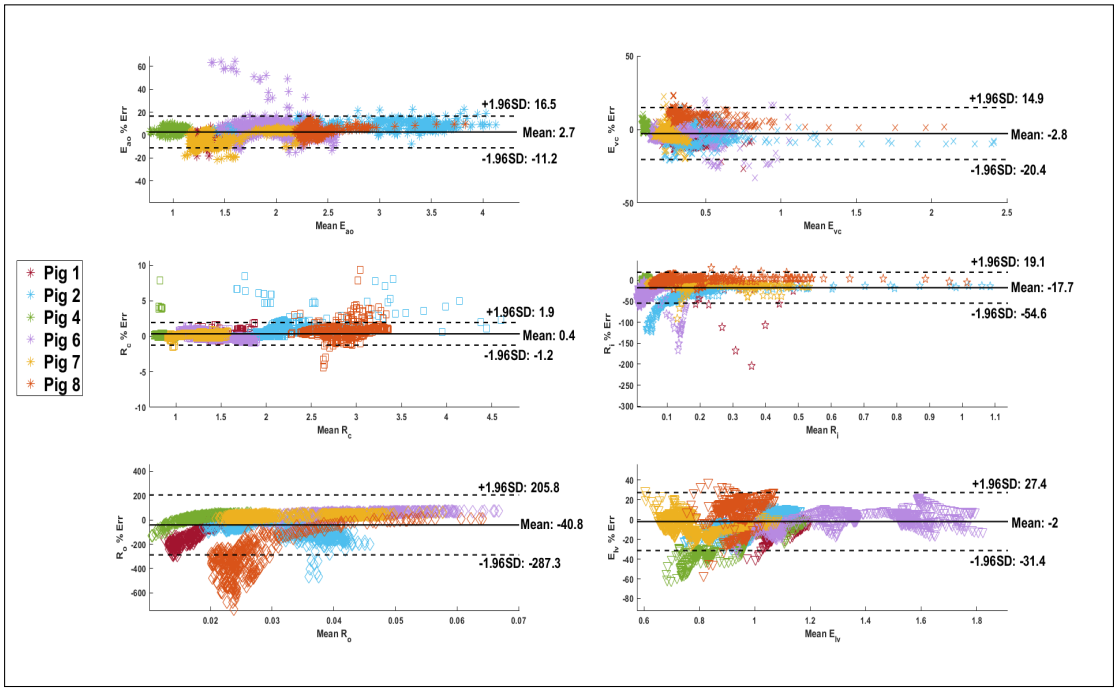

Figure 5.11: Bland-Altman analysis of the remaining TCM model parameters, given as a % error relative to TCM_{FM} identified SBV_m. Mean bias and limits of agreement ($\pm$ 1.96 standard deviations) are given to show expected variation.

5.5 Discussion

Using the TCM_{RM} method, the model parameters SBV_m, E_{vc}, E_{ao} and R_c were identified with high accuracy relative to their corresponding values produced using the full set of direct, invasive measurements. Mean bias and LoA were 0.2(-14.5, 14.9)%, 2.7(-11.2, 16.5)%, -2.8(-20.4, 14.9)%, 0.4(-1.2, 1.9)%, were found for SBV_m, E_{ao}, E_{vc} and R_c, respectively. These results are not entirely unexpected, as identification of these are parameters primarily relies on aortic and central venous pressure measurements for reference values. These measurements were available for use in this section and allowed for accurate identification. However, the circulation is modelled as a closed loop so parameter interdependence is present and removing ventricular measurements presents a considerable loss in information about CVS dynamics. Therefore, the $\leq 10\%$ mean absolute difference, detailed in Table 5.2, for these parameters speaks to the robustness of the TCM in capturing critical, fundamental dynamics.

The remaining parameters, R_i, R_o and E_{lv}, are directly influenced by the shape of the driver function thus, the resulting errors are higher. Elevated errors associated with R_i can be attributed to the assumed decay and growth rates of the exponentials describing $P_{lv,est}$ during diastole. These exponential terms directly influence when ventricular pressure falls below venous pressure, initiating simulated filling of the ventricle, and when it rises above again, dictating the closing of the input valve. Modifying these exponential terms results in R_i being adjusted accordingly to allow the ventricle to fill

properly, as dictated by the driver function and SV. This effect is evident in Figure 5.3, with the decay rate of $P_{lv,TCM_{RM}}$ underestimating both $P_{lv,TCM_{FM}}$ and $P_{lv,mea}$.

In Chapter 4, by assuming V_u to be zero, E_{lv} could be calculated directly from $P_{lv,mea}$ and $V_{lv,mea}$. In contrast, the error introduced into the model through continual estimation of $P_{lv,est}$ and $V_{lv,est}$ results in a small error drift associated with E_{lv}, which is defined by the ventricular pressure-volume relation. Errors can be partially attributed to the simplification of the ventricular volume waveform shape, using the sine functions described in Equation 5.11, and the difference between measurements of $\Delta V_{lv,mea}$ taken from the volume admittance catheter, and SV_{mea} take from the aortic flow probe. However, the majority of error is likely due to the assumed shape of $P_{lv,est}$ and the error drift associated with estimating V_{es} using Equation 5.10.

While changes in heart rate are a primary mechanism for adapting to altered hemodynamic demand, it is an incomplete metric and may explain the inability of E_{lv} to capture some of the higher frequency changes. Furthermore, the endotoxin induced septic shock potentially impairs the contractile state of the ventricle, testing the initial calibrated approximation of V_u. Despite these estimates being used, relative to the direct measurements of E_{lv}, errors of the TCM_{RM} identified elastance were modest, producing a pooled mean absolute error of 12.8% across all experiments.

The primary source of error using the proposed TCM_{RM} method is associated with R_o. This result can be attributed to using $P_{ao,mea}$ as a direct estimate for $P_{lv,est}$ during systole, resulting in the driver function and thus, model left ventricle pressure, having very similar contour to arterial pressure. As flow through the aortic valve is driven by the

pressure differential between the ventricle and arterial chambers, changes in reference ventricular pressures directly affects identified R_o. While similar, $P_{ao,mea}$ and $P_{lv,mea}$ have necessary differences in order for flow to occur, information which is lost when estimating $P_{lv,est}$. Specifically, the inertial effects of the blood being ejected by the heart will result in a deviation of the $P_{ao,mea}$ and $P_{lv,mea}$ waveforms near end-systole. Furthermore, the similarities between the $P_{ao,mea}$ and $P_{lv,est}$ contour means R_o becomes primarily dependent on the phase shift (δ) used in Equation 5.5. As a result, Figures 5.4-5.9 show TCM_{RM} identified R_o to be relatively constant throughout each experiment, reflecting the constant phase shift separating identical systolic pressures.

5.6 Limitations

Aside from the inherent limitation of the TCM, discussed in previous chapters, several limitations must be addressed as to the clinical feasibility of the proposed method.

The method presented in this chapter aimed to identify the TCM parameters from a more clinically feasible set of measurement inputs. However, the method intrinsically relies on the availability of continuous central aortic pressure, which is very unlikely to ever be directly measured in the ICU. Peripheral artery pressures are more widely used in intensive care environments due to the reduced risk of infection and accessibility to the measurement site.

The generalizability of the exponential terms used to describe diastolic ventricular pressure needs to be explored further. Although the values presented in the original work

by Davidson *et. al.* [73] were found to produce a satisfactory fit to $P_{lv,mea}$, visual inspection of the waveforms at the start of each experiment allowed for a non trivial reduction in error. This result is characteristic of applying population based parameters to individuals. These exponential parameters were also derived for porcine subjects and will likely not translate one-for-one to human patients.

5.7 Summary

For the TCM to be feasibly implemented in a clinical environment, the reliance on direct measurements for left ventricle pressure and volume, used to derive the cardiac driver function and during the parameter ID process, needs to be removed. This chapter showed left ventricle pressure ($P_{lv,est}$) and volume ($V_{lv,est}$) can be accurately estimated from continuous aortic pressure measurements and implemented into the TCM. Model parameters SBV_m, E_{ao}, E_{vc} and R_c were found to be practically identical to those derived using the full measurement input set, with errors $\leq 10\%$.

The remaining three parameters, R_i, E_{lv} and R_o were directly affected by the aforementioned waveform estimates and saw a corresponding increase in error. R_i was affected by the generalized exponential terms used to estimate the diastolic components of $P_{lv,est}$, thus dictating the venous-ventricle pressure differential driving ventricular filling. E_{lv} errors can be primarily attributed to the estimates for V_{es}, which were described using an initial calibration and forward simulated in terms of the constant elastance term (E_c and heart rate. Despite producing higher errors than the previously mentioned param-

eters, E_{lv} and R_i mean errors were still modest at 12.8% and 16.3%, relative to the TCM_{FM} parameters, respectively.

The largest model errors were associated with R_o. With $P_{ao,mea}$ used to directly approximate $P_{lv,est}$ during systole, model simulated arterial and ventricular pressure will be similar, simply shifted in phase. As a result, R_o was largely determined by the predefined constant phase shift, δ.

Chapter 6

Determinants of the Arterial Pulse

6.1 Introduction

The arterial system is a network of variably sized blood vessels with location dependent mechanical properties, allowing the high pressure blood ejected from the heart to be safely transported to the micro-vasculatre and deliver vital oxygen and nutrients [1]. Variations in arterial properties, both geometric, through changes in vessel diameter and branching, and changes in elasticity, augment the pulse generated by the heart [99–101]. These changes in the arterial system also cause waves generated by the heart to be reflected back through the arterial system [99, 102–105]. Wave reflections interfere with the forward travelling waves, also augmenting the pulse in a location dependent

manner. Pulse augmentation generally produces an increased, narrower systolic pressure peak and a slight overall widening of the pulse, relative to centrally located pulses. As a result, measurements take at peripheral arteries can vary significantly to those taken in the aorta. The current chapter details the mechanisms causing these observed changes in arterial pulse contour and compares the central and peripheral pulses.

6.2 Physiology of the Systemic Arterial System

In Chapter 1 the CVS is briefly described as a system of a variably sized blood vessels, divided into the pulmonary and systemic circulations. These circulations are fed by blood expelled from the right and left ventricle, respectively. This section presents a more in-depth overview of the vessels making up the arterial system and the changes in vessel properties seen moving from proximal to distal locations in the body [1].

The major arteries near the heart, including the pulmonary and aortic arteries, are the largest, most elastic vessels in the body, allowing them to significantly deform without injury. These *elastic arteries* are crucial for accommodating the initial high pressure pulse delivered by the heart and directing flow toward the lesser arteries. The ability of vessel walls to significantly stretch, enables the arteries to accommodate the ventricular pulse, while maintaining a constant pressure gradient. They thus elongate the initial pulse every beat via this elastic storage.

Further from the heart are the *muscular arteries*, which are the anatomically named peripheral arteries, including the iliac, femoral, radial and brachial arteries. These

vessels have higher quantities of smooth muscle capable of exerting active tension for distributing blood throughout the body. Variations in muscle composition between elastic and muscular vessels may also result in peripheral and central arteries having different responses to the various pharmacological interventions used in the ICU [106].

The arterioles are the smallest arteries, primarily comprised of smooth muscle. The high proportion of smooth muscle allows the arterioles to regulate blood flow throughout the body and to the major organs. The small diameter (8 - 60μm) and low compliance of smooth muscle fibres make the arterioles highly resistive vessels, which, as above, may be further affected by drug therapies employed in hemodynamic management.

6.3 Determinants of Arterial Pulse

Measurements of arterial pressure and flow taken at different locations in the circulation produce a range of pulse contours. Figure 6.1 illustrates the typical changes to the central pulse as it moves towards the lower limb arteries [101]. Pressure pulses are amplified while maintaining a relatively constant (but decreasing) mean pressure [99, 107]. Flow waveforms diminish markedly while travelling to the periphery. As a pulse propagates from the heart to the periphery, changes in the vasculature geometry, mechanical properties and interactions with other waves augment the pulse.

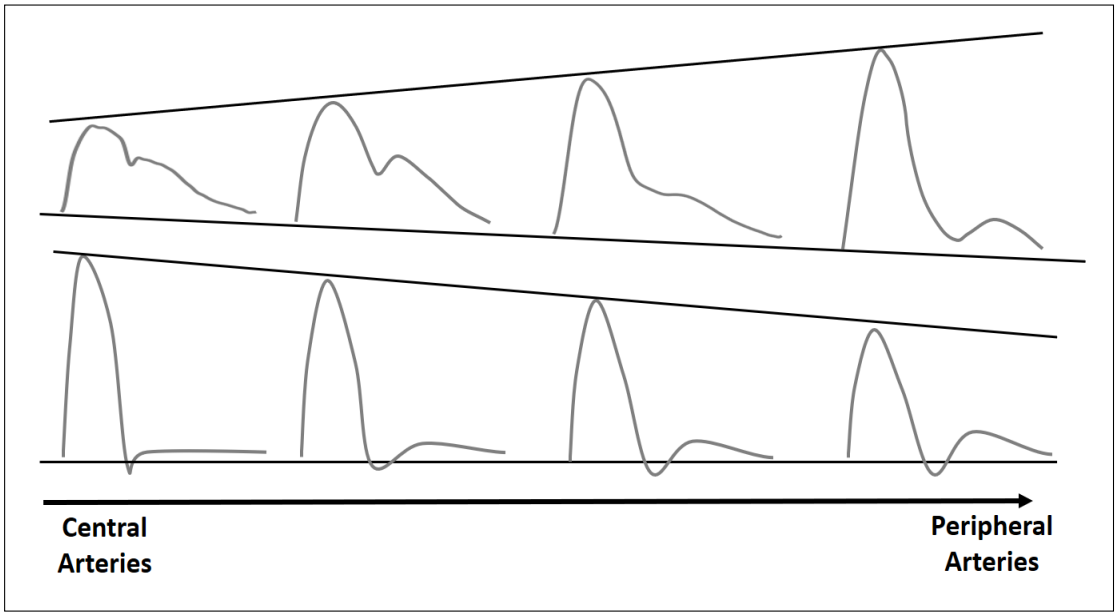

Figure 6.1: Illustration of the typical augmentation to the (top) pressure and (bottom) flow pulse contour, moving from the central (ascending aorta) to the lower limb (femoral) arteries.

6.3.1 Pulse Generation

With the contraction of the heart and the expulsion of blood from the ventricle, a forward travelling flow (Q_f) and corresponding pressure (P_f) wave is generated [99, 108, 109]. Both Q_f and P_f wvaes are termed forward travelling to indicate the entire pulse is travelling in the downstream direction. The rate blood is ejected from the heart depends on myocardial contractility and determines the upstroke gradient of both forward pulses. At the end of ejection, ventricular pressure rapidly declines causing the semilunar valves to close.

When the aortic valve closes a notch in the pulse measured pressure, called the *incisura*, can be observed. The incisura is augmented by the arrival of reflected waves from the body. The combined effects of wave reflections and valve closure produces the more

commonly referenced *dicrotic notch* [110]. With the semilunar valves closed, flow in the central arteries is largely passive and decays in an exponential manner.

P_f and Q_f are proportional to one another, scaled by the arterial *characteristic impedance (Z_c)* [111, 112], defined:

$$\Delta P_f = Z_c \times \Delta Q_f \tag{6.1}$$

Equation 6.1 implies P_f and Q_f will have identical contours. This feature is due to both P_f and Q_f representing the pressure and flow waves produce by the heart contracting and are unaffected by and wave reflection [99]. This contour match is illustrated in Figure 6.6, showing the decomposition of the measured aortic pressure and flow into their respective forward and reflected components.

6.3.2 WAVE REFLECTION

As forward waves propagate distally they encounter discontinuities in the vascular architecture, with each discontinuity causing some portion of P_f and Q_f to be reflected. Reflected pressure (P_r) and flow (Q_r) waves travel back through the arterial system towards the heart [108, 113]. Reflection sites occur where a non-uniformity in the geometric or mechanical properties of the artery exists. Potential reflection sites include arterial branching, vessel tapering, changes in elastance and the high resistance arterioles [99].

Reflected waves travel back through the arterial tree and interfere with the forward travelling waves. It should be noted the complex geometry of the arterial system will

produces a large number of forward travelling and reflected waves travelling in any combination of directions. Therefore it is common to use P_f to represent the sum of all forward travelling pressure waves proximal to the measurement site, and P_r the sum of all reflected waves arriving from the vasculature distal to the measurement site.

Upon encountering a reflection site, forward travelling pressure waves produce a positively interfering reflected wave. When P_r interacts with P_f it will result in an amplification of P_f. This interaction is known as *pulse pressure amplification (PPA)*. This PPA is responsible for the significant differences in SP and PP between peripheral and central artery measurements. The effect of PPA means peripheral measurements often vary significantly from those taken in the central arteries.

Conversely, the reflection of forward travelling flow waves produces negatively interfering reflected waves causing some portion of the Q_f pulse to decelerate. Similar to forward travelling waves, P_r and Q_r are related via Z_c. However, due to the destructive nature of Q_r it is now a negative relation, defined:

$$\Delta P_r = Z_c \times -\Delta Q_f \tag{6.2}$$

Equations 6.1 and 6.2 detail the intrinsic link between pressure and flow throughout the arterial system. The pulse contour for P_f and Q_f are identical. So too is the contour of P_r and Q_r, with Q_r being inverted upon reflection. These principles mean any differences in pulse contour between pressure and flow waveforms recorded simultaneously at the same site is due to the effects of wave reflection [99, 108, 114].

Previous studies attempting to identify the dominant reflection site in the body identified the high resistance arterioles as the main reflection site [99, 101]. These studies used vasodilator agents to alter peripheral vascular resistance by increasing the diameter of muscular blood vessels, such as the larger peripheral arteries and arterioles. Peripheral pulse pressure reduced with no change in arrival time of the reflected wave, relative to the forward wave, indicating the reflection site had been altered and the magnitude of the reflected waves were reduced.

The concept of an effective reflection site is commonly used to simplify the complex wave reflection phenomenon [99, 100, 108, 115]. Using the notion of an effective reflection site, a wave propagation path is considered to terminate at a single location. The magnitude of wave reflection is characterized by mismatch between the characteristic impedance and the impedance load at the reflection site.

6.3.3 Pulse Transit Time

Pulse transit time (PTT) refers to the time taken for a pulse to travel from the aorta to the arterial measurement site [105, 116–118] The PTT is inversely proportional to the pulse wave velocity and is determined by the geometrical and mechanical properties of the arteries. Increased arterial stiffness results in a faster travelling pulse and a lower PTT, while increased vessel diameter reduces pulse speed, increasing PTT.

Along with heart rate [119], PTT is a key determinant in the level of interaction between forward and reflected waves [99]. For a given set of P_f and P_r, a low PTT implies a

fast travelling wave resulting in reflected waves arrive earlier in the pulse relative to the forward travelling wave.

With an earlier arrival of P_r, the degree of constructive interference is increased, producing a significant pressure amplification of the peripheral measurement relative to central pressures. Conversely, Q_r waves arriving earlier have a greater deceleration of Q_f, which can alter the contour of the pulse, changing it from convex, to linear, and in some situations to concave, depending on the interaction [99, 108]. As PTT is progressively increased, assuming all else constant, reflected wave interactions will occur later relative to the forward wave and have less influence on the systolic component of the pulse.

Clinically, PTT can be a useful diagnostic in assessing arterial health and cardiac afterload. If PTT is low the implication is the arteries are stiff, which in turn means waves arrive back to the heart earlier, amplifying central pressure. This increased pressure acts against the heart during ejection, increasing afterload and cardiac metabolic demand. This behaviour is often seen in elderly patients [101]. In contrast, lower PTT levels have been shown to help cardiac function by elevating arterial pressure during diastole, aiding in coronary perfusion [115].

6.4 Arterial Pulse Characteristics

Although the determinants of the pulse can be combined to produce a wide range of arterial pressure and flow measurements, they usually manifest in a predictable, loca-

tion dependent manner, assuming no injury or disease is present. This section briefly describes the characteristics of the central pressure and flow, and peripheral pressure waveforms. Arterial pulses are usually analysed in terms of their systolic and diastolic components. Figure 6.2 shows the separation of pressure and flow into systolic and diastolic components.

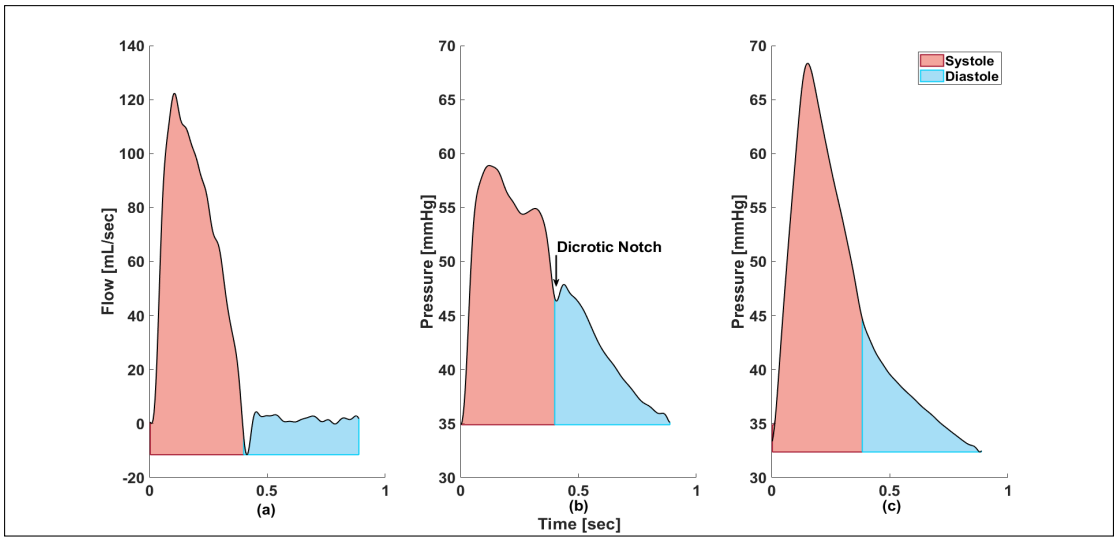

Figure 6.2: Systolic and diastolic components of the (a) central (aortic) flow; (b) central pressure; (c) peripheral (femoral) pressure pulses.

6.4.1 CENTRAL PRESSURE

The central pressure pulse can be classified in terms of the *augmentation index* (AI_x) [99–101, 108, 118, 120]. The AI_x describes the degree of systolic pressure amplification occurring, relative to total pulse pressure. Positive and negative values for AI_x are possible depending on when the relative interactions between waves occurs. The AI_x can provide indirect information about ventricular loading conditions and arterial stiffness.

A negative AI_x indicates the later arrival of P_r, manifesting in a secondary systolic shoulder at a lower pressure than the primary systolic peak. This behaviour is seen in Figure 6.3(a) and is common in younger patients [108]. A negative AI_x is desirable, as the late-systolic pressure amplification does not increase ventricular afterload and work demanded of the heart.

A positive AI_x is produced by early arriving reflected waves, possibly resulting from increased arterial stiffness or heart rate, commonly seen in elderly patients. A distinct primary systolic shoulder and inflection point are often seen prior to maximum pressure, as shown in Figure 6.3(b).

Intermediate cases also exist, where interactions between P_f and P_r occur in a manner which produces no inflection points, early or late in systole, on the measured pulse. To one extreme, P_f and P_r occur almost simultaneously and merge into a single peak, not shown here. To the other, the offset is sufficiently large P_r occurs during diastole, such as in Figure 6.4(a), resulting in a pronounced diastolic pressure peak.

End-systole, marking the end of the injection period, is identifiable from the *dicrotic notch*. The dicrotic notch occurs due to a combination of the aortic valve closing and arrival of reflected waves. Through arterial pressure measurements taken at progressively distal locations O'Rourke *et. al* showed the pulse became wider and a dulling of the dicrotic notch occurred [110]. During diastole, central pressure behaviour is largely passive and decays exponentially.

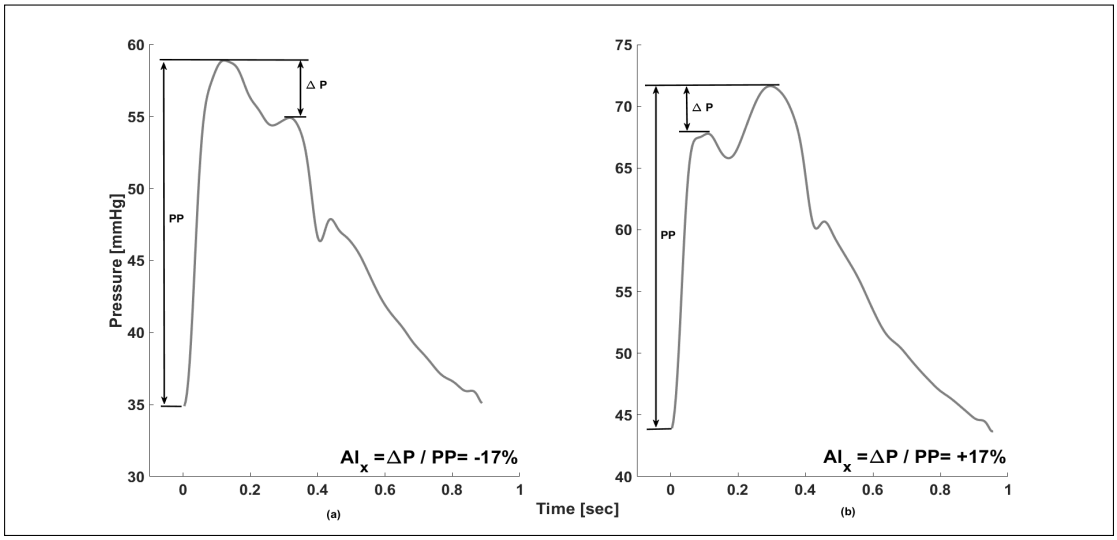

Figure 6.3: (a) late arrival of P_r relative to P_f causing low level amplification in late-systole resulting in a negative AI_x; (b) early arrival of P_r relative to P_f amplifying the late-systolic pressure above the early systolic peak resulting in a positive AI_x.

6.4.2 Central Flow

Central flow is characterized by an initial systolic peak reaching a maximum at approximately 30% of the duration of ejection [118]. Peak flow is strongly correlated with the primary systolic shoulder/peak of the corresponding pressure pulse, as both are the result of the forward wave [6, 118]. Late arriving reflected waves have minimal impact on the forward wave because the aortic valve is closed and flow is essentially negligible. Thus, the measured flow contour will maintain a convex shape, as seen in Figure 6.4(d). Reflected waves arriving in mid-systole have a slight negative contribution to measured flow, reducing the convexity of the pulse, as shown in Figure 6.4(e). Waves arriving in early-systole have a significant deceleration effect, resulting in the almost linearly descending portion of the pulse seen in Figure 6.4(f) [108].

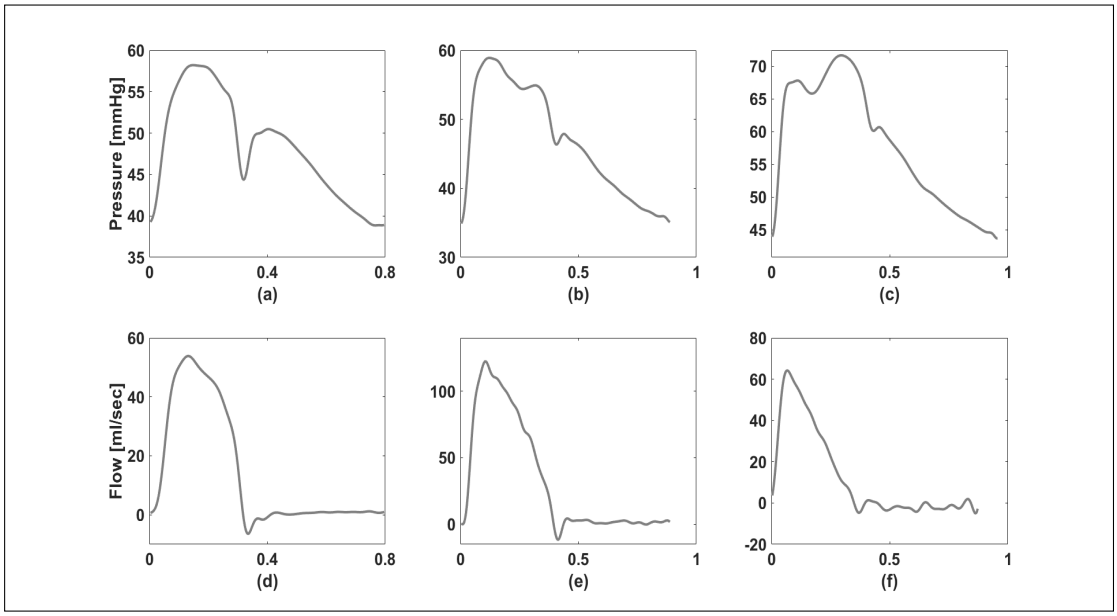

Figure 6.4: Influence of the interaction between forward travelling and reflected pressure and flow waves on the resulting arterial measurements.

6.4.3 Peripheral Arteries

Peripheral arteries are located closer to the effective reflection sites meaning reflected waves have less distance to travel before encountering forward travelling waves. Therefore, a greater degree of interaction occurs promoting PPA. As a result, peripheral pulse pressures are generally significantly greater than central pressure, predominantly due to increased systolic pressure [99, 100], as opposed to a reduction in diastolic pressure.

Variations in pressure contour can be seen between waves measured in the the upper and lower limbs. Lower limb measurements usually display a single systolic peak with a later, less defined shoulder and a significantly distorted dicrotic notch. In some cases, such as the femoral artery, the dicrotic notch is often undetectable.

Upper limb measurements, including the commonly used brachial and radial arteries,

experience significant systolic pressure amplification due to the short distance between the reflection and measurement sites. Upper limb wave reflections often occur effectively simultaneously with forward travelling waves, maximizing the constructive interference leaving no identifiable inflection or shoulder [101, 121–123]. However, a secondary systolic peak can often be observed in the upper limb pulse due to the arrival of a second reflected wave arriving from the lower limb, resulting in a secondary systolic peak.

The amplification of the aortic and radial pulse by waves reflected from lower limbs has led some researchers to investigate the correlation between central and upper limb pressures [121–125]. Specifically, the central SP and late systolic shoulder ($pSBP_2$) of the radial pulse were compared and a strong correlation was identified, even when changes to the pressure pulse were induced through atrial pacing and administration of nitroglycerin.

6.5 Pulse Analysis Techniques

Arterial pulse analysis is commonly used to extract information from the pulse relating to wave dynamics and the condition of the arterial system [99, 122, 126, 127]. Quantifying the interaction between P_f and P_r can give insight into potential arterial stiffening as well as cardiac afterload. The two most common techniques used are *pulse wave analysis (PWA)* and *wave separation analysis (WSA)*

6.5.1 Pulse Wave Analysis

PWA generally refers to any process by which information, in excess of absolute pressures, is extracted from the pulse. A range of information can be obtained using PWA including, assessing cardiac contractility using the maximum rate of change of the central pulse, deriving model parameters for cardiac output monitors, and assessing the influence of P_f and P_r on the measured pulse.

One common implementation of PWA is to identify the effects of the interaction between P_f and P_r on the measured pulse using higher order time derivatives of a waveform. Figure 6.5 shows two examples of central and peripheral artery pressure measurements and their corresponding second derivatives. Using the second derivative, the interaction between P_f and P_r can be identified for each measurement.

For both central pressures presented in Figure 6.5, the local maximum of the second derivative provides a reference point, labelled as such in Figure 6.5, for calculating the AI_x of the the pulse. As previously stated, the AI_x can be used to categorize the pulse and infer information about P_f and P_r.

As eluded to in Section 6.4.3, the late systolic shoulder of peripheral arterial measurements have been shown to strongly correlate with central SP. The $pSBP_2$ is also indicative of the P_f and P_r interaction. The magnitude of pressure at $pSBP_2$ is thought to represent the relatively maintained peak pressure of P_f thus, correlate with central SP. Figure 6.5 shows how $pSBP_2$ corresponds with central SP presenting a positive

and negative AI_x. The accuracy of estimating central SP from $pSBP_2$ using lower limb measurements is further explored in Chapter 8.

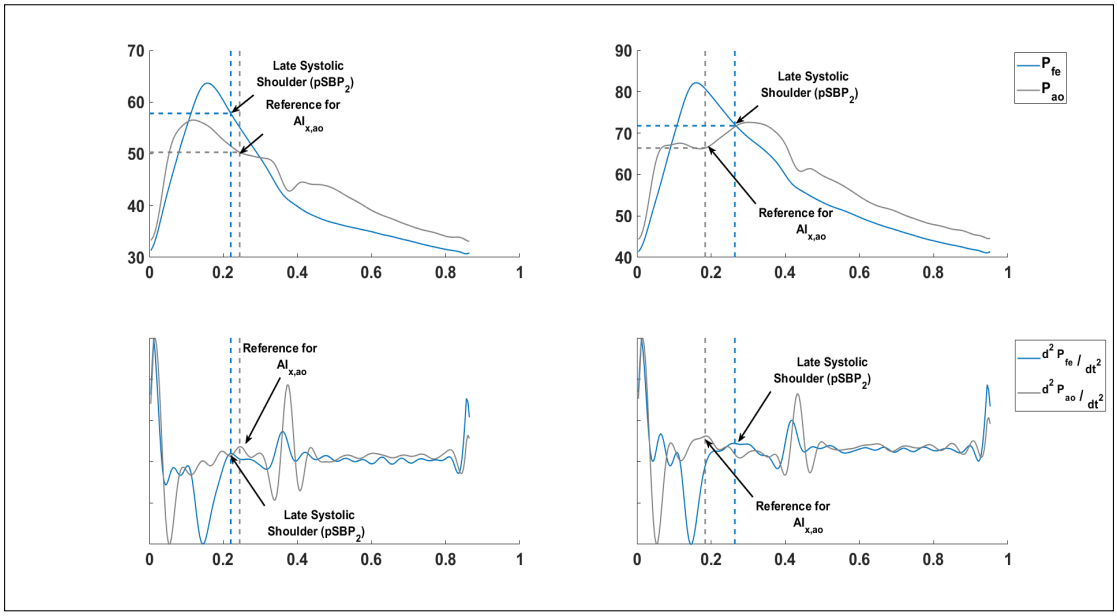

Figure 6.5: Example of PWA used to identify the influence of P_f and P_r on measured femoral ($P_{fe,mea}$) and central ($P_{ao,mea}$) waveforms.

6.5.2 Wave Separation Analysis

WSA uses simultaneous measurements of pressure and flow to calculate the characteristic impedance of the artery and separate the measured pulses into their forward and reflected components [111, 112]. Figure 6.6 shows the key relationship between simultaneous pressure and flow recordings. The component forward and reflected waves have identical contour, although negative for Q_r, in both pressure and flow, scaled by Z_c. Figure 6.6 clearly shows the influence of reflected on forward waves and how these interactions produce the observed differences in measured P_{ao} and Q_{ao}.

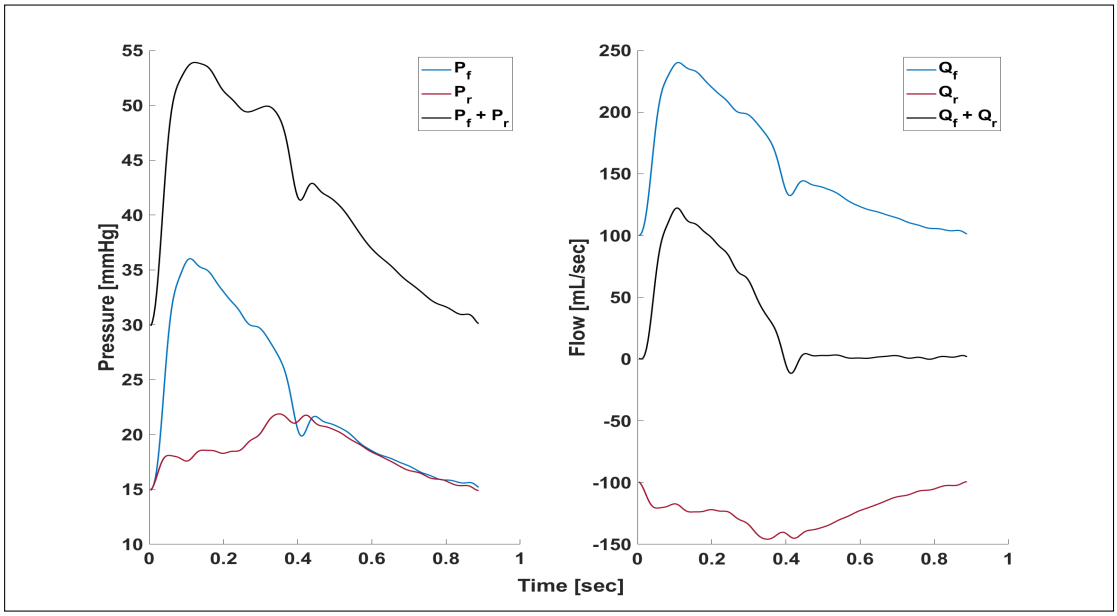

Figure 6.6: Illustration of wave reflection in the aorta detailing the constructive contribution of P_r to measured pressure, in the $P_f + P_r$ line, and the destructive contribution of Q_r to measured flow, in the combined $Q_f + Q_r$ line.

6.6 Arterial Measurements

6.6.1 Pressure

Arterial BP measurements can be taken using either invasive or non-invasive techniques and are usually reported with units of *millimetres of mercury (mmHg)*. The most common method of arterial BP monitoring is the sphygmomanometer, consisting of an inflatable pressure cuff able to be attached to the body at an arterial site, typically around the brachial artery. The cuff is inflated to exceed pressure in the artery, compressing the vessel against the bone making the pulse undetectable downstream of the cuff. Cuff pressure is then steadily decreased until the pulse again becomes audible. Continually decreasing cuff pressure causes the pulse to become increasingly muffled, eventually dis-

appearing. The sounds heard throughout this process are called the *Korotkoff sounds*. The pressure measured at the first and last detectable sounds are the systolic and diastolic pressures, respectively. Modern versions of these devices replace the auscultatory method with automated oscillometric devices measuring pressure oscillations in place of audible beats [100, 128, 129].

Non-invasive methods for continuous BP monitoring have recently been developed and are widely used for the increased information inherent in full continuous beats, versus intermittent systolic-diastolic measurements. Two principles are used for non-invasive devices; *applanation tonometry*, and *volume clamp*. Applanation tonometry applies a sensor to the body over an arterial site able to be compressed against a bone, usually the radial artery, and measures the pressure change during heart beats. Measurements are scaled based on proprietary algorithms to give arterial BP. Volume clamp devices use an inflatable cuff fitted with an infrared transmission plethysmograph to measure the diameter of the finger artery. As pressure in the artery increases with the pulse, so too does pressure in the cuff to maintain a constant vessel diameter. Arterial pressure is obtained by measuring cuff pressure [130].

Patients requiring critical care, such as in the ICU, often have their BP monitored using invasive catheter-based methods, which remain the gold standard. Pressure catheters can be inserted directly into the larger peripheral arteries, commonly the brachial, radial or femoral arteries, and when calibrated correctly provide very accurate continuous pressure measurements. By nature, there is an increased risk associated with invasive, relative to non-invasive, measurements limiting the applicability of obtaining invasive

measurements. Occlusion of the artery, permanent ischaemic damage, infection and haemorrhage are some potential complications associated with invasive BP measurements [131].

6.6.2 Cardiac Output

Cardiac output (CO) can also be obtained from invasive or non-invasive measurements. True CO measurements require an ultrasonic transit-time flow probe to be surgically placed at the aorta and are thus limited only to animal studies [132]. However, various methods have been developed to determine CO from non-invasive and non-additionally invasive methods using currently available measurements and arterial system models [58, 60, 61].

6.6.2.1 Pulmonary Artery Catheter

As the name implies, a *pulmonary artery catheter (PAC)* is inserted into the pulmonary artery via the jugular or subclaivian vein. After insertion, the PAC is pushed downstream to the right atrium where a balloon attached to the distal end of the device is inflated. The balloon aligns the PAC with the direction of blood flow and slows the device, allowing it to enter the right atrium, move through the right ventricle, and into the pulmonary artery. The inflated balloon obstructs flow through the artery, while the sensor down stream of the balloon records the *pulmonary artery occlusion pressure* [132–134].

With the PAC in place, CO can be measured via thermodilution. Earlier devices used a cold fluid bolus administered through an opening in the PAC prior to the right atrium, and a thermistor at the distal end of the device, to detect the drop in temperature near the end of the PAC. More recent devices have an inbuilt heating coil to perform the same task. The relation between temperature and CO is explained in the next section.

Although PACs are commonplace for intensive care hemodynamic monitoring, several studies have reported errors as high as 83% when contrasted to measurements obtained using the Fick technique (the Fick technique was considered the gold-standard CO measurement prior to the PAC's) [132]. Clinically acceptable CO error is often defined as ±30% [59, 135]. However, it has been suggested ±45% is more realistic [136].

6.6.2.2 TRANSPULMONARY THERMODILUTION

Transpulmonary thermodilution (TPTD) uses the change in blood temperature, after receiving a cold fluid bolus, across the pulmonary circulation to calculate CO. A cold volume of fluid is introduced to the circulation via a central venous catheter, which moves through the pulmonary circulation before being expelled from the left ventricle into the systemic circulation where a thermistor, commonly placed in the femoral artery, can measure the change in temperature. Temperature will begin to return to normal at a rate proportional to CO, as defined by the *Stewart-Hamilton equation*:

$$CO = \frac{(T_b - T_f) \cdot V_f K}{\int (T_b - T_d(t))dt} \tag{6.3}$$

where K is a correction coefficient, T_b is the temperature of the blood prior to thermodilution, T_f is the temperature of the fluid introduced, V_f is the volume introduced, and T_d is the drop in temperature detected by the downstream thermistor.

TPTD measurements of CO have been shown to have higher precision than PAC relative to the Fick method (7% vs 25%, respectively)[132, 134]. Similar approaches exist based on the dilution of a known concentration of a dye in place of a cold volume fluid.

6.6.2.3 Pulse Contour Analysis

Pulse contour methods assume the area under the systolic portion of an arterial pressure waveform is proportional to the stroke volume. The PiCCO (Pulse Contour Cardiac Output) device uses a combination of thermodilution, to provide an initial calibration, and pulse contour analysis to give continuous cardiac output. Although widely used, pulse contour methods have shown limited accuracy in hemodynamically unstable patients, such as patients presenting with septic shock, and thus most in need of accurate measurements and monitoring. Pulse contour methods using non-invasive arterial pressure measurements have also been developed, but have the drawback of compounding the error produced by each component of the method [58, 61].

6.6.2.4 Transthoracic Echocardiography

Transthoracic echocardiography (TTE) is a non-invasive method of measuring CO using an ultrasonic transthoracic probe. Changes in area assessed from the ultrasonic images

taken are used to approximate the left ventricular ejection fraction and CO. The non-invasiveness of TTE has led to a rise in popularity. However, the requirements for highly skilled operators to interpret results does lead to operator dependent accuracy and thus, limited clinical use due to the need for skilled operators in a highly demanding clinical environment. Finally, this measure is intermittent, rather than continuous, limiting clinical utility. The indeterminacy of these measurements may prove useful for calibrating alternate methods but insufficient to provide required information during dynamic situations where patient condition can rapidly deteriorate, such as during CVS shock [137], and when assessing fluid responsiveness.

6.6.3 PTT MEASUREMENTS

Gold-standard measurements for PTT measure the time delay between simultaneous measurements of central and peripheral pulses, as shown in Figure 6.7. The diastolic feet of the pressure waveforms are commonly used as they are less influenced by wave reflections. However, while direct peripheral arterial pressure measurements are common in clinical environments, the corresponding aortic measurements are not. The Q-wave of the QRS complex from the *electrocardiogram (ECG)* recordings have been proposed as a surrogate indicator for pulse departure time [138, 139]. However, this measurement includes the *pre-ejection period (PEP)* [140, 141] , in which the left ventricle undergoes isovolumetric contraction. Thus, it is actually a measure of the *pulse arrival time (PAT)* and will over estimate PTT.

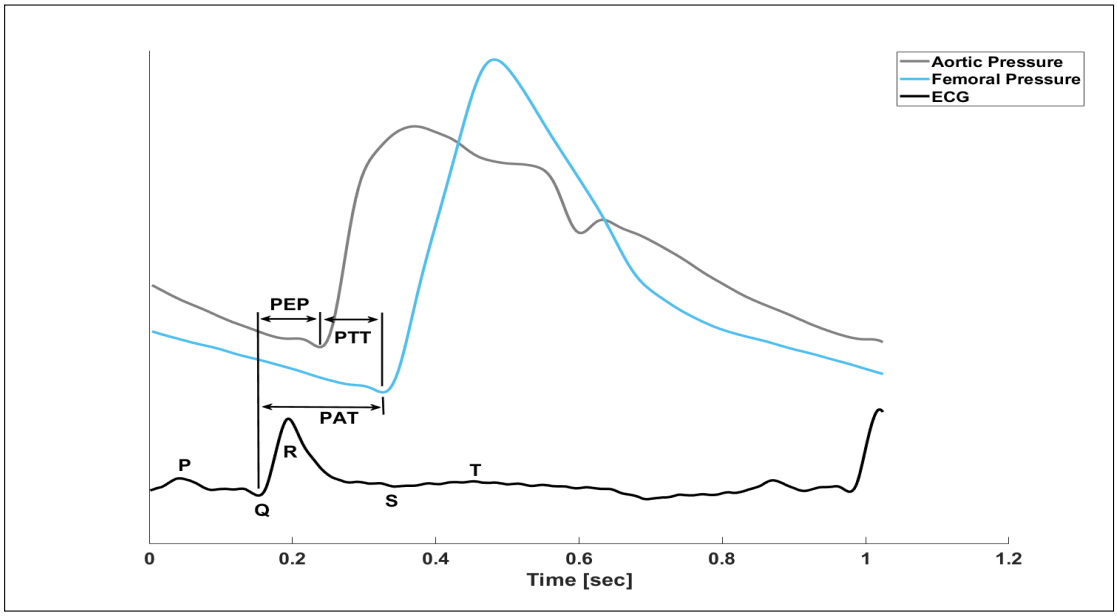

Figure 6.7: Comparison of the different stages of a pulse travelling from the left ventricle to the femoral artery.

6.7 Clinical Importance of Central Pressure

Direct central blood pressure measurements require a catheter placed in the aorta and is usually reserved for the cardiac catheterization laboratory. Invasive arterial blood pressure measurements are predominantly taken from peripheral arteries as they are considered less invasive and present a reduced risk to the patient. However, there is some evidence that central blood pressures better relate to future cardiovascular events [142–144] and respond differently to certain drug therapies [145]. Additionally, the major organs of the body are exposed to central arterial pressures [146], as illustrated in Figure 6.8, not peripheral pressures, which can be significantly different due to peripheral pulse pressure amplification.

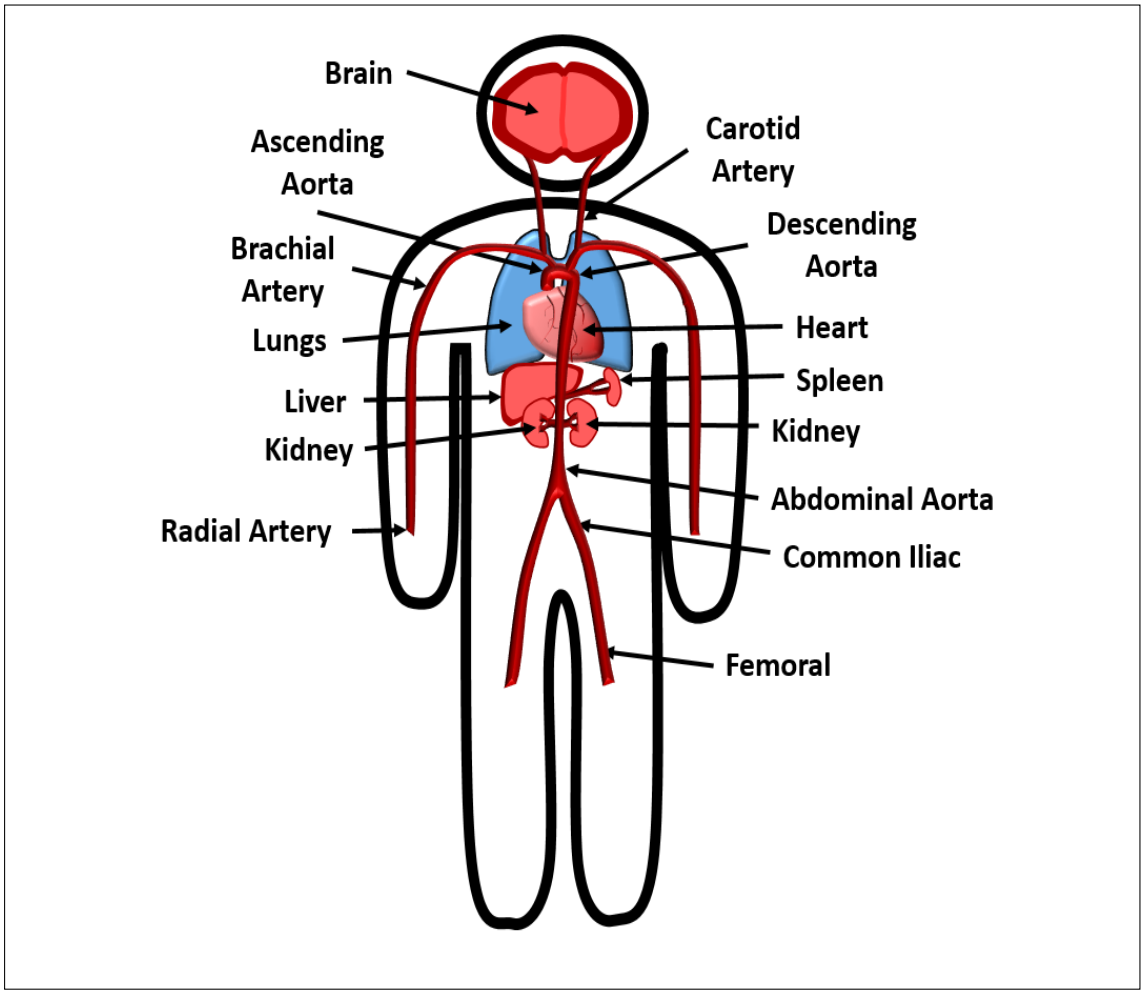

Figure 6.8: Illustration of the relative proximity of the major organs, including the kidneys, liver, spleen and brain, to the central aortic, rather than peripheral pressures. Central pressures are more reflective of organ arterial pressure loads than peripheral pressure surrogates, such as the femoral artery and radial artery.

6.8 Summary

This chapter presented an overview of the arterial system with a primary focus on the determinants of the arterial pulse at different locations throughout the body. Blood ejected from the heart generates a pressure wave, and a corresponding flow wave, which travel in the forward direction to the periphery. Various discontinuities in the architecture of the arterial system will cause these forward waves to be partially reflected and travel back towards the heart. The combined effects of all forward travelling waves can be summed to give a single P_f or Q_f wave. Similarly all reflected waves can be summed to give an effective P_r or Q_r wave. Arterial measurements represent the combined effect of the respective forward and reflected waves.

Arterial pulse analysis techniques, PWA and WSA, can be used to analyse pressure and flow measurements to extract information additional to their absolute values. Specifically, identifying the influence of reflected waves on forward waves can indicate a patients level of arterial stiffness and cardiac afterload.

Measurements of arterial pressure and flow can be obtained using invasive, less-invasive or non-invasive techniques. However, generally as measurements become more non-invasive they have an associated loss of accuracy.

Chapter 7

Arterial System Models

7.1 Introduction

Models of the arterial system are often used to extract clinically relevant information about the central arteries from the readily available peripheral measurements. Arterial system models range in complexity from low dimensional lumped parameter models to high dimensional 3D models [147]. This work is primarily concerned with applications to clinical diagnostics, making high dimensional models less suitable due to additional computational cost and higher number of input parameters required [67].

This chapter introduces a distributed parameter model of the arterial system called a *tube-load (TL)* model. Each tube of the TL model describes a wave propagation path for a pulse travelling from the heart to a peripheral artery. The terminal end of each tube describes the effective reflection site, generating the P_r and Q_r waves. The parameters

of TL models are commonly identified by reforming the governing equations into an *arterial transfer function (TF)* relating measurements taken at peripheral arteries with central waveforms [148].

Early arterial TF models were not derived from TL models, but instead used simultaneous central and peripheral pressure measurements to define population based relations. These relationships can be derived from the amplitude and phase ratios of the signal harmonics using a Fourier frequency analysis [149]. Using a database of recordings from a variety of patients experiencing a range of hemodynamic settings, and averaging the relations, a *generalized transfer function (GTF)* can be obtained. The GTF can be applied to new peripheral measurements to estimate central BP. Similar approaches have used autoregressive exogenous models to identify model parameters relating central and peripheral pressures and formulate a GTF from them [150]. The limitation of a GTF is evident in their name, they are a generalization based on population averages, and are thus less suited to adapt to inter- and intra subject variability [148].

To account for inter-patient variability, measurements of arterial PTT have been introduced into a TL model-derived arterial TF to tailor central pressure estimates on a per patient basis. This process produced *individualized transfer functions (ITF)*. Stergiopulos *et. al.* used WSA to deconstruct peripheral pressure measurements into P_f and P_r, then shifted these component waves using measurements of PTT to reconstruct the central pressure pulse [117, 118].

More recent attempts at individualizing TF models use parametric models for the terminal load of the tube [148]. The parameters describing the load can be tuned to fit some

aspect of a patient's peripheral pressure to individualize the general TF model. Model parameters are usually identified using some minimization criteria based on *apriori* knowledge of the central pressure [151–153] or flow waveform [154, 155], or using two diametric peripheral BP measurements and assuming a common origin of the central pulse [156, 157].

Finally, Hahn *et. al.* proposed a method for estimating central BP from a single peripheral measurement [151, 158] to remove the need for an additional PTT measurement, which may have inherent error depending on the method of acquisition, or not be available all together in retrospective data sets. The authors reformulated Equation 7.11 into a linear regression in terms of only peripheral BP. Model parameters were selected by solving the linear regression for a range of PTT and selecting the central BP estimates which minimize a *sharpness function* developed by the authors based on the second derivative of the potential central pressure estimates.

7.2 Arterial Transfer Functions

This section details how wave reflection principles are used to derive the TL model equations and how these equations can be used to formulate a transfer function relating central and peripheral arterial waveforms.

As previously mentioned, the arterial system can be modelled as a series of parallel tubes with each tube representing a wave propagation path from the aorta to a peripheral

measurement site. Each tube is terminated by a load representing the effective reflection site. A schematic of the TL model is shown in Figure 7.1.

The TL model used in this work assumes uniform, frictionless tubes with pulse waves propagating to the reflection site without distortion, where they travel back through the system, again without distortion. The degree to which waves are reflected is described by the *reflection coefficient* (Γ) and is dependent on the mismatch between the characteristic impedance of the tube and the impedance dependent load. The general form for Γ is defined:

$$\Gamma_i(j\omega) = \frac{Z_i(j\omega) - Z_{ci}}{Z_i(j\omega) + Z_{ci}} \tag{7.1}$$

where Γ_i is the reflection coefficient of the i^{th} tube, Z_{ci} is the characteristic impedance of the tube and $Z_i(j\omega)$ is the frequency dependent impedance load. Models can differ by adjusting the definition of $Z_{Li}(j\omega)$.

This work aims to produce central BP estimates from a single peripheral pressure measurement. Thus, a single tube model is used. The model equations discussed from here on relate to this version of the model.

Pressure and flow at any point x along the tube is described by the combination of the forward and reflected components:

$$P_i(x, j\omega) = P_{f,i}(x, j\omega) + P_{r,i}(x, j\omega); \tag{7.2}$$

$$Q_i(x, j\omega) = Q_{f,i}(x, j\omega) + Q_{r,i}(x, j\omega); \tag{7.3}$$

where $P_i(x, j\omega)$ and $Q_i(x, j\omega)$ are the pressure and flow at some point x along the i^{th} tube and the subscripts f and r represent the forward and reflected component of the pulse, respectively.

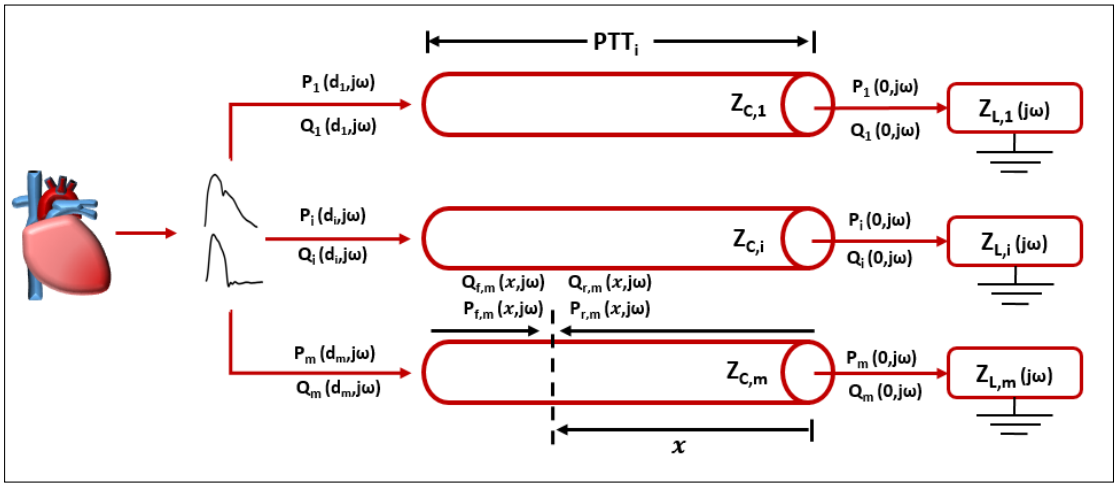

Figure 7.1: Schematic of an arterial tube load model describing the multiple pulse wave propagation paths from the heart to an effective reflection site, characterized by some frequency dependent impedance (Z_L).

Pressure and flow are intrinsically linked through the characteristic impedance of the tube ($Z_{c,i}$), defined:

$$Q_{f,i}(x, j\omega) = \frac{P_{f,i}(x, j\omega)}{Z_{c,i}}; \tag{7.4}$$

$$Q_{r,i}(x, j\omega) = -\frac{P_{r,i}(x, j\omega)}{Z_{c,i}} \tag{7.5}$$

The negative sign present in Equation 7.5 details the destructive interference between forward and reflected components of flow, compared to the constructive pressure interference.

Reflected waves are proportional to the forward wave, differing by the magnitude of the

reflection coefficient:

$$P_{ri}(0, j\omega) = P_{fi}(0, j\omega) \times \Gamma_i(j\omega) \tag{7.6}$$

where $\mathrm{P_{ri}}(\mathrm{x}, \mathrm{j}\omega)$ is the reflected pressure wave and $\mathrm{P_{fi}}(0, \mathrm{j}\omega)$ is the forward travelling wave at the distal end of the tube i.e the reflection site. Note, the model presented here is from the perspective of the peripheral site, with wave reflection occurring at x=0.

Pressure at a distance x along the tube can be described as the summation of the forward and reflected waves, offset by some time constant corresponding to the time taken for the pulse to reach the reflection site, PTT.

$$P_{fi}(x, j\omega) = P_{fi}(0, j\omega)e^{j\omega PTT_i \frac{x}{d_i}} \tag{7.7}$$

$$P_{ri}(x, j\omega) = P_{ri}(0, j\omega)e^{-j\omega PTT_i \frac{x}{d_i}} \tag{7.8}$$

where $\mathrm{d_i}$ is the length of the tube and the exponential terms represent the time shift of each wave, represented in the frequency domain.

Substituting Equation 7.6 into Equation 7.8, and summing with Equation 7.7 gives the general equation for the peripheral pressure at a distance x along the $\mathrm{i^{th}}$ tube.

$$\begin{aligned} P_i(j\omega) &= P_{fi}(0, j\omega)e^{j\omega PTT_i \frac{x}{d_i}} + \Gamma_i(j\omega) \times P_{fi}(0, j\omega)e^{-j\omega PTT_i \frac{x}{d_i}} \\ &= P_{fi}(0, j\omega)\left[e^{j\omega PTT_i \frac{x}{d_i}} + \Gamma_i(j\omega)e^{-j\omega PTT_i \frac{x}{d_i}}\right] \end{aligned} \tag{7.9}$$

Equations 7.4 - 7.5 are used to derive the corresponding generalized flow equation.

$$Q_i(x, j\omega) = \frac{P_{fi}(0, j\omega)}{Z_{c,i}} e^{j\omega PTT_i \frac{x}{d_i}} - \Gamma_i(j\omega) \times \frac{P_{fi}(0, j\omega)}{Z_{c,i}} e^{-j\omega PTT_i \frac{x}{d_i}}$$
$$= \frac{P_{fi}(0, j\omega)}{Z_{ci}} \left[e^{j\omega PTT_i \frac{x}{d_i}} - \Gamma_i(j\omega) e^{-j\omega PTT_i \frac{x}{d_i}} \right] \tag{7.10}$$

Using Equations 7.9 and 7.10, central-peripheral transfer functions can be defined:

$$\frac{P_c(j\omega)}{P_i(0, j\omega)} = \frac{e^{j\omega PTT_i} + \Gamma_i(j\omega) e^{-j\omega PTT_i}}{1 + \Gamma_i(j\omega)} \tag{7.11}$$

$$\frac{Q_{ci}(j\omega)}{P_i(0, j\omega)} = \frac{e^{j\omega PTT_i} - \Gamma_i(j\omega) e^{-j\omega PTT_i}}{[1 + \Gamma_i(j\omega)] \cdot Z_{ci}} \tag{7.12}$$

where P_c is central BP, P_i is the peripheral input pressure, and Q_{ci} is the component of total flow entering the tube.

Equations 7.11 and 7.12 are the general central-peripheral TF equations used in many TL models [116, 117, 147, 148, 152, 153, 155, 157]. These equations are characterized by Γ_i, defined by Equation 7.1. Previous implementations of TF models primarily differentiate by the description of the impedance load used to describe the terminal end of the tube. For simplicity and robustness in the parameter ID process, a generic pole-zero load was selected for this work, specifically defined:

$$Z_{Li}(\omega) = \frac{Z_{ci}(j\omega + B_i)}{j\omega + A_i} \tag{7.13}$$

Where A_i and B_i characterize the capacitance and resistance of the tube and are bounded by $0 < A_i < B_i$.

Combining Equations 7.13 and 7.1 and substituting in the resulting reflection coefficient into Equation 7.11 yields:

$$\frac{P_c(j\omega)}{P_{pi}(j\omega)} = \frac{\left(\frac{B_i+A_i}{2} + j\omega\right) e^{j\omega PTT_i} + \frac{B_i-A_i}{2} e^{-j\omega PTT_i}}{B_i + j\omega} \tag{7.14}$$

$$\frac{Q_{ci}(\omega)}{P_{pi}(\omega)} = \frac{\left(\frac{B_i+A_i}{2} + j\omega\right) e^{j\omega PTT_i} - \frac{B_i-A_i}{2} e^{-j\omega PTT_i}}{Z_{ci}\,(B_i + j\omega)} \tag{7.15}$$

Equations 7.14 and 7.15 can be reformulated into discrete time series equations by taking the inverse Laplace and discretizing via the backward Euler method [58, 159]:

$$p_c[n] = \alpha_i p_c[n-1] + \beta_i p_{pi}[n + ptt_{di}] - \alpha i p_{pi}[n + ptt_i - 1]$$

$$+ (1 - \beta_i)\, p_{pi}[n - ptt_i] \tag{7.16}$$

$$q_{ci}[n] = \frac{1}{Z_{ci}} \alpha_i q_{ci}[n-1] + \beta_i p_{pi}[n + ptt_i] - \alpha i p_{pi}[n + ptt_i - 1]$$

$$- (1 - \beta_i)\, p_{pi}[n - ptt_i] \tag{7.17}$$

where n is the discrete time step; $\mathrm{ptt_i}$ is the number of discrete data points in the central-peripheral PTT; $\alpha_\mathrm{i} = \mathrm{F_s}/(\mathrm{B_i} + \mathrm{F_s})$; and $\beta_\mathrm{i} = ((\mathrm{B_i} + \mathrm{A_i})/2 + \mathrm{F_s})/(\mathrm{B_i} + \mathrm{F_s})$. $\mathrm{F_s}$ is the sampling frequency. Finally, α_i and β_i are bounded by $0 < \alpha_i < \beta_i < 1$. Equations 7.16 and 7.17 can now be applied to the measured peripheral pressure to obtain central pressure after the three model parameters $\{\alpha_i,\, \beta_i,\, ptt_i\}$ are identified.

7.2.1 LOAD TYPE

Model complexity can be adjusted using higher or lower order loads to define Γ. Additional to the generic pole-zero load described by Equation 7.13, a range of loads have been utilized in the literature including variations of three element Windkessel models, and purely resistive loads. Figure 7.2 shows some common variations of the terminal load ($Z_L(j\omega)$).

The left most load is a simplest description, representing the terminal end of the tube as a purely resistive load [152]. The middle two loads are variations of three-element Windkessel model loads [160]. The advantage of these Windkessel descriptions is the inclusion of parameters with physical meaning and limitations allowing them to be interpreted in terms of the aspects of arterial system they represent. Identification of these parameters will provide insight into the lumped arterial dynamics which may be clinically useful.

The final load description is a generic pole-zero load and is included in Equations 7.14-7.17. This last model structure was the load selected for this work as it allows a flexible system order [148], thought to help with the overall goal of identifying parameters from the very limited single information contained in a single peripheral pressure input [154].

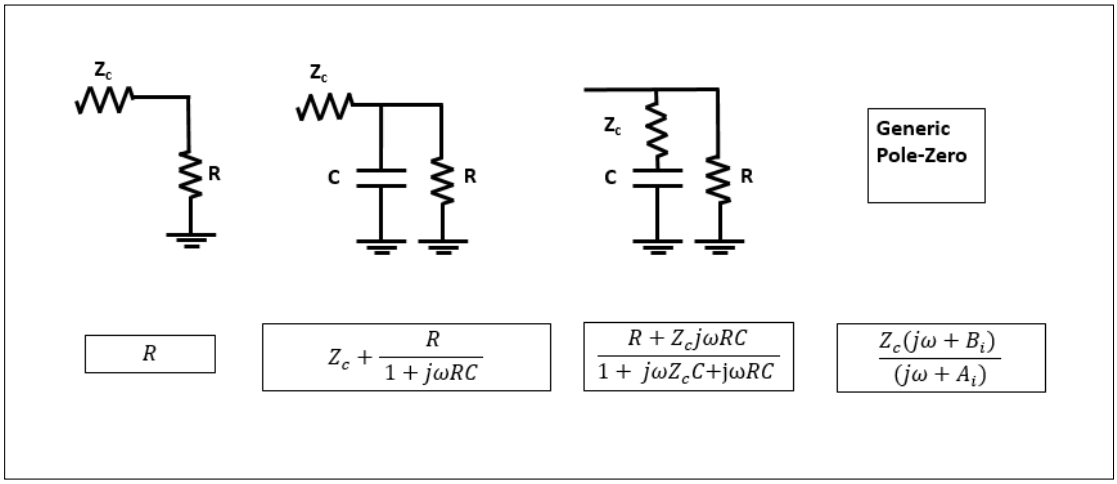

Figure 7.2: Various definitions of terminal loads used in previous TF models, including the generic pole-zero structured load implemented in this work.

7.3 Previous TF model identification

Various methods have been previously employed to identify TF model parameters. Generally, these methods exploit *a priori* knowledge of the central pressure/flow pulse to define some minimization criteria which model parameters are adjusted to best satisfy. Table 7.1 presents the reported errors for several previous implementations of arterial TF models used to estimate central BP, as well as the errors of the peripheral pressure measurements used. Multi-channel [156, 157] and waveform decomposition [161] method approaches were not considered as they require multiple simultaneous arterial pressure measurements. This section briefly describes the methods used to identify the model parameters in each of the methods presented in Table 7.1.

Table 7.1: Performance of central BP estimates reported from previous, minimal input, TF models relative to invasive central BP measurements (mmHg). Radial and femoral arterial pressures are commonly used as inputs into TF models and are also included.

TF Method	SP	PP	RMSE	Reference
Radial	6.9-21.6	6.1-21.6	2.9-9.1	[151–155, 158]
Femoral	3.1-17.1	4.7-20.3	2.9-8.6	[154]
GTF_{sphyg}	3.1-7.4	4.7-10.9	2.9-4.7	[152]
GTF_{arx}	3.5-6.2	4.3-7.6	2.9-5.3	[155, 159]
ITF	3.6	3.8	4.3	[151, 158]
ATF_{press}	3.4	3.8	3.1	[152]
ATF_{flow}	4.3	3.4	4.1-4.8	[154, 155, 159]

7.3.1 EXPONENTIAL DECAY

The closing of the aortic valve at end-systole causes aortic pressure to behave passively during diastole, characterized by a generalized exponential decay. This exponential decay has been used to identify TF model parameters by way of a log transform of a candidate model pressure estimate during diastole and minimizing the root-mean-squared-error of a fitted line [152]. This method produced the results labelled ATF_{press} in Table 7.1 and used a purely resistive description of the terminal.

7.3.2 NEGLIGIBLE DIASTOLIC FLOW

Like pressure, the central flow waveform behaves predictably during diastole because the aortic valve is closed. Specifically, flow during this period can be assumed negligible. Therefore, using Equation 7.12, the model parameters can be identified by finding the parameter set which minimizes the flow variance of candidate flow waveforms during diastole [154, 155, 159]. This method was implemented using a generic pole-zero load and a measurement for PTT to produce the ATF_{flow} results.

7.3.3 Sharpness Function

The difference in travel time for a pulse moving through the upper and lower limbs will stagger the arrival of the respective reflected waves as the return to the aorta. This staggered arrival will minimize constructive interference. Assuming minimal overlap between forward travelling wave and reflected waves, the central pulse will be display a rounded contour, which can be used to identify TL model parameters. Interpreting the contour of model candidate pressure using the time dependent second derivative allows a sharpness function to be developed which is minimized to identify model parameters [151, 158]. The authors called this modelling approach the individualized transfer function (ITF) method.

7.4 Assumptions and Limitations

The main assumptions for the TL model are: 1) single tube between central and peripheral arteries; 2) lossless tube; 3) linear geometric and elastic vessel wall properties resulting in a single effective reflection site. In actuality, none of these assumptions are true. Branching of the arterial tree occurs almost immediately after the heart, meaning a single tube is a simplistic approximation of the wave propagation path even between major arteries (i.e. aorta to femoral artery). Small ($\approx 2-3mmHg$) pressure losses between arterial sites are seen, even between the major arteries. Arterial trees are a complex network of gradually tapering blood vessels with differing elastic properties causing innumerable partial wave reflections. A single reflection site can be justified

through various works identifying the high resistance arterioles as the major reflection site [99]. Changes in elastic properties will produce wave reflections but such changes occur gradually so accompanying reflections are small. The effects of tapering and branching have also been thought to have a cancelling effect [148].

7.4.1 TUBE-LOAD MODEL VARIATIONS

Variations of the standard TL models have aimed capture the additional complexity of the arterial system [147]. *Lossey models* include additional model parameters to account for differences in mean pressure between arterial sites, especially prevalent in instances of disease [162]. *Non-uniform models* attempt to more accurately represent the changing geometry of arteries [163]. Exponentially decaying and segmental changes in vessel geometry have been used. *Non-linear models* have described arterial compliance as a function of the BP using an exponential relation [164].

Although each of these variations has improved model accuracy compared to the baseline TL model presented in this chapter, the difference may not be significant [148]. Finally, the increased complexity comes with higher numbers of model parameters to be identify, which may be impractical in clinical settings with relatively limited and noisy or biased measurements.

7.5 Modelling Central Blood Flow

Aortic blood flow is often modelled using a simple triangular approximation presented by Westerhof *et. al* [102, 118, 165]. The systolic component of the flow waveform is a triangle with a base width equal to the ejection period and a peak occurring at the primary systolic peak of the corresponding pressure waveform. This approximation uses the notion of P_f and Q_f having identical contour and thus manifest in their respective measured waveforms in the same location, as seen in Figure 7.3.

The amplitude of peak flow is set at an arbitrary level, as specific values of flow can not be obtained from a single pressure measurement. Although the location of peak flow was better estimated from the primary shoulder of the pressure pulse, using 30% of the ejection period was been shown to provide a consistent, trivially obtainable approximation [118]. Diastolic flow is set to zero, assuming negligible flow through the aortic valve when closed.

However, the triangular approximation frequently underestimates true flow contour [166]. A quadrangular flow wave was also proposed by Westerhof *et. al.* to capture the convex/concave profile of systolic flow, but the authors also stated the method required fitting an additional point during late-systole based on visual inspection of the measured pulse. Hence, it is impractical in a limited measurement scenario typical of the ICU application considered in this thesis.

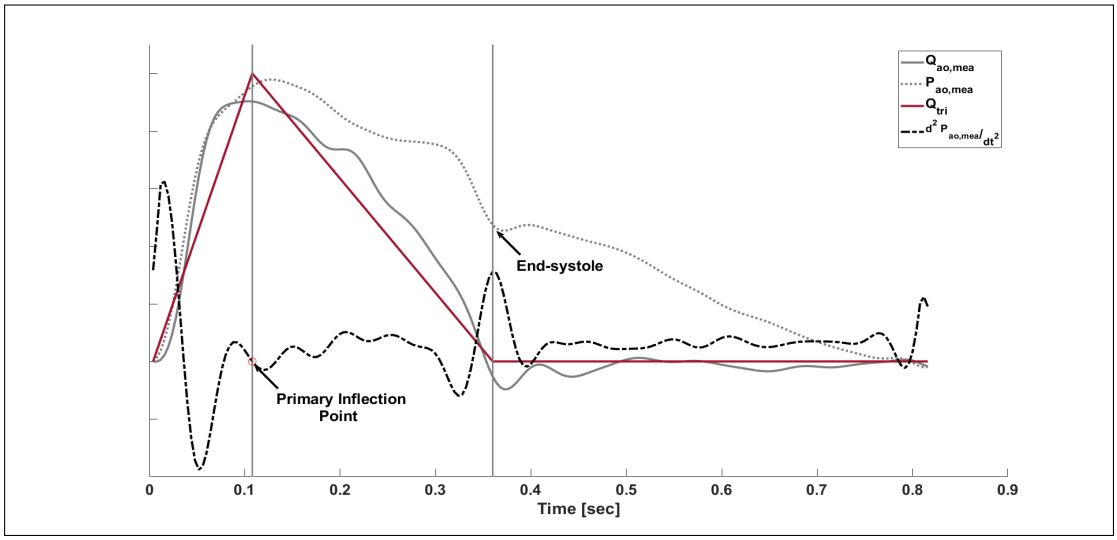

Figure 7.3: Triangular flow approximation of flow showing the correlation between the primary systolic shoulder of the corresponding central pressure measurement and peak flow.

7.6 Summary

This chapter introduces an arterial TF derived from a single channel TL model of the arterial system. The TF can be used to relate peripheral and central pressure using the concept of a common forward and reflected wave produces both measurements, differing by the PTT. A generic pole-zero structure is used to describe the terminal load of the tube and characterizes the reflection coefficient.

A simple model for estimating the central flow waveform using a triangular approximation during systole, and zero flow during diastole is also presented. This simple model provides a good insight into the general shape of the flow wave contour. Subsequent chapters will validate its strengths and weaknesses using experimental data.

Chapter 8

Central Pressure and Flow Estimation via Pulse wave Analysis

8.1 Introduction

Arterial transfer functions (TF), derived from tube load models of the arterial system, provide accurate estimates of central blood pressure given the model parameters can be identified accurately [117, 147, 148, 151, 152, 154, 155]. Ideally, model parameters would be adjusted on a per patient basis to capture inter and intra subject variability, as opposed to population average based generalized TF models. However, parameter

identification and thus, the accuracy of pressure estimation, is limited by the quality and availability of measurements in a clinical environment [67].

Recent approaches using TF models to estimate central BP have used measurements of PTT to adapt the general TF model equations to a specific patient, then fit to some *a priori* aspect of the central pressure [152] or flow pulse [154]. This approach requires PTT be measured prior to implementation and updated to account for changes in patient condition.

In Section 6.6.3 the measurement procedure for obtaining PTT clinically, using ECG recordings, was outlined. Direct measurement of PTT requires simultaneous central and peripheral recordings, which not only needs highly trained physicians to perform time consuming, invasive procedures, but also negates the need for central BP estimation, as it is directly measured. Q-waves of the ECG recordings, used as a surrogates for pulse departure time, have also been shown to produce unreliable outputs due to the pre-ejection period between initiation of ventricular contraction and opening of the aortic valve [141]. Thus, there are significant clinical and technical reasons to avoid these limitations. Furthermore, if data sets do not contain ECG or simultaneous pressure recordings, PTT is very difficult to obtain retrospectively.

Therefore, a method capable of accurately estimating central BP solely from widely available peripheral pressure measurements is desirable. This chapter presents a novel method for estimating central BP from a single peripheral pressure measurement and a validated TF model by first constructing initial central pressure ($P_{ao,int}$) and flow ($Q_{ao,int}$) estimates which are used to identify all model parameters, including PTT.

Using PWA, features of a peripheral pressure pulse relating to the P_f and P_r waves are identified. The identified features are combined with simple physiological assumptions about wave propagation dynamics to approximate full pressure and flow waveforms for a given beat.

8.2 Pulse Wave Analysis

Information contained in the peripheral pulse relating to the component P_f and P_r waves are identified from the time dependent second derivative. Three general categories of peripheral pulse were identified in this work. Pulses had either an inflection point during early systole, an inflection in late systole, or no identifiable inflection points during systole. Figure 8.1 shows these variations, their corresponding second derivatives, and the associated measured $P_{ao,mea}$ waveforms. Depending on the contour of the pulse, 3 or 4 points are identified from the second derivative, as shown.

8.2.1 End-systole ($P_{fe,mea}(t_{es})$)

End-systole (t_{es}) is a key feature of the central pulse, signifying the end of ejection and closing of the aortic valve. Measured $P_{ao,mea}$ waveforms typically present a dicrotic notch used to easily identify t_{es}. However, due to peripheral pressure amplification, the pulse contour may be augmented to the point where the dicrotic notch becomes unidentifiable.

Identification of t_{es} on dicrotic-notchless waveforms can be achieved using a weighting

function applied to the second derivative of the descending portion of the pulse [61]. This weighting function is constructed with a maximum positioned at the approximate location of end-systole, based on the equation:

$$Tes = -0.1 \cdot HR + 0.45 \tag{8.1}$$

Note, while Figure 8.1 shows a prominent peak at t_{es} this feature is not always present making the weighting function necessary.

8.2.2 Systolic Pressure Reference ($pSBP_2$)

As mentioned several times in this thesis already, $pSBP_2$ and central systolic pressure are strongly correlated [121–123]. These works suggested reflected waves arriving from the lower limbs similarly influence the radial and central pulse and maintain a constant pressure. Although work in this section uses femoral artery pressure measurements ($P_{fe,mea}$), it is a common reflected wave augmenting both femoral and radial pulses. Therefore, this approach was deemed suitable for estimating central systolic pressure, albeit more difficult to identify $pSBP_2$.

The $P_{fe,mea}$ pulse rarely has any distinct peak at $pSBP_2$, as is common on the radial pulse. Therefore, to identify $pSBP_2$ the pulse is first classified into one of three general categories based on it's second derivative, corresponding to those depicted in Figure 8.1, and $pSBP_2$ is determined based on the classification of the pulse.

The first classification, and most commonly encountered in this work, were waves which

had a clear inflection point in late-systole, as seen in the left images of Figure 8.1. This inflection point is produced by the interaction between forward and reflected waves, and $pSBP_2$ is taken as the local maximum of the second derivative between peak pressure and t_{es}.

Next, waves which presented with no inflection point in late-systole but had multiple inflections in early-systole prior to the systolic peak, as seen in the middle figures of Figure 8.1, formed a classification. These waves were encountered in subjects which initially presented with a clear inflection point in late-systole, but was diminished due to the onset of septic shock causing reflected waves to arrive earlier in systole. This wave classification also used the local maximum of the second derivative to define $pSBP_2$.

The last class of wave was indicative of those which had the forward and reflected waves merge into a single systolic peak. These waves had no early or late inflection points characteristic of wave interference. Therefore, $pSBP_2$ was defined by the inflection point immediately preceding t_{es}, termed the end-systolic inflection point (ES_{infl}). With the points noted above identified, $P_{ao,int}$ and $Q_{ao,int}$ can be constructed.

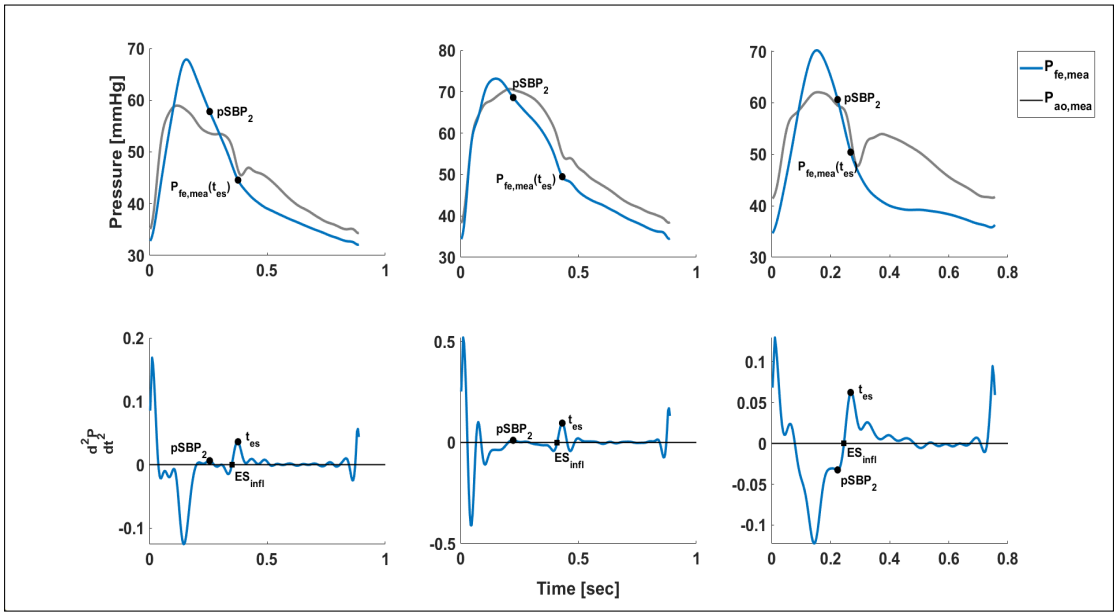

Figure 8.1: Examples of the three general classifications of peripheral pressure waves encountered in this work and how pulse wave analysis is used to identify relevant features for $P_{ao,int}$ and $Q_{ao,int}$.

8.3 Central Pulse Approximations

$P_{ao,int}$ and $Q_{ao,int}$ are characterized by early systolic, late systolic and diastolic components. Because a common forward and reflected wave generates both pulses, features of each pulse correlate to one another. Although, absolute values extracted from the peripheral pressures can provide accurate estimates for central pressure, obtaining absolute values for flow requires additional knowledge of the characteristic impedance. Therefore, $Q_{ao,int}$ is constructed arbitrarily between 0 and 1, and only the pulse contour is used in the subsequent parameter identification process.

Previous methods for estimating central flow contour [102, 118] have assumed a triangular contour to the pulse. However, this assumed shape is likely to underestimate flow

due to the convexity of the pulse. Thus, a novel quadrangular method was developed to better estimate the flow velocity profile and avoid significant underestimation.

8.3.1 $P_{ao,int}$ from $P_{fe,mea}$

Six key points are used to define $P_{ao,int}$; the two diastolic feet of $P_{fe,mea}$, a primary (SS_{pri}) and secondary (SS_{sec}) systolic shoulder, the systolic pressure reference $pSBP_2$, and an estimate for central end-systolic pressure $P_{ao,int}(t_{es})$.

The SS_{pri} is defined by the intercept of upstroke peripheral pressure with the horizontal projection of $pSBP_2$. Assuming P_r has little effect on P_f during the initial portion of the pulse, the early systolic component of both $P_{ao,mea}$ and $P_{fe,mea}$ waveforms are both indicative of the relatively unaltered common forward wave. Therefore, pressure up to SS_{pri} on $P_{fe,mea}$ is equivalent to $P_{ao,mea}$, over the same time period. This match can be seen in Figure 8.2.

The augmentation of $P_{fe,mea}$ in late systole prevents this method from being extended to identify the SS_{sec}. However, identifying the peripheral secondary systolic shoulder ($SS_{fe,mea}$) does provide a useful reference point for the timing, not magnitude, of SS_{sec}. Although in reality, the timings of $SS_{fe,mea}$ and $SS_{ao,mea}$ will differ slightly due to the increased travel time for P_r to return to the aorta, this difference is small relative to overall beat length. Therefore, $SS_{fe,mea}$ provides a useful reference point for SS_{sec}.

To identify $SS_{fe,mea}$, a line is constructed between $pSBP_2$ and ES_{infl}, and the SS_{sec} can be identified as the point of maximum perpendicular distance between $P_{fe,mea}$ and this line,

as illustrated in Figure 8.2. The SS_{pri} and SS_{sec} points are connected using a constant pressure approximation, with a value equal to $pSBP_2$.

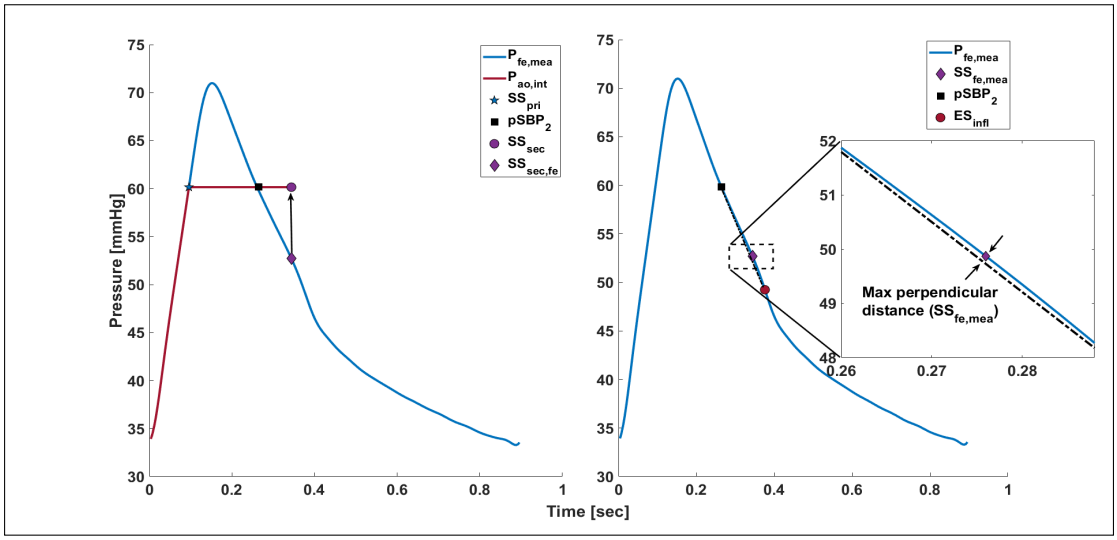

Figure 8.2: Example of the process used to construct the linearised approximation of $P_{ao,int}$ during early systole. (left) $pSBP_2$ defines the systolic pressure of $P_{ao,int}$ which extends from SS_{pri} to SS_{sec}. (right) example identification of $SS_{fe,mea}$ used to identify the timing of SS_{sec}.

The late systolic pressure drop ($P_{ESD,int}$) from SS_{sec} to the estimated central end-systolic pressure ($P_{ao,int}(t_{es})$), is assumed to be proportional to the relative pressure drop from $pSBP_2$ to $P_{fe,mea}(t_{es})$, divided by peripheral pulse pressure (PP_{fe}). Specifically:

$$P_{ESD,int} = \frac{PP_{ao,int}}{PP_{fe,mea}} \cdot P_{ESD,fe} \tag{8.2}$$

Equation 8.2 assumes the pressure drop during late systole on the central pulse is proportional to the corresponding drop in pressure of the peripheral pulse ($P_{ESD,fe}$). Additionally, it is assumed $P_{ESD,fe}$ is amplified by the same amount as peripheral systolic

pressure and thus, $P_{ESD,int}$ is proportional to the ratio of the two pulse pressures, $PP_{ao,int}$ and $PP_{fe,mea}$.

Finally, the diastolic component of $P_{ao,int}$ is approximated by fitting an exponential model to $P_{fe,mea}$ during diastole. Care should be taken to fit to only the passively behaving portion of the curve to minimize any affects of late arriving reflected waves. Once fit, this line is rotated clockwise, shown in Figure 8.3, until the end-systolic end intercepts with a reference line drawn from $P_{ao,int}(t_{es})$ to the foot of the pulse. This line is used as an approximation for the expected location of the pulse during diastole. The curve is then shifted to join the end-systolic end with $P_{ao,int}(t_{es})$, completing $P_{ao,int}$.

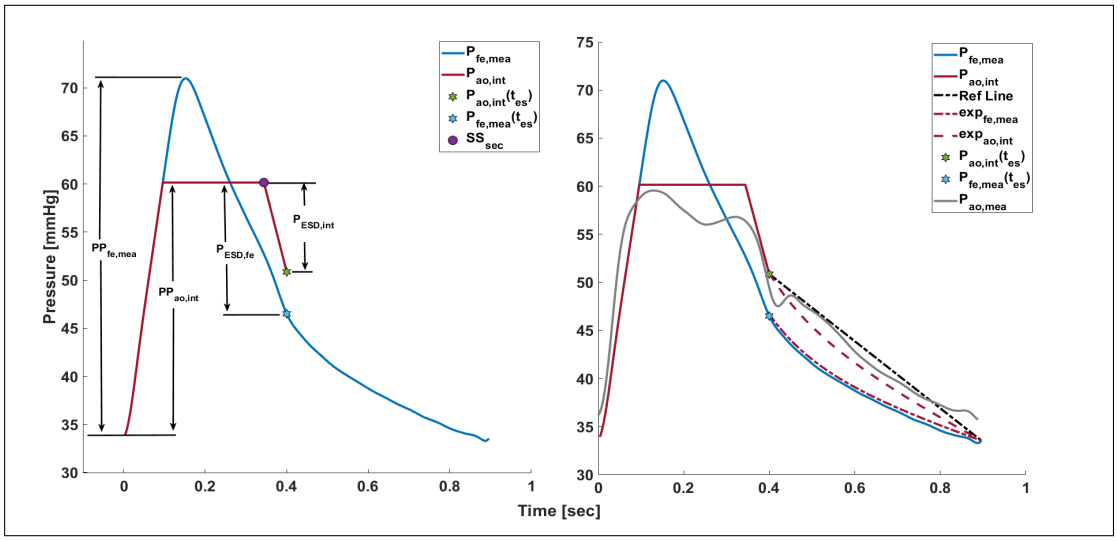

Figure 8.3: Example of the process used to construct the linearised approximation of $P_{ao,int}$ during late systole and diastole. (left) the ratio of the $P_{ESD,int}$, taken from $pSBP_2$ to $P_{fe,mea}(t_{es})$, to $PP_{fe,mea}$ is used to estimate $P_{ao,int}(t_{es})$. (right) an exponential model is fit to $P_{fe,mea}$ during diastole and rotated into the correct position to estimate diastolic $P_{ao,int}$.

8.4 $Q_{ao,int}$ from $P_{fe,mea}$

Unlike pressure, little information is contained in peripheral pressure pulses relating to the central flow pulse. Therefore, $Q_{ao,int}$ is constructed with values between 0 and 1, and is only used in later chapters as a guide to flow wave contour, not for references of specific value. Previous approximations for central flow waves have used a triangular representation during systole [102, 118, 167]. However, an initial trial of the triangular approach was found to significantly underestimate true flow. Therefore, a novel quadrangular approximation was developed.

The SS_{pri} of both $P_{ao,int}$ and $Q_{ao,int}$ are produced by the forward wave ejected from the heart and occur simultaneously. Early systolic $Q_{ao,int}$ thus extends from the origin to a maximum of 1 at a time equal to SS_{pri}.

As mentioned in Section 6.3, the arrival of reflected flow waves relative to forward waves determines the shape of the pulse. Earlier arriving waves have a significant deceleration effect, producing a more linear systolic portion of the pulse. Later arriving waves have less affect and the pulse remains concave [99, 108, 166]. Although opposite in effect, reflected flow and pressure waves arrive at the aorta at the same time, $pSBP_2$. This interaction of flow waves is similar to that producing $P_{ESD,int}$, however, because of the destructive effect of the reflected flow wave, the late systolic drop in the flow wave is considered to be inversely proportional to $P_{ESD,int}$, specifically:

$$Q_{ESD,int} = 1 - \frac{P_{ESD,int}}{PP_{ao,int}} \tag{8.3}$$

Equation 8.3 states the earlier wave reflection arrive relative to forward travelling waves, the grater the pressure amplification and thus, the greater the deceleration effect on the flow pulse, reducing $Q_{ESD,int}$, which is physiologically consistent.

Finally, diastolic flow is assumed negligible and held constant at zero. Figure 8.4 shows two examples of $Q_{ao,int}$ produced using this method. It also shows the corresponding $P_{ao,mea}$ waveforms to illustrate how the arrival of P_r affects both pressure and flow waveforms.

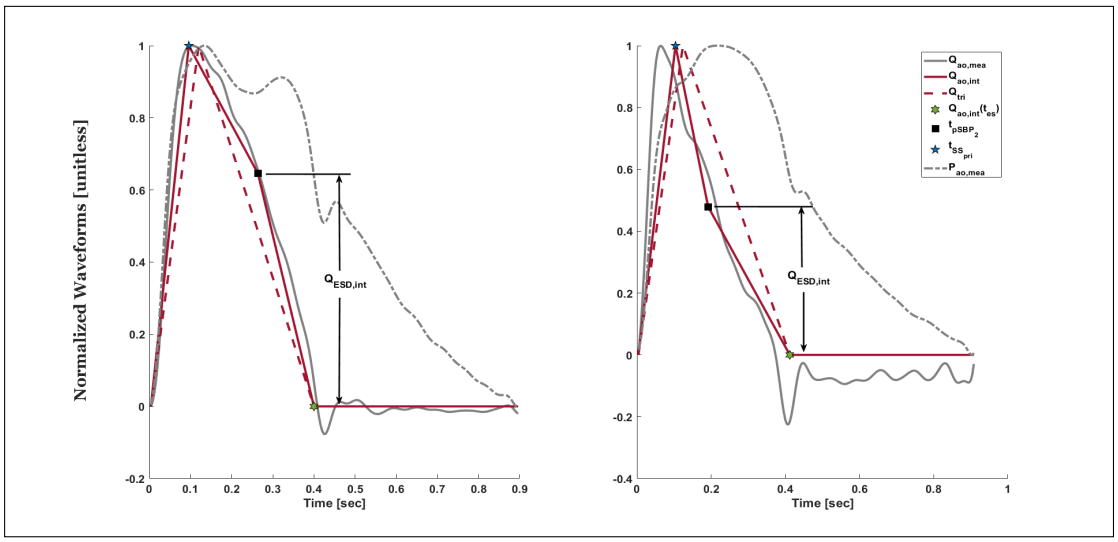

Figure 8.4: Illustration of $Q_{ao,int}$ derived using the proposed quadrangular method in opposing arterial wave dynamic. (left) P_r arrives later in systole producing an negative AI_x and maintaining the convexity of $Q_{ao,mea}$. (right) P_r arrives earlier in systole causing a deceleration of $Q_{ao,mea}$, and an amplification of $P_{ao,mea}$. Triangular approximations (Q_{tri}) are also shown to illustrate their limitations.

8.5 Evaluation of Approach

A series of approximations have been made in this chapter and used to identify the characteristic features of the central pulse to construct $P_{ao,int}$ and $Q_{ao,int}$. To test the validity of these simple approximations in capturing central pressure and flow pulse contour, the RMSE of $P_{ao,int}$ and $Q_{ao,int}$ relative to their measured counterparts is considered.

Measured central systolic pressure is compared to $pSBP_2$, using a linear regression analysis, to investigate the validity of using femoral arterial pressure as opposed to the radial pressure. Two versions of $pSBP_2$ are presented, one showing estimates taken directly from $P_{fe,mea}$, and another showing the same estimates, but with the $P_{fe,mea}$ pulse calibrated to mean central pressure. These two approaches were considered to determine how much the difference in mean pressures contributed to total error, compared to the error associated with equating $pSBP_2$ with central systolic pressure.

Triangular flow approximations, according to [118], were also considered to investigate if the proposed quadrangular flow approximation better captures pulse contour, as intended.

8.6 Experimental Data

Data from Pigs 1-5 and 7-8 were used. Femoral pressure measurements from Pig 6 were corrupted and unsuitable. The required waveforms, $P_{fe,mea}$, $P_{ao,mea}$ and $Q_{ao,mea}$, were taken at 15 sec intervals for the entire duration of each experiment.

8.7 Results

Example $P_{ao,int}$, compared to the $P_{fe,mea}$ pulse used to derive it and the $P_{ao,mea}$ pulse it is estimating is shown in Figures 8.5 and 8.6. The corresponding $Q_{ao,int}$ and $Q_{ao,mea}$ waves are shown in Figures 8.7 and 8.8. Figure 8.9 shows a strong correlation between measured and estimated central SP ($r^2 = 0.82$). When $P_{fe,mea}$ is calibrated to mean $P_{ao,mea}$ the strength of this correlation is improved ($r^2 = 0.91$). The pooled systolic pressure estimate error produced a mean of 6.7 mmHg, across all subjects. This absolute error is reduced to 2.9 mmHg with mean arterial pressure calibration.

Table 8.1 details the RMSE of the pressure and two flow estimates relative to invasive reference measurements. The reported RMSE of $P_{ao,int}$ is derived from the point to point absolute difference with $P_{ao,mea}$. Flow RMSE, both $Q_{ao,int}$ and Q_{tri}, is relative to the normalised measured $Q_{ao,mea}$ pulse. Normalization is performed using the range of the pulse from mean $Q_{ao,mea}$ during diastole and peak flow.

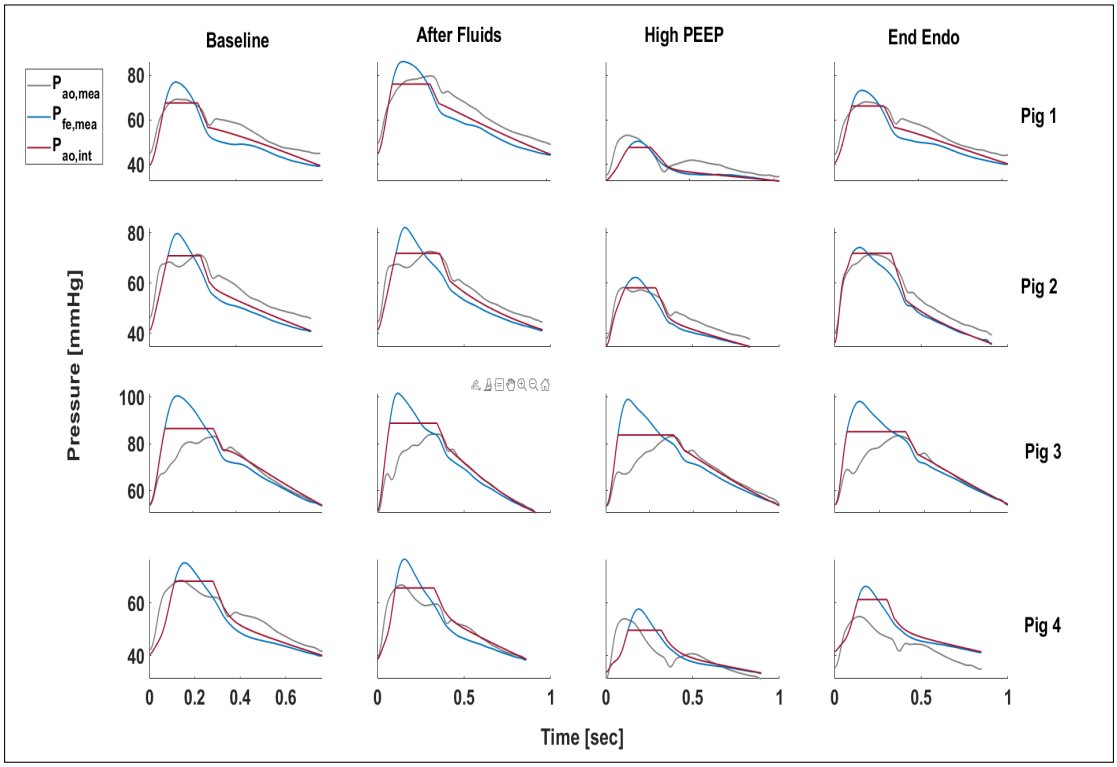

Figure 8.5: Example $P_{ao,int}$ waveforms for Pigs 1, 2, 3 and 4 at different stages of the experiment, compared to the $P_{fe,mea}$ waveform used to construct it and the corresponding $P_{ao,mea}$ waveform.

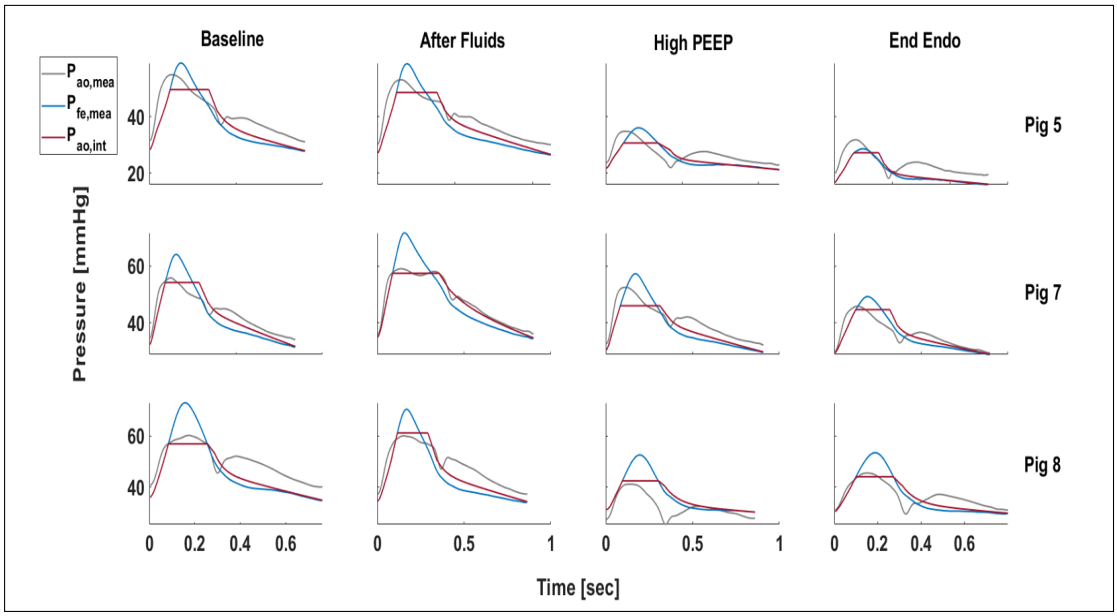

Figure 8.6: Example $P_{ao,int}$ waveforms for Pigs 5, 7 and 8 at different stages of the experiment, compared to the $P_{fe,mea}$ waveform used to construct it and the corresponding $P_{ao,mea}$ waveform.

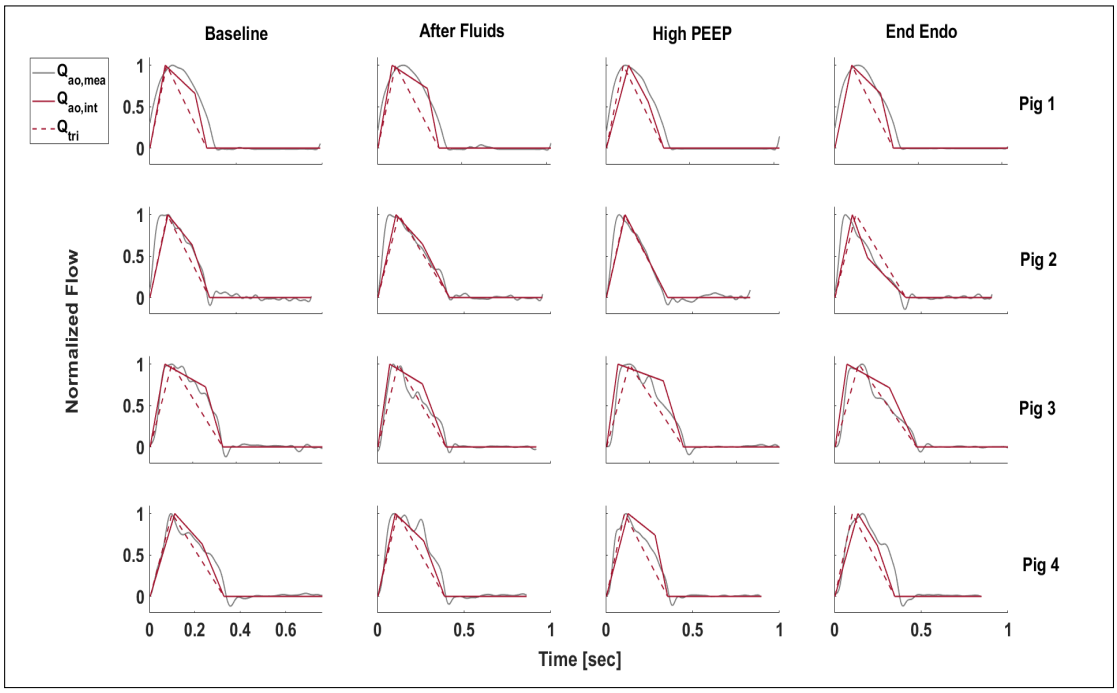

Figure 8.7: Example $Q_{ao,int}$ waveforms for Pigs 1, 2, 3 and 4 at different stages of the experiment, compared to the corresponding $Q_{ao,mea}$ and Q_{tri} waveforms.

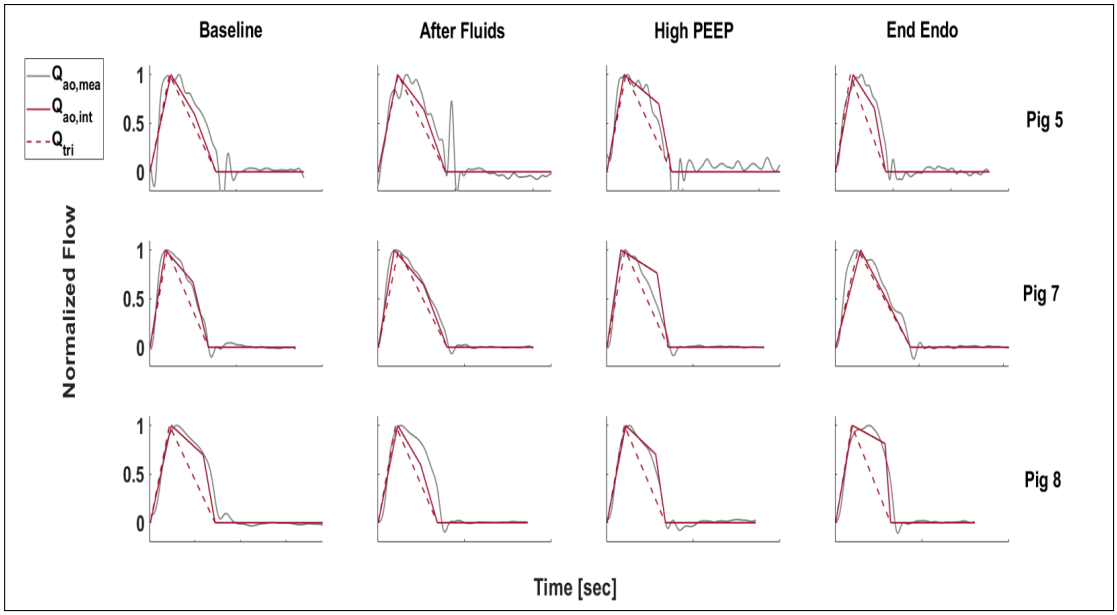

Figure 8.8: Example $Q_{ao,int}$ waveforms for Pigs 5, 7 and 8 at different stages of the experiment, compared to the corresponding $Q_{ao,mea}$ and Q_{tri} waveforms.

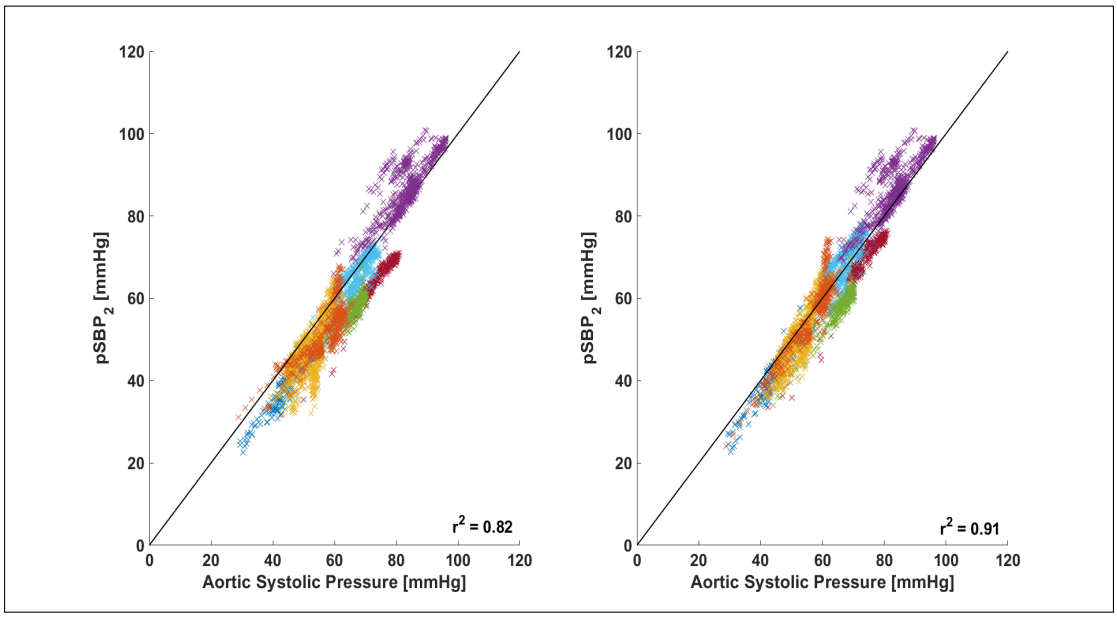

Figure 8.9: (left) Correlation between measured central SP and uncalibrated femoral $pSBP_2$; (right) correlation of $pSBP_2$ calibrated to mean central pressure.

Table 8.1: Mean errors of the central arterial waveform estimates for each pig. The RMSE of $P_{ao,int}$ area assessed by direct comparison with $P_{ao,mea}$ [mmHg]. $Q_{ao,int}$ and Q_{tri} are compared to normalized $Q_{ao,mea}$ [unitless]. $pSBP_2$ and $pSBP_2$ are compared to the maximum pressure of corresponding $P_{ao,mea}$ waveforms [mmHg].

Pig	$P_{ao,int}$	$Q_{ao,int}$	Q_{tri}	$pSBP_2$	$pSBP_{2,cal}$
1	5.9	0.11	0.17	9.4	4.1
2	3.7	0.12	0.13	2.5	2.0
3	6.8	0.10	0.98	2.1	2.1
4	4.9	0.13	0.14	8.9	5.7
5	3.9	0.19	0.21	5.3	2.5
7	3.9	0.09	0.11	4.4	2.1
8	5.6	0.09	0.19	5.7	1.8
Mean	5.0	0.12	0.15	6.7	2.9

8.8 Discussion

This chapter presents a novel method of constructing simple estimations of central pressure ($P_{ao,int}$) and flow ($Q_{ao,int}$) pulses. The motivation for developing these estimates is to provide a robust, accurate way of identifying all model parameters of an arterial TF, derived from a previously validated tube load model [154]. Arterial TF models are powerful tools for estimating clinically unavailable central waveforms from readily available peripheral measurement. However, they are either generalised, and thus unable to properly account for patient variability, or require additional problematic [141] measurements. The proposed $P_{ao,int}$ and $Q_{ao,int}$ pulses are intended to allow all TF model parameters to be identified from a single peripheral pressure measurement. This outcome provides patient specific central pressure at no additional clinical cost. In short, $P_{ao,int}$ and $Q_{ao,int}$ can be considered as full beat objective functions.

Key to this method is the accurate estimation of central systolic pressure using the late systolic peak ($pSBP_2$) of $P_{fe,mea}$. It has been observed $pSBP_2$, identified on the radial pulse, had a strong correlation with central systolic pressure [121–124]. These authors hypothesized the reflected waves arriving from the lower limbs have a similar influence on central systolic pressure and the late systolic portion of the radial pulse. This lower limb reflection is common to both radial and femoral arteries thus, it stands to reason $pSBP_2$ identified from $P_{fe,mea}$ would also correlate with central systolic pressure. Indeed, linear regression analysis, shown in Figure 8.9, confirmed central systolic pressure could be accurately identified from the available $P_{fe,mea}$ measurements. Furthermore, it was found

when mean pressure of $P_{fe,mea}$ were calibrated to mean $P_{ao,mea}$ pressure, the estimates of $pSBP_2$ produced a very strong correlation with central systolic pressure ($r^2 = 0.91$). This result indicates femoral, as well as radial, arterial pressure measurements offer a viable estimate of central systolic pressure.

Previous TF models have had success fitting model outputs to individual wave characteristics, expected to be present in the central pulses, to identify model parameters defining the terminal load, excluding PTT. These features have included fitting to zero diastolic flow [154, 155] or identifying the parameter set producing an exponentially decaying diastolic pressure [152]. However, without the inclusion of PTT, single feature identification becomes difficult, with multiple parameter combinations producing very similar errors for widely varying outputs. The estimates $P_{ao,int}$ and $Q_{ao,int}$ aim to provide additional information during the ensuing parameter ID process, to ensure robust and accurate identification of the TF model. To be successful $P_{ao,int}$ and $Q_{ao,int}$ must themselves be reasonable approximations for measured $P_{ao,mea}$ and $Q_{ao,mea}$.

The first two columns in Table 8.1 detail the RMSE of $P_{ao,int}$ and $Q_{ao,int}$ relative to their measurement counterparts for each pig. Given the simplistic, mostly linear approximations used for $P_{ao,int}$, reasonable accuracy was achieved with a pooled mean RMSE of 5.0 mmHg. The examples illustrated in Figures 8.5 and 8.6 show the limitations of $P_{ao,mea}$.

The constant pressure approximation, used for the majority of systole, is unable to capture the effects of arriving reflected waves arriving in early systole. Some application of waveform decomposition of $P_{fe,mea}$, using $Q_{ao,int}$ and Equations 6.1 and 6.2, may provide an approximation of the forward wave pulse contour, which in turn could be

used to approximate the central pulse during systole. A similar approach has been used in [166] to decompose the radial pulse into its component waves using a linearised approximation of the expected flow pulse.

During diastole, $P_{ao,int}$ is modelled from the passively behaving portion of $P_{fe,mea}$. Therefore, much of the central pressure dynamics during diastole are not accounted for, specifically, the dicrotic notch and any subsequent diastolic peak. If significant diastolic variation is present in $P_{ao,mea}$, as is evident in Pig 8, fitting to the purely exponentially decaying $P_{ao,int}$ may result in elevated errors.

Pigs 3 and 4 show the limitations of assuming a direct relation between $P_{fe,mea}$ and $P_{ao,mea}$ during the early systole. This assumption relies on reflected waves having negligible influence during this time on either pulse, allowing an equivalence to be made between the two waveforms. However, arterial pressure wave mechanics are a complex interaction between innumerable waves all influencing the measured pulse contour and thus, a single peripheral pressure may be inadequate in certain situations.

Central flow approximations are commonly constructed using a triangular approximation during systole. However, assuming flow deceleration to be linear can produce a significant deviation from true flow during systole, depending on the level of interaction between Q_f and Q_r [99, 108]. The proposed method for deriving $Q_{ao,int}$ attempted to identify an additional point relating to the interaction between Q_f and Q_r to better represent flow contour. Indeed, the results shown in Table 8.1 show the $Q_{ao,int}$ was a more accurate representation of $Q_{ao,mea}$ than Q_{tri}. Using $pSBP_2$ to locate the expected

interaction between Q_f and Q_r, and an inverse relation with $P_{ESD,int}$, allowed $Q_{ao,int}$ to account for both convex, concave and linear flow profiles.

These differences are highlighted in Figure 8.4. The left image shows a $P_{ao,mea}$ waveform indicative of a reflected wave arriving later in systole, producing a negative AI_x with a clear secondary systolic peak. This later arrival means the corresponding $Q_{ao,mea}$ waveform maintains the convexity produced by Q_f. This convex characteristic is captured well using $Q_{ao,mea}$. The right image shows the opposite behaviour, with an early arriving reflected wave producing a positive pressure AI_x, and a concave flow deceleration. Again, $Q_{ao,int}$ captures this dynamic well. The Q_{tri} approximation can be seen to under and overestimate flow in the respective scenarios.

8.9 Limitations

Constructing $P_{ao,int}$ and $Q_{ao,int}$ using the proposed method inherently relies on the required features being identifiable on $P_{fe,mea}$. Specifically, the accuracy of $P_{ao,int}$ and $Q_{ao,int}$ appears to be directly linked to how well $pSBP_2$ can be located. This dependence makes sense, as $pSBP_2$ not only defines the systolic pressure of $P_{ao,int}$, and thus SS_{pri} and SS_{sec}, but also the timing of forward and reflected wave interaction in $Q_{ao,int}$. Measurements of $P_{fe,mea}$ where $pSBP_2$ were unidentifiable from the second derivative produced increased errors, most evident in Pigs 1 and 8. Radial pressure measurements may provide a more consistent identification of $pSBP_2$. Higher order derivatives may also be more suitable for identifying $pSBP_2$ [124, 168], compared to the second derivative method presented here.

Changes to normal arterial wave dynamics produced by the progression of disease will also limit the applicability of this method. During severe septic shock, a decoupling can occur between central an peripheral arteries [169, 170], producing atypical pressure measurements. Specifically, $P_{fe,mea}$ systolic pressure can reduce to levels below $P_{ao,mea}$ systolic pressure. This decoupling effect was observed in the pigs surviving after the endotoxin infusion, although not shown here. As a consequence, $pSBP_2$ is guaranteed to be inaccurate in these situations.

Finally, the methods for constructing $P_{ao,int}$ and $Q_{ao,int}$ were developed and tested using central and femoral pressures and central flow taken from 7 porcine experiments. These methods need to be further tested on a larger cohort of data. Ideally, these tests would include measurements taken at different arterial sites to investigate their generalizability.

8.10 Summary

This chapter presents a method for estimating $P_{ao,int}$ and $Q_{ao,int}$ from a $P_{fe,mea}$ measurement. Both $P_{ao,int}$ and $Q_{ao,int}$ are intended to form an objective function used to identify all parameters of an arterial TF model, given in Equations 7.16 and 7.17, including PTT. For this approach to be viable, $P_{ao,int}$ and $Q_{ao,int}$ must provide reasonable estimations of $P_{ao,mea}$ and $Q_{ao,mea}$ in their own right. Relative to $P_{ao,mea}$, $P_{ao,int}$ produced a mean RMSE of 5.0 mmHg in a wide range of hemodynamic states, including circulatory failure due to endotoxin induced septic shock. The corresponding $Q_{ao,int}$ waveforms produced a mean RMSE of 0.12 or 12%, relative to the normalized measured $Q_{ao,mea}$ pulse. The

$Q_{ao,int}$ better captured true pulse contour compared to the commonly used Q_{tri} method, which produced a RMSE of 0.15 or 15%.

Chapter 9

Central Blood Pressure Estimation via Arterial Transfer Function

9.1 Introduction

Chapter 8 introduced a novel method deriving initial central aortic pressure ($P_{ao,int}$) and flow ($Q_{ao,int}$) estimates using linear approximations for various aspects of the pulse contour. These estimates were developed with the intent of providing a robust method of identifying an arterial transfer function (TF) model, derived from the previously validated tube-load (TL) model [148]. This method was developed to allow identification

of all model parameters, including central-peripheral PTT, from a single peripheral pressure measurement, and nothing else.

The proposed single measurement transfer function method of central pressure estimation described here is referred to as the $P_{ao,est}$ method. It implements the $P_{ao,est}$ method to estimate central aortic pressure from femoral pressure measurements taken in 7 of the porcine experiments.

9.2 Method

Using the method presented in Chapter 8, beat-wise $P_{ao,int}$ and $Q_{ao,int}$ are constructed from the input peripheral pressure pulse. The peripheral measurements available were from the femoral artery, $P_{fe,mea}$.

9.2.1 Constructing $P_{ao,int}$ from $P_{fe,mea}$

Constructing $P_{ao,int}$ from $P_{fe,mea}$ begins by analysing the time dependent second derivative to identify any characteristic inflection points during systole, relating to the forward (P_f) travelling and reflected (P_r) waves. If present, these inflection points have been shown to provide a reliable indication of aortic SP, denoted as $pSBP_2$ [121–124]. Next, timings for the primary and secondary systolic shoulders are identified.

In particular, the primary shoulder is located at the intercept of $P_{fe,mea}$ and the estimated systolic pressure. Assuming minimal interference of P_f and P_r waves during early in

systole, $P_{ao,int}$ up to the primary systolic shoulder is equal to $P_{fe,mea}$, for the same time period. The secondary systolic shoulder is identified from $P_{fe,mea}$ using a straight line constructed from $pSBP_2$ to the end systolic inflection point, defined as the inflection point immediately prior to end-systole. The shoulder is defined as the point on $P_{fe,mea}$ furtherest from the line, as shown in Figure 8.2. Primary and secondary shoulders both have a magnitude equal $pSBP_2$, producing the flat top of $P_{ao,int}$. The systolic portion of $P_{ao,int}$ is completed by assuming the drop in pressure from $pSBP_2$ to end-systole on $P_{fe,mea}$, changes as a function of PP from central to peripheral sites.

Finally, the diastolic component of $P_{ao,int}$ is constructed by fitting an exponential model to $P_{fe,mea}$ during diastole. Care should be taken to only fit to the passively behaving portion of the curve to avoid effects of higher frequency reflected waves. Once fitted, this curve is rotated about the diastolic foot, so the initial point has a magnitude equal to $P_{ao,int}(t_{es})$.

9.2.2 CONSTRUCTING $Q_{ao,int}$ FROM $P_{fe,mea}$

Obtaining absolute values of central flow from a single peripheral measurement is not practical [102, 118, 167]. Therefore, $Q_{ao,int}$ is constructed between 0 and 1 and used to approximate flow contour only. The primary systolic shoulder's of $Q_{ao,int}$ and $P_{ao,int}$ occur simultaneously [99] thus, the early systolic component of $Q_{ao,int}$ begins at the origin and reaches a maximum of 1 at the primary shoulder [118].

$Q_{ao,int}$ includes an additional feature prior to end-systole to better approximate true

flow pulse contour. The destructive interference of reflected flow waves decelerates flow velocity [99, 108], which, depending on when interference occurs, determines the convexity of the resulting flow pulse. As the reflected pressure and flow waves are inversely related, an inverse relation with $P_{ESD,int}$ is used to identify the relative value of flow at a time corresponding to $pSBP_2$. Specifically, drop in flow to end-systole, previously shown in Figure 8.3, equals $1 - \frac{P_{ESD,int}}{PP_{ao,int}}$. The remaining decelerating portion of the pulse is constructed by linearly interpolating between peak flow and flow at the time corresponding to $pSBP_2$. $Q_{ao,int}$ is assumed to have negligible flow during diastole and remains at zero from end-systole to the end of the beat.

9.2.3 Parameter Identification

$P_{ao,int}$ and $Q_{ao,int}$ are used to identify the TF model parameters $(\alpha_i, \beta_i, ptt_i)$ in Equations 7.16 and 7.17. Model parameters are identified by minimizing the weighted combination of the RMSE produced between TF model output pressure and flow, relative to $P_{ao,int}$ and $Q_{ao,int}$, respectively. As $Q_{ao,int}$ is only representative of flow contour, not actual flow velocity, TF output flows were normalized to between 0 and 1 prior to comparison. The relative contributions of each RMSE are weighted to reflect the fact only flow contour is able for comparison. In contrast, $P_{ao,int}$ provides estimates of the magnitude of $P_{ao,mea}$. Therefore, a 2 to 1 pressure to flow weighting is applied to the respective RMSE outputs.

As pressure and flow are of significantly different magnitude, each experiment begins by independently optimizing for pressure and flow contour, giving the maximum and minimum errors for each pulse. These ranges are used to normalize their respective errors

during subsequent estimation [82, 83]. Weightings are applied to the normalized errors. Parameter identification is conducted using a genetic algorithm based on [171, 172], implemented in MATLAB 2020a. Finally, limits for potential ptt were set between 5ms and double the measured PTT. α and β are in the range $0 < \alpha \leq \beta \leq 1$.

9.2.4 Alternate Central Pressure Estimation Methods

Three additional central BP estimates were also considered in this chapter to investigate the efficacy of the $P_{ao,est}$ method. Two additional TF methods, using the same governing Equations 7.16 and 7.17, were used to investigate how well the $P_{ao,est}$ performed compared to the same model implemented with progressively more input information. This approach thus quantifies the impact of each assumption used to minimize the input measurement data required .

The first alternate TF method is identical to the $P_{ao,est}$ method, except for the inclusion of measured PTT as a model input, removing the need for identification. This method, termed the $P_{ao,PTT}$ method, is used to assess the impact of estimating PTT on the accuracy of the $P_{ao,est}$ method. It provides a comparator to what would be possible if this measurement were available from clinical measurements. Measured PTT was obtained from the corresponding feet of simultaneously recorded $P_{ao,mea}$ and $P_{fe,mea}$ pulses.

The second alternate TF method simply identifies the set of model parameters which minimize the RMSE of model output pressure with respect to reference $P_{ao,mea}$. This

approach is called the $P_{ao,RMSE}$ method and provides the theoretical best central pressure estimate achievable given the governing equations and input pressures. The $P_{ao,RMSE}$ method provides the asymptotic best estimate, which can be used to assess the relative accuracy of the $P_{ao,est}$. It should be noted, although the $P_{ao,RMSE}$ method gives the best pressure estimate, no attention is paid to the corresponding flow output.

Invasive femoral pressure measurements, $P_{fe,mea}$, are also considered. Peripheral pressure measurements are widely available in clinical settings and commonly used as direct surrogates for central pressure. Therefore, any proposed method must, at a minimum, provide a significant improvement on the accuracy of these measurements. This latter comparison provides a contrast between the $P_{ao,est}$ method and the likely best clinical estimate.

9.2.5 Analysis

Results for each method of estimating aortic pressure were assessed in terms of systolic pressure (SP), pulse pressure (PP) and RMSE. SP and PP are clinically relevant parameters commonly used in decision making regarding treatment and RMSE details the ability of the estimates to capture reference pulse contour.

To the authors knowledge there is no specific threshold of determining the accuracy of TF derived central pressure from invasive measurements. Therefore, threshold accuracy in this study was set at 5±8mmHg, taken from the Association for the Advancement of Medical Instrumentation [173], used for assessing non-invasive measurements of central

pressure. While some issue exists with how this threshold is reported [174], specifically regarding the use of the 'zero-error' approach, the more intuitive absolute errors are reported in this work.

Standardized Bland-Altman plots are used to show the pooled mean bias and limits of agreement (LoA) for each method relative to invasive aortic pressure measurements. Linear regression plots are also shown to illustrate the strength of the correlation between SP and PP derived using each method and reference values.

9.2.6 Experimental Data

Data from 7 porcine experiments were used in this work, Pigs 1 to 5 and 7 to 8. Pig 6 had corrupted femoral pressure recordings making it unusable. Pig 3 presented an apparent issue with either the $P_{ao,mea}$ or $P_{fe,mea}$ measurements, as $P_{fe,mea}$ consistently had a diastolic pressure greater than the $P_{ao,mea}$ systolic pressure. For this reason, the diastolic pressure of $P_{fe,mea}$ was equated to the diastolic pressure of the corresponding $P_{ao,mea}$ pulse.

All pigs included at least one 500ml fluid bolus and a PEEP driven RM prior to an endotoxin infusion. Pigs 2, 3, and 7 received further additional fluids post endotoxin. The sampled $P_{fe,mea}$ measurements were taken every 15sec for the duration of the experiments.

9.3 Results

A total of 3810 heartbeats were sampled to assess the accuracy of the $P_{ao,est}$ method. As mentioned, reference PTT is taken from the simultaneously recorded diastolic feet of measured $P_{ao,mea}$ and $P_{fe,mea}$ waveforms. Reference values from the measured waveforms are given in Table 9.1. Results are parsed into two stages of each experiment, pre- and post- endotoxin infusion.

Table 9.1: Reference values of clinical metrics from invasive aortic pressure measurements.

	Pulse Pressure		Systolic Pressure		Pulse Transit Time	
Pig	Pre	Post	Pre	Post	Pre	Post
1	27.6(2.9)	29.3(5.9)	73.4(6.3)	71.2(7.8)	114.2(8.0)	116.0(1.4)
2	26.2(2.3)	28.6(5.6)	70.3(7.0)	65.1(3.9)	69.4(2.8)	67.4(7.0)
3	32.0(3.1)	32.5(3.2)	83.5(3.7)	83.1(7.5)	93.7(2.1)	91.2(4.9)
4	26.8(2.5)	26.5(6.1)	65.1(5.3)	65.3(7.8)	110.7(4.9)	116.6(4.2)
5	21.8(2.4)	21.8(5.1)	49.7(5.5)	46.5(7.6)	139.5(10.1)	145.1(12.6)
7	23.2(1.2)	21.4(5.5)	57.8(2.1)	51.0(7.1)	99.0(2.0)	100.5(7.3)
8	21.0(2.0)	24.3(6.5)	58.7(5.2)	56.8(7.8)	113.0(5.8)	119.0(3.8)

9.3.1 Systolic Pressure

Correlation analysis between the estimated SP for each method relative to $P_{ao,mea}$ for all Pigs is shown in Figure 9.3. Reference 1-to-1 lines (solid) are shown in each figure to show a perfect match with reference $P_{ao,mea}$ systolic pressure. Additional lines at ±5 (dash-dot) and ±10mmHg (dashed) are shown to highlight error distribution.

The $P_{ao,est}$ method achieved an accuracy of 81.1 and 77.1% of SP estimates within ±5

mmHg of reference SP for pre- and post- endotoxin periods, respectively. Estimated SP accuracy was 92.2 and 79.3%, 80.5 and 76.4%, 22.3 and 51.4% for the $P_{ao,RMSE}$, $P_{ao,PTT}$ and $P_{fe,mea}$ methods, respectively. All TF methods produced strong correlations with measured $P_{ao,mea}$ SP producing a RMSE of 4.3, 3.6, and 4.5 mmHg for the $P_{ao,est}$, $P_{ao,RMSE}$ and $P_{ao,PTT}$, respectively. $P_{fe,mea}$ systolic pressure produced a significantly reduced correlation with reference central pressure, RMSE = 8.4 mmHg.

Standardized Bland-Altman plots for SP error according to [173] are shown in Figure 9.2. The pooled mean bias and limits of agreement for each method were 0.9 (-7.4, 9.2), 0.5 (-6.6, 7.5), -0.4 (-8.3, 9.2) and -6.3 (-17.2, 4.7) mmHg for the $P_{ao,est}$, $TF_{Min,RMSE}$, $TF_{Mea,PTT}$ and $P_{fe,mea}$, respectively. Reference lines at ±5 and ±10 mmHg error are also displayed. Table 9.2 present the mean absolute SP errors and standard deviation for each pig, during both stages of the experiment.

Table 9.2: Absolute systolic pressure error of method relative to invasive aortic pressure measurements, given as mean(std) [mmHg].

	$P_{ao,est}$		$P_{ao,RMSE}$		$P_{ao,PTT}$		$P_{fe,mea}$	
Pig	Pre	Post	Pre	Post	Pre	Post	Pre	Post
1	5.0(1.6)	5.7(0.9)	3.2(1.4)	3.0(0.8)	5.1(1.9)	6.1(1.3)	6.4(1.9)	3.1(1.5)
2	1.2(1.7)	2.2(2.0)	2.7(1.3)	1.6(1.0)	1.1(0.9)	1.5(1.0)	8.7(1.8)	4.0(2.6)
3	5.1(2.0)	5.2(2.0)	4.8(1.5)	5.3(1.1)	6.1(1.8)	6.3(1.6)	14.5(2.8)	9.9(2.3)
4	3.3(2.6)	1.9(2.6)	1.8(1.5)	4.7(1.4)	3.6(1.8)	2.1(1.8)	7.4(1.7)	3.0(1.4)
5	3.9(1.3)	3.1(4.1)	2.3(1.1)	2.6(4.1)	2.9(1.1)	2.6(4.3)	3.2(2.2)	4.8(3.6)
7	1.5(1.8)	4.0(1.1)	1.4(1.3)	3.1(0.9)	1.8(1.6)	3.8(1.1)	8.5(2.8)	7.2(1.5)
8	2.3(1.8)	2.2(1.1)	1.9(1.3)	1.4(0.9)	2.3(1.6)	2.3(1.1)	8.2(2.8)	7.2(1.5)
Mean	3.0(2.1)	3.1(2.9)	2.3(1.4)	2.6(2.6)	3.2(2.3)	3.0(2.9)	7.8(3.5)	6.0(4.1)

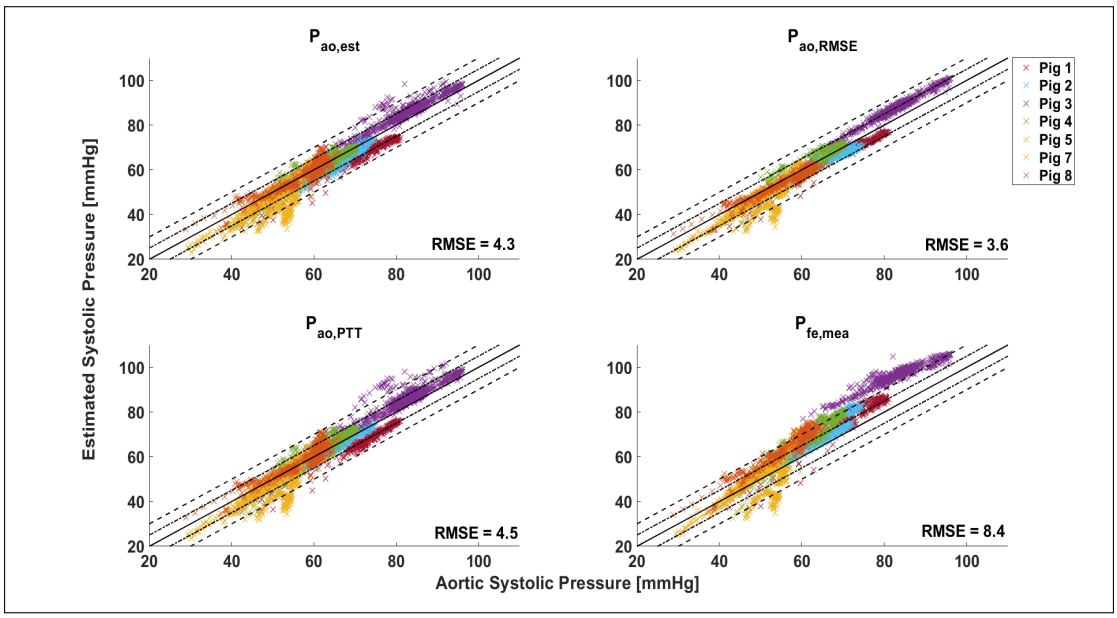

Figure 9.1: Correlation analysis of systolic pressure estimates relative to invasive aortic pressure measurements for each method. The RMSE of each method is indicated on their respective plots, detailing the variation from the 1:1 reference line indicative of a perfect match with $P_{ao,mea}$ systolic pressure.

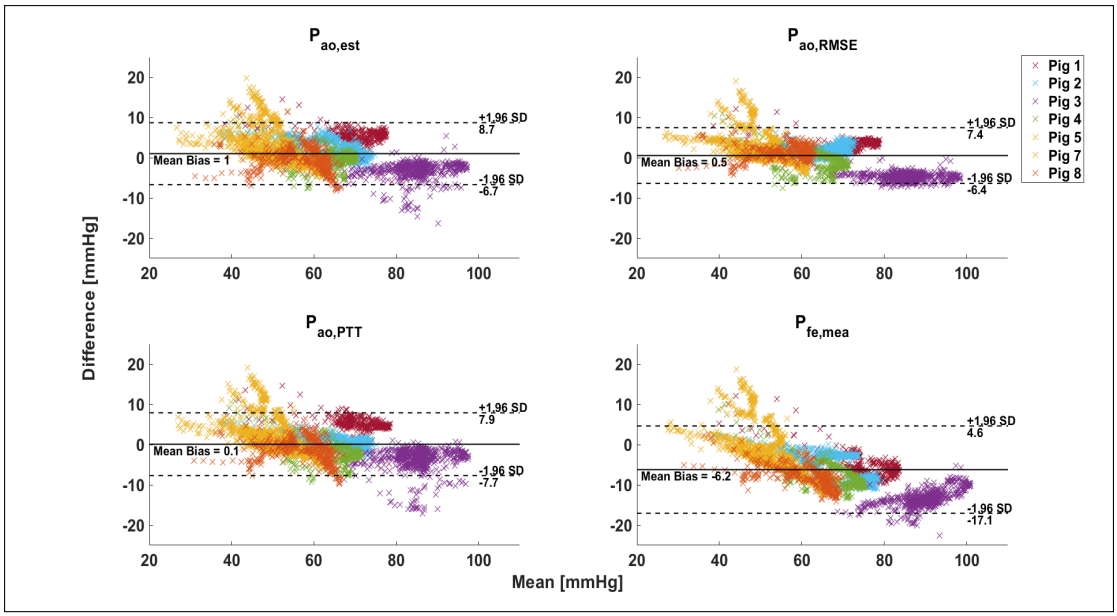

Figure 9.2: Standardized Bland-Altman plots for each method. Mean bias between reference and estimated central systolic pressure are shown as well as limits of agreement (± 1.96 standard deviations).

9.3.2 Pulse Pressure

Correlation analysis of PP derived from each method relative to $P_{ao,mea}$ for all subjects are shown in Figure 9.3. $P_{ao,est}$ method PP fell within ±5mmHg at rates of 83.0 and 81.3% for pre- and post endotoxin periods, respectively. PP accuracy was 97.6 and 95.7%, 79.0 and 78.3%, 9.5 and 28.8% for the $P_{ao,RMSE}$, $P_{ao,PTT}$ and $P_{fe,mea}$ methods, respectively. These results show the biggest advantage between $P_{ao,est}$ and $P_{fe,mea}$, with the latter consistently producing double figure errors and a weak correlation to reference pulse pressure. Pulse pressure is an often used clinical metric in the treatment decision making process, and these results highlight the errors introduced when using peripheral measurements as direct substitutes for central pressures.

The Bland-Altman plots in Figure 9.4, show a mean bias and LoA of -1.0 (-9.3, 7.3), -1.1 (-8.2, 6.0), -1.5 (-10.3, 7.2), -9.1 (-20.1, 1.8) mmHg for the $P_{ao,est}$, $P_{ao,RMSE}$, $P_{ao,PTT}$ and $P_{fe,mea}$ methods, respectively. Table 9.3 details absolute PP errors pre- and post-endotoxin.

Table 9.3: Pulse pressure error of each estimate relative to invasive aortic pressure measurements, given as mean(std) [mmHg].

	$P_{ao,est}$		$P_{ao,RMSE}$		$P_{ao,PTT}$		$P_{fe,mea}$	
Pig	Pre	Post	Pre	Post	Pre	Post	Pre	Post
1	1.7(2.0)	3.4(1.0)	1.5(1.5)	0.5(0.5)	1.6(2.0)	3.7(1.5)	11.4(2.9)	6.7(1.8)
2	3.8(1.4)	3.0(1.5)	0.7(0.6)	1.1(0.8)	3.8(0.8)	3.0(1.2)	13.0(1.7)	7.2(2.7)
3	5.1(2.1)	5.2(1.7)	3.1(1.5)	3.5(0.8)	6.1(1.9)	6.2(1.2)	16.0(2.8)	14.5(3.3)
4	4.0(1.8)	3.4(1.1)	1.5(1.1)	1.2(0.8)	4.2(1.5)	3.2(1.0)	8.2(2.7)	6.1(2.8)
5	1.5(1.3)	1.4(2.4)	1.5(1.0)	1.4(2.1)	1.5(1.3)	1.7(2.7)	6.0(1.9)	5.7(2.7)
7	2.8(2.8)	2.7(1.1)	2.5(1.3)	2.0(1.0)	3.2(2.6)	2.5(1.3)	11.1(4.5)	4.7(3.3)
8	4.0(2.8)	1.5(1.1)	3.1(1.3)	1.9(1.0)	4.3(2.6)	1.7(1.3)	13.8(4.5)	9.3(3.3)
Mean	3.2(2.4)	3.2(2.2)	2.1(1.5)	1.9(1.6)	3.5(2.8)	3.4(2.6)	11.3(4.3)	7.9(4.4)

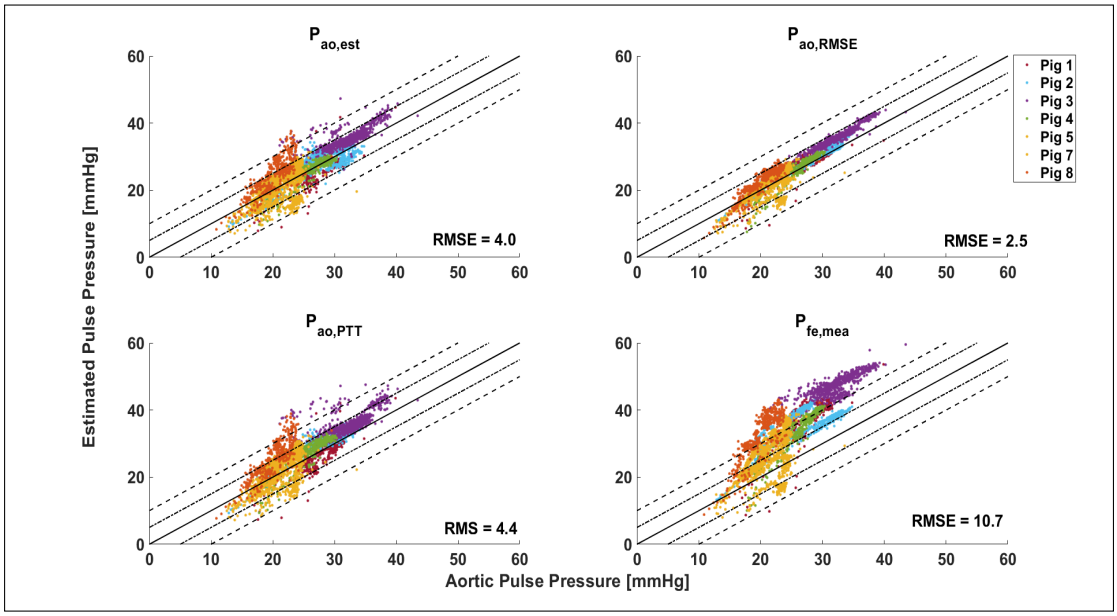

Figure 9.3: Correlation analysis of pulse pressure estimates relative to invasive aortic pressure measurements for each method. The RMSE of each method is indicated on their respective plots, detailing the variation from the 1:1 reference line indicative of a perfect match with $P_{ao,mea}$ pulse pressure.

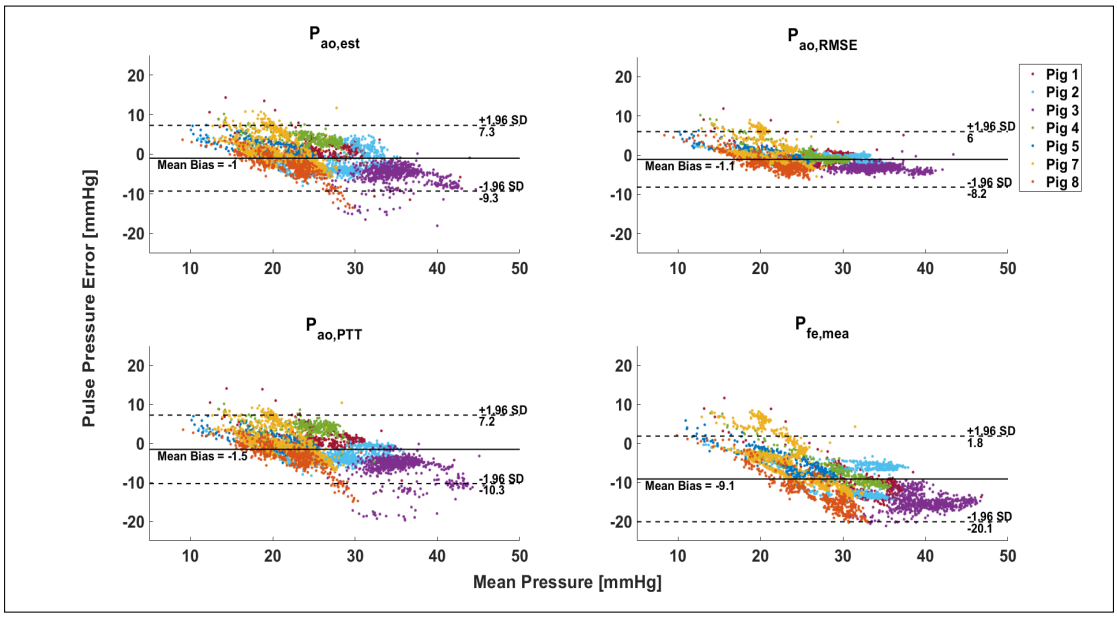

Figure 9.4: Standardized Bland-Altman plots for each method. Mean bias between reference and estimated central pulse pressure are shown as well as limits of agreement ($\pm$ 1.96 standard deviations).

9.3.3 Root-mean-squared-error

Table 9.4 details the point-by-point RMSE of each method relative to invasive aortic pressure measurements, a clinically unavailable gold-standard. These results indicate the ability of each method in capturing total pulse contour information. The key result to highlight is the relative accuracy of the $P_{ao,est}$ method compared to the $P_{ao,RMSE}$, which, by definition, is the best RMSE achievable given the governing TF model equations.

Table 9.4: Root-mean-squared-error of each central pressure estimate relative to invasive aortic pressure measurements, given as mean(std) [mmHg]. Results are partitioned into pre- and post-endotoxin sections of the experiment.

	$P_{ao,est}$		$P_{ao,RMSE}$		$P_{ao,PTT}$		$P_{fe,mea}$	
Pig	Pre	Post	Pre	Post	Pre	Post	Pre	Post
1	4.9(0.6)	4.7(0.5)	4.6(0.4)	4.3(0.5)	4.8(0.6)	4.7(0.5)	6.7(0.6)	5.2(0.5)
2	4.8(0.8)	3.8(0.7)	4.4(0.7)	3.4(0.4)	5.0(0.7)	3.9(0.6)	6.8(0.6)	4.5(0.7)
3	5.9(0.9)	6.1(0.9)	2.4(0.7)	2.3(0.9)	6.1(0.8)	6.3(0.9)	10.1(0.4)	9.6(0.5)
4	4.6(0.9)	5.1(0.9)	4.0(0.7)	4.6(0.9)	4.6(0.8)	5.0(0.9)	5.4(0.4)	5.6(0.5)
5	4.8(0.4)	4.5(0.2)	4.3(0.3)	4.1(0.2)	4.5(0.4)	4.3(0.2)	4.9(0.5)	4.7(0.3)
7	3.8(0.6)	4.3(2.4)	3.2(0.6)	3.9(2.5)	3.6(0.6)	4.3(2.5)	5.1(0.4)	4.5(2.3)
8	6.2(1.2)	4.6(0.7)	5.6(1.4)	3.8(1.0)	6.0(1.3)	4.4(0.8)	7.9(1.6)	5.7(0.9)
Mean	5.0(0.8)	4.7(0.8)	4.1(0.7)	3.8(0.8)	5.0(0.7)	4.7(0.8)	6.7(0.7)	5.7(0.8)

9.3.4 Pulse Transit Time Error

Finally, Table 9.5 shows $P_{ao,est}$ derived PTT alongside the mean absolute PTT error relative to the measured PTT. Also shown is the PTT error produced from the $P_{ao,RMSE}$ method. The $P_{ao,est}$ method can be seen to produce significantly better estimates of PTT than the $P_{ao,RMSE}$ method, showing simply optimizing for the measured $P_{ao,mea}$ waveforms does not necessarily produce the correct model parameters. This is likely

because only the pressure waveform was optimised for and the associated flow waveform ignored. Additionally, the minimization of model RMSE relative to $P_{ao,mea}$, included the diastolic portion of the pulse which may have limited the accuracy of $P_{ao,RMSE}$. If the reference wave had significant diastolic fluctuations, as was present in pigs 4, 5, and 8, the identified PTT would be increased to produce a diastolic peak in the resulting $P_{ao,RMSE}$ wave. While this may reduce the RMSE, it will likely result in the optimal parameters, specifically PTT, being misidentified. These results further validate the utility of the $P_{ao,est}$ method, as including $Q_{ao,int}$ prevents very large PTT values being identified as it would result in a non-physiologic flow output. Figures 9.5 and 9.6 show the time series comparison between model identified and measured PTT for the $P_{ao,est}$ and $P_{ao,RMSE}$ methods.

Table 9.5: Model identified pulse transit time and the absolute error relative to the measured aortic-femoral PTT. Also shown is the PTT error using the $P_{ao,RMSE}$ method relative to direct measurements

	$P_{ao,est}$ PTT		$P_{ao,est}$ PTT Error		$P_{ao,RMSE}$ PTT Error	
Pig	Pre	Post	Pre	Post	Pre	Post
1	119.3(10.7)	124.2(3.9)	9.8(10.4)	8.5(2.6)	9.4(13.9)	6.9(5.2)
2	91.0(9.6)	82.1(15.8)	15.2(8.8)	16.2(14.2)	23.6(10.8)	35.7(16.5)
3	85.6(12.6)	87.7(12.4)	11.6(12.1)	14.6(10.5)	4.3(2.2)	8.0(3.9)
4	109.9(10.1)	110.5(8.6)	8.8(7.8)	9.8(8.6)	24.1(17.1)	36.3(24.7)
5	108.6(13.4)	116.1(21.3)	29.6(10.2)	29.2(24.4)	41.0(11.3)	34.7(12.5)
7	87.0(12.2)	104.8(26.9)	12.0(8.5)	21.1(20.2)	34.5(11.9)	53.5(28.4)
8	100.1(11.3)	107.5(7.3)	11.5(11.9)	11.5(9.2)	27.9(9.5)	44.1(8.3)
Mean	100.2(11.4)	103.1(13.8)	14.1(10.0)	15.8(12.8)	23.5(10.9)	31.3(14.2)

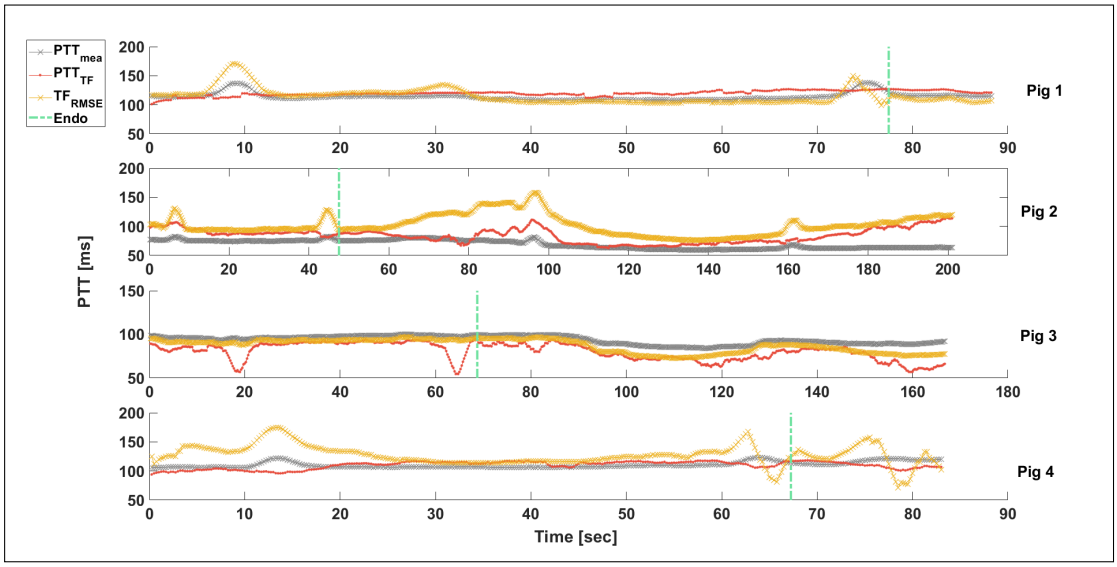

Figure 9.5: Results of pulse transit time estimation using the $P_{ao,est}$ and $P_{ao,RMSE}$ methods, compared to direct aortic-femoral PTT, for Pigs 1-4.

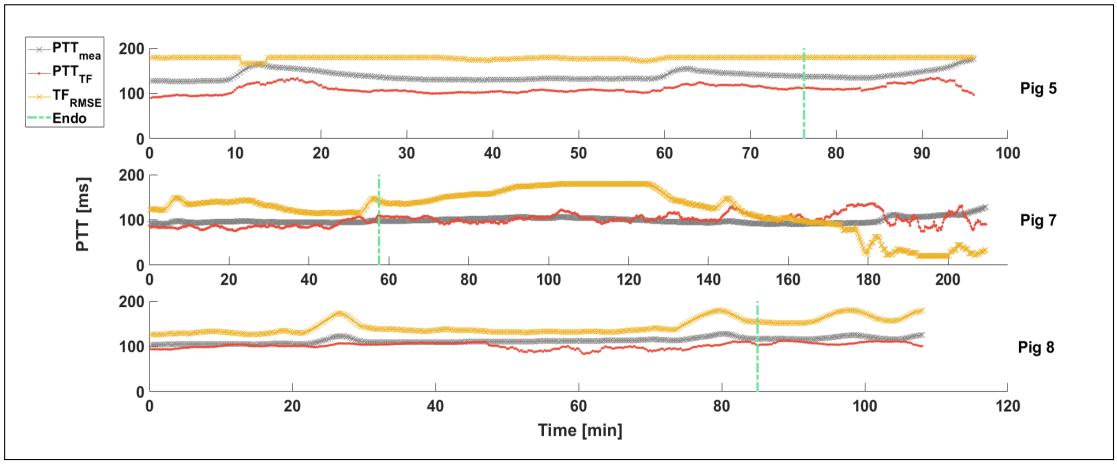

Figure 9.6: Results of pulse transit time estimation using the $P_{ao,est}$ and $P_{ao,RMSE}$ methods, compared to direct aortic-femoral PTT, for Pigs 5, 7 and 8.

9.3.5 Example $P_{ao,est}$ pressure waveforms

Example $P_{ao,est}$ generated pressure estimates, along with the corresponding $P_{ao,mea}$ and $P_{fe,mea}$ pulses, at four stages throughout each experiment are shown in Figures 9.7 and 9.8. The labeled sections correspond the start of the experiment, immediately concluding the first 500ml fluid bolus, at maximum PEEP during the RM after the fluid bolus, and at the end of the endotoxin infusion.

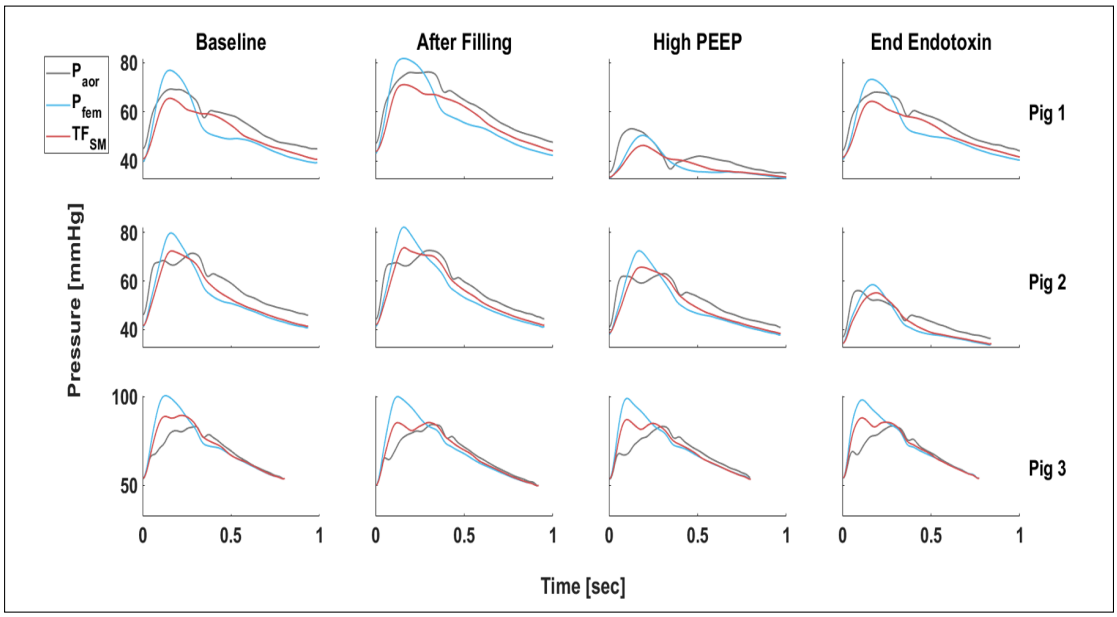

Figure 9.7: Example central pressure estimates using the $P_{ao,est}$ method (pink) compared with aortic (grey) and femoral (blue) pressures over a range of clinical conditions.

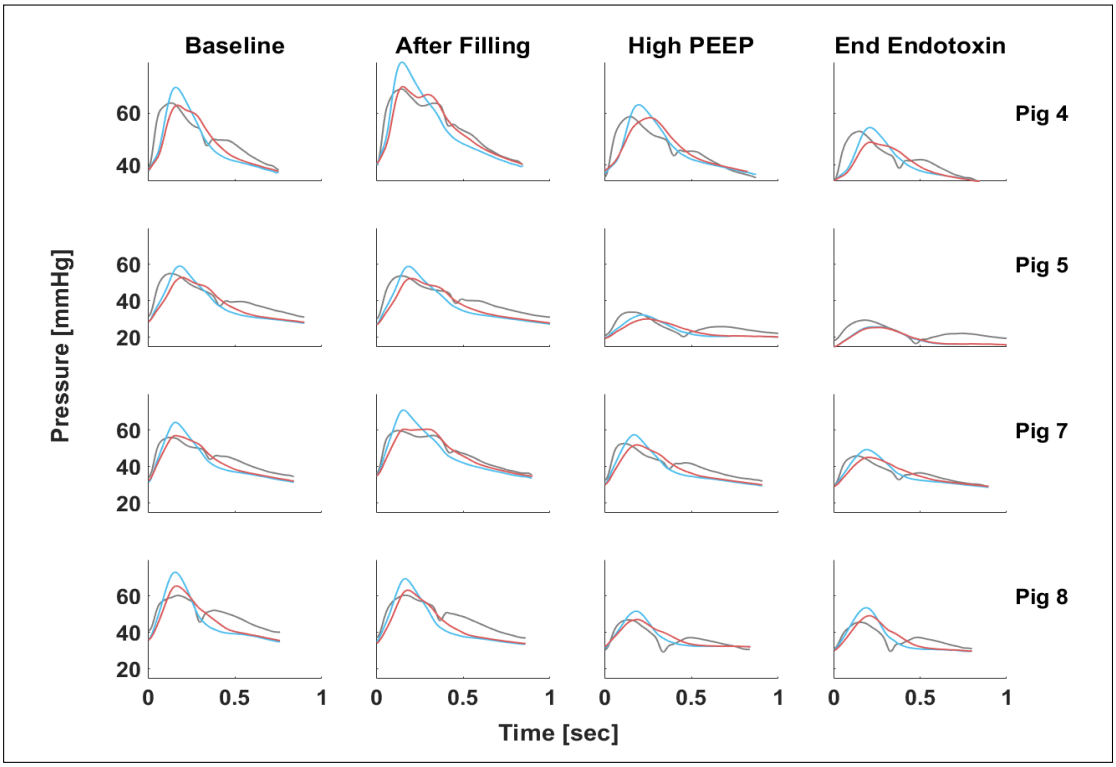

Figure 9.8: Example central pressure estimates using the $P_{ao,est}$ method (pink) compared with aortic (grey) and femoral (blue) pressures over a range of clinical conditions.

9.4 Discussion

9.4.1 $P_{ao,est}$ Accuracy

Overall, the proposed $P_{ao,est}$ method produced accurate estimates of central pressure in a diverse range of clinical states. The pooled mean errors across all pigs were $\leq$5 mmHg for both SP and PP, meeting threshold accuracy. Only pigs 1 and 3 failed to meet the threshold during any stage of the experiment. Furthermore, only Pig 3 exceeded threshold prior to endotoxin infusion. These results show the $P_{ao,est}$ method can produce accurate estimates of central pressure solely from a peripheral pressure input.

$P_{fe,mea}$ errors relative to $P_{ao,mea}$ were included in this study due to the prevalent use of peripheral BP measurements often being used as direct surrogates for central BP in clinical environments [129]. Obviously, any proposed method must significantly improve on peripheral measurements to be a viable alternative. Pre-endotoxin, the $P_{ao,est}$ saw a reduction in error of 4.1-73.9% relative to $P_{fe,mea}$. The high errors using $P_{fe,mea}$ are unsurprising as pressure amplification at peripheral arteries cause significant augmentation of the pulse, primarily seen as an increase in systolic pressure [99, 100]. Clinically, these results highlight the necessity for better central pressure estimates than can be offered by peripheral pressure surrogates, if clinical decisions are to be made based on target pressures [41, 142, 144, 145]. Key to these results is the $P_{ao,est}$ method can be implemented with no additional clinical measurements and is thus as minimally invasive as currently possible in ICU care.

The mean RMSE of the $P_{ao,est}$ method also met the desired threshold accuracy, showing the methods ability to capture total pulse contour. However, while overall mean RMSE met threshold accuracy Pigs 3 and 6 did exceed it. Pig 3 displayed diminished contractility, as assessed using the maximum gradient of $P_{ao,mea}$, and was reported to have a left ventricle catheter pressed against the heart wall for periods of the experiment, which likely influenced these errors.

Three additional factors were identified as contributing to the RMSE. First, the initial estimates of $P_{ao,int}$ and $Q_{ao,int}$ present a limit to the achievable RMSE. By design, these estimates are used to identify the model parameters by minimising the RMSE with

model outputs, and thus, a perfect fit would result in the $P_{ao,est}$ and $Q_{ao,est}$ being equal to $P_{ao,int}$ and $Q_{ao,int}$, not $P_{ao,mea}$ and $Q_{ao,mea}$.

Second, the diastolic component of $P_{ao,int}$ was modelled to be a pure exponentially decaying pressure, without and dicrotic notch. With diastole comprising of a significant, often the majority, portion of the pulse, errors in this region will greatly contribute to overall RMSE. The $P_{ao,int}$ method is unable to account for any diastolic peaks which produced the elevated RMSE associated with pig 8. However, obtaining perfect $P_{ao,mea}$ contour from a single peripheral measurement is exceedingly unlikely, and the robustness of the $P_{ao,est}$ method during circulatory failure validates this approach.

Third, the differences between central and peripheral mean pressure, while small in the larger arteries, significantly contribute to the RMSE. Aside from Pig 3, no calibration of pressures were used, so any deviation in MAP will directly translate into the resulting RMSE. Indeed, when mean pressures are equated, the pooled RMSE for all subjects over the entirety of each experiment is reduced to 3.1mmHg.

9.4.2 Comparison with $P_{ao,RMSE}$ Method

Using a single peripheral pressure measurement to estimate central pressure is inherently limited. Although it is necessary to compare model estimates with reference $P_{ao,mea}$, this alone does not fully assess the performance of the $P_{ao,est}$ method. For this purpose, the $P_{ao,RMSE}$ method was used to produce the theoretical best pressure estimates achievable using Equation 7.16 by minimizing the RMSE relative to $P_{ao,mea}$.

Differences between the RMSE of the $P_{ao,est}$ and $P_{ao,RMSE}$ methods, shown in Table 9.4, ranged from 0.3 to 3.8 mmHg. The upper limits of these errors were produced by Pig 3, and, if excluded, the maximum relative error falls to 0.8 mmHg. These results suggest the $P_{ao,est}$ method is a viable way of identifying TF model parameters.

Similarly, SP and PP errors in both stages of the experiment differed from the $P_{ao,RMSE}$ method by only 0.7-1.2 mmHg. The PTT errors for both $P_{ao,est}$ and $P_{ao,RMSE}$ methods, detailed in Table 9.5, indicate simply optimising for $P_{ao,mea}$, using the TF model, may not be sufficient for accurate identification of model parameters, due to the limitations on the information contained in the peripheral pulse. The poor performance of the $P_{ao,RMSE}$ method in identifying PTT is likely due to the method attempting to capture the diastolic fluctuations in $P_{ao,mea}$. While the model equations assume a single forward travelling and reflected wave, in reality the pulse is made up of a complex series of waves from all areas of the body, information not available from single peripheral pressure measurement. Therefore, for the $P_{ao,RMSE}$ method to account for any diastolic fluctuations present in $P_{ao,mea}$, the identified PTT will be increased.

The similarity of errors produced by these two methods show a significant amount of the $P_{ao,est}$ method error, relative to $P_{ao,mea}$, is produced by the inherit limitations of the model equations and the limited availability of information contained in single peripheral pressure measurements. Furthermore, because the $P_{ao,RMSE}$ method only considered pressure, some of the corresponding flow outputs produced had contours vastly different from those produced by the aortic flow probe measurements. If flow

were also considered, $P_{ao,RMSE}$ error would increase, reducing the gap in error with $P_{ao,est}$.

9.4.3 Comparison with $P_{ao,PTT}$ Method

The $P_{ao,PTT}$ method used measured PTT as an additional input, but otherwise, was identical to the $P_{ao,est}$ method. Largely, the errors produced by the two methods are very similar. For SP and PP the $P_{ao,est}$ method performs better with the reverse true for RMSE. The PTT measurement provides information about forward and reflected wave interaction, which directly influences pulse contour so improved RMSE using the $P_{ao,PTT}$ method is not surprising. However, despite the use of PTT drastically reducing the set of potential parameter combinations, the $P_{ao,est}$ method could be considered equally, if not more accurate.

One reason using PTT did not significantly improve results is likely due to a mismatch between the 'central' locations described by the TF model and the measurement site. The central location for a TF model describes a hypothetical origin point from which wave propagate throughout the body, illustrated in Figure 7.1. In contrast, the aortic pressure measurements are taken at distinct, real locations in the aorta. This inconsistency in central locations may mean measured PTT is not optimal for the TF model, resulting in some of the observed error. This observation was also made by Hahn *et. al.* [153] when estimating PTT using two pressure waveforms.

Table 9.5 details model identified PTT and error relative to measured aortic-femoral

PTT. Figures 9.5 and 9.6 compares measured and model PTT for all pigs over the entire length of the experiment, with the vertical dashed lined indicating when endotoxin was administered. Generally, these results were better than was expected considering only singular peripheral pressure measurements were used. Increasing PEEP during a RM, observable in Figures 9.5 and 9.6 as the times when measured PTT suddenly peaks, most noticeable in Pig 1, resulted in model PTT becoming inaccurate. During a RM, peripheral SP was often observed falling below central SP indicating a temporary disruption to normal pulse wave propagation, testing the underlying assumptions used to construct $P_{ao,int}$ and $Q_{ao,int}$. Specifically this means and identified $pSBP_2$ will be wrong. Pig 5 did not see this crossover in SP and can be seen to track PTT well during each RM.

9.4.4 LIMITATIONS

Besides the well documented limitations associated with estimating central pressure using a single channel TL model [147, 148], several limitations exist using the $P_{ao,est}$ method.

The $P_{ao,est}$ method relies on key features of the peripheral pulse being identifiable. Specifically, inaccurate identification of $pSBP_2$ significantly reduces the $P_{ao,est}$ method accuracy, as this dictates the majority of systole for both $P_{ao,int}$ and $Q_{ao,int}$. In particular, $pSBP_2$ was most difficult to identify during periods of increased PEEP and when circulatory failure became evident. High PEEP causes a reduction in ventricular preload [175–177], leading to an observed drop in $P_{fe,mea}$ SP, falling below $P_{ao,mea}$ SP, and thus,

any estimate of $pSBP_2$ will be off by at least this difference. However, these effects are only transitory.

Circulatory collapse due to the progressive effects of sepsis results in a decoupling of normal central-peripheral pulse wave propagation, also reducing peripheral SP. This decoupling has been observed in similar porcine experiments where endotoxin induced septic shock was present [91, 178]. These authors hypothesised the different muscular composition of central and peripheral arteries may produce different reactions to inflammatory vasoactive substances produced in response to the infection.

Systemic inflammation has been observed to inhibit endothelial generation of *nitric oxide (NO)* [91, 92, 178], which is partially responsible for the regulation of arterial tone. Reduced NO availability may lead to stiffening of the central arteries. The cellular generation of NO is thought to occur in smooth muscle, which is more abundant in peripheral, rather than central, arteries. Inflammatory cytokines stimulate the production of NO synthase, raising levels of NO, resulting in vasodilation of peripheral blood vessels. These opposing changes in vascular tone compromise normal wave propagation, testing the underlying model assumptions. In addition to changes in arterial tone, sepsis also increases vascular permeability, producing similar effects as the loss in arterial tone.

One effect of sepsis induced decoupling is a reduction in peripheral SP. Figure 9.9 shows the SP and PP for Pig 7 where, at approximately 150 min, $P_{fe,mea}$ SP and PP diverge from $P_{ao,mea}$, eventually falling below $P_{ao,mea}$. This indicates normal arterial pressure propagation mechanisms have been compromised, likely due to degradation of the blood vessels caused by the response to infection. The decoupling has a clear effect on estimates

produced by the $P_{ao,est}$ method. However, since it is late in septic shock, this error has more limited potential clinical impact, as the goal would be to intervene before decoupling occurs, if possible.

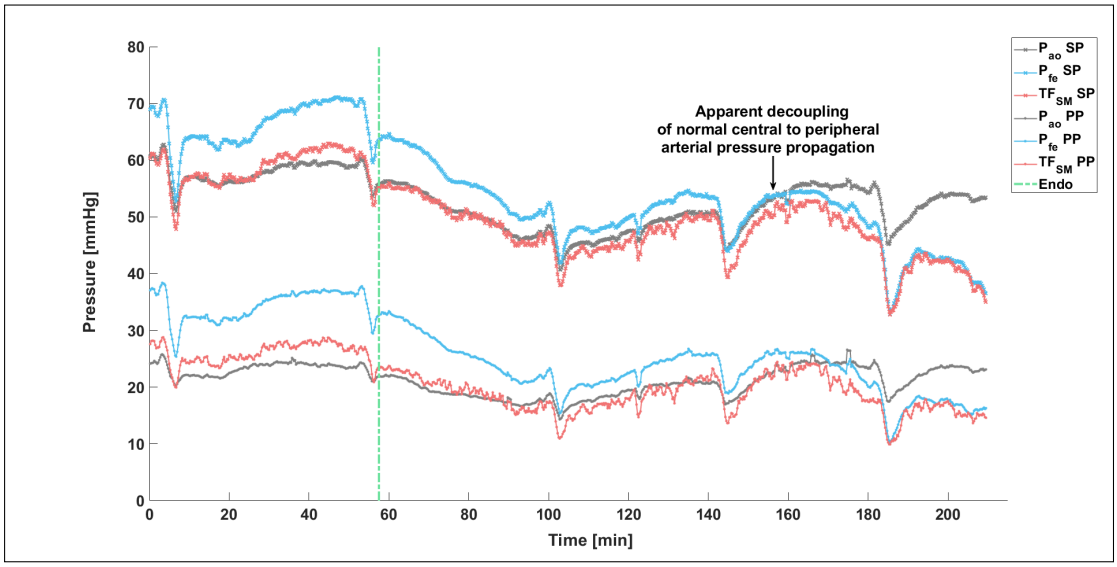

Figure 9.9: Time series comparison of systolic and pulse pressure derived from invasive aortic and femoral measurements and central BP derived using the $P_{ao,est}$ method for Pig 7.

Finally, the study again consists of only six porcine subjects, sample size and the applicability to the human cardiovascular system must be considered. Despite the small sample size, these experiments allowed the model to be tested in a range of patient conditions and provided direct, invasive measurements for validation. Such invasive measurements are seldom or never available from typical ICU data.

9.5 Summary

This chapter presented a method of estimating $P_{ao,mea}$ from a single, simultaneously recorded $P_{fe,mea}$ pulse, with no requirement of an additional PTT measurement. Pulse wave analysis is performed on $P_{fe,mea}$ to identify key features pertaining to the component forward and reflected waves. This information is used to construct initial estimates for central pressure and flow, $P_{ao,int}$ and $Q_{ao,int}$, respectively, which in turn is used to identify all parameters of a validated single channel TL model of the arterial system.

Accuracy of $P_{ao,est}$ estimates was assessed in terms of SP, PP and RMSE relative to reference $P_{ao,mea}$, and resulted in mean errors of 3.4, 3.2 and 5.9 mmHg, respectively. The $P_{ao,est}$ method was also compared to the best possible pressure estimates achievable using the governing equations. Relative to these outputs errors were a relatively small 1.8, 2.1 and 1.3 mmHg.

Finally, no significant advantage was observed when using the measured PTT as an additional model input. PTT identified using the $P_{ao,est}$ method provided a reasonable estimate for measured PTT. Mean PTT error over all subjects was 15.8 ms.

Chapter 10

Tube Load Model Derived Stroke Volume

10.1 Introduction

Stroke volume is a critical component to many CVS models, including the TCM, and a necessity when assessing the fluid responsiveness of a patient (ΔCO). Current gold standard measurements via indicator dilution techniques provide accurate measurements of CO, but are cumbersome techniques only able to be performed intermittently [132, 133] . Several pulse contour methods are commercially available, which use an initial SV measurement, performed using an indicator dilution method or echocardiograph to calibrate a proprietary algorithm used to continuously estimate CO from pulse contour

analysis of peripheral arterial pressure [61, 132–134] . However, they lack accuracy and are black box models [132].

Recently Smith *et. al.* investigated using an arterial TF model to estimate SV in a series of porcine experiments, subjected to a range of clinical procedures [58]. The TF model was used to derive the component of flow entering the peripheral tube which, after an initial calibration with measured SV to scale the pulse and account for the characteristic impedance, was used for continuous SV estimation. Unlike pulse contour methods, TL models are capable of capturing wave reflection dynamics which directly influence the contour of the arterial flow pulse, and thus, SV. The authors found SV could be reasonably tracked during hemodynamic instability and within acceptable accuracy. This chapter investigates how well the proposed single measurement transfer function method (TF_{SM}), presented in the previous chapter, can estimate and track changes in invasively measured stroke volume (SV_{mea}).

10.2 Method

The equations and method for identifying model parameters is identical to the TF_{SM} method used in Chapter 9. Specific attention was paid to the corresponding model flow waveform, labelled q_{ci} in Equation 7.17. This flow represents flow through the tube, scaled by the characteristic impedance of the tube (Z_{ci}). However, q_{ci} is only the component of total flow entering the i^{th} tube being considered, with the sum of flows through all i tubes equal to central aortic flow. Therefore, an additional scaling factor needs to be included to capture information about total flow. Modifying Equation 7.17

to include this scaling factor yields:

$$q_{ci}[n] \cdot Z_{cal} = \alpha_i q_{ci}[n-1] + \beta_i p_{pi}[n + ptt_i] - \alpha i p_{pi}[n + ptt_i - 1]$$

$$- (1 - \beta_i)\, p_{pi}[n - ptt_i] \tag{10.1}$$

Where Z_{cal} is a calibration factor combining Z_{ci} with some scaling factor (C), such that $Z_{cal} = Z_{ci} \cdot C$. The left side of Equation 10.1 can be combined into a single variable $Q_{ao,est}$, such that $Q_{ao,est} = q_{ci} \cdot Z_{cal}$, representing the estimated aortic flow wave. Calculating Z_{cal} can be achieved using a small set of calibration measurements and enforcing the equality:

$$SV_{mea} = \frac{1}{Z_{cal}} \int_{t_0}^{t_{es}} Q_{ao,est}(\tau) d\tau \tag{10.2}$$

Where SV_{mea} is the direct measurement for stroke volume, t_0 is the start of the beat and t_{es} occurs at end-systole. Z_{cal} is obtained for each beat of an initial 10 beat section and the average value used to calculate beat wise SV estimates (SV_{est}) from $Q_{ao,est}$. Fundamental to this method is the assumption $Q_{ao,est}$ and $Q_{ao,mea}$ will have similar contours.

10.2.1 Experimental Data

Data from 7 of the porcine experiments were used in this chapter, with pig 6 having issues with the femoral pressure catheter making it unsuitable for use in the TF_{SM} method.

Pig 1 has an issue with the aortic flow probe measurements, so Z_{cal} was derived using measurements of the left ventricle volume obtained from the admittance catheter.

10.3 Analysis

Simultaneous measurements of beat wise aortic flow, ventricular volume (for Pig 1 only) and femoral pressure were sampled every 15sec, for the entire duration of each experiment. Tabulated results are partitioned into 2 or 3 stages depending on the duration of the experiment. Pigs 1, 4, 5 and 8 have pre- and during endotoxin stages, but have severe reactions and the experiments shortly concludes. Pigs 2, 3 and 7 survive beyond the endotoxin infusion, and results for these stages are labelled post- endotoxin.

Results for SV_{est} are reported for each stage of the experiment. The post endotoxin stages for the surviving pigs have two variations of SV_{est}, one using the initial calibration taken during baseline operating conditions at the very start of the experiments, and another where SV_{est} is recalibrated after the conclusion of the endotoxin infusion. This recalibration is performed to investigate SV_{est} accuracy during progressive circulatory failure, assuming Z_{cal} has changed due to the endotoxin induced changes in the vasculature [27, 29, 96].

Errors for SV_{est} are presented as a percentage error relative to the corresponding SV_{mea} value. Standardized Bland-Altman plots are used to show the mean bias and limits of agreement (LoA) of SV_{est} relative to SV_{mea}. Desirable limits of accuracy are taken from Critchley *et. al.* [59, 135] as ±30%. Plots are presented to show both the accuracy for

each pig, and for each stage of the experiments. The Bland-Altman plots show two sets of mean bias and LoA. One set details a subset of results including the pre- and during endotoxin stages, and the other set includes the post endotoxin stages.

The ability of SV_{est} to track changes in SV_{mea} is assessed using polar plot analysis. Changes in measured and estimated SV are found for each data set, giving ΔSV_{mea} and ΔSV_{est}. Each ΔSV_{mea}, ΔSV_{est} pair is converted to polar coordinates with the polar angle representing the deviation from the identity line i.e. where changes in SV_{est} perfectly match changes in SV_{mea}. The radius of each coordinate is the mean change of each ΔSV_{mea}, ΔSV_{est} pair [59, 135].

Two processes were applied to the data to make the plots more intuitive. Coordinates are rotated by 45 deg so the identity line coincides with the polar axis. The absolute changes are used, as directional changes are not important when assessing trends. Thus, all data points of the polar plot are grouped into the positive direction. Trending results are reported in terms of mean polar angle and angular limits of agreement (95% confidence interval). An exclusion zone of $\leq 10\%$ was used when calculating mean polar angle and limits of agreement [59, 135]. Finally, the percentage errors for each pig in each stage of the experiment are given in tabular form.

Table 10.1: Reference values of SV_{mea} taken from continuous aortic flow probe measurements (or left ventricle admittance catheter for Pig 1) detailing the min, max and mean values for each pig (ml).

Pig	Min	Max	Mean
1	19.5	43.3	33.0
2	6.5	34.4	20.1
3	52.2	90.3	74.2
4	28.4	46.9	39.9
5	9.4	37.5	25.1
7	12.5	31.6	21.0
8	5.6	15.8	11.7

10.4 Results

Table 10.1 provides reference min, max and mean reference values for SV_{mea}. Table 10.2 gives the mean and standard deviation of SV_{est} error, relative to the corresponding SV_{mea} value, during each stage if the experiment.

Figure 10.1 shows the Bland-Altman plots comparing SV_{est} and SV_{mea}. The top row of plots show the accuracy of SV_{est} for the entire length of the experiments using only a single baseline calibration for Z_{cal}, taken at the start of each experiment. The mean bias and LoA for all data using a single calibration event for Z_{cal} was -27.25 (-115.21 60.72)%. When considering estimates up to the conclusion of the endotoxin infusion the mean bias and LoA was -6.09(-43.49 31.32)%.

The bottom row of plots uses a secondary calibration after the conclusion of the endotoxin infusion for the surviving pigs (2,3,7). With the additional calibration event, the mean bias and LoA became -14.19 (-55.27, 26.89)%. Plots on the left side show the

results of SV_{est} for each pig, and on the right side, plots present results for each stage of the experiments.

Figure 10.2 details the ability of SV_{est} to track absolute changes in SV_{mea}. The two plots show the same data broken down by pig, left, and experimental stage, right. The mean polar angle was 1.0° and the polar limits of agreement were (+29.9, -27.8)°. Both plots show data from a single calibration event of 10 beats at the start of each experiment.

Recalibration post- endotoxin infusion produces negligible change in the tracking ability of the method. The red dashed circle at the centre of each polar plot indicates an exclusion zone at ±10%. Data inside this zone did not contribute to the calculation of mean and LoA of the polar plots, as they are very small changes which can largely be attributed to noise.

Figures 10.3 and 10.4 show examples of the model output flow, $Q_{ao,est}$, compared to the corresponding aortic flow waveform, $Q_{ao,mea}$. Example flow wave estimates were taken from a hemodynamically diverse range of clinical scenarios, highlighting the ability of the model to capture changes in patient condition. Outputs for pig 1 were omitted due to left ventricle volume being used in place of the corrupted aortic flow measurements

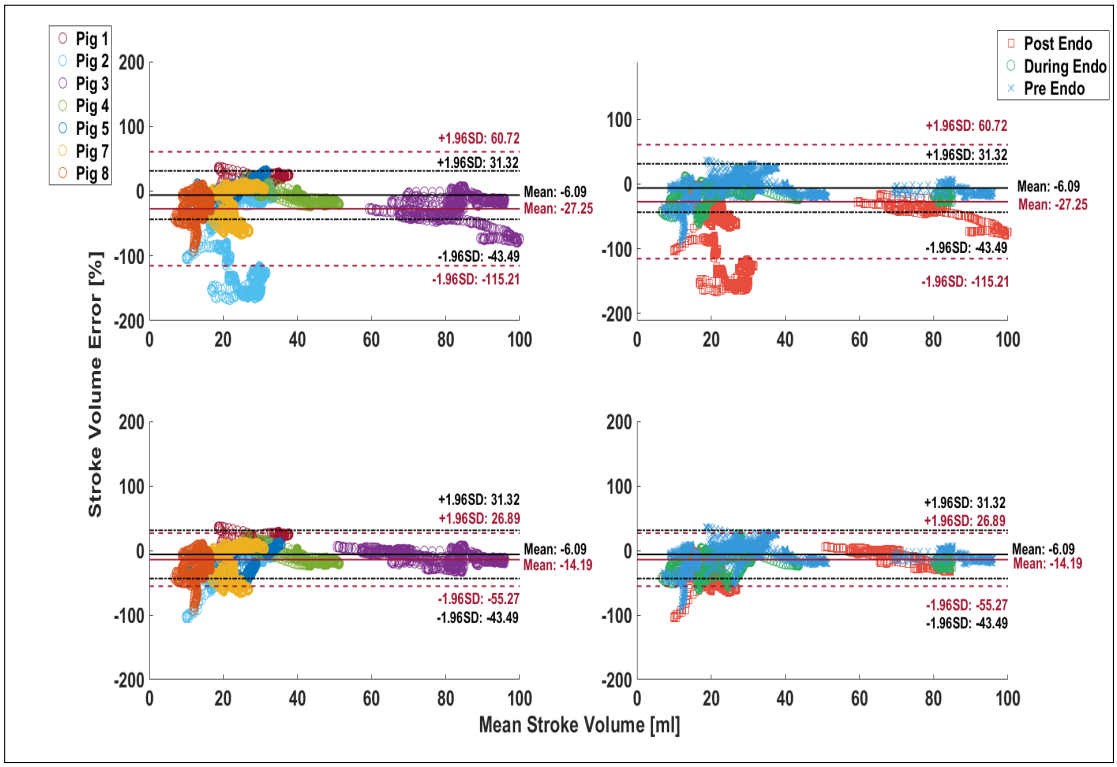

Figure 10.1: Bland-Altman plots showing the mean bias and limits of agreements of stroke volume estimated from the arterial TL model using (left) a single calibration, and (right) calibration prior to each clinical procedure.

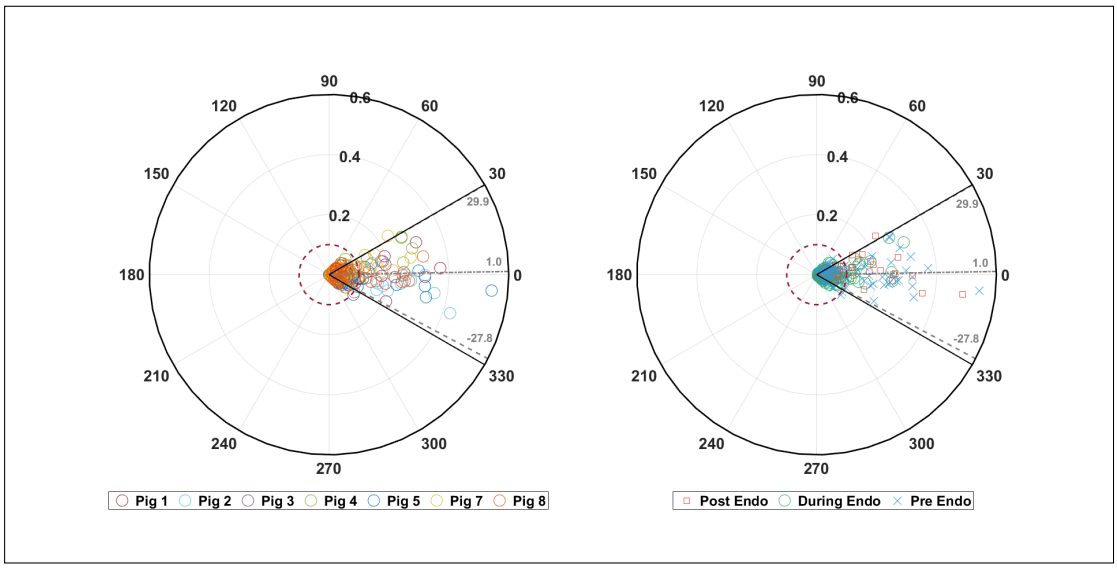

Figure 10.2: Polar plot analysis showing the ability of SV_{est} obtained using the TF_{SM} method and a single calibration at tracking SV_{mea}. (left) results of SV_{est} tracking for each pig. (right) results of SV_{est} tracking for each experimental stage including, pre (blue), during (green), and post (red) endotoxin infusion.

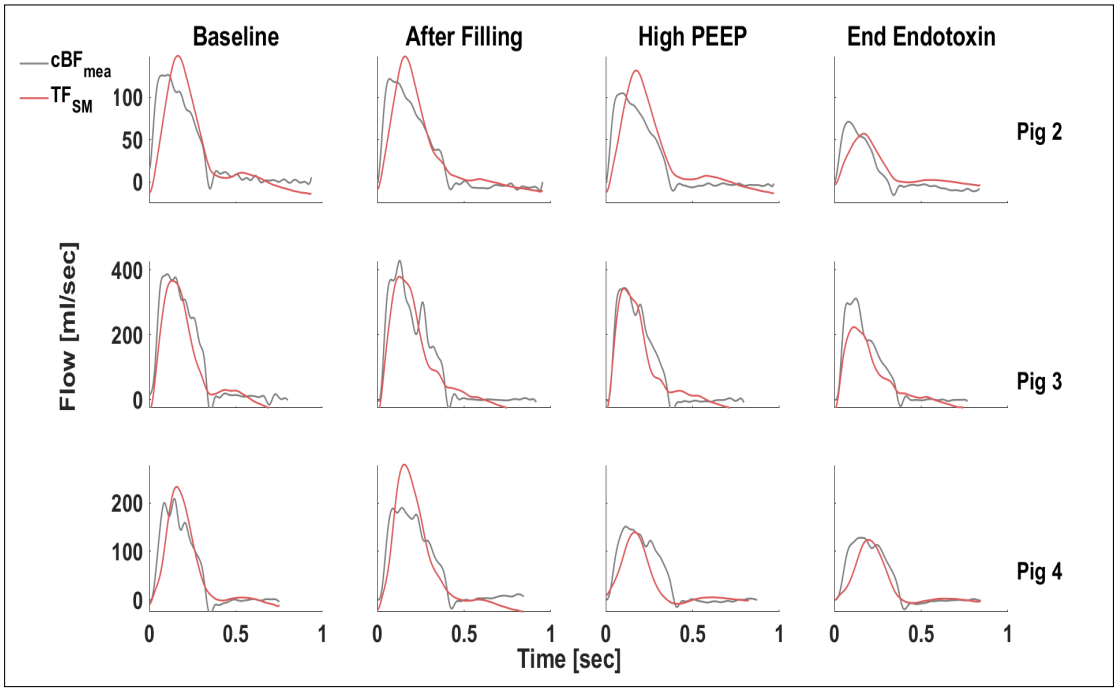

Figure 10.3: Example central flow estimates obtained using the TF_{SM} method and calibrated using Z_{cal} (pink), compared with aortic flow probe waveforms (grey), over a range of clinical conditions, for Pigs 2 to 4.

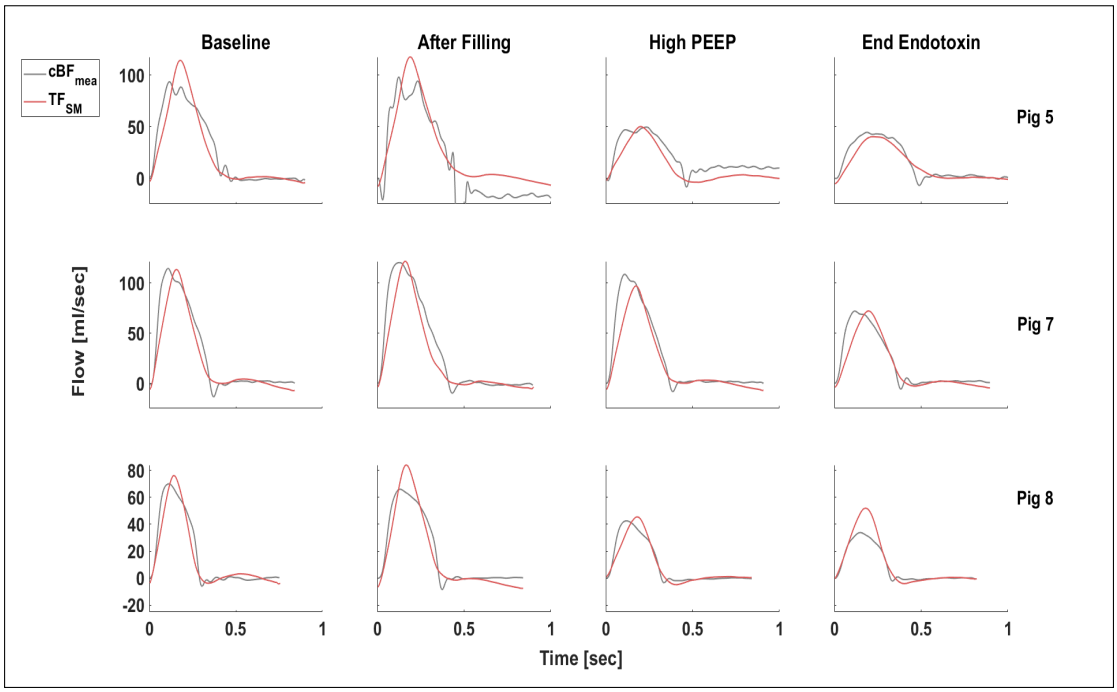

Figure 10.4: Example central flow estimates obtained using the TF_{SM} method and calibrated using Z_{cal} (pink), compared with aortic flow probe waveforms (grey), over a range of clinical conditions, for Pigs 5, 7 and 8.

Table 10.2: Relative error of SV_{est} compared to the corresponding values of SV_{mea}, given as a percentage (%) of SV_{mea}. The column labelled post (recalibrated) indicates results of SV_{est} during the post endotoxin stage after recalibration of Z_{cal}. Pigs 1, 4, 5 and 8 experienced severe reactions to endotoxin infusion and did not include a post- endotoxin experimental stage.

Pig	Pre	During	Post	Post (Recalibrated)
1	16.9(7.5)	18.1(3.0)	-	-
2	6.2(4.6)	27.7(14.8)	132.1(25.6)	29.5(17.3)
3	11.1(5.6)	18.9(5.0)	46.2(17.5)	11.2(11.1)
4	13.3(5.7)	11.4(7.7)	-	-
5	15.6(9.8)	36.7(4.7)	-	-
7	6.0(3.0)	2.2(1.5)	32.7(21.7)	31.8(21.3)
8	26.5(20.8)	24.6(15.2)	-	-
Mean	13.7(8.1)	19.9(7.4)	70.3(21.6)	24.2(16.6)

10.5 Discussion

Using the TF_{SM} method to estimate SV produced LoA outside the target threshold of ±30%. During the combined pre- and during endotoxin stages of the experiments, the mean bias and LoA were -6.09 (-43.49 31.32). These values are more consistent with the levels of accuracy stated by Peyton *et. al.* in their review of CO monitoring devices, who suggested acceptable LoA of ±45% to be a *'more reasonable expectation of achievable precision in clinical practice'* [136].

A major factor contributing to the elevated percentage errors pre- and during endotoxin infusion, are the low SV levels observed in some pigs. Specifically, pigs 2, 5 and 8 all present single digit measurements of SV at some stage in their respective experiments, detailed in Table 10.1. For Pigs 5 and 8, these measurements occur prior to the end of the endotoxin infusion, and may be a factor in their severe response to the infection and inability to survive the endotoxin infusion for a meaningful period of time. Direct

omparison of SV_{est} to SV_{mea} at these low levels, results in even small absolute errors having a large influence of the relative error, contributing significantly to the elevated LoA.

The majority of SV_{est} error from using only a single initial calibration was produced in the post endotoxin experimental stages. Specifically, pig 2 sees a significantly increased SV_{est} error during this stage of the experiment, as indicated in Figure 10.1. In response to the endotoxin infusion, mean SV_{mea} for pig 2 falls by approximately 50%, producing the single digit SV_{mea} values presented in Table 10.1. Again, these low absolute values will contribute to the elevated percentage error.

Compounding to the effect of low absolute values of SV_{mea}, is the inevitable error drift occurring with prolonged application of a model without re-calibration. Given the severity of changes to the CVS occurring from the interventions performed, specifically the endotoxin infusion [30, 56, 91, 92, 178], it is reasonable to expect structural changes occur to the vasculature, altering the characteristic impedance of the tube and the wave propagation dynamics used to for the model equations [99]. Indeed, when recalibration is performed after the endotoxin infusion, a significant amount of error is eliminated, shown in the comparison of upper and lower Bland-Altman plots in Figure 10.1. Hence, errors are acceptable across major clinically relevant, but infrequent, changes in vasculature and hemodynamics, and are much smaller if recalibration is possible after these changes are recognised, clinically.

Examining the flow estimates produced by the TF_{SM} method post endotoxin infusion reveals a limitation of the method. Figure 10.5 shows estimates for the surviving pigs,

taken approximately one hour after the end of the endotoxin infusion, and the effects of shock on the circulatory system have had time to set in. All pigs present a flow profile with a linearly descending late systolic component, indicating the early arrival of Q_r [99, 108]. This effect produces a central pressure pulse with an amplified secondary shoulder and a more rounded profile during systole [100], as shown in Figure 8.4. Sepsis is known to cause systemic inflammation [26, 27, 29, 30, 96, 179], arterial stiffening and reducing PTT, resulting in these effects [120, 165, 168]. The reduction in accuracy of $Q_{ao,est}$ estimates in this situation is likely due to the constant systolic pressure approximation used to construct $P_{ao,int}$. If $pSBP_2$ underestimates central SP, the flat profile of $P_{ao,int}$ will prevent the model from identifying the low values of PTT, as this would produce a greater degree of P_f and P_r interaction, which in turn, would produce a narrower, pointed systolic peak. This effect is amplified for Pig 7 as peripheral and central pressures have become decoupled at this stage and peripheral SP is lower than central SP.

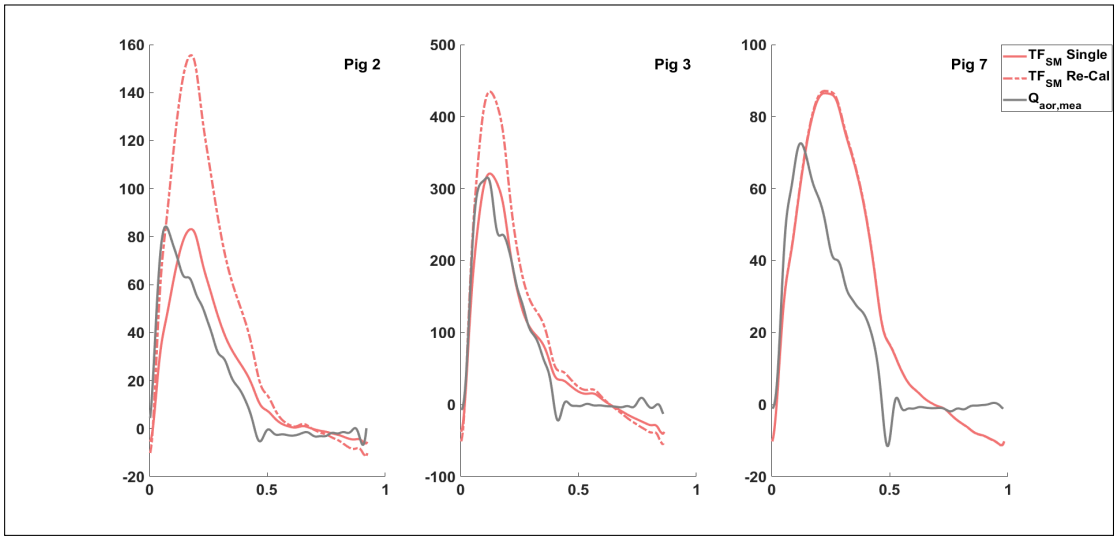

Figure 10.5: Example flow profiles for pigs 2, 3 and 7 post endotoxin infusion compared to measured flow velocity taken from and aortic flow probe. Both single and re-calibrated flow profiles are shown.

Despite the progressive increase in percentage error, SV_{est} showed good tracking of SV_{mea}. Figure 10.2 shows the polar mean bias and LoA within the desired $\pm 30°$ [59, 135]. This trending ability extended for the entirety of the experiment, including the post endotoxin stage. The ability for SV_{est} to track SV_{mea}, combined with the significant improvement in relative error after recalibration, indicates some structural change in the arterial system caused by the endotoxin. This outcome after such a major clinical change, resulting in the death of over half of the pigs, is unsurprising, as changes in arterial tone, increased vascular permeability, and myocardial dysfunction are known effects of septic shock [96, 179–181].

10.6 Summary

This chapter used the TF_{SM} method to estimate SV from the output model flow profile and an initial calibration using invasive SV_{mea}. Calibration was performed using on an initial 10 beat section to identify Z_{cal}, which combines the characteristic impedance with a scaling factor. The scaling factor is required as even if Z_c were known, flow estimates produced by the TF_{SM} method represent the component of total flow entering the tube, not overall flow.

Two sets of results were produced. One set used an initial calibration for the entirety of each experiments. The other used a recalibration after the endotoxin infusion had finished. Method accuracy was assessed using standardized Bland-Altman plots and the ability of SV_{est} to track changes in SV_{mea} was assessed using polar plot analysis. The mean bias and LoA for the Bland-Altman plots fell outside the desired $\pm 30\%$. However,

polar mean bias and LoA were within ±30 °, meeting the requirements for good tracking ability.

Chapter 11

Three-Chambered Model: Clinically Feasible Measurement Set

11.1 Introduction

The work presented in this thesis has aimed to provide methods for implementing the TCM of the CVS in a clinical environment, given the very limited currently available measurements. Chapter 11 illustrated an initial implementation of the TCM, highlighting the diagnostic potential of monitoring the TCM model parameters during endotoxin induced sepsis and subsequent fluid-based treatment. The clinical implausibility of invasive $P_{lv,mea}$ and $V_{lv,mea}$ being available for model identification promoted the devel-

opment of a reduced measurement method, presented in Chapter 5, using $P_{ao,mea}$ to establish estimates for $P_{lv,est}$ and $V_{lv,est}$. However, continuous measurements of aortic pressure being routinely available in critical care is equally unlikely. The unavailability of these critical waveforms led to the work presented in Chapter 8 and Chapter 9, where a novel method of estimating central aortic pressure from routinely taken peripheral pressure measurements, and nothing else, was developed and tested.

The present Chapter integrates all previous methods to advance the clinical applicability of the TCM and show how the parameters can be identified from a currently available set of clinical measurements. Two implementations of this clinically feasible method are presented and compared to the reference TCM_{FM} parameter sets, which are the best possible solutions, achievable only through direct catheterization of the cardiac chambers.

Both methods use arterial TF model estimated central blood pressure but different stroke volumes. One method uses stroke volume derived from the pulse contour analysis of the corresponding arterial TF model flow waveforms and an initial calibration, as detailed in Chapter 10, while the other uses aortic flow probe measurements. The two methods are referred to as the $TCM_{CM,est}$ and $TCM_{CM,mea}$ methods, designating estimated and measured SV, respectively.

11.2 Method

11.2.1 Experimental data

Table 11.1 presents the required reference measurements for model identification and the measurements assumed available in the ICU. To reproduce this availability of measurements the following data were used: continuous central venous pressure ($P_{vc,mea}$); continuous femoral pressure ($P_{fe,mea}$); a single end-systolic volume measurement (V_{es}); continuous stroke volume (SV_{mea}), for the $TCM_{CM,mea}$ method only; and one or two stroke volume measurements for calibration of estimated stroke volume (SV_{est}), used in the $TCM_{CM,est}$ method. The second calibration of SV was performed only for Pigs 2 and 7 after and took place immediately after the conclusion of the endotoxin infusion, the remaining pigs used a single initial calibration measurement at the beginning of the experiment.

Pigs 3, 5 and 6 were excluded from the analysis in this Chapter. Pigs 3 and 5 had unreliable $V_{lv,mea}$ for calibration of V_{es}. Pig 6 had corrupted $P_{fe,mea}$ data rendering it unusable for estimating central blood pressure.

11.2.2 Central pressure estimation

Estimates for central blood pressure ($P_{ao,est}$) are required not only to obtain arterial chamber reference values, but also to construct the cardiac driver function through the intermediary step of estimating left ventricle pressure and volume. The arterial TF,

Table 11.1: Comparison of the required inputs for the TCM to derive the necessary reference values for identification and construct the cardiac driver function for simulations and the set of measurements assumed available in and ICU setting.

Full Measurement Set		Clinically Feasible Set	
Measurement	Description	Measurement	Description
Continuous $V_{lv,mea}$	Provides reference $\Delta V_{s,lv}$ and $\bar{V}_{s,lv}$. Full beats used to construct the cardiac driver function	**Calibration** V_{es}	Required to estimate ventricular unstressed volume per Equation 5.6 allowing forward simulation of $V_{lv,est}$. Available via echocardiography
Continuous $P_{lv,mea}$	Used to construct the driver function	N/A	
Continuous $P_{ao,mea}$	Provides reference $\Delta P_{ao,TCM}$ and $\bar{P}_{ao,mea}$ for the arterial chamber parameter identification	**Continuous** P_p	Peripheral arterial pressure is required to estimate central blood pressure. Commonly available via direct catheterization of peripheral arteries
Continuous $P_{vc,mea}$	Provides reference $\Delta P_{vc,TCM}$ and $\bar{P}_{vc}$ venous chamber parameter identification	**Continuous** $P_{vc,mea}$	Often available as a continuous measurement via catheterization of the jugular vein
Continuous SV	Provides reference $\Delta V_{s,lv}$ in the absence of direct ventricular measurements	**Calibration SV**	required to calibrate methods for continuous SV estimation. Available via indicator dilution technique. Continuous SV estimation methods are becoming increasingly available

described by Equations 7.16 and 7.17, derived from a TL model of the arterial system, presented in Chapter 7 and validated in Chapter 9, is used to provide $P_{ao,est}$ from continuous peripheral pressure measurements. The corresponding flow waveforms are also used to estimate continuous SV after an initial calibration to the aortic flow probe measurements.

11.2.3 DRIVER FUNCTION

The cardiac driver function ($e(t)$) is derived from the $P_{ao,est}$ using a modified version of the method presented in Chapter 5 [97], to account for inter-subject variability and $P_{lv,mea}$ unavailability. Estimates for $P_{lv,est}$ and $V_{lv,est}$ are still derived from $P_{ao,est}$ using Equations 5.5 and 5.11, respectively, with the following amendments.

First, the asymptotic minimum pressure of $P_{lv,est}$, described by α in Equation 5.5, is no longer a constant 6mmHg, but to set to 25% of $\bar{P}_{vc,mea}$. Second, the local maxima and minima of the $P_{vc,mea}$ waveform are identified to provide a reference point for the intercept of $P_{vc,mea}$ and $P_{lv,mea}$ waveforms.

During diastole ventricular pressure drops, eventually falling below the cardiac filling pressure, allowing the ventricle to fill. Because the TCM is only concerned with the systemic circulation, this filling pressure is taken to be equal to the central venous pressure. As filling commences, pressure in the venous system begins to fall, producing a peak in the waveform. If measurements of left atrial pressure were available, this peak would correspond to the intercept with ventricular pressure, as blood would begin to

exit the atrium and enter the ventricle at this moment with the loss in volume causing the reduction in pressure. However, central venous pressure is typically lower than left atrial pressure, so using the local maxima as the intercept reference will underestimate the diastolic decay of $P_{lv,mea}$. Therefore, the peak in the $P_{vc,mea}$ wave is used as a reference point and an offset pressure after this peak is used, as illustrated in Figure 11.1.

The negative exponential term in Equation 5.5 is adjusted to minimize the error between the $P_{vc,mea}$ and $P_{lv,est}$ intercept and the intercept reference point. Finally, the positive exponential term is fixed at double the absolute value of the previous term. Figure 11.1 illustrates and example of this process.

Normalization of $e(t)$ is theoretically no longer necessary for practical identifiability of R_i, as $P_{vc,mea}$ is used to set the asymptotic limit for $P_{lv,est}$ during diastole. Thus, the inconsistencies between venous and ventricular pressure during filling no longer exist [66]. However, for consistency in comparison with the TCM_{FM} parameters, $e(t)$ is still normalized between 0 and 1.

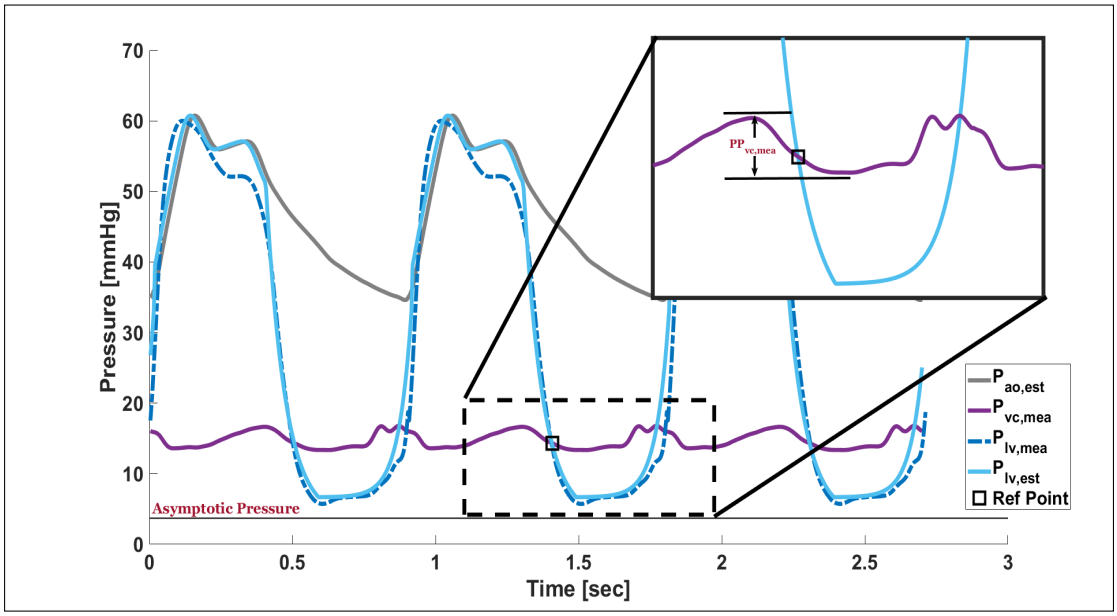

Figure 11.1: Illustration of the adaptive method for determining the exponential terms in Equation5.5 using the expected location of the ventricular and venous pressure diastolic intercept, as indicated by the reference point.

11.2.4 STROKE VOLUME

Stroke volume is required for accurate estimation of the cardiac driver function through $V_{lv,est}$, and provides reference values for $\Delta V_{s,lv}$ [62, 65, 66, 73]. Continuous SV measurements are becoming increasingly more common in ICU environments [61, 132, 134]. After an initial calibration using a high precision method, commonly indicator dilution, pulse contour analysis of a peripheral pressure waveform can be used for continuous SV. However, some currently available devices have shown sufficiently high errors to be deemed unacceptable for clinical use [132–134]. Therefore, two methods of obtaining SV are used to assess the impact of SV accuracy on model parameters, aortic flow probe measurements (SV_{mea}) and arterial TF based pulse contour analysis (SV_{TF}), as presented in Chapter 10.

Table 11.3: Equivalences made between reference measurements and TCM outputs during the parameter identification process.

Reference	Model Output
$\Delta P_{vc,mea}$	$\Delta P_{vc,TCM}$
$\Delta P_{ao,est}$	$\Delta P_{ao,TCM}$
$\Delta V_{lv,est}$	$\Delta V_{s,lv,TCM}$
$\bar{P}_{vc,mea}$	$\bar{P}_{vc,TCM}$
$\bar{P}_{ao,est}$	$\bar{P}_{ao,TCM}$
$\bar{V}_{lv,est}$	$\bar{V}_{s,lv,TCM}$
$\left(\frac{dP_{ao,est}}{dt}\right)_{max}$	$\left(\frac{dP_{ao,TCM}}{dt}\right)_{max}$

11.3 Parameter Identification

The parameter identification process is consistent with the previous two implementations of the TCM, with optimization variables vector, $\mathbf{p}$, defined:

$$\mathbf{p} = \{SBV, E_{lv}, E_{ao}, E_{vc}, R_i, R_c, R_o\} \tag{11.1}$$

and output vector, $\mathbf{y}$, defined:

$$\mathbf{y} = \{\Delta P_{vc}, \Delta P_{ao}, \Delta V_{lv} \bar{P}_{vc}, \bar{P}_{ao}, \bar{V}_{lv}, \left(\frac{dP_{ao}}{dt}\right)_{max}\} \tag{11.2}$$

Table 11.3 summarizes the equivalences made between reference values and the TCM outputs used in the output vector, highlighting the only remaining direct comparison with measurement waveforms exists with $P_{vc,mea}$. The parameter identification process is performed using MATLAB's inbuilt *lsqnonlin* function.

11.4 Analysis

The TCM parameters were identified for two combinations of input waveforms, differing by the stroke volume used. Both methods use the $P_{ao,est}$ waves approximated from $P_{fe,mea}$, but whereas one uses SV_{mea}, obtained from direct measurement of aortic flow, the other uses SV_{est}, obtained from the arterial TF flow waveform, calibrated using an initial measurement, which is the most clinically feasible case. Both methods were compared to model parameters derived using the full set of direct measurement reference values, referred to herein as the *reference set*.

The errors of each parameter are calculated as a percentage difference relative to the reference set. Bland-Altman plots are used to show the mean bias and limits of agreement of each method. Time series plots are presented to show the clinical ability of each method at tracking their respective parameters in the reference set.

11.5 Results

Figure 11.2 shows an example of the TCM output waveforms, comparing the TCM_{CM} and TCM_{FM} methods, and the corresponding direct measurements, over the same cardiac cycle. Specifically, Figure 11.2 shows the impact of using $P_{ao,est}$ in the model identification process. The TCM_{CM} output central pressure can be seen to have a significantly reduced maximum positive gradient, compared to the measure pulse and the TCM_{FM} output. This is largely a consequence of the model input, $P_{ao,est}$, being esti-

mated solely from $P_{fe,mea}$ and thus, having similar contours early in systole. With the output vector including this gradient, model simulated central pressure will be directly affected.

Figures 11.3-11.7 show the direct time series comparison of $TCM_{CM,mea}$, $TCM_{CM,est}$ and TCM_{FM} methods of identifying all model parameters. Figures 11.8-11.9 show the Bland-Altman plots for the pooled error of each parameter across all experiments. Finally, Tables 11.4 and 11.5 summarize the mean errors of each parameter compared to the reference set for the SV_{mea} and SV_{est} sets, respectively.

Table 11.4: Relative percentage error (%) of $TCM_{CM,mea}$ parameters, identified using SV_{mea}, compared to the reference set. Results are given as mean(standard deviation).

Pig	SBV_m	E_{ao}	E_{vc}	R_c	R_i	R_o	E_{lv}
1	11.1(9.4)	10.1(8.5)	32.3(15.6)	17.7(3.9)	15.2(8.1)	179.6(77.9)	2.8(9.4)
2	4.8(3.0)	12.0(8.7)	8.9(6.4)	16.0(6.7)	13.3(15.1)	210.8(95.9)	10.7(5.6)
4	7.2(3.5)	14.4(5.1)	9.5(8.0)	4.6(4.2)	10.7(9.8)	36.2(23.4)	26.6(15.5)
7	9.4(4.0)	20.2(10.1)	15.2(13.3)	7.6(9.7)	6.4(8.4)	75.3(38.3)	10.2(6.1)
8	10.6(10.0)	17.3(11.7)	12.0(9.5)	10.0(5.0)	22.7(16.1)	931.1(465.4)	16.4(8.3)
Mean	8.7(6.2)	15.0(8.9)	15.6(10.1)	11.1(5.9)	13.7(11.5)	286.6(140.2)	13.4(7.7)

Table 11.5: Relative percentage error (%) of $TCM_{CM,est}$ parameters, identified using SV_{est}, compared to the reference set. Results are given as mean(standard deviation).

Pig	SBV_m	E_{ao}	E_{vc}	R_c	R_i	R_o	E_{lv}
1	8.4(5.8)	14.5(9.9)	19.0(15.7)	11.6(7.0)	16.2(12.2)	271.1(150.0)	32.8(27.6)
2	27.8(22.4)	39.2(17.7)	38.5(19.4)	42.1(17.2)	42.3(23.1)	137.1(92.9)	11.0(5.1)
4	6.2(6.1)	23.0(7.2)	11.1(12.5)	15.4(9.3)	14.3(12.5)	41.7(22.9)	26.1(15.5)
7	11.0(5.8)	23.2(9.8)	16.7(19.7)	11.8(10.5)	12.6(11.7)	80.2(37.5)	10.3(6.0)
8	14.8(12.3)	9.5(7.1)	18.4(13.2)	24.4(6.2)	18.4(15.6)	764.8(328.2)	16.6(8.3)
Mean	13.7(10.5)	21.9(10.3)	20.8(16.1)	21.1(10.2)	20.8(15.0)	259.0(126.3)	13.5(7.5)

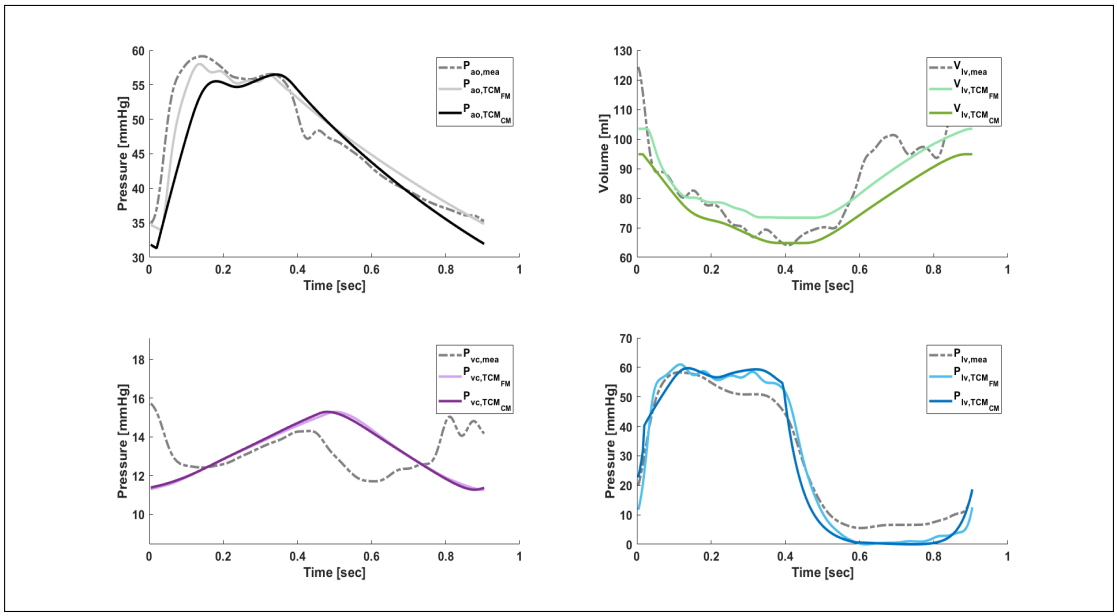

Figure 11.2: Example outputs of the TCM_{CM} output and reference waveforms after parameter identification, compared to the TCM_{FM} method for the same beat, showing the progression of the method from validation to clinically feasible implementation.

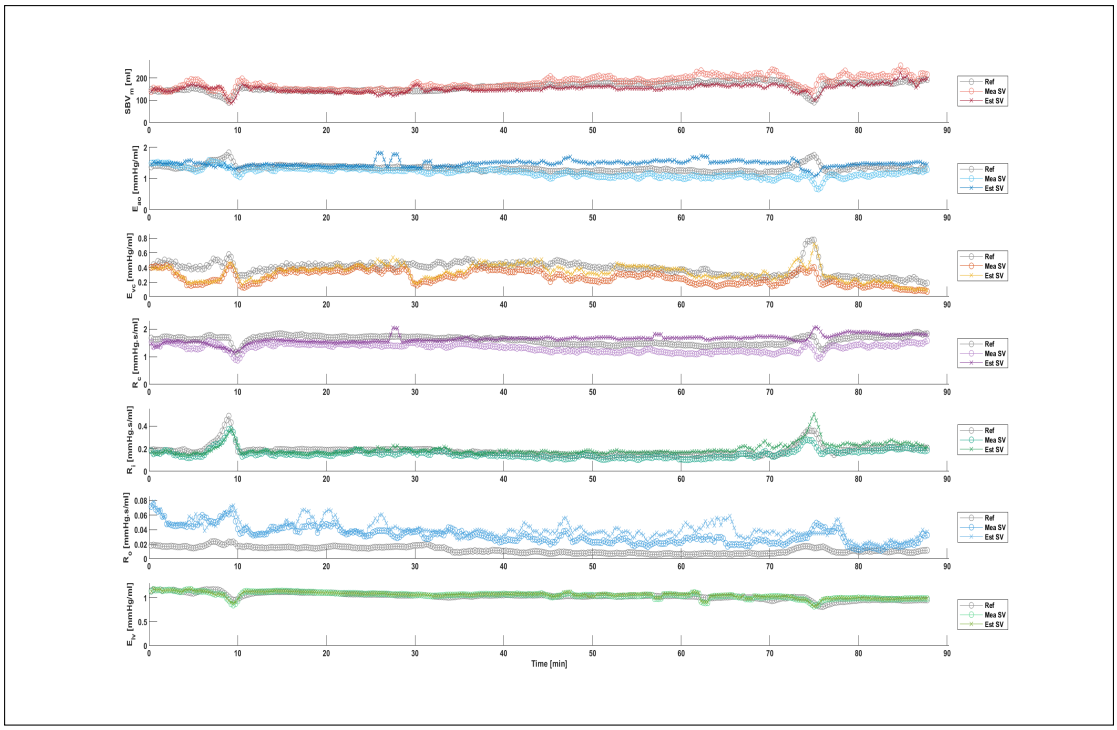

Figure 11.3: Time series comparison of identified TCM parameters using the two TCM_{CM} methods and TCM_{FM} method for Pig 1.

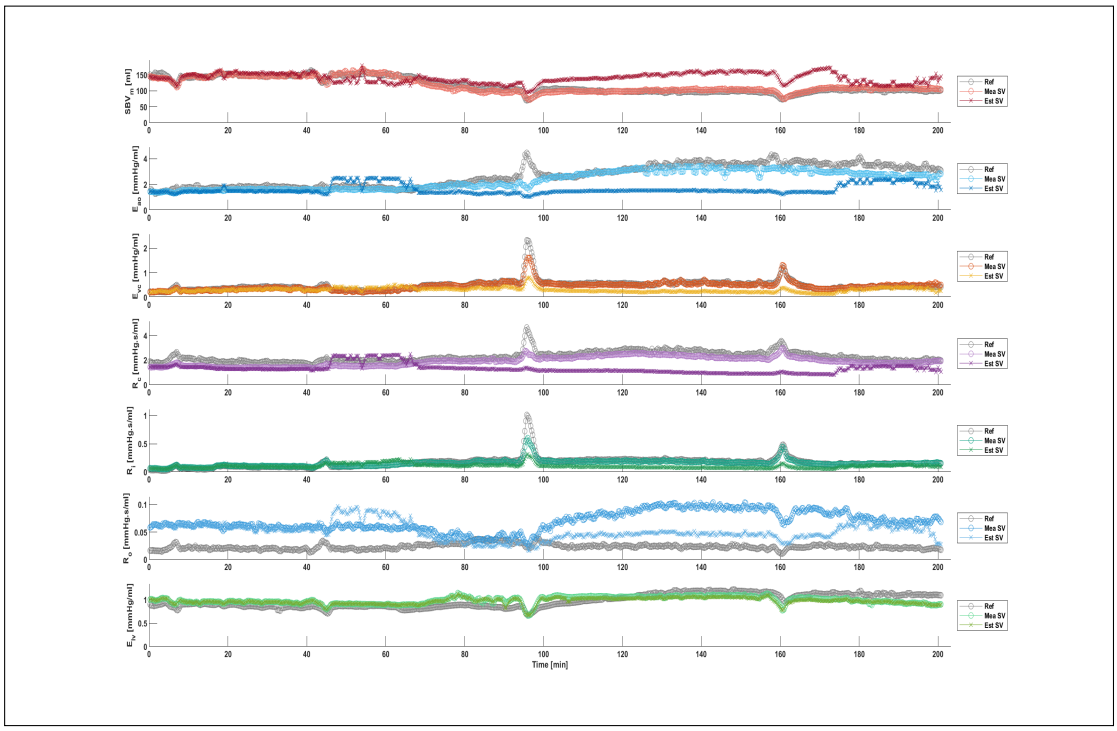

Figure 11.4: Time series comparison of identified TCM parameters using the two TCM_{CM} methods and TCM_{FM} method for Pig 2.

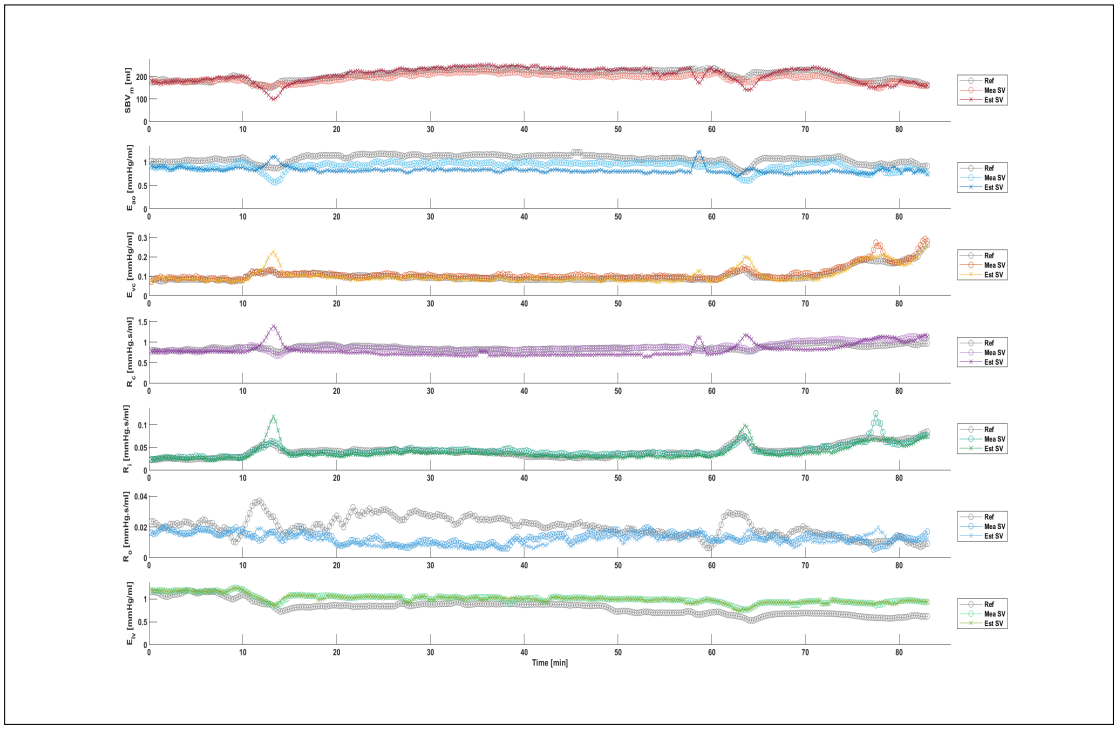

Figure 11.5: Time series comparison of identified TCM parameters using the two TCM_{CM} methods and TCM_{FM} method for Pig 4.

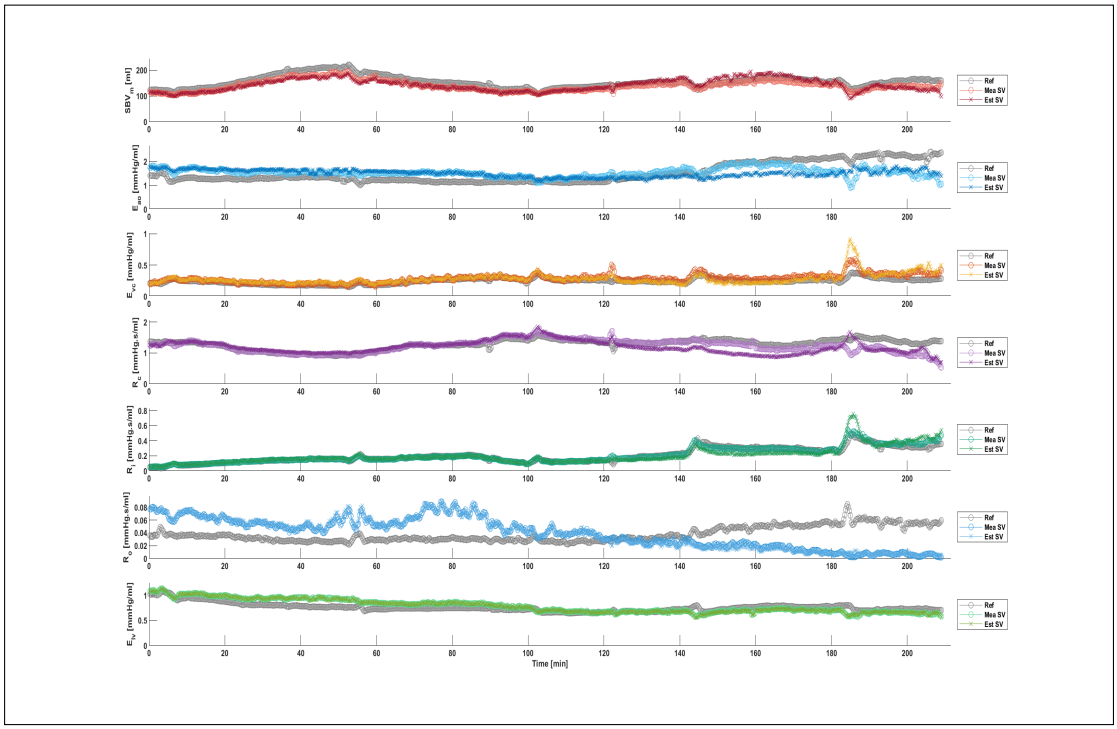

Figure 11.6: Time series comparison of identified TCM parameters using the two TCM_{CM} methods and TCM_{FM} method for Pig 7.

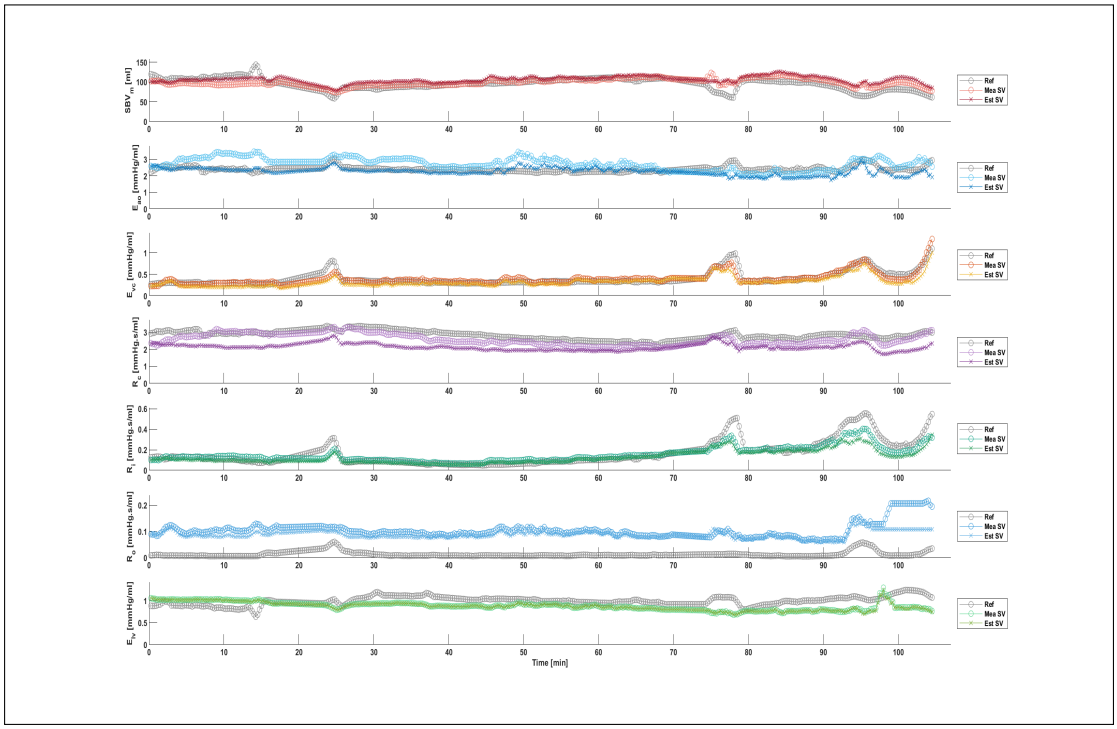

Figure 11.7: Time series comparison of identified TCM parameters using the two TCM_{CM} methods and TCM_{FM} method for Pig 8.

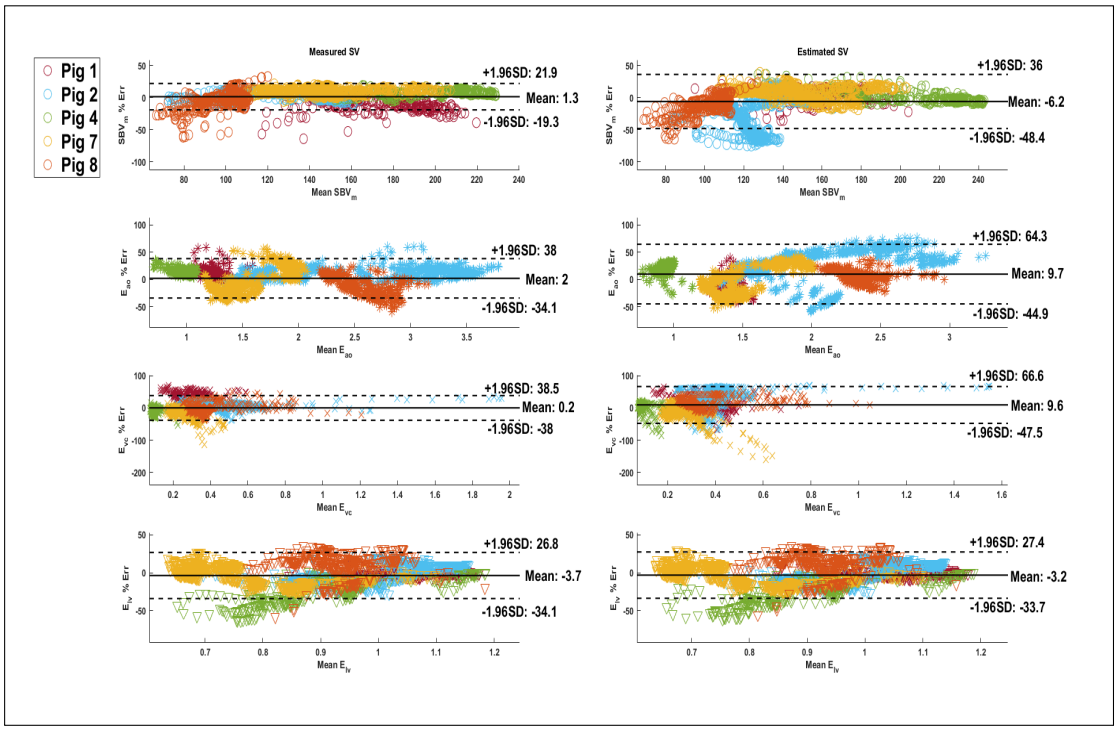

Figure 11.8: Bland-Altman analysis of TCM identified stressed blood volume and chamber elastances SBV_m, V_{ao}, E_{vc}, and E_{lv}, for all pigs, versus calculated values using left ventricle pressure and volume and aortic pressure and flow. (left) measured SV_{mea}. (right) estimated SV_{est}.

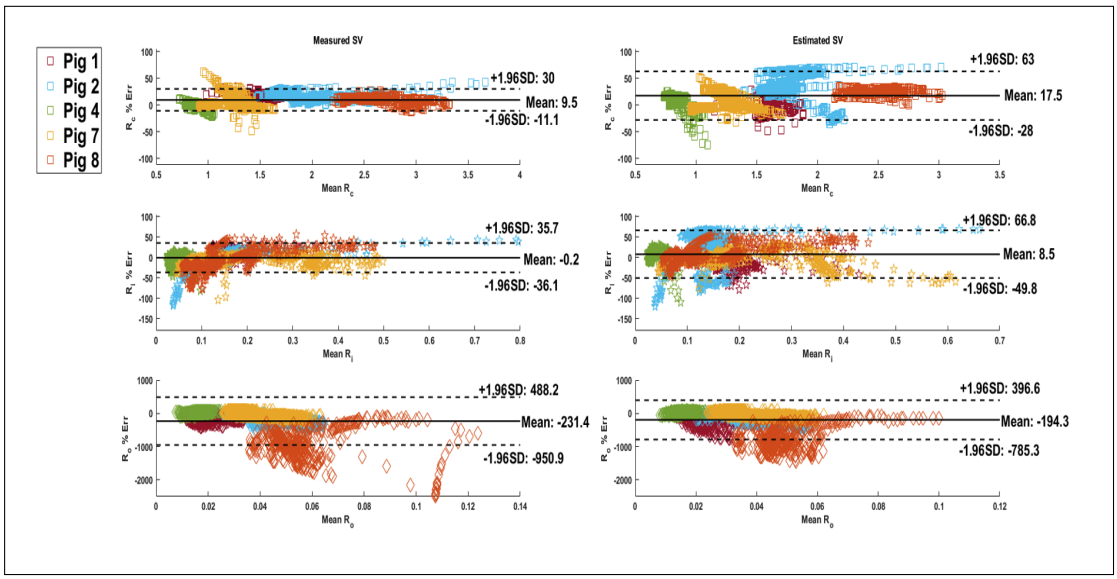

Figure 11.9: Bland-Altman analysis of TCM identified resistances R_c, R_i, and R_o, for all pigs, versus calculated values using left ventricle pressure and volume and aortic pressure and flow. (left) measured SV_{mea}. (right) estimated SV_{est}.

11.6 Discussion

The two TCM_{CM} methods presented in the present chapter use a limited, entirely typical and clinically feasible set of measurements, expected to be available in a current ICU setting, to construct the cardiac driver functions and provide reference values for to identification of the model. Specific attention is given to the accuracy of SBV_m identification due to its intrinsic relation to VR and thus, fluid responsiveness. The errors associated with SBV_m identification using the $TCM_{CM,mea}$ and $TCM_{CM,est}$ methods produced a mean bias and limits of agreement of 1.3 (-19.3, 21.9)% and -6.2 (-48.4 36.0)%, respectively, relative to the TCM_{FM} method. These results show the TCM_{CM} method could be accurately implemented into current critical care with no additional clinical cost.

Figures 11.3-11.7 show the impact of using a clinically feasible set of measurements versus direct measurements for all required model reference values. One limitation of using an arterial TF model to estimate central pressure, is the resulting estimate will have a mean pressure equal to the mean pressure of the peripheral measurement used. Although pressure throughout the larger conduit arteries, including the aorta and femoral artery, can be considered constant ($\leq$2mmHg difference) [99, 148], the difference in mean pressure directly influences identified parameters due to the inclusion of $\bar{P}_{ao,est}$ in the output vector. The lower peripheral pressure reduces the pressure differential between $P_{lv,est}$ and $P_{ao,est}$ driving flow out of the ventricle, and $P_{ao,est}$ and $P_{vc,mea}$ driving flow through the circulation thus, primarily impacts identification of R_c and R_o.

Identified R_c for Pig 7, depicted in Figure 11.6, shows a very good fit to the TCM_{FM} identified R_c early in the experiment. However, a progressive divergence towards the end of the experiment is evident. As was eluded to in Chapter 9, the central and peripheral arterial pressures became decoupled during septic shock [91, 178], most evident in pig 7, causing $\bar{P}_{fe,mea}$ to diverge from $\bar{P}_{ao,mea}$. This divergence translates through to $P_{ao,est}$, illustrating the impact of $P_{ao,est}$ on R_c.

In Chapter 5, the dependence of R_o on the predetermined phase lag (δ), used to estimate $P_{lv,est}$, was discussed and remains relevant in the current chapter. However, using $P_{ao,est}$ further contributed to this error due to the difference between $\frac{P_{ao,est}}{dt}_{max}$ and $\frac{P_{ao,mea}}{dt}_{max}$. The upstroke gradient of the arterial chamber pressure defines the contractile state of the model, and changes to this gradient cause R_o to be adjusted adjusted in order produce the reference $\Delta V_{s,lv}$. This effect is maximized when $\frac{P_{ao,mea}}{dt}_{max}$ and $\frac{P_{fe,mea}}{dt}_{max}$ differ significantly, as there is an intrinsic correlation between the upstroke pressure of $P_{ao,est}$ and $P_{fe,mea}$, due to a common forward wave characterizing pressure during this period for both waveforms. Figure 11.2 illustrates this similarity.

Using SV_{est} expectedly increased estimated parameter error for all parameters, with the exception of R_o, due to the physiological significance of SV in the CVS. The $TCM_{CM,est}$ method uses SV_{est} as reference $\Delta V_{s,lv}$ and thus, primarily affects R_o and E_{ao}. Figure 11.4 presents the greatest contrast between $TCM_{CM,est}$ and $TCM_{CM,mea}$. Given chamber pressures for each method are identical, the significant overestimation of SV_{est} seen in Pig 2 after the endotoxin infusion, reduces R_o, R_c and E_{ao} to allow for the elevated flow rate.

Finally, the new method of adaptively identifying the exponential terms defining $P_{lv,est}$, helped to produce a reduction in error associated with R_i, when compared to the TCM_{RM} method implemented in Chapter 5. This result is promising as it allows the driver function specifically tailored to a patient by using commonly available central venous measurements.

11.7 Summary

Models of the CVS are useful tools capable of taking raw data from typical pressure and volume measurements and extracting clinically relevant information about a patients system dynamics [62, 67, 73]. However, the accuracy of such model is dependent on the measurements available for identifying the models parameters. While, previous CVS models are able to provide very accurate information about a patients cardiac dynamics, the measurements required to identify the model may render them unable to be implemented clinically [62, 72, 85]. Even with a low number of parameters describing the TCM, previous implementations of the model still required continuous, direct measurement of left ventricle pressure and volume, and aortic pressure [62, 66, 80, 81]. All three measurements will not be available in critical care, outside of a catheterization lab.

This chapter presents a method for identifying the TCM using measurements currently available in a typical ICU, removing the reliance on left ventricle pressure and volume, and aortic pressure as reference waveforms. A novel arterial TF model allowed $P_{ao,est}$ to be estimated from beat wise femoral pressure measurements, which could be used to

formulate the cardiac driver function, and provide accurate arterial chamber reference values for model identification. An adaptive method for approximating $P_{lv,est}$, uses a patients own central venous pressure measurements to fit the exponential terms describing ventricular diastolic pressure, improving the generalizability of the model. Using these estimates, the primary parameter of interest, SBV_m, was identified with a mean bias and limits of agreement of 1.3 (-19.3, 21.9)%, relative to the best possible case of SBV_m identified given a complete set of continuous, invasive measurements for model identification.

Chapter 12

SBV as an Index of Fluid Responsiveness: Human Study

12.1 Introduction

This thesis has aimed to produce methods for implementing the TCM of the CVS in a current, typical intensive care environment. In contrast to the animal studies used to develop and validate the model [62, 65, 66, 80, 81], clinical data is significantly more limited in the quantity and quality of measurements. Specifically, the wealth of information pertaining to cardiovascular dynamics and efficiency, obtained from direct measurements of ventricular and aortic pressures and volumes, are unavailable in standard clinical care and thus, can not be relied on for model identification.

This thesis has presented a number of methods for estimating clinically unavailable

waveforms, required to implement the TCM, from datasets expected to be available in intensive care environments. These methods were tested and validated in a series of porcine endotoxin experiments, subjected to a variety of clinical procedures designed to significantly alter hemodynamic conditions [80, 81]. Model parameters were able to be accurately identified relative to those obtained using direct measurements for all model reference values.

This chapter uses retrospective clinical data recorded from human patients who received treatment in the Christchurch hospital ICU, to test the applicability of the TCM under true clinical conditions. Patients receiving at least one fluid therapy, as part of their treatment course, were identified and model based SBV_m was calculated. PiCCO measured changes in CO, in response to the fluid infusion, were compared with SBV_m prior to fluid therapy to test the validity of SBV_m as an index of fluid responsiveness, as well as to assess the difference between fluid responsiveness and, clinically more important, perfusion.

12.2 Method

12.2.1 Clinical Data

Data from 10 patients receiving a fluid therapy greater than 500 ml were obtained from the Christchurch hospital ICU in New Zealand. These data included continuous central venous pressure, some peripheral artery pressure and cardiac output, all recorded using the BedMasterEx data acquisition software. The corresponding de-identified patient

bedsheets were also supplied by the hospital providing specific information about patient treatment and catheter placement.

Demographic data for each patient are summarized in Table 12.1. Arterial catheter line (ART) placement included the radial artery (Rad), brachial artery (Brach), and antecubital fossa (ACF). Three different fluid types were administered across all patients; Normal saline solution (N/Sal), Hartmans solution, and plasmalyte (PLSM). PiCCO and central venous lines for all patients were placed in the femoral artery and internal jugular vein, respectively.

Table 12.1: Summary of patient data available for identification of the TCM including type and volume of fluid given.

Patient	ART	Ht [m]	Wt [kg]	Volume [ml]	Type	Diagnostic
1	Rad	1.70	100	500	N/Sal	Asp. Pneumonia
2	Rad	1.68	78	1000	N/Sal	C.A. Bypass Grafts
3	ACF	1.68	90	1000	N/Sal	Bac. Pneumonia
4	Brach	1.75	71	1000	Hartmans	GI Obst.
5	Rad	1.76	67	500	PLSM	GI Obst.
6	Rad	1.73	131	500	N/Sal	Pancreatitis
7	Rad	1.70	100	500	N/Sal	Other CVS Disease
8	Rad	1.78	106	500	N/Sal	Other GI Diseases
9	Brach	1.60	52	500	N/Sal	Other GI Diseases
10	Rad	1.81	100	2000	N/Sal,PLSM	Bac.Pneumonia

12.2.2 Fluid Identification

The supplied patient bedsheets provided the volume, type, and approximate timing of each fluid therapy. However, recordings were only reported to the nearest hour, meaning the exact timing of fluid delivery was unknown. As this work is concerned with assessing patient-specific response to fluid therapy, a more accurate representation of

when fluids were administered was required. Because fluids are administered through the central venous line, the associated pressure recordings were examined to identify disturbances in the recordings, such as the one shown in Figure 12.1, indicating fluids being administered. After consultation with healthcare staff and examination of the data, a period of 30 min was selected to assess the changes in CO. Calculations for the change in CO used the identified start of fluid therapy and the maximum value of CO during the subsequent 30 min period.

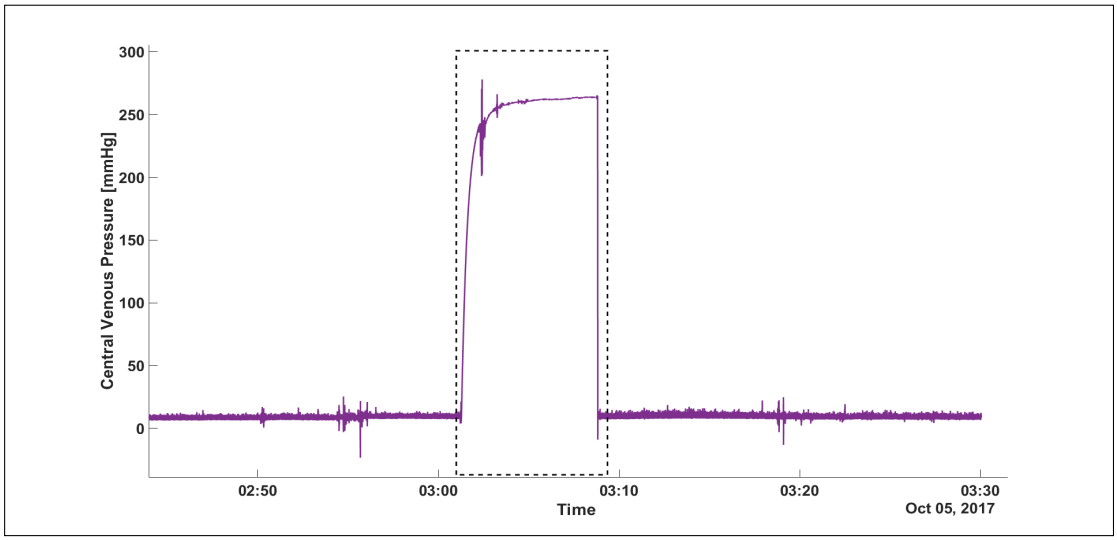

Figure 12.1: Example of the disturbance to central venous pressure measurements used to better identify the start of a fluid therapy. The dashed box indicates the assumed time fluids are passing through the central venous line, producing the physiologically inconsistent recordings of pressure.

12.2.3 Waveform Estimation

Central pressure estimates ($P_{ao,est}$) were derived from the peripheral arterial pressure measurements, using the TF_{SM} method developed and tested in Chapter 8 and Chapter

9, respectively. The TF_{SM} method was critical to the feasibility of this study as no ECG data were available for PTT estimation. Sections of data 20 sec in duration were used to obtain approximately 20 beats before and after fluid administration.

For each $P_{ao,est}$ waveform, left ventricle pressure ($P_{lv,est}$) and volume ($V_{lv,est}$) estimates were constructed using the method presented in Chapter 11. To ensure physiologically reasonable estimates of $P_{lv,est}$ were produced, when no clear reference peak and trough were present in the central venous pulse, as described in Figure 11.1, a constant delay of 10% of beat length from end-systole (t_{es}) was used.

Estimates of $V_{lv,est}$ required a calibration measurement of end-systolic volume (V_{es}). While echocardiography measurements are becoming more prevalent in intensive care, they were not retrospectively available for this study. Therefore, V_{es} was calculated in terms of body surface area (BSA) [182–185] :

$$V_{es} = 25 \cdot BSA \tag{12.1}$$

where BSA is calculated from the Dubois and Dubois equation [186], defined:

$$BSA = 0.20247 \cdot Height[m]^{0.725} \cdot Weight[kg]^{0.425} \tag{12.2}$$

Continuous cardiac output measurements were available in these data sets and were used to calculate stroke volume using the relationship with heart rate (HR), defined:

$$CO = SV \cdot HR \tag{12.3}$$

12.2.4 Parameter Identification

The TCM parameters were identified in a consistent manner to all previous implementations of the model presented in this thesis, detailed fully in Chapter 4. Table 12.2 details the equivalences made between model outputs and reference values.

Table 12.2: Equivalences made between reference measurements and TCM outputs during the parameter identification process.

Reference	Model Output
$\Delta P_{vc,mea}$	$\Delta P_{vc,TCM}$
$\Delta P_{ao,est}$	$\Delta P_{ao,TCM}$
$\Delta V_{lv,est}$	$\Delta V_{s,lv,TCM}$
$\bar{P}_{vc,mea}$	$\bar{P}_{vc,TCM}$
$\bar{P}_{ao,est}$	$\bar{P}_{ao,TCM}$
SV	$\bar{V}_{s,lv,TCM}$
$\left(\frac{dP_{ao,est}}{dt}\right)_{max}$	$\left(\frac{dP_{ao,TCM}}{dt}\right)_{max}$

12.3 Analysis

Using the TCM, SBV_m was identified for all beats present in the 20 sec section, and the average was taken. To assess SBV_m as a potential index of fluid responsiveness, linear regression analysis of SBV_m prior to fluid therapy with resulting change in CO is performed. As with the work in Chapter 4, SBV_m is normalized to the record weight of the patient. These results were then compared to PPV recordings taken for the same fluid therapy.

As shown in Table 12.2, the volumes of fluid administered across the 10 patients were not uniform. To assess the effect of the fluid bolus in a consistent manner, the resulting

changes in CO were normalized by the volume of fluid given. Therefore, results are presented in terms of the change in CO per millilitre of fluid given ($\frac{\Delta CO\%}{ml}$).

12.4 Results

Figure 12.2 shows the linear regression analysis of SBV_m and relative change in CO over each fluid therapy, compared to PPV. The horizontal dashed lines on each plot indicate a change in CO of $\frac{0.024\%}{ml}$ fluid administered, which is equivalent to a 12% change in CO for a 500ml fluid bolus, although values ranging from 10-15% are commonly reported [13, 33, 36, 180]. Identified SBV_m and PPV perform similarly, producing regression coefficients of $r^2 = 0.43$ and 0.47, respectively. However, the PVV plot shows most patients would be deemed to respond positively to fluid therapy, even though most, in fact, did not. These results provide a first ever implementation of SBV_m as an index of fluid responsiveness in human patients, and provide the justification for continued study as they are on par with the current clinically used metrics.

Figure 12.3 shows the relative change in SBV_m compared to the change in CO over each fluid therapy. As expected there is a clear positive correlation between increasing SBV_m, which increases the pressure differential driving venous return, and induced changes in CO. Tus, increasing SBV_m yields increasing CO, but as ΔCO grows, change in SBV_m are more variable. Equally, little or no gain in CO is clearly strongly associated with change in SBV_m.

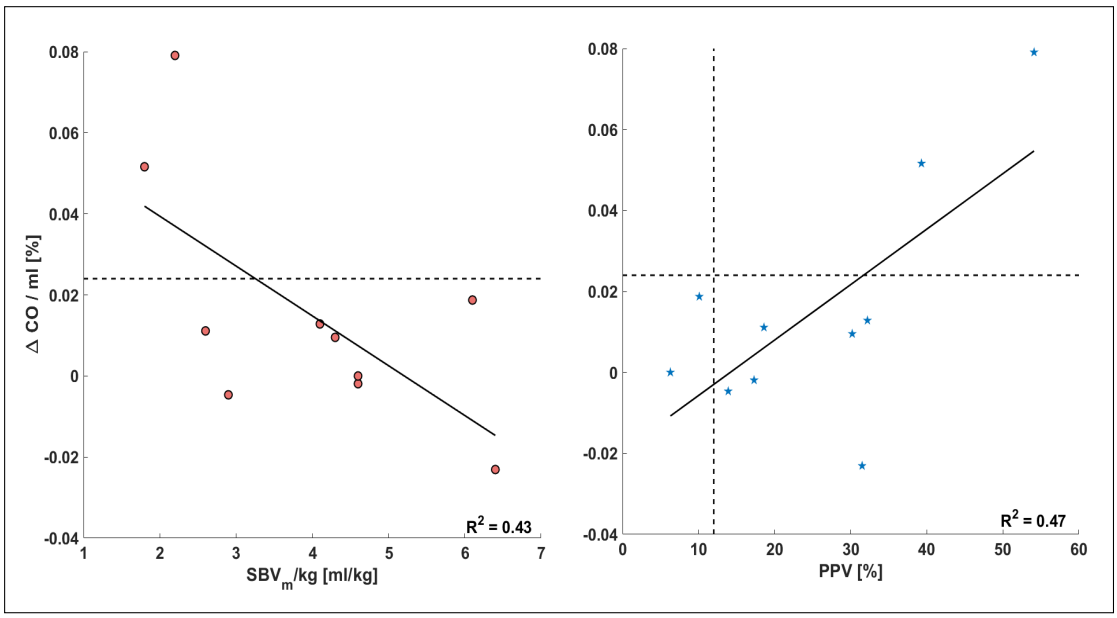

Figure 12.2: (left) Relative change in CO after each fluid bolus compared to identified SBV_m per kg of patient bodyweight prior to infusion. (right) Relative change in CO after each fluid bolus compared to PPV prior to infusion. Horizontal dashed lines indicate the fluid responsive threshold and are equivalent to a 12% increase in CO for a 500ml bolus.

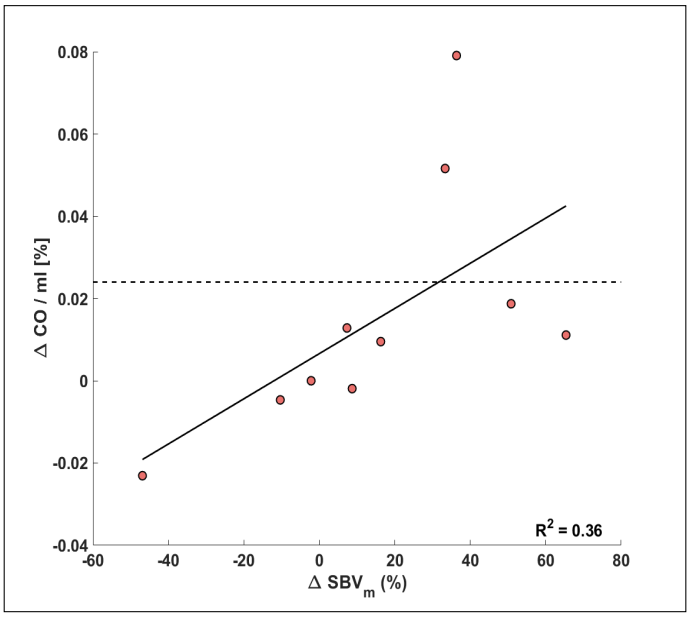

Figure 12.3: Relative change in CO compared to the relative change in identified SBV_m over each fluid therapy.Horizontal dashed lines indicate the fluid responsive threshold and are equivalent to a 12% increase in CO for a 500ml bolus.

12.5 Discussion

To combat the effects of circulatory shock, clinicians often administer intravenous fluids to increase cardiac output [14, 34, 51]. By increasing the total volume in the circulation, the aim is to raise the MSFP, increasing the pressure differential with the right atrium and increasing venous return [3, 4]. With more blood returning to the heart, cardiac preload, and subsequently CO, are increased. This increase in CO helps restore and maintain adequate perfusion pressure, thus limiting organ dysfunction [180].

However, continual or overly aggressive fluid therapy has been associated with negative patient outcomes, and can even cause the opposite of the desired effect and reduce organ perfusion [13] [46, 50, 187]. According to the Frank-Starling mechanism, increasing cardiac preload will increase CO until some optimal level associate with the maximal overlap of the actin-myosin myofibrils [33, 180]. Further increasing preload will cause significant increases in right atrial pressure, which directly opposes the MSFP, hindering venous return. Furthermore, the increase in right atrial pressure is transmitted back through the venous system, increasing organ venous pressure and effecting microcirculatory flow [180]. Therefore, fluids should only ever be given to patients if they are hypovolemic and also expected to be fluid responsiveness.

This chapter demonstrated a first implementation of SBV_m, a model based equivalent of stressed blood volume, in 10 human ICU patients to assess fluid responsiveness. Using the methods developed in this thesis, estimates for left ventricle pressure and volume, and aortic pressure were derived from the available peripheral artery and central venous

pressure measurements, and used to identify the TCM parameters, including SBV_m, using only typical clinically available measurements. The results presented use the relative change in CO per ml of fluid administered to account for the different volumes given to some patient, detailed in Table 12.1.

When correcting for patient weight and volume of fluid given, SBV_m prior to fluid therapy produced a coefficient of determination with relative change in CO of $r^2 = 0.43$, shown in Figure 12.2. As expected, a negative correlation between SBV_m and CO was observed, indicating patients with a higher SBV_m were likely already operating on the plateaued region of the Frank-Starling curve and the increase in volume from the fluid bolus was transmitted to an increase in right atrial pressure. These results are consistent with the original validation study conducted in Chapter 4 and shown in Figure 4.2.

Also shown in Figure 12.2 is the correlation between PPV and relative change in CO for the same fluid therapies. All patients were mechanically ventilated, meeting the primary requirement for using PPV as an index of fluid responsiveness [36, 51, 54]. The results of PPV display the expected positive correlation between elevated PPV and change in CO. The coefficient of determination between PPV and relative change in CO was $r^2 = 0.47$, showing SBV_m to be as good as the current clinical practice. However, a significant proportion of patients presented false positives when PPV was assessed using a threshold of 12%. As this is a first study, the threshold for SBV_m indicating fluid responsiveness is unknown and requires a larger study for accurate assessment.

A main advantage of SBV_m as an index of fluid responsiveness is the underlying physiological association between venous return and stressed blood volume is true regardless

of a patients' breathing conditions. Therefore, SBV_m may improve upon current cardio-pulmonary based indices, as it does not require patients to be mechanically ventilated. Future work comparing SBV_m and PPV in the limiting cases of spontaneously breathing and low tidal volume patients, may show SBV_m to be a more applicable index of fluid responsiveness to a larger population of patients with not additional clinical cost.

Finally, Figure 12.3 shows the change in SBV_m compared to the relative change in CO per millilitre of fluid administered. The positive correlation observed is consistent with the physiological idea at the foundation of fluid therapy. Specifically, intravenous fluid infusions will increase the stressed volume in the circulation, stimulating greater VR and increasing CO. The negative changes in SBV_m observed in some patients may indicate the potential effects of fluid overload. Fluid overload can cause the release of natriuretic peptides in response to elevated cardiac filling pressures, which can significantly increase endothelial permeability, shifting fluid into the interstitial space and reducing SBV_m [50, 180, 187].

12.6 Limitations

Several limitations exist with the present study. First, the sample size is small making it difficult to draw conclusions about the general population. Future works are required to expand the number of patients included, also allowing specific threshold values of SBV_m relating to fluid responsiveness to be established.

As illustrated in Figure 12.1, an ad hoc method for identifying the specific timing of each

fluid therapy was used, due to the supplied patient bedsheets only recording when fluids were administered to the nearest hour. To properly assess the effect of the fluid bolus, a more accurate indication of when fluid infusion began was required. However, some fluid infusions did not present with such clear indications, possibly due to a slower infusion rate. In these situations, a period of 30min, within the stated hour, encompassing the maximum observed change in CO was used, meaning misidentification is possible.

Fluid therapy in the ICU is often not conducted in isolation, with a variety of drugs used in treatment to stabilize a patient's hemodynamics. The patients in this work were no exception. Combinations of noradrenaline, adrenaline, and vasopressin were also administered to many of the patients, which may influence SBV_m in ways not accounted for in this study. Additionally, the types of fluids administered were not consistent across all patients.

Finally, to estimate left ventricle volume waveforms, an estimate of the left ventricle end-systolic volume was required for each patient. These estimates used population averages based on the patients body surface area. Although recordings of patient height and weight were included in the corresponding bedsheets, some measurements were indicated as being estimates, potentially leading to significant error relative to true measurements. Furthermore, 2 patients were recorded as having weights in excess of 130kg. It is likely some scaling error was introduced when estimating V_{es} from a constant multiplier in these higher weight patients.

12.7 Summary

This chapter presented a first implementation of SBV_m as an index of fluid responsiveness in human data recorded in a variety of ICU patients. The measurements available for this study included; continuous peripheral artery pressure, taken at either the radial artery, brachial artery or antecubital fossa, continuous central venous pressure, taken from the internal jugular vein, and continuous cardiac output monitoring, taken from a PiCCO line placed in the femoral artery.

Linear regression analysis of SBV_m against the relative change in CO per ml of fluid administered produced an $r^2 = 0.43$, almost identical to the currently used index of fluid responsiveness, PPV with $r^2 = 0.47$. A negative correlation was observed between SBV_m and change in CO, shown in Figure 12.3, which is physiologically consistent with the Guytonian model of venous return. Furthermore, a positive correlation with the change in SBV_m and change in CO was observed also indicating the more stressed volume is increased, the greater the expected increase in CO.

These results further validate SBV_m as a potential index of fluid responsiveness, and may present an improvement on current clinically used metrics as there is no requirements for a fluid challenge or mechanical ventilation.

Chapter 13

Conclusion

Fluid therapy is one of the most common treatments administered to patients presenting with some form of circulatory shock. By increasing the total volume of fluid in the circulation, clinicians aim to increase the mean systemic filling pressure, the driving force of venous return, thereby increasing cardiac output to restore and maintain critical perfusion pressure [3, 4, 15, 40, 41]. However, unguided fluid therapies produce desired increases in cardiac output in only approximately 50% of patients [14, 44, 45]. This failure rate presents a significant problem for medical staff as unnecessary or excessive fluid administration has been linked to increased hospital stay and worsened patient outcomes. Furthermore, due to the complexities of the CVS and changing patient condition, an initial positive response to fluids does not guarantee continued success. Therefore, accurate assessment of patient-specific time-varying fluid responsiveness is necessary for optimizing care and improving outcomes.

Currently, fluid responsiveness is assessed using either static or dynamic clinical indices. Although 73% of American and 84% of European anaesthesiologists have stated using static indices [37], specifically central venous pressure, when making decision regarding fluid therapy, static indices have repeatedly shown poor ability to predict fluid responsiveness [37, 52, 53]. Dynamic indices present a significant improvement over static indices, but have several associated limitations restricting their clinical implementation and validity.

A recently developed model based surrogate of stressed blood volume (SBV_m), a primary determinant of the mean systemic filling pressure and thus venous return, has been shown to be a potential index of fluid responsiveness [62, 65, 66]. Using a three-chambered lumped parameter model of the CVS, SBV_m can be identified from a minimal set of measurements [62, 80, 81]. However, the measurement set required for model simulation included continuous, precise recordings of left ventricle pressure and volume, aortic pressure and central venous pressure. Aside from central venous pressure, these measurements are almost never available in critical care.

The research presented in this thesis aimed to provide methods for obtaining accurate estimates for all required model inputs, providing a clinically feasible method of identifying the TCM in a current, typical ICU environment. The main goals of this thesis were:

- Validate the TCM and highlight the clinical potential of the associated parameters.

- Demonstrate the model can be identified from a clinically feasible, significantly reduced subset of input measurements.
- Provide a first ever implementation of the TCM on human data to assess fluid responsiveness.

Chapter 1 provided a macro description of the relevant CVS anatomy and physiology. Specifically, the cardiac cycle was introduced describing the contraction and relaxation of the cardiac muscles, allowing the heart to eject blood into, and receive blood from, the circulation. The principles of circulation relating venous return and cardiac output to the effective circulating blood volume, known as the stressed blood volume, were discussed. Cardiac pressure-volume relations were introduced, along with the concept of elastance, and their relations to cardiac performance. Finally, the experimental data used in this work was detailed.

Chapter 2 introduced the clinical utility of fluid therapy and the associated risks of fluid overload. Several of the currently used indices of fluid responsiveness were presented, both static and dynamic. Finally, stressed blood volume was discussed in the context of fluid therapy, detailing how increasing total volume in the circulation aims to increase the MSFP, increasing the pressure differential relative to right atrial pressure, increasing venous return and cardiac output. The unethical nature of direct measurement of SBV also provided the motivation for using a model based surrogate.

The TCM of the CVS used to identify SBV was presented in Chapter 3. The arterial and venous chambers were described as passive chambers, describing pressure in the

chamber in terms of a constant elastance and the stressed volume. The cardiac chamber, representing the left ventricle, used an additional term describing the time-varying elastance of the muscle fibres to account for the contraction and relaxation of the heart. The TVE curves used the P-V relations presented in Chapter 1. Next, the equations used to calculate initial vales for all model parameters were detailed. Finally, a description of the process by which the error vector and driver function were normalized, to prevent parameter dominance and ensure practical identification, was presented.

An initial validation of the model using data from 6 of the porcine endotoxin experiments was presented in Chapter 4. Identified SBV_m was shown to better predict fluid responsiveness than PPV and SVV, providing a second validation of SBV_m as a index of fluid responsiveness. Analysis of the remaining model parameters revealed the clinical utility of the TCM in monitoring changes during sepsis and septic shock, and simulated volume based treatment.

Chapter 5 presented a first step towards making the TCM more clinically applicable by removing the need for continuous measurements of left ventricle pressure and volume. Using key features from continuous aortic pressure measurements, and an initial calibration of left ventricle end-diastolic volume, estimates of the two ventricular waveforms were produced. The results of this reduced measurement method were compared to the parameters identified from the full measurement reference method. Minimal error was introduced into the model, given the significant loss of information from omitting ventricular measurement, with identified SBV_m closely correlating with reference values. While Chapter 5 presented an important intermediate step, aortic pressure measure-

ments are usually only available in a catheter lab, not in general intensive care. The unavailability and necessity of central pressure prompted the development of a novel method for estimating central pressure from a single peripheral pressure input.

Chapter 6 presented an in-depth description of the arterial system and the determinants of arterial pressure and flow waveforms throughout the body. Specific attention was paid to the concept of wave reflections. An overview of several current methods for measuring central and peripheral pressure and central flow were also given.

Chapter 7 presents a tube-load model of the arterial system used to develop an arterial transfer function, to estimate central waveforms from peripheral measurements. Specifically, a single tube, lossless model with a generic pole-zero structured terminal load was described. This version of the tube-load model was selected due to its ability to characterize central pressure given knowledge of only three model parameters.

Previous implementations of arterial TF models have relied on central-peripheral pulse transit time measurements to characterise the model, and identify the remaining parameters by fitting to some *a priori* aspect of the expected pulse. Because of the inherent error associated with measuring PTT using an ECG recording, and the potential unavailability of such recordings when using partial or retrospective data sets, a novel method of identifying TF model parameters was developed in Chapter 8 Pulse wave analysis of peripheral arterial pressure measurements was used to exact information about interaction of forward travelling and reflected waves, which were combined with simple physiological assumptions to estimate central pressure and flow pulses. The pro-

posed quadrangular method produced a better fit to aortic flow probe measurements than the commonly used triangular approximation.

In Chapter 9, central pressure estimates were derived for 7 pig experiments using the initial estimates obtained through PWA of the femoral pressure measurements. Despite only using a singular measurement, the proposed TF_{SM} method accurately estimated invasive $P_{ao,mea}$ measurements. Furthermore, little improvement was seen when utilizing measurement PTT in the model. Finally, the TF_{SM} method produced errors very similar to pressure estimates produced using $P_{ao,mea}$ to identify model parameters, via minimization of the RMSE with model outputs.

The corresponding flow waveform output produced using the TF_{SM} method was further investigated in Chapter 10. Using an initial calibration measurement of SV, the TF_{SM} method produced estimates for SV for 7 of the porcine experiments up to, and including endotoxin infusion. Three of the experiments survived post- endotoxin infusion. Original and re-calibrated SV_{est} were assessed for these subjects. Threshold accuracy fell between two recommendation from the literature, but SV_{est} was able to track SV_{mea} adequately by all standards.

Chapter 11 presented an initial validation of the clinically feasible implementation of the TCM model in porcine endotoxin experiments. Two versions of the method were considered, both using $P_{ao,est}$ derived from the TF_{SM} method, but differing in the SV used, either SV_{est} from Chapter 10 or SV_{mea}. A new method for determining the exponential terms characterizing left ventricle diastolic pressure based on the central venous pulse was implemented. This method showed an improvement over the constant terms,

even though the constants were determined by eye to best fit the data, improving the generalizability of the model. The primary parameter of interest, SBV_m, was identified with a mean bias and limits of agreement of 1.3 (-19.3, 21.9)% and -6.2 (-148.4, 36.0)% using SV_{mea} and SV_{est}, respectively, compared to the reference TCM_{FM} parameters. This chapter represented the achievement of the second objective of this thesis.

Finally, Chapter 12 included a first application of the TCM on human data, obtained from patients in the ICU, to assess fluid responsiveness. While only 10 fluid therapies each from different patients were available for analysis, identified SBV_m performed equally as well as the current clinical metric of PPV. However, SBV_m does not have the same limitations as PPV, specifically, the requirements for patients to be mechanically ventilated. Thus, further study on a larger set of patients is warranted. This chapter represents the achievement of the final goal of this thesis.

In meeting the main goals stated above, this thesis has provided a first ever validation of model-based stressed blood volume as an index of fluid responsiveness in human patients. The proposed methods required no additional measurements to what are currently available in an ICU, allowing it to be easily and widely implemented. The clinical utility of the remaining model parameters in describing cardiac efficiency, and offering insight into a patients response to fluids was also investigated for the first time.

In order to be successful, this work required novel advancements in methods of estimating left ventricle pressure and volume and central pressure. A novel method of identifying the parameters of an arterial transfer function model produced central pressure estimated close to the best achievable, given the model equations.

An adaptive method for estimating left ventricle diastolic flow was developed, using a patient's own measurements of central venous pressure. This method was instrumental allowing the method to be transferred from porcine to human data, and still produce physiologically reasonable estimates.

Finally, the arterial transfer function model was also used, with a single calibration SV measurement, to continuously estimate SV in several porcine experiments. This method was able to track aortic flow probe measurement within acceptable limits during the effects of septic shock, even when peripheral and central arterial pressures became decoupled.

Chapter 14

Future Work

Several avenues of potential future work are explored in this section to highlight some of the unresolved limitations of this thesis. First and foremost, SBV_m needs to be validated on a significantly larger cohort of patient data. Although Chapter 12 was successful in providing an initial implementation of the model, justifying further research, patient numbers too few to draw conclusions about the applicability of the model. A larger cohort of patients is required in order to determine the likely thresholds for SBV_m in predicting fluid responsiveness.

Future works including observational trials are required to have a better understanding of the timing and duration of fluid therapies, required for accurate assessment of a patients' response to fluids. Ideally, echocardiography would be used to obtain the ventricular V_{es} instead of the population averages used for the human study in this thesis. The assumed relation between V_{es} and body size is likely a significant source during identification,

producing value of SBV_m differing from true stressed blood volume by at least the error in the V_{es} estimate.

Additionally an observational study would allow for an investigation into monitoring the elastance parameters during treatment of hypertension may provide a useful diagnostic tool for assess the impact of vasoactive drugs, as well as assess overall cardiac efficiency defined by the VAC. Monitoring VAC in patients presenting with septic shock may provide a crucial diagnostic tool to clinicians when a patient is deemed to be fluid unresponsive. While fluid therapy is an important treatment, it is far from the only means of treating circulatory shock, and restoring cardiac efficiency in unresponsive patients, through the use of vasoactive drugs, could be guided using the TCM and the identified elastances which may justify further investigation into these parameters.

The central pressure estimates obtained using the TF_{SM} method saw a reduction in accuracy in data presenting with low pulse transit times and early arriving reflected waves. This effect is attributable to the pressure estimate obtained from pulse wave analysis of the peripheral measurement. Specifically, the constant pressure approximation used for the majority of systole, prevents the TF model from identifying lower PTT values as this would produce a narrower systolic peak increasing the RMSE. A potential modification to the method may involve the decomposition of the peripheral pulse into its forward and reflected components using an assumed flow shape. The forward waveform contour would then provide a better approximation of central pressure during systole, compared to a constant pressure. This will also improve the corresponding flow waveform accuracy and thus, estimated SV.

A primary limitation associated with the central blood pressure estimation method developed in this thesis, $P_{ao,est}$, was the assumption $Q_{ao,est}$ and $Q_{ao,mea}$ had similar contours. While this was seen to be true for large parts of the experiment, once septic shock was induced a significant disparity was seen between the two flow profiles. This is because $Q_{ao,est}$ actually represents the component of total flow entering the tube, not the central flow. Therefore, $Q_{ao,est}$ is more associated with the femoral artery flow than central flow. Adjusting the proposed $Q_{ao,int}$ to reflect this fact, by adjusting the timing of peak flow and not necessarily enforcing the zero diastolic flow criteria, may improve the accuracy of the parameter identification.

Furthermore, using $Q_{ao,est}$ to approximate stroke volume may not be applicable to other peripheral arteries which have an associated flow contour with a significantly different contour than $Q_{ao,mea}$. The femoral flow wave often has a similar profile to the central wave, albeit very different absolute values, however, the radial pulse may not produce such consistent results. As radial artery pressure measurement are very common in the ICU, the applicability of the proposed method needs to be tested on alternate peripheral locations.

Finally, two further avenues of study are concerned with assumptions used in the TCM itself. First, the effects of blood flow inertia during ejection needs to be considered. Although previous works showed the inertial effects had little influence on the identified model parameters, these works also used reference values taken from direct measurements for identification, which may have allowed these effects to be inherently included. Specifically, including measured left ventricle pressure in the driver function would re-

duce model error by differentiating simulated ventricular pressure from central pressure. In contrast, this work used central pressure to estimate ventricular pressure and thus, the two profiles were identical during systole. Accounting for inertial effects in the driver function and in the TCM itself, by integrating an inertial term into the arterial flow equations, may improve the models ability to accurately simulate the output waveforms.

Second, the ventricular unstressed volume in this work was assumed to be zero. Physiologically, it is reasonable to assume it would actually be some positive number. This would directly influence the shape of the driver function and the resulting parameter identification. The zero assumption used may explain why the VAC values presented in Chapter 4 were slightly elevated at the start of the experiments, from what would be expected in a healthy subject. A positive V_u value would result in an increased cardiac contractility, E_{lv}, reducing VAC. Considering non-zero V_u values, non-linear or bi-linear end-systolic pressure-volume relations would likely improve the accuracy of the TCM.

Bibliography

[1] Gary A Thibodeau and Kevin T Patton. Anatomy & physiology. Mosby, 2003.

[2] John KJ Li. Dynamics of the vascular system, volume 1. World scientific, 2004.

[3] Simon Gelman. Venous Function and Central Venous Pressure. 108(4):14, 2008.

[4] S. Magder. Volume and its relationship to cardiac output and venous return. Critical Care, 20(1):271, December 2016.

[5] David Berger and Jukka Takala. Determinants of systemic venous return and the impact of positive pressure ventilation. Annals of Translational Medicine, 6(18):350–350, September 2018.

[6] Tao Shen and Keith Baker. Venous return and clinical hemodynamics: how the body works during acute hemorrhage. Advances in Physiology Education, 39(4):267–271, December 2015.

[7] David A. Berlin and Jan Bakker. Understanding venous return. Intensive Care Medicine, 40(10):1564–1566, October 2014.

[8] Daniel A. Beard and Eric O. Feigl. Understanding Guyton's venous return curves.

American Journal of Physiology-Heart and Circulatory Physiology, 301(3):H629–H633, September 2011.

[9] Arthur C Guyton. Determination of cardiac output by equating venous return curves with cardiac response curves. Physiological reviews, 35:123–129, 1955.

[10] Simon Gelman and Luca Bigatello. The physiologic basis for goal-directed hemodynamic and fluid therapy: the pivotal role of the venous circulation. Canadian Journal of Anesthesia/Journal canadien d'anesthésie, 65(3):294–308, March 2018.

[11] S. Magder and Benoit De Varennes. Clinical deth and the measurement of stressed vascular volume. Critical care medicine, 26(6):1061–1064, 1998.

[12] Anthony V. Delicce and Amgad N. Makaryus. Physiology, Frank Starling Law. StatPearls Publishing, Treasure Island (FL).

[13] Paul E. Marik. The Physiology of Volume Resuscitation. Current Anesthesiology Reports, 4(4):353–359, December 2014.

[14] Paul E Marik, Xavier Monnet, and Jean-Louis Teboul. Hemodynamic parameters to guide fluid therapy. page 9, 2011.

[15] Rachel Smith, J. Geoffrey Chase, Christopher G. Pretty, Shaun Davidson, Geoffrey M. Shaw, and Thomas Desaive. Preload & Frank-Starling curves, from textbook to bedside: Clinically applicable non-additionally invasive model-based estimation in pigs. Computers in Biology and Medicine, 135:104627, August 2021.

[16] Hiroyuki Suga, Kiichi Sagawa, and Artin A. Shoukas. Load Independence of the Instantaneous Pressure-Volume Ratio of the Canine Left Ventricle and Effects of

Epinephrine and Heart Rate on the Ratio. Circulation Research, 32(3):314–322, March 1973.

[17] Hiroyuki Suga and Kiichi Sagawa. Instantaneous Pressure-Volume Relationships and Their Ratio in the Excised, Supported Canine Left Ventricle. Circulation Research, 35(1):117–126, July 1974.

[18] Philippe Morimont, Bernard Lambermont, Thomas Desaive, Nathalie Janssen, Geoffrey Chase, and Vincent D'Orio. Arterial dP/dtmax accurately reflects left ventricular contractility during shock when adequate vascular filling is achieved. BMC Cardiovascular Disorders, 12(1):13, December 2012.

[19] Astrid Lambrecht, Michael Vandenheuvel, Eck Mauermann, and Patrick Wouters. Single-Beat Estimation of Ventricular Contractility. SN Comprehensive Clinical Medicine, 3(4):1002–1017, April 2021.

[20] Hideaki Senzaki, Chen-Huan Chen, and David A Kass. Single-beat estimation of end-systolic pressure-volume relation in humans: a new method with the potential for noninvasive application. Circulation Research, 94(10):2497–2506, 1996.

[21] Ignatios Ikonomidis, Victor Aboyans, Jacque Blacher, Marianne Brodmann, Dirk L. Brutsaert, Julio A. Chirinos, Marco De Carlo, Victoria Delgado, Patrizio Lancellotti, John Lekakis, Dania Mohty, Petros Nihoyannopoulos, John Parissis, Damiano Rizzoni, Frank Ruschitzka, Petar Seferovic, Eugenio Stabile, Dimitrios Tousoulis, Dragos Vinereanu, Charalambos Vlachopoulos, Dimitrios Vlastos, Panagiotis Xaplanteris, Reuven Zimlichman, and Marco Metra. The role of ventricular–arterial coupling in cardiac disease and heart failure: assessment, clinical

implications and therapeutic interventions. A consensus document of the European Society of Cardiology Working Group on Aorta & Peripheral Vascular Diseases, European Association of Cardiovascular Imaging, and Heart Failure Association. European Journal of Heart Failure, 21(4):402–424, April 2019.

[22] Bernard Cholley and Arthur Le Gall. Ventriculo-arterial coupling: the comeback? Journal of Thoracic Disease, 8(9):2287–2289, September 2016.

[23] David A. Kass and Raymond P. Kelly. Ventriculo-arterial coupling: Concepts, assumptions, and applications. Annals of Biomedical Engineering, 20(1):41–62, January 1992.

[24] Manuel Ignacio Monge García and Arnoldo Santos. Understanding ventriculo-arterial coupling. Annals of Translational Medicine, 8(12):795–795, June 2020.

[25] Michael R. Pinsky and Fabio Guarracino. How to assess ventriculoarterial coupling in sepsis:. Current Opinion in Critical Care, 26(3):313–318, June 2020.

[26] Vinay Kumar. Robbins basic pathology (8th ed.). Elsevier, 8 edition, 2007.

[27] Jr Greer. Pathophysiology of cardiovascular dysfunction in sepsis. BJA Education, 15(6):316–321, December 2015.

[28] Warren L Lee. Sepsis and Endothelial Permeability. n engl j med, page 4, 2010.

[29] Abdalsamih M. Taeb, Michael H. Hooper, and Paul E. Marik. Sepsis: Current Definition, Pathophysiology, Diagnosis, and Management. Nutrition in Clinical Practice, 32(3):296–308, June 2017.

[30] Richard S. Hotchkiss, Lyle L. Moldawer, Steven M. Opal, Konrad Reinhart, Isaiah R. Turnbull, and Jean-Louis Vincent. Sepsis and septic shock. Nature Reviews Disease Primers, 2(1):16045, December 2016.

[31] Michael Bauer, Herwig Gerlach, Tobias Vogelmann, Franziska Preissing, Julia Stiefel, and Daniel Adam. Mortality in sepsis and septic shock in Europe, North America and Australia between 2009 and 2019— results from a systematic review and meta-analysis. Critical Care, 24(1):239, December 2020.

[32] Jean-Louis Vincent, Gabriel Jones, Sholto David, Elena Olariu, and Kevin K. Cadwell. Frequency and mortality of septic shock in Europe and North America: a systematic review and meta-analysis. Critical Care, 23(1):196, December 2019.

[33] Søren R. Boysen and Kris Gommeren. Assessment of Volume Status and Fluid Responsiveness in Small Animals. Frontiers in Veterinary Science, 8:630643, May 2021.

[34] Xavier Monnet and Jean-Louis Teboul. Assessment of fluid responsiveness: recent advances. Current Opinion in Critical Care, 24(3):190–195, June 2018.

[35] Xavier Monnet and Jean-Louis Teboul. Passive leg raising: five rules, not a drop of fluid! Critical Care, 19(1):18, December 2015.

[36] Xavier Monnet and Michael R. Pinsky. Predicting the determinants of volume responsiveness. Intensive Care Medicine, 41(2):354–356, February 2015.

[37] Xavier Monnet, Paul E. Marik, and Jean-Louis Teboul. Prediction of fluid responsiveness: an update. Annals of Intensive Care, 6(1):111, December 2016.

[38] Rostislav Enev, Plamen Krastev, and Filip Abedinov. Prediction of fluid responsiveness: a review. Biotechnology & Biotechnological Equipment, 35(1):1147–1155, January 2021.

[39] Sabrina Arshed and Michael R. Pinsky. Applied Physiology of Fluid Resuscitation in Critical Illness. Critical Care Clinics, 34(2):267–277, April 2018.

[40] Fabio Guarracino, Pietro Bertini, and Michael R. Pinsky. Cardiovascular determinants of resuscitation from sepsis and septic shock. Critical Care, 23(1):118, December 2019.

[41] R. Phillip Dellinger, Christa A. Schorr, and Mitchell M. Levy. A Users' Guide to the 2016 Surviving Sepsis Guidelines:. Critical Care Medicine, 45(3):381–385, March 2017.

[42] Jonathan D. Casey, Ryan M. Brown, and Matthew W. Semler. Resuscitation fluids:. Current Opinion in Critical Care, 24(6):512–518, December 2018.

[43] Diego Orbegozo Cortés, Teresa Gamarano Barros, Hassane Njimi, and Jean-Louis Vincent. Crystalloids Versus Colloids: Exploring Differences in Fluid Requirements by Systematic Review and Meta-Regression. Anesthesia & Analgesia, 120(2):389–402, February 2015.

[44] Jorge Iván Alvarado Sánchez, William Fernando Amaya Zúñiga, and Manuel Ignacio Monge García. Predictors to Intravenous Fluid Responsiveness. Journal of Intensive Care Medicine, 33(4):227–240, April 2018.

[45] Xavier Monnet, Paul Marik, and Jean-Louis Teboul. Passive leg raising for pre-

dicting fluid responsiveness: a systematic review and meta-analysis. Intensive Care Medicine, 42(12):1935–1947, December 2016.

[46] Diana J. Kelm, Jared T. Perrin, Rodrigo Cartin-Ceba, Ognjen Gajic, Louis Schenck, and Cassie C. Kennedy. Fluid Overload in Patients With Severe Sepsis and Septic Shock Treated With Early Goal-Directed Therapy Is Associated With Increased Acute Need for Fluid-Related Medical Interventions and Hospital Death. Shock, 43(1):68–73, January 2015.

[47] J. Lee, E. de Louw, M. Niemi, R. Nelson, R. G. Mark, L. A. Celi, K. J. Mukamal, and J. Danziger. Association between fluid balance and survival in critically ill patients. Journal of Internal Medicine, 277(4):468–477, April 2015.

[48] Ling Zhang, Zhiwen Chen, Yongshu Diao, Yingying Yang, and Ping Fu. Associations of fluid overload with mortality and kidney recovery in patients with acute kidney injury: A systematic review and meta-analysis. Journal of Critical Care, 30(4):860.e7–860.e13, August 2015.

[49] Meiping Wang, Bo Zhu, Li Jiang, Ying Wen, Bin Du, Wen Li, Guangxu Liu, Wei Li, Jing Wen, Yan He, and Xiuming Xi. Dose–response association between fluid overload and in-hospital mortality in critically ill patients: a multicentre, prospective, observational cohort study. BMJ Open, 10(12):e039875, December 2020.

[50] Paul E. Marik, Liam Byrne, and Frank van Haren. Fluid resuscitation in sepsis: the great 30 mL per kg hoax. Journal of Thoracic Disease, 12(S1):S37–S47, February 2020.

[51] Laurent Guerin, Xavier Monnet, and Jean-Louis Teboul. Monitoring volume and fluid responsiveness: From static to dynamic indicators. Best Practice & Research Clinical Anaesthesiology, 27(2):177–185, June 2013.

[52] Bilal A. Jalil and Rodrigo Cavallazzi. Predicting fluid responsiveness: A review of literature and a guide for the clinician. The American Journal of Emergency Medicine, 36(11):2093–2102, November 2018.

[53] K Bendjelid. Fluid responsiveness in mechanically ventilated patients: a review of indices used in intensive care. page 9.

[54] Federico Piccioni, Filippo Bernasconi, Giulia T. A. Tramontano, and Martin Langer. A systematic review of pulse pressure variation and stroke volume variation to predict fluid responsiveness during cardiac and thoracic surgery. Journal of Clinical Monitoring and Computing, 31(4):677–684, August 2017.

[55] Abhishek Rathore, Shalendra Singh, Ritesh Lamsal, Priya Taank, and Debashish Paul. Validity of Pulse Pressure Variation (PPV) Compared with Stroke Volume Variation (SVV) in Predicting Fluid Responsiveness. Turkish Journal of Anesthesia and Reanimation, 45(4):210–217, August 2017.

[56] G. Marx, T. Cope, L. McCrossan, S. Swaraj, and C. Cowan. Assessing fluid responsiveness by stroke volume variation in mechanically ventilated patients with severe sepsis. European Journal of Anaesthesiology, 21(2):132–138, 2004.

[57] Joya D. Pickett, Elizabeth Bridges, Patricia A. Kritek, and JoAnne D. Whitney. Passive Leg-Raising and Prediction of Fluid Responsiveness: Systematic Review. Critical Care Nurse, 37(2):32–47, April 2017.

[58] Rachel Smith, Liam Murphy, Christopher G. Pretty, Thomas Desaive, Geoffrey M. Shaw, and J. Geoffrey Chase. Tube-load model: A clinically applicable pulse contour analysis method for estimation of cardiac stroke volume. Computer Methods and Programs in Biomedicine, 204:106062, June 2021.

[59] Lester A H Critchley. A Meta-Analysis of Studies Using Bias and Precision Statistics to Compare Cardiac Output Measurement Techniques. page 7.

[60] S. Kamoi, C.G. Pretty, Y.S. Chiew, A. Pironet, S. Davidson, T. Desaive, G.M. Shaw, and J.G. Chase. Stroke Volume estimation using aortic pressure measurements and aortic cross sectional area: Proof of concept. In 2015 37th Annual International Conference of the IEEE Engineering in Medicine and Biology Society (EMBC), pages 1005–1008, Milan, August 2015. IEEE.

[61] Joel Balmer, Christopher G. Pretty, Shaun Davidson, Tashana Mehta-Wilson, Thomas Desaive, Rachel Smith, Geoffrey M. Shaw, and J. Geoffrey Chase. Clinically applicable model-based method, for physiologically accurate flow waveform and stroke volume estimation. Computer Methods and Programs in Biomedicine, 185:105125, March 2020.

[62] A Pironet, P Dauby, J G Chase, S Kamoi, N Janssen, P Morimont, B Lambermont, and T Desaive. Model-Based Stressed Blood Volume is an Index of Fluid Responsiveness. page 6, 2015.

[63] Jacinta J. Maas, Michael R. Pinsky, Leon P. Aarts, and Jos R. Jansen. Bedside Assessment of Total Systemic Vascular Compliance, Stressed Volume, and Car-

diac Function Curves in Intensive Care Unit Patients. Anesthesia & Analgesia, 115(4):880–887, October 2012.

[64] Kapil Gupta, Soren Sondergaard, Geoffrey Parkin, Mark Leaning, and Anders Aneman. Applying mean systemic filling pressure to assess the response to fluid boluses in cardiac post-surgical patients. Intensive Care Medicine, 41(2):265–272, February 2015.

[65] Antoine Pironet, Pierre C. Dauby, J. Geoffrey Chase, Paul D. Docherty, James A. Revie, and Thomas Desaive. Structural identifiability analysis of a cardiovascular system model. Medical Engineering & Physics, 38(5):433–441, May 2016.

[66] Antoine Pironet, Paul D. Docherty, Pierre C. Dauby, J. Geoffrey Chase, and Thomas Desaive. Practical identifiability analysis of a minimal cardiovascular system model. Computer Methods and Programs in Biomedicine, 171:53–65, April 2019.

[67] J. Geoffrey Chase, Jean-Charles Preiser, Jennifer L. Dickson, Antoine Pironet, Yeong Shiong Chiew, Christopher G. Pretty, Geoffrey M. Shaw, Balazs Benyo, Knut Moeller, Soroush Safaei, Merryn Tawhai, Peter Hunter, and Thomas Desaive. Next-generation, personalised, model-based critical care medicine: a state-of-the art review of in silico virtual patient models, methods, and cohorts, and how to validation them. BioMedical Engineering OnLine, 17(1):24, February 2018.

[68] Antoine Pironet. Model-Based Prediction of the Response to Vascular Filling Therapy. page 243.

[69] Antoine Pironet, Thomas Desaive, J. Geoffrey Chase, Philippe Morimont, and

Pierre C. Dauby. Model-based computation of total stressed blood volume from a preload reduction manoeuvre. Mathematical Biosciences, 265:28–39, July 2015.

[70] Ali Nasimi. Hemodynamics. In The Cardiovascular System. IntechOpen, 2012.

[71] Bram W. Smith, J.Geoffrey Chase, Roger I. Nokes, Geoffrey M. Shaw, and Graeme Wake. Minimal haemodynamic system model including ventricular interaction and valve dynamics. Medical Engineering & Physics, 26(2):131–139, March 2004.

[72] Bram W. Smith, J. Geoffrey Chase, Geoffrey M. Shaw, and Roger I. Nokes. A minimal cardiovascular system haemodynamic model for rapid diagnostic assistance. IFAC Proceedings Volumes, 36(15):427–432, August 2003.

[73] Shaun Davidson, Chris Pretty, Antoine Pironet, Shun Kamoi, Joel Balmer, Thomas Desaive, and J. Geoffrey Chase. Minimally invasive, patient specific, beat-by-beat estimation of left ventricular time varying elastance. BioMedical Engineering OnLine, 16(1):42, December 2017.

[74] David Stevenson, James Revie, J Geoffrey Chase, Christopher E Hann, Geoffrey M Shaw, Bernard Lambermont, Alexandre Ghuysen, Philippe Kolh, and Thomas Desaive. Beat-to-beat estimation of the continuous left and right cardiac elastance from metrics commonly available in clinical settings. BioMedical Engineering OnLine, 11(1):73, December 2012.

[75] David Stevenson, James Revie, J Geoffrey Chase, Christopher E Hann, Geoffrey M Shaw, Bernard Lambermont, Alexandre Ghuysen, Philippe Kolh, and Thomas Desaive. Algorithmic processing of pressure waveforms to facilitate estimation of cardiac elastance. BioMedical Engineering OnLine, 11(1):28, December 2012.

[76] Shaun M. Davidson, D. Oliver Kannangara, Chris G. Pretty, Shun Kamoi, Antoine Pironet, Thomas Desaive, and J. Geoffrey Chase. Modelling of the nonlinear end-systolic pressure-volume relation and volume-at-zero-pressure in porcine experiments. In 2015 37th Annual International Conference of the IEEE Engineering in Medicine and Biology Society (EMBC), pages 6544–6547, Milan, August 2015. IEEE.

[77] D A Kass, R Beyar, E Lankford, M Heard, W L Maughan, and K Sagawa. Influence of contractile state on curvilinearity of in situ end-systolic pressure-volume relations. Circulation, 79(1):167–178, January 1989.

[78] Moriz A Habigt, Michelle Krieger, Jonas Gesenhues, Maike Ketelhut, Mare Mechelinck, and Marc Hein. Non-linearity of end-systolic pressure–volume relation in afterload increases is caused by an overlay of shortening deactivation and the Frank–Starling mechanism. Scientific Reports, 11(1), 2021.

[79] Jan-Willem Lankhaar, Fleur A. Rövekamp, Paul Steendijk, Theo J. C. Faes, Berend E. Westerhof, Taco Kind, Anton Vonk-Noordegraaf, and Nico Westerhof. Modeling the Instantaneous Pressure–Volume Relation of the Left Ventricle: A Comparison of Six Models. Annals of Biomedical Engineering, 37(9):1710–1726, September 2009.

[80] L.F Murphy, J. G Chase, S. M Davidson, R. Smith, and T. Desaive. Minimally Invasive Model Based Stressed Blood Volume as an Index of Fluid Responsiveness. IFAC-PapersOnLine, 53(2):16257–16262, 2020.

[81] Liam Murphy, Shaun Davidson, J. Geoffrey Chase, Jennifer L. Knopp, Tony Zhou,

and Thomas Desaive. Patient-Specific Monitoring and Trend Analysis of Model-Based Markers of Fluid Responsiveness in Sepsis: A Proof-of-Concept Animal Study. Annals of Biomedical Engineering, 48(2):682–694, February 2020.

[82] R. Timothy Marler and Jasbir S. Arora. Function-transformation methods for multi-objective optimization. Engineering Optimization, 37(6):551–570, September 2005.

[83] Helmut Mausser. Normalization and Other Topics in MultiObjective.pdf, 2006.

[84] Bram W Smith, J Geoffrey Chase, Roger I Nokes, Geoffrey M Shaw, and Tim David. Velocity profile method for time varying resistance in minimal cardiovascular system models. Physics in Medicine and Biology, 48(20):3375–3387, October 2003.

[85] C. Starfinger, C.E. Hann, J.G. Chase, T. Desaive, A. Ghuysen, and G.M. Shaw. Model-based cardiac diagnosis of pulmonary embolism. Computer Methods and Programs in Biomedicine, 87(1):46–60, July 2007.

[86] Thomas Desaive, Oswaldo Horikawa, Jayme Pinto Ortiz, and J. Geoffrey Chase. Model-based management of cardiovascular failure: Where medicine and control systems converge. Annual Reviews in Control, 48:383–391, 2019.

[87] Antoine Pironet, Pierre C. Dauby, Sabine Paeme, Sarah Kosta, J. Geoffrey Chase, and Thomas Desaive. Simulation of Left Atrial Function Using a Multi-Scale Model of the Cardiovascular System. PLoS ONE, 8(6):e65146, June 2013.

[88] Fabio Guarracino, Baldassare Ferro, Andrea Morelli, Pietro Bertini, Rubia Bal-

dassarri, and Michael R Pinsky. Ventriculoarterial decoupling in human septic shock. Critical Care, 18(2):R80, 2014.

[89] Ranu Baral, Brodie Loudon, Michael P. Frenneaux, and Vassilios S. Vassiliou. Ventricular-vascular coupling in heart failure with preserved ejection fraction: A systematic review and meta-analysis. Heart & Lung, 50(1):121–128, January 2021.

[90] Marta Carrara, Manuela Ferrario, Bernardo Bollen Pinto, and Antoine Herpain. The autonomic nervous system in septic shock and its role as a future therapeutic target: a narrative review. Annals of Intensive Care, 11(1):80, December 2021.

[91] Marta Carrara, Antoine Herpain, Giuseppe Baselli, and Manuela Ferrario. Vascular Decoupling in Septic Shock: The Combined Role of Autonomic Nervous System, Arterial Stiffness, and Peripheral Vascular Tone. Frontiers in Physiology, 11:594, July 2020.

[92] Federico Montealegre and Bridget M. Lyons. Fluid Therapy in Dogs and Cats With Sepsis. Frontiers in Veterinary Science, 8:622127, February 2021.

[93] Lisa Smart and Dez Hughes. The Effects of Resuscitative Fluid Therapy on the Endothelial Surface Layer. Frontiers in Veterinary Science, 8:661660, May 2021.

[94] G. Marx. Fluid therapy in sepsis with capillary leakage. Cambridge University Press, 20(6):429–442, 2003.

[95] Elena V Dolmatova, Keke Wang, Rohan Mandavilli, and Kathy K Griendling. The effects of sepsis on endothelium and clinical implications. Cardiovascular Research, 117(1):60–73, January 2021.

[96] Elio Antonucci, Enrico Fiaccadori, Katia Donadello, Fabio Silvio Taccone, Federico Franchi, and Sabino Scolletta. Myocardial depression in sepsis: From pathogenesis to clinical manifestations and treatment. Journal of Critical Care, 29(4):500–511, August 2014.

[97] Shaun M. Davidson, Chris Pretty, Shun Kamoi, Joel Balmer, Thomas Desaive, and J. Geoffrey Chase. Real-Time, Minimally Invasive, Beat-to-Beat Estimation of End-Systolic Volume Using a Modified End-Systolic Pressure-Volume Relation. IFAC-PapersOnLine, 50(1):5456–5461, July 2017.

[98] Antoine Vieillard-Baron, Michel Slama, Bernard Cholley, Gérard Janvier, and Philippe Vignon. Echocardiography in the intensive care unit: from evolution to revolution? Intensive Care Medicine, 34(2):243–249, February 2008.

[99] Wilmer Nichols, Michael O'Rourke, and Charalambos Vlachopoulos. McDonald's Blood Flow in Arteries, Sixth Edition: Theoretical, Experimental and Clinical Principles. Number Book, Whole. CRC Press LLC, London, 2011.

[100] Alberto P Avolio, Mark Butlin, and Andrew Walsh. Arterial blood pressure measurement and pulse wave analysis-–their role in enhancing cardiovascular assessment. Physiological Measurement, 31(1):R1–R47, January 2010.

[101] Alberto P. Avolio, Luc M. Van Bortel, Pierre Boutouyrie, John R. Cockcroft, Carmel M. McEniery, Athanase D. Protogerou, Mary J. Roman, Michel E. Safar, Patrick Segers, and Harold Smulyan. Role of Pulse Pressure Amplification in Arterial Hypertension: Experts' Opinion and Review of the Data. Hypertension, 54(2):375–383, August 2009.

[102] Ahmed Qasem and Alberto Avolio. Determination of Aortic Pulse Wave Velocity From Waveform Decomposition of the Central Aortic Pressure Pulse. Hypertension, 51(2):188–195, February 2008.

[103] Ion Codreanu. Chasing the reflected wave back into the heart: a new hypothesis while the jury is still out. Vascular Health and Risk Management, page 365, June 2011.

[104] Marc L De Buyzere and Ernst R Rietzschel. Is It the Forward Wave Pressure That Matters? American Journal of Hypertension, 31(9):970–972, August 2018.

[105] N. Westerhof, N. Stergiopulos, M. I. M Noble, and B. E. Westerhof. Snapshots of hemodynamics : An aid for clinical research and graduate education. 2018.

[106] Arthur J. A. Leloup, Cor E. Van Hove, Annick Heykers, Dorien M. Schrijvers, Guido R. Y. De Meyer, and Paul Fransen. Elastic and Muscular Arteries Differ in Structure, Basal NO Production and Voltage-Gated Ca2+-Channels. Frontiers in Physiology, 6, December 2015.

[107] Joaquín Flores Gerónimo, Eugenia Corvera Poiré, Philip Chowienczyk, and Jordi Alastruey. Estimating Central Pulse Pressure From Blood Flow by Identifying the Main Physical Determinants of Pulse Pressure Amplification. Frontiers in Physiology, 12:608098, February 2021.

[108] Jonathan P. Mynard, Avinash Kondiboyina, Remi Kowalski, Michael M. H. Cheung, and Joseph J. Smolich. Measurement, Analysis and Interpretation of Pressure/Flow Waves in Blood Vessels. Frontiers in Physiology, 11:1085, August 2020.

[109] Chloe M. Park, Alun D. Hughes, Michael Y. Henein, and Ashraf W. Khir. Mechanisms of Aortic Flow Deceleration and the Effect of Wave Reflection on Left Ventricular Function. Frontiers in Physiology, 11:578701, November 2020.

[110] M F O'Rourke. Pressure and flow waves in systemic arteries and the anatomical design of the arterial system. Journal of Applied Physiology, 23(2):139–149, August 1967.

[111] John. K.-J. Li. Time Domain Resolution of Forward and Reflected Waves in the Aorta. IEEE Transactions on Biomedical Engineering, BME-33(8):783–785, August 1986.

[112] Jean-Pierre L. Dujardin and Dana N. Stone. Characteristic impedance of the proximal aorta determined in the time and frequency domain: a comparison. Medical & Biological Engineering & Computing, 19(5):565–568, September 1981.

[113] Gérard M. London and Alain P. Guerin. Influence of arterial pulse and reflected waves on blood pressure and cardiac function. American Heart Journal, 138(3):S220–S224, September 1999.

[114] Orestis Vardoulis, Theodore G. Papaioannou, and Nikolaos Stergiopulos. Validation of a novel and existing algorithms for the estimation of pulse transit time: advancing the accuracy in pulse wave velocity measurement. American Journal of Physiology-Heart and Circulatory Physiology, 304(11):H1558–H1567, June 2013.

[115] Wilmer W. Nichols, Scott J. Denardo, Ian B. Wilkinson, Carmel M. McEniery, John Cockcroft, and Michael F. O'Rourke. Effects of Arterial Stiffness, Pulse

Wave Velocity, and Wave Reflections on the Central Aortic Pressure Waveform. The Journal of Clinical Hypertension, 10(4):295–303, April 2008.

[116] Berend E. Westerhof, Ilja Guelen, Wim J. Stok, Karel H. Wesseling, Jos A. E. Spaan, Nico Westerhof, Willem Jan Bos, and Nikos Stergiopulos. Arterial pressure transfer characteristics: effects of travel time. American Journal of Physiology-Heart and Circulatory Physiology, 292(2):H800–H807, February 2007.

[117] Nikos Stergiopulos, Berend E. Westerhof, and Nico Westerhof. Physical basis of pressure transfer from periphery to aorta: a model-based study. American Journal of Physiology-Heart and Circulatory Physiology, 274(4):H1386–H1392, April 1998.

[118] Berend E. Westerhof, Ilja Guelen, Nico Westerhof, John M. Karemaker, and Alberto Avolio. Quantification of Wave Reflection in the Human Aorta From Pressure Alone: A Proof of Principle. Hypertension, 48(4):595–601, October 2006.

[119] Ian B. Wilkinson, Helen MacCallum, Laura Flint, John. R. Cockcroft, David. E. Newby, and David. J. Webb. The influence of heart rate on augmentation index and central arterial pressure in humans. The Journal of physiology, 525(1):263, 2000.

[120] Gary F. Mitchell. Arterial stiffness and wave reflection: Biomarkers of cardiovascular risk. Artery Research, 3(2):56, 2009.

[121] Shahzad Munir, Antoine Guilcher, Tamra Kamalesh, Brian Clapp, Simon Redwood, Michael Marber, and Philip Chowienczyk. Peripheral Augmentation Index Defines the Relationship Between Central and Peripheral Pulse Pressure. Hypertension, 51(1):112–118, January 2008.

[122] A.L. Pauca, N.D. Kon, and M.F. O'Rourke. The second peak of the radial artery pressure wave represents aortic systolic pressure in hypertensive and elderly patients. British Journal of Anaesthesia, 92(5):651–657, May 2004.

[123] K Kohara, Y Tabara, H Tomita, T Nagai, M Igase, and T Miki. Clinical usefulness of the second peak of radial systolic blood pressure for estimation of aortic systolic blood pressure. Journal of Human Hypertension, 23(8):538–545, August 2009.

[124] Shin-ichiro Katsuda, Hiroshi Miyashita, Kazuyuki Shimada, Yoshinori Miyawaki, Iwao Kojima, Yuri Shiogai, and Akihiro Hazama. Subservient relationship of the peripheral second systolic pressure peak to the central hemodynamic parameters is preserved, irrespective of atherosclerosis progression in hypercholesterolemic rabbits. Hypertension Research, 37(1):19–25, January 2014.

[125] Stacey S Hickson, Mark Butlin, Fraz A Mir, Johann Graggaber, Joseph Cheriyan, Fakhar Khan, Andrew A Grace, Yasmin, John R Cockcroft, Ian B Wilkinson, and Carmel M McEniery. The accuracy of central SBP determined from the second systolic peak of the peripheral pressure waveform. Journal of Hypertension, 27(9):1784–1788, September 2009.

[126] Nico Westerhof, Patrick Segers, and Berend E. Westerhof. Wave Separation, Wave Intensity, the Reservoir-Wave Concept, and the Instantaneous Wave-Free Ratio: Presumptions and Principles. Hypertension, 66(1):93–98, July 2015.

[127] Nicolaas Westerhof and Berend E. Westerhof. Waves and Windkessels reviewed. Artery Research, 18(C):102, 2017.

[128] Bernd Saugel, Ron Dueck, and Julia Y. Wagner. Measurement of blood pres-

sure. Best Practice & Research Clinical Anaesthesiology, 28(4):309–322, December 2014.

[129] H Lehman Li-wei, Mohammed Saeed, Daniel Talmor, Roger Mark, and Autl Malhotra. Methods of blood pressure measurement in the ICU. 41(1):34, 2013.

[130] Agnes S. Meidert and Bernd Saugel. Techniques for Non-Invasive Monitoring of Arterial Blood Pressure. Frontiers in Medicine, 4:231, January 2018.

[131] Yenly Nguyen and Vaibhav Bora. Arterial Pressure Monitoring. 2020.

[132] Paul E Marik. Chapter 91: Cardiac Output Measurement. page 12.

[133] Johan Huygh, Yannick Peeters, Jelle Bernards, and Manu L. N. G. Malbrain. Hemodynamic monitoring in the critically ill: an overview of current cardiac output monitoring methods. F1000Research, 5:2855, December 2016.

[134] Mainak Majumdar. Haemodynamic Monitoring in the Intensive Care Unit. In Nissar Shaikh, editor, Intensive Care. InTech, July 2017.

[135] Lester A. Critchley, Xiao X. Yang, and Anna Lee. Assessment of Trending Ability of Cardiac Output Monitors by Polar Plot Methodology. Journal of Cardiothoracic and Vascular Anesthesia, 25(3):536–546, June 2011.

[136] Philip J. Peyton and Simon W. Chong. Minimally Invasive Measurement of Cardiac Output during Surgery and Critical Care. Anesthesiology, 113(5):1220–1235, November 2010.

[137] Paul E. Marik. Noninvasive Cardiac Output Monitors: A State-of the-Art Review. Journal of Cardiothoracic and Vascular Anesthesia, 27(1):121–134, February 2013.

[138] R. P Smith, J. Argod, J.-L. Pepin, and P. A Levy. Pulse transit time: an appraisal of potential clinical applications. Thorax, 54(5):452–457, May 1999.

[139] R. A. Payne, C. N. Symeonides, D. J. Webb, and S. R. J. Maxwell. Pulse transit time measured from the ECG: an unreliable marker of beat-to-beat blood pressure. Journal of Applied Physiology, 100(1):136–141, January 2006.

[140] Guanqun Zhang, Mingwu Gao, Da Xu, N. Bari Olivier, and Ramakrishna Mukkamala. Pulse arrival time is not an adequate surrogate for pulse transit time as a marker of blood pressure. Journal of Applied Physiology, 111(6):1681–1686, December 2011.

[141] Joel Balmer, Christopher Pretty, Shaun Davidson, Thomas Desaive, Shun Kamoi, Antoine Pironet, Philippe Morimont, Nathalie Janssen, Bernard Lambermont, Geoffrey M Shaw, and J Geoffrey Chase. Pre-ejection period, the reason why the electrocardiogram Q-wave is an unreliable indicator of pulse wave initialization. Physiological Measurement, 39(9):095005, September 2018.

[142] Carmel M. McEniery, John R. Cockcroft, Mary J. Roman, Stanley S. Franklin, and Ian B. Wilkinson. Central blood pressure: current evidence and clinical importance. European Heart Journal, 35(26):1719–1725, July 2014.

[143] Ki-Hyun Jeon, Hack-Lyoung Kim, Woo-Hyun Lim, Jae-Bin Seo, Sang-Hyun Kim, Joo-Hee Zo, and Myung-A Kim. Associations between measurements of central blood pressure and target organ damage in high-risk patients. Clinical Hypertension, 27(1):23, December 2021.

[144] Mary J. Roman, Richard B. Devereux, Jorge R. Kizer, Elisa T. Lee, James M.

Galloway, Tauqeer Ali, Jason G. Umans, and Barbara V. Howard. Central Pressure More Strongly Relates to Vascular Disease and Outcome Than Does Brachial Pressure: The Strong Heart Study. Hypertension, 50(1):197–203, July 2007.

[145] Michel E. Safar and Piotr Jankowski. Central blood pressure and hypertension: role in cardiovascular risk assessment. Clinical Science, 116(4):273–282, February 2009.

[146] Michael Kostapanos, Carmel M. McEniery, and Ian B. Wilkinson. Clinical relevance of central blood pressure - a critical review. Vasa, 45(6):451–460, November 2016.

[147] Shuran Zhou, Lisheng Xu, Liling Hao, Hanguang Xiao, Yang Yao, Lin Qi, and Yudong Yao. A review on low-dimensional physics-based.pdf, 2019.

[148] Guanqun Zhang, Jin-Oh Hahn, and Ramakrishna Mukkamala. Tube-Load Model Parameter Estimation for Monitoring Arterial Hemodynamics. Frontiers in Physiology, 2, 2011.

[149] James E. Sharman, Richard Lim, Ahmad M. Qasem, Jeff S. Coombes, Malcolm I. Burgess, Jeff Franco, Paul Garrahy, Ian B. Wilkinson, and Thomas H. Marwick. Validation of a Generalized Transfer Function to Noninvasively Derive Central Blood Pressure During Exercise. Hypertension, 47(6):1203–1208, June 2006.

[150] Chen-Huan Chen, Erez Nevo, Barry Fetics, Peter H Pak, Frank CP Yin, W L Maughan, and D A Kass. Estimation of central aortic pressure waveform by mathematical transformation of radial tonometry pressure: validation of generalized transfer function. Circulation, 95(7):1827–1836, 1997.

[151] Jin-Oh Hahn. Individualized Estimation of the Central Aortic Blood Pressure Waveform: A Comparative Study. IEEE Journal of Biomedical and Health Informatics, 18(1):215–221, January 2014.

[152] Mingwu Gao, William C. Rose, Barry Fetics, David A. Kass, Chen-Huan Chen, and Ramakrishna Mukkamala. A Simple Adaptive Transfer Function for Deriving the Central Blood Pressure Waveform from a Radial Blood Pressure Waveform. Scientific Reports, 6(1):33230, December 2016.

[153] Jin-Oh Hahn, Andrew T. Reisner, and H. Harry Asada. Estimation of pulse transit time using two diametric blood pressure waveform measurements. Medical Engineering & Physics, 32(7):753–759, September 2010.

[154] Gokul Swamy, Da Xu, N. Bari Olivier, and Ramakrishna Mukkamala. An adaptive transfer function for deriving the aortic pressure waveform from a peripheral artery pressure waveform. American Journal of Physiology-Heart and Circulatory Physiology, 297(5):H1956–H1963, November 2009.

[155] Gokul Swamy, Ramakrishna Mukkamala, and N. Bari Olivier. Estimation of the aortic pressure waveform from a peripheral artery pressure waveform via an adaptive transfer function. In 2008 30th Annual International Conference of the IEEE Engineering in Medicine and Biology Society, pages 1385–1388, Vancouver, BC, August 2008. IEEE.

[156] Jin-Oh Hahn, Andrew T. Reisner, and H. Harry Asada. Blind Identification of Two-Channel IIR Systems With Application to Central Cardiovascular Monitor-

ing. Journal of Dynamic Systems, Measurement, and Control, 131(5):051009, September 2009.

[157] G. Swamy and R. Mukkamala. Estimation of the Aortic Pressure Waveform and Beat-to-Beat Relative Cardiac Output Changes From Multiple Peripheral Artery Pressure Waveforms. IEEE Transactions on Biomedical Engineering, 55(5):1521–1529, May 2008.

[158] J. Hahn, A. T. Reisner, F. A. Jaffer, and H. H. Asada. Subject-Specific Estimation of Central Aortic Blood Pressure Using an Individualized Transfer Function: A Preliminary Feasibility Study. IEEE Transactions on Information Technology in Biomedicine, 16(2):212–220, March 2012.

[159] G. Swamy, Da Xu, and R. Mukkamala. Estimation of the aortic pressure waveform from a radial artery pressure waveform via an adaptive transfer function: Feasibility demonstration in swine. In 2009 Annual International Conference of the IEEE Engineering in Medicine and Biology Society, pages 2362–2364, Minneapolis, MN, September 2009. IEEE.

[160] Masaru Sugimachi, Toshiaki Shishido, Kunio Miyatake, and Kenji Sunagawa. A New Model-Based Method of Reconstructing Central Aortic Pressure from Peripheral Arterial Pressure. The Japanese Journal of Physiology, 51(2):217–222, 2001.

[161] Berend E. Westerhof, Ilja Guelen, Wim J. Stok, Han A. J. Lasance, Carl A. P. L. Ascoop, Karel H. Wesseling, Nico Westerhof, Willem Jan W. Bos, Nikos Stergiopulos, and Jos A. E. Spaan. Individualization of transfer function in estimation of

central aortic pressure from the peripheral pulse is not required in patients at rest. Journal of Applied Physiology, 105(6):1858–1863, December 2008.

[162] Majid Abdollahzade, Chang-Sei Kim, Nima Fazeli, Barry A. Finegan, M. Sean McMurtry, and Jin-Oh Hahn. Data-Driven Lossy Tube-Load Modeling of Arterial Tree: In-Human Study. Journal of Biomechanical Engineering, 136(10):101011, October 2014.

[163] Azin Mousavi, Ali Tivay, Barry Finegan, Michael Sean McMurtry, Ramakrishna Mukkamala, and Jin-Oh Hahn. Tapered vs. Uniform Tube-Load Modeling of Blood Pressure Wave Propagation in Human Aorta. Frontiers in Physiology, 10:974, August 2019.

[164] Mingwu Gao and R. Mukkamala. Perturbationless calibration of pulse transit time to blood pressure. In 2012 Annual International Conference of the IEEE Engineering in Medicine and Biology Society, pages 232–235, San Diego, CA, August 2012. IEEE.

[165] Ru-Wen Chang, Chun-Yi Chang, Liang-Chuan Lai, Ming-Shiou Wu, Tai-Horng Young, Yih-Sharng Chen, Chih-Hsien Wang, and Kuo-Chu Chang. Determining arterial wave transit time from a single aortic pressure pulse in rats: vascular impulse response analysis. Scientific Reports, 7(1):40998, February 2017.

[166] Wenyan Liu, Daiyuan Song, Yang Yao, Lin Qi, Liling Hao, Jun Yang, Hongxia Ning, and Lisheng Xu. Determination of aortic pulse transit time based on waveform decomposition of radial pressure wave. Scientific Reports, 11(1):20154, December 2021.

[167] Ninette Shenouda, Joseph M. Stock, Jordan C. Patik, Julio A. Chirinos, and David G. Edwards. Personalized physiologic flow waveforms improve wave reflection estimates compared to triangular flow waveforms in adults. American Journal of Physiology-Heart and Circulatory Physiology, 320(5):H1802–H1812, May 2021.

[168] Yong-Liang Zhang, Ying-Ying Zheng, Zu-Chang Ma, and Yi-Ning Sun. Radial pulse transit time is an index of arterial stiffness. Hypertension Research, 34(7):884–887, July 2011.

[169] Feras Hatib, Jos R C Jansen, and Michael R Pinsky. Peripheral vascular decoupling in porcine endotoxic shock. J Appl Physiol, 111:8, 2011.

[170] Marta Carrara, Antoine Herpain, Giuseppe Baselli, and Manuela Ferrario. Vascular Decoupling in Septic Shock: The Combined Role of Autonomic Nervous System, Arterial Stiffness, and Peripheral Vascular Tone. Frontiers in Physiology, 11:594, July 2020.

[171] Rainer Storn. Differential Evolution – A Simple and Efficient Heuristic for Global Optimization over Continuous Spaces. DIFFERENTIAL EVOLUTION, page 19.

[172] Lachlan McKenzie. Development of a Hybrid Assist-as-need Hand Exoskeleton for Stroke Rehabilitation. page 231.

[173] George S Stergiou, Bruce Alpert, Stephan Mieke, Roland Asmar, Neil Atkins, Siegfried Eckert, Gerhard Frick, Bruce Friedman, Thomas Gra, Peter Lacy, Richard McManus, Alan Murray, Martin Myers, Paolo Palatini, Gianfranco Parati, David Quinn, Josh Sarkis, Andrew Shennan, Takashi Usuda, Jiguang Wang,

Colin O Wu, and Eoin O'Brien. A Universal Standard for the Validation of Blood Pressure Measuring Devices. page 7.

[174] Sang-Hyun Kim, Marc Lilot, Kulraj S. Sidhu, Joseph Rinehart, Zhaoxia Yu, Cecilia Canales, and Maxime Cannesson. Accuracy and Precision of Continuous Noninvasive Arterial Pressure Monitoring Compared with Invasive Arterial Pressure. Anesthesiology, 120(5):1080–1097, May 2014.

[175] Thomas Luecke and Paolo Pelosi. [No title found]. Critical Care, 9(6):607, 2005.

[176] Patrick A. Ross, Robinder G. Khemani, Sarah S. Rubin, Anoopindar K. Bhalla, and Christopher J. L. Newth. Elevated Positive End-Expiratory Pressure Decreases Cardiac Index in a Rhesus Monkey Model. Frontiers in Pediatrics, 2, December 2014.

[177] Lili Zhou, Guoen Cai, Zhihui Xu, Qinyong Weng, Qinyong Ye, and Cunrong Chen. High positive end expiratory pressure levels affect hemodynamics in elderly patients with hypertension admitted to the intensive care unit: a prospective cohort study. BMC Pulmonary Medicine, 19(1):224, December 2019.

[178] Feras Hatib, Jos R C Jansen, and Michael R Pinsky. Peripheral vascular decoupling in porcine endotoxic shock. J Appl Physiol, 111:8, 2011.

[179] Konstantinos Drosatos, Anastasios Lymperopoulos, Peter Johannes Kennel, Nina Pollak, P. Christian Schulze, and Ira J. Goldberg. Pathophysiology of Sepsis-Related Cardiac Dysfunction: Driven by Inflammation, Energy Mismanagement, or Both? Current Heart Failure Reports, 12(2):130–140, April 2015.

[180] P. Marik and R. Bellomo. A rational approach to fluid therapy in sepsis. British Journal of Anaesthesia, 116(3):339–349, March 2016.

[181] M.W. Merx and C. Weber. Sepsis and the Heart. Circulation, 116(7):793–802, August 2007.

[182] Steffen E. Petersen, Nay Aung, Mihir M. Sanghvi, Filip Zemrak, Kenneth Fung, Jose Miguel Paiva, Jane M. Francis, Mohammed Y. Khanji, Elena Lukaschuk, Aaron M. Lee, Valentina Carapella, Young Jin Kim, Paul Leeson, Stefan K. Piechnik, and Stefan Neubauer. Reference ranges for cardiac structure and function using cardiovascular magnetic resonance (CMR) in Caucasians from the UK Biobank population cohort. Journal of Cardiovascular Magnetic Resonance, 19(1):18, December 2017.

[183] Erlend Aune, Morten Bækkevar, Olaf Rødevand, and Jan Erik Otterstad. Reference values for left ventricular volumes with real-time 3-dimensional echocardiography. Scandinavian Cardiovascular Journal, 44(1):24–30, January 2010.

[184] Nadine Kawel-Boehm, Alicia Maceira, Emanuela R Valsangiacomo-Buechel, Jens Vogel-Claussen, Evrim B Turkbey, Rupert Williams, Sven Plein, Michael Tee, John Eng, and David A Bluemke. Normal values for cardiovascular magnetic resonance in adults and children. Journal of Cardiovascular Magnetic Resonance, 17(1):29, December 2015.

[185] S. Kou, L. Caballero, R. Dulgheru, D. Voilliot, C. De Sousa, G. Kacharava, G. D. Athanassopoulos, D. Barone, M. Baroni, N. Cardim, J. J. Gomez De Diego, A. Hagendorff, C. Henri, K. Hristova, T. Lopez, J. Magne, G. De La Morena, B. A.

Popescu, M. Penicka, T. Ozyigit, J. D. Rodrigo Carbonero, A. Salustri, N. Van De Veire, R. S. Von Bardeleben, D. Vinereanu, J.-U. Voigt, J. L. Zamorano, E. Donal, R. M. Lang, L. P. Badano, and P. Lancellotti. Echocardiographic reference ranges for normal cardiac chamber size: results from the NORRE study. European Heart Journal - Cardiovascular Imaging, 15(6):680–690, June 2014.

[186] DELAFIELD Du BOIS and EUGENE F. Du BOIS. CLINICAL CALORIMETRY: TENTH PAPER A FORMULA TO ESTIMATE THE APPROXIMATE SURFACE AREA IF HEIGHT AND WEIGHT BE KNOWN. Archives of Internal Medicine, XVII(6_2):863–871, June 1916.

[187] Bernie Hansen. Fluid Overload. Frontiers in Veterinary Science, 8:668688, June 2021.

Appendix A

Reference pressures

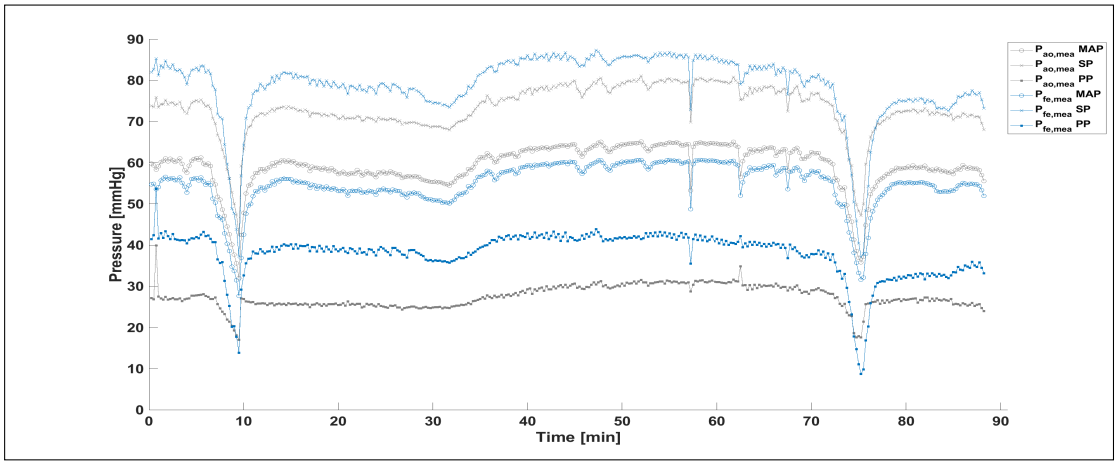

Figure A.1: Reference aortic mean, systolic and diastolic pressures for Pig 1.

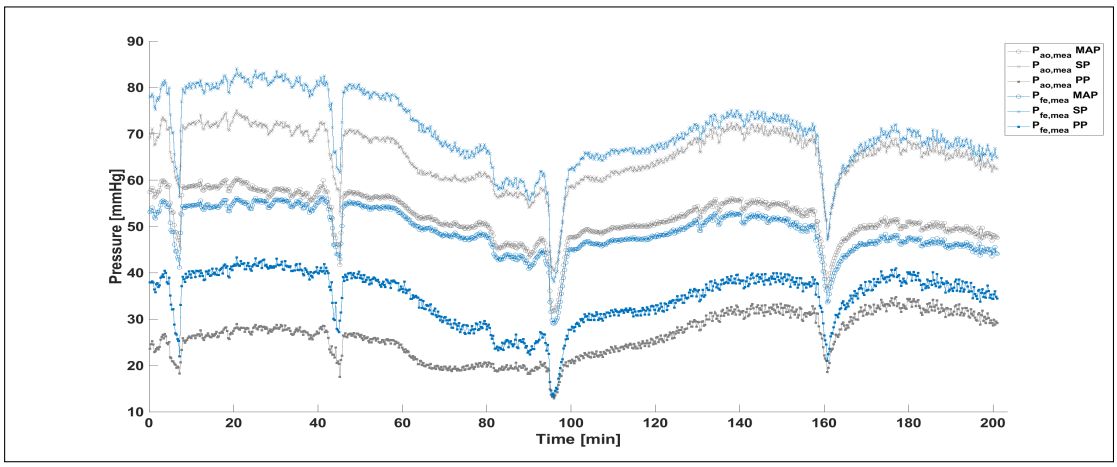

Figure A.2: Reference aortic mean, systolic and diastolic pressures for Pig 2.

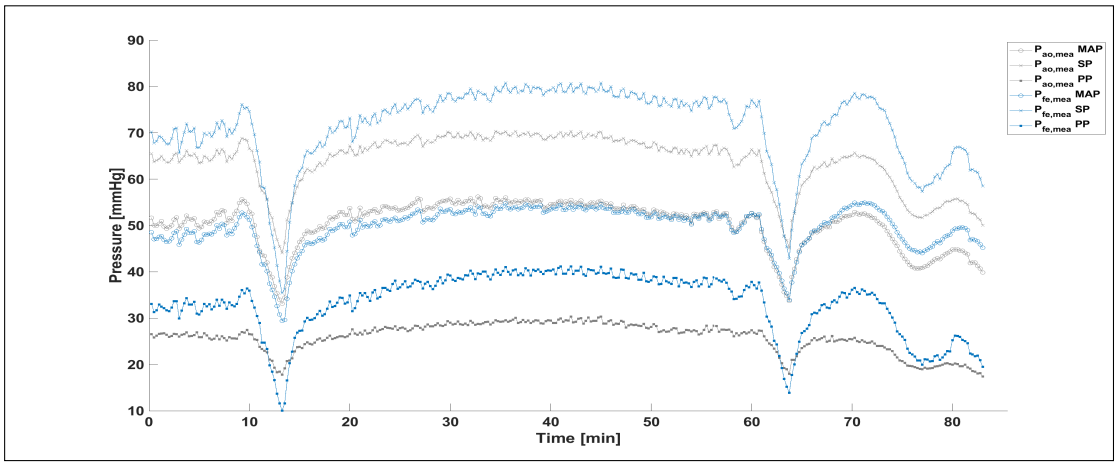

Figure A.3: Reference aortic mean, systolic and diastolic pressures for Pig 4.

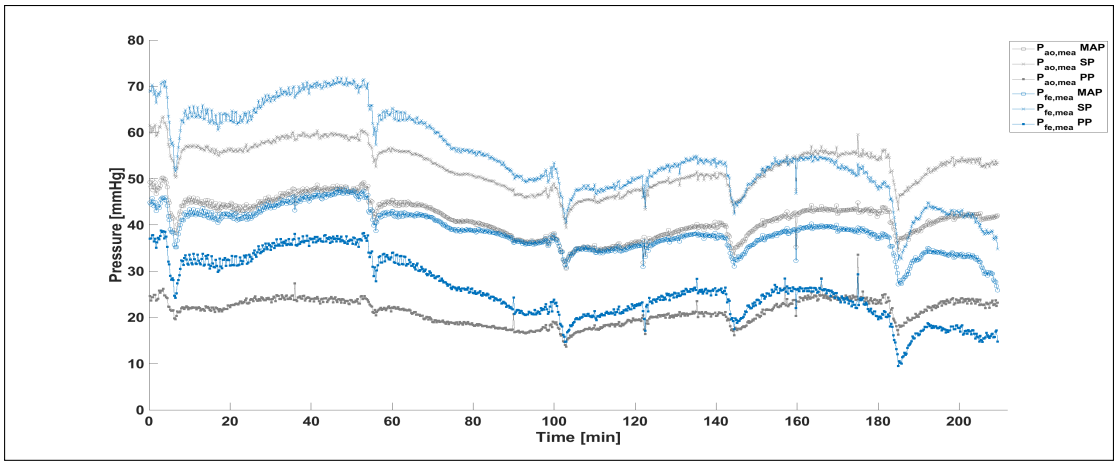

Figure A.4: Reference aortic mean, systolic and diastolic pressures for Pig 7.

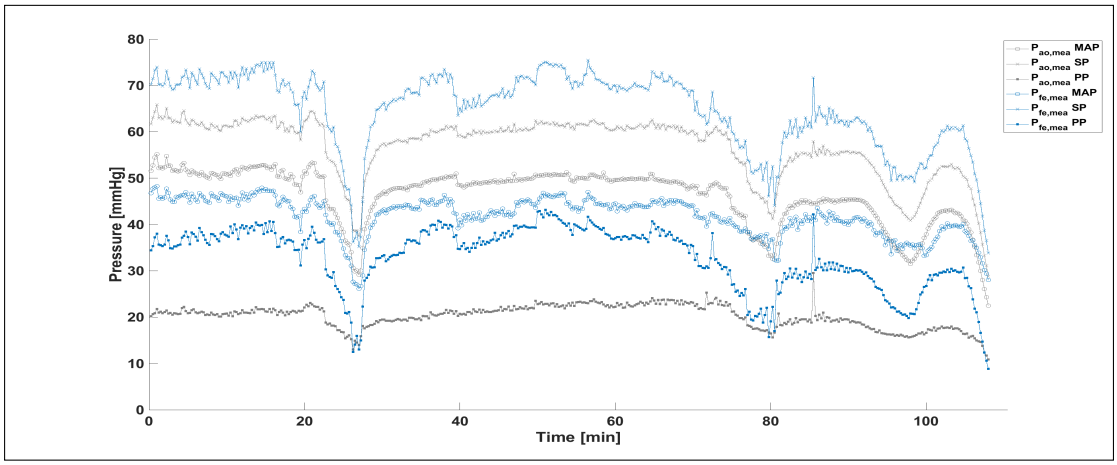

Figure A.5: Reference aortic mean, systolic and diastolic pressures for Pig 8.

Appendix B

TCM Parameters: Full measurement

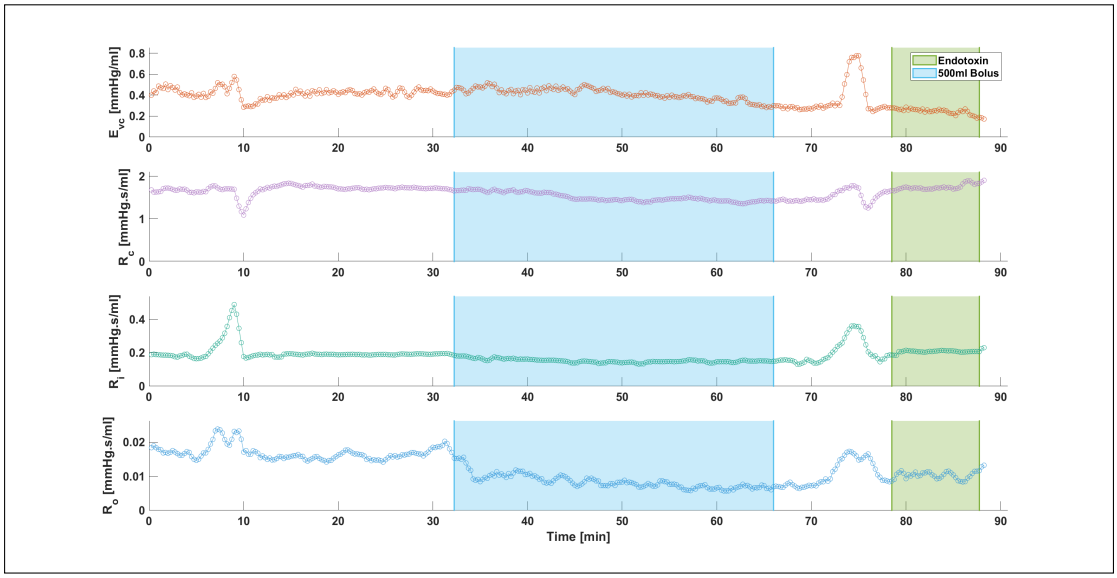

Figure B.1: Additional TCM parameters of E_{vc}, R_c, R_i and R_o identified for Pig 1.

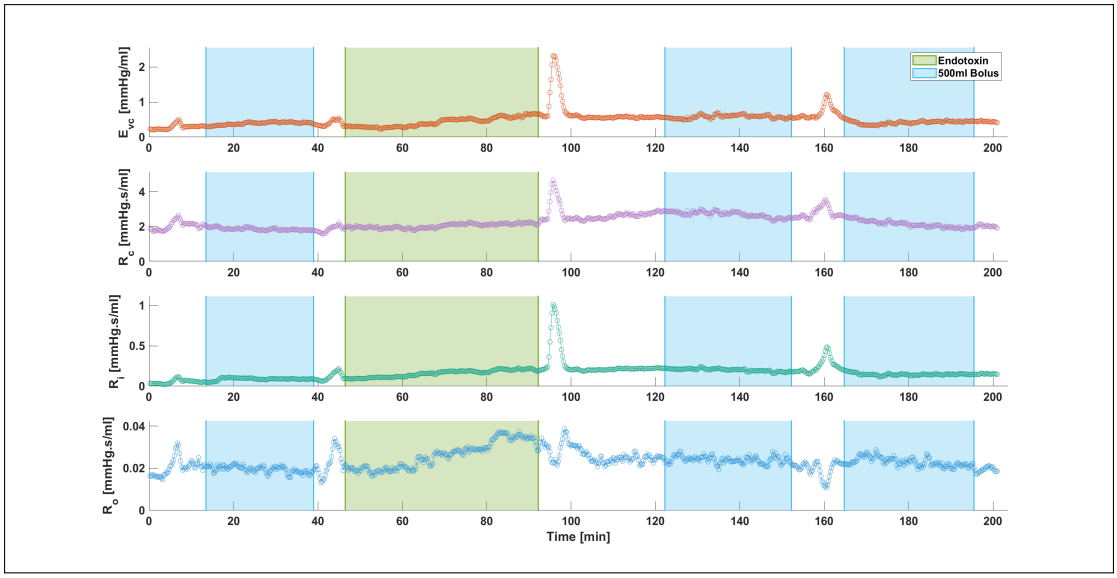

Figure B.2: Additional TCM parameters of E_{vc}, R_c, R_i and R_o identified for Pig 2.

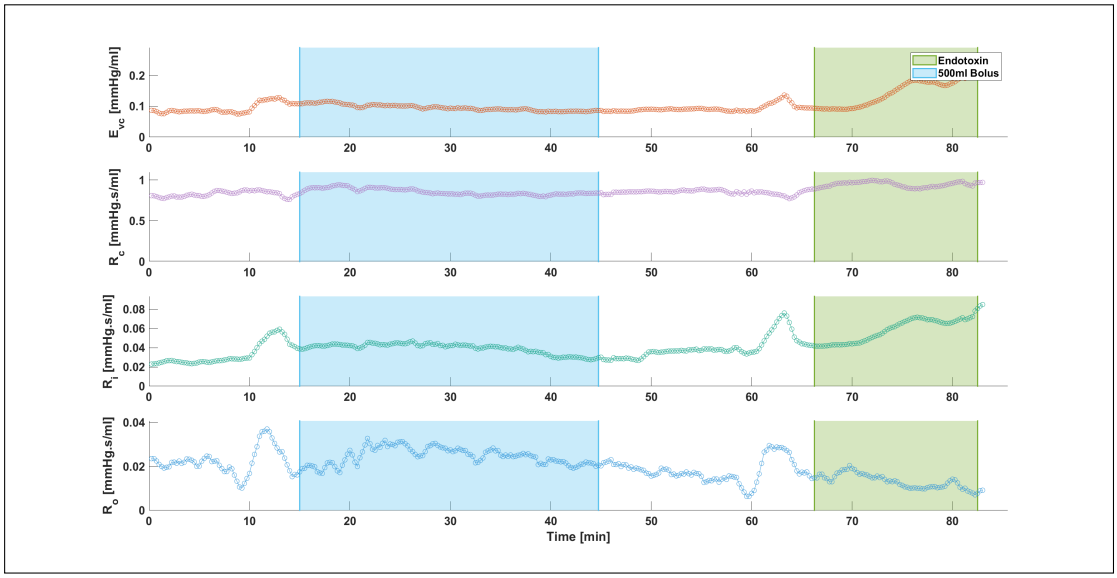

Figure B.3: Additional TCM parameters of E_{vc}, R_c, R_i and R_o identified for Pig 4.

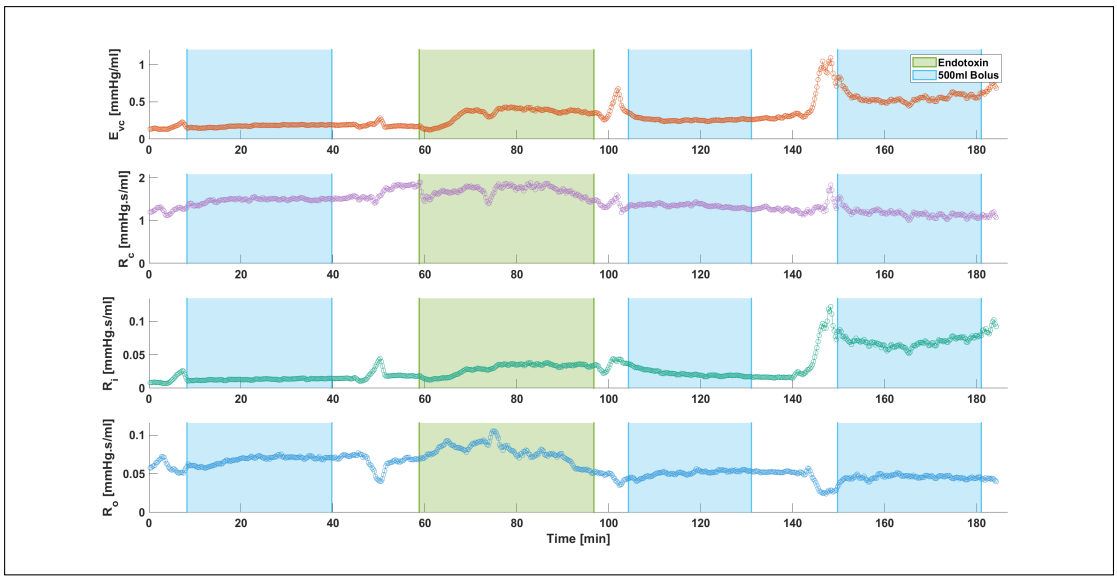

Figure B.4: Additional TCM parameters of E_{vc}, R_c, R_i and R_o identified for Pig 6.

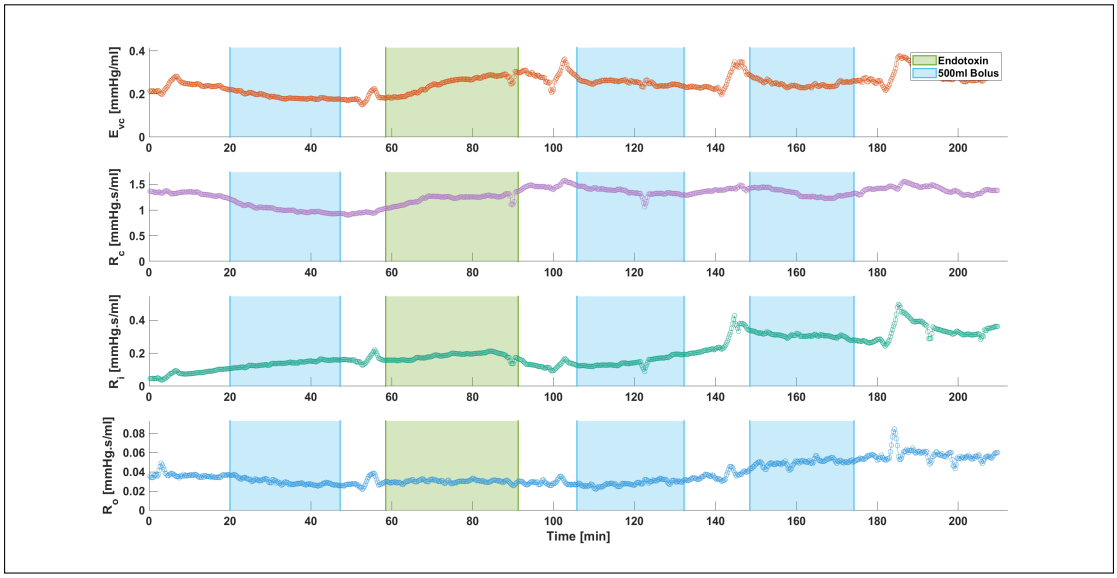

Figure B.5: Additional TCM parameters of E_{vc}, R_c, R_i and R_o identified for Pig 7.

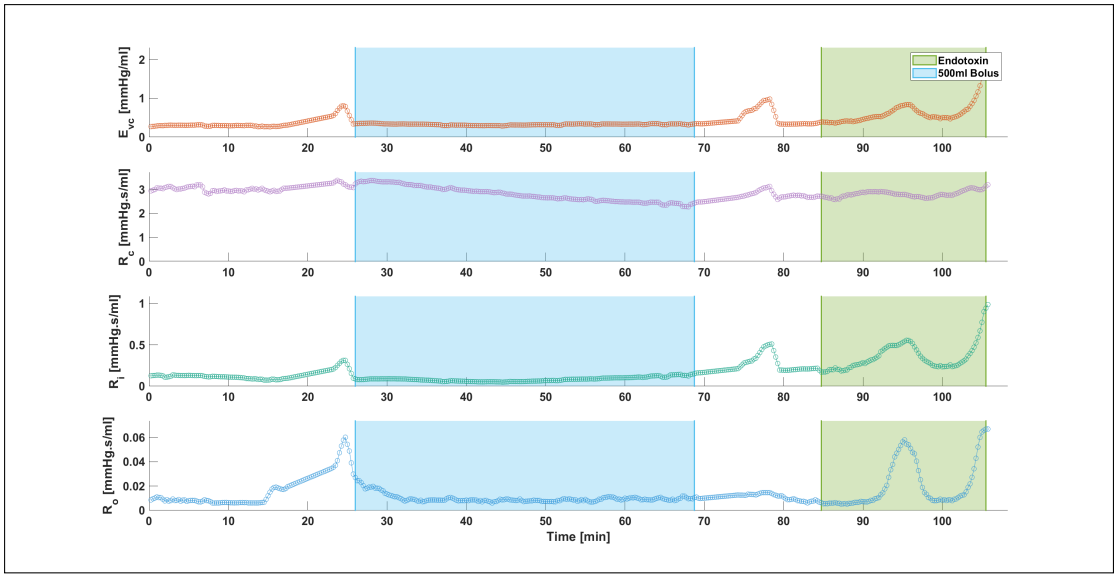

Figure B.6: Additional TCM parameters of E_{vc}, R_c, R_i and R_o identified for Pig 8.